



Skolkovo Institute of Science and Technology

ADVANCED CHARACTERIZATION METHODS OF MATERIALS AND REDOX  
MECHANISMS IN FLOW BATTERIES

*Doctoral Thesis*

by

NATALIYA GVOZDIK

DOCTORAL PROGRAM IN MATERIALS SCIENCE AND ENGINEERING

Supervisor  
Professor Keith Stevenson

Moscow - 2022

© Nataliya Gvozdk 2022

I hereby declare that the work presented in this thesis was carried out by myself at Skolkovo Institute of Science and Technology, Moscow, except where due acknowledgement is made, and has not been submitted for any other degree.

Candidate (Nataliya Gvozdk)

Supervisor (Prof. Keith Stevenson)

## Abstract

Energy storage systems are the essential elements of renewable-based power grids. Redox Flow Batteries (RFBs) are recognized as a perspective technology for such grids due to long cycle life, fast response, and independent power-capacity scaling. RFBs utilize liquid electrolytes, stored in reservoirs, and pumped through the electrochemical cell, where the redox reactions occur. The maximum specific capacity of RFB is determined by a solubility limit of redox-active materials in the electrolytes ( $< 40 \text{ Wh L}^{-1}$ ). Moreover, complete capacity utilization at rated power is rarely achieved in practice, which leads to high energy cost.

The incomplete capacity utilization is attributed either to ineffective cell design or to improper redox response in the case of newly developed chemistries. In this thesis, methods for identification of the insufficient capacity utilization reasons for both cases were developed based on the examples of vanadium RFB and redox-active colloids, as a new approach to the electrolyte capacity enhancement.

Vanadium RFB is a verified system with sluggish kinetics that requires effective cell design and material selection (bipolar plates and porous electrodes) for high capacity utilization. In this thesis, I proposed a benchmarking protocol for bipolar plate characterization and developed methods for kinetics investigation in porous electrodes.

Poor vanadium kinetics results in activation losses that become significant at low states of charges, decreasing the available capacity. The vanadyl oxidation reaction pathway on the carbon paper electrode for the first time was tracked by a spectroelectrochemical method based on in-situ Raman spectroscopy. The result of the

study was the reaction pathways scheme, indicating that the formation of vanadium complexes starts at lower overpotentials and occurs only on oxidized surfaces of the electrode. Furthermore, the numerical kinetic parameters for vanadium redox reactions were derived using a new method. Polarization curves from symmetrical cell equipped with reference electrodes were fitted by the upgraded model with activation losses. As a result, the apparent rate constants were evaluated, and noticeable asymmetry was observed for charge transfer coefficients with lower values for reduction reactions in both anolyte and catholyte.

Besides vanadium chemistry, I investigated minor capacity utilization issues of two redox-active colloids based on  $\text{LiMn}_2\text{O}_4$  nanoparticles and polymer microgels anchored by TEMPO molecules. A low conductivity of nanoparticles was the limiting factors in both cases, proven by a single-particle collision method.

Overall, this thesis proposes the state-of-the-art framework of material characterization methods, which are effective and industry applicable tools for diagnostic of inefficient capacity utilization of RFB.

## Publications

### Articles included in this thesis:

1. N. Gvozdik, K. Stevenson, In situ spectroelectrochemical Raman studies of vanadyl-ion oxidation mechanisms on carbon paper electrodes for vanadium flow batteries, *Electrochim. Acta.* 383 (2021) 138300. <http://dx.doi.org/10.1016/j.electacta.2021.138300>
2. E. Ruban, A. Stepashkin, N. Gvozdik, D. Konev, N. Kartashova, A. Antipov, M. Lyange, A. Usenko, Carbonized elastomer composite filled with hybrid carbon fillers for vanadium redox flow battery bipolar plates, *Mater. Today Commun.* 26 (2021) 101967. <http://dx.doi.org/10.1002/er.7088>
3. P. Loktionov, N. Kartashova, D. Konev, L. Abunaeva, A. Antipov, E. Ruban, A. Terent'ev, N. Gvozdik, M. Lyange, A. Usenko, K. Stevenson, Fluoropolymer impregnated graphite foil as a bipolar plates of vanadium flow battery, *Int. J. Energy Res.* (2021) 1–10. <https://doi.org/10.1002/er.7088>
4. E. Kozhunova, N. Gvozdik, M. Motyakin, O. Vyshivannaya, K. Stevenson, D. Itkis, A. Chertovich, Redox-Active Aqueous Microgels for Energy Storage Applications, *J. Phys. Chem. Lett.* 11 (2020) 1–5. <https://doi.org/10.1016/j.mtcomm.2020.101967>
5. N. Gvozdik, A. Kurbatova, N. Ovsyannikov, M. Pogosova, K. Stevenson, Influence of conductive additives in a nano-impact electrochemistry study of single LiMn<sub>2</sub>O<sub>4</sub> particles, *Electrochem. Commun.* (2022) 107304. <https://doi.org/10.1016/j.elecom.2022.107304>

## Conferences

1. Nataliya A. Gvozdik, Keith J. Stevenson, Factors leading to improved vanadium flow battery performance with thermally treated carbon paper electrodes. International Flow Battery Forum, July 2019, Lyon, France. (Poster) PP 100.
2. Nataliya A. Gvozdik, Keith J. Stevenson, Raman Spectroelectrochemical Studies of Vanadyl-Ion Oxidation on Carbon Paper Electrodes for Vanadium Redox Flow Batteries. The 239th ECS Meeting with the 18th International Meeting on Chemical Sensors (IMCS), May 2021, Online (Presentation) L01-1784.
3. Anna A. Kurbatova, Nataliya A. Gvozdik, Viktoria A. Nikitina, Keith J. Stevenson, Nanoimpact experiments of lithium-ion intercalating nanoparticles for redox flow batteries with solid boosters. XII International Conference on Chemistry for Young Scientists (Mendeleev 2021), September 2021, Saint Petersburg, Russia, Russia. (Poster) PP 1-52.
4. Nataliya A. Gvozdik, Aleksander A. Kurilovich, Keith J. Stevenson, Identification of Overpotentials in Vanadium Redox Flow Battery with Reference Electrodes and Determination of Apparent Electrochemical Rate Constants. The 241th ECS Meeting, May 2022, Online (Poster) L04-2033

## Acknowledgments

*This thesis is dedicated to my adorable parents, who supported me during this long path.*

I would like to sincerely thank Professor Keith Stevenson, who welcomed me to Skoltech and supervised my research for six years for his support and patience. I really appreciate that my supervisor gave me the opportunity to work on different projects and encouraged me to work independently. Professor Keith Stevenson supported a lot of my initiatives; probably, this is the reason, why my articles are devoted to various topics.

I am grateful to the jury committee who revised my thesis: Prof. Evgeny Antipov, Prof. Stanislav Fedotov, Prof. Oleg Levin, Prof. Zhumabay Bakenov, and Prof. Dmitry Shchukin. Their support and patience were very important for me. Additionally, I thank Prof. Artem Abakumov, Prof. Dmitry Gorin, and Prof. Alexei Buchachenko for their great courses and support during my Skoltech years.

I would like to thank all Skoltech facilities for creating an inspiring atmosphere with a comfortable infrastructure. The organization of the education process always stimulated me to get new experiences and try new things. I have the pleasure to meet many wonderful people, who shared their knowledge and experience. I want to say a huge thank to Prof. Vladimir Sergeyev and Prof. Victoria Nikitina for their mentoring. They were always ready to share their expertise and discuss strategies how to overcome experimental difficulties. Moreover, I appreciate how Dr. Andrey Usenko involved and trained me in the business side of flow batteries projects. Understanding connections between fundamental problems and real devices greatly stimulated further research activities.

I am glad that I witnessed the creation of a new laboratory (CEST labs). Being a part of a huge CEST team with many different interesting projects expands my scientific

background and shows alternative options for research. The open mindset and patience of all colleagues in the lab create a comfortable working environment. I would like to thank all the scientists who closely assisted me in the research activity. I am very grateful to the CEST laboratory staff for their support and assistance in the preparation of complex experiments. I am sure it would be difficult to implement at least one experiment without Artem Zaikin and Mikhail Afonin. A special acknowledgment to the awesome Skoltech Fablab headed by Vladimir Kalyaev, who provides high-quality parts of experimental setup very fast and without exhausting paperwork.

Coming now to the colleagues in the Flow Battery group, I would like to express gratitude to Mikhail Pugach, Aleksander Kurilovich, Nikita Akhmetov, Yaroslav Vlasov, and Prof. Federico Martin Ibanez. I feel that looking at the scientific problems of flow batteries from different points of view and learning how to work together was a valuable experience. I am immensely proud of two master's students who graduated during my Ph.D.: Nikolay Ovsyannikov and Valentin Vlasov.

Skoltech brought me to wonderful friends, who always supported me during the preparation of my thesis. I am grateful to those who periodically checked my texts, listened to the rehearsals of presentations, and switch-off weekend experiments: Anya Yarchuk, Alyona Alekseeva, Alyona Komayko, Yulia Kuzminova, Aram Mkrtchyan.

Finally, I express my sincere gratitude to my family: my husband Nikolay, who fed me chocolate and listened to my complaints; and my parents, who have always been the biggest support and the island of love for me.

## Table of Contents

<b>Abstract</b> .....	3
Publications.....	5
Conferences.....	6
Acknowledgments.....	7
Table of Contents .....	9
List of Symbols, Abbreviations .....	11
List of Figures .....	13
List of Tables .....	14
<b>Chapter 1. Introduction</b> .....	<b>15</b>
1.1 Energy Storage technologies.....	16
1.2 Battery energy storage systems overview .....	24
1.2.1 Lithium-ion batteries (LIBs) .....	24
1.2.2 Post Lithium-ion batteries.....	29
1.3 Redox flow batteries (RFBs) .....	33
1.3.1 Working principle of RFBs.....	34
1.3.2 General logic for the RFB system development .....	36
1.4 Electrolyte compositions for RFBs .....	39
1.4.1 Chemistry in industrialized RFBs .....	39
1.4.2 Inorganic-based and hybrid RFBs .....	42
1.4.3 Organic-based RFBs .....	46
1.4.4 RFBs based on insoluble solid active materials.....	50
1.4.5 Electrolyte characterization methods and RFB performance metrics.....	54
1.4.6 Characterization of insoluble solid redox-active materials.....	59
1.5 Main components in the electrochemical cell.....	62

1.5.1 Main function of cell components .....	62
1.5.2 Material requirements for each component .....	64
1.5.3 Benchmarks for electrode material for vanadium RFB .....	68
1.5.4 Benchmarks for bipolar plate material.....	73
1.6 Summary from the literature review .....	77
1.7 Goals and objectives of the Thesis.....	79
<b>Chapter 2. Reaction mechanisms on porous electrodes in Vanadium RFB.....</b>	<b>81</b>
2.1 Overview of the Chapter 2 .....	81
2.2 In situ spectroelectrochemical Raman studies of vanadyl-ion oxidation mechanisms on carbon paper electrodes for vanadium RFB.....	83
2.3 Determination of kinetics parameters in Vanadium RFB with reference electrodes..	94
Determination of Kinetics Parameters in Vanadium RFB with Reference Electrodes. ...	95
2.4 Conclusions from the Chapter 2 .....	112
<b>Chapter 3. Material selection protocol of bipolar plate for Vanadium RFB .....</b>	<b>114</b>
3.1. Overview of the Chapter 3 .....	114
3.2 Carbonized elastomer composite filled with hybrid carbon fillers for vanadium RFB bipolar plates .....	116
3.3 Fluoropolymer impregnated graphite foil as a bipolar plates of vanadium RFBs ....	121
3.4 Conclusions from the Chapter 3 .....	132
<b>Chapter 4. Suspensions investigation as redox-active compounds for RFB.....</b>	<b>134</b>
4.1 Overview of the Chapter 4 .....	134
4.2 Redox-Active Aqueous Microgels for Energy Storage Applications.....	136
4.3 Influence of Conductive Additives for Nano-impact Electrochemistry Study of Single LiMn <sub>2</sub> O <sub>4</sub> Particles .....	142
4.4 Conclusions from the Chapter 4 .....	148
<b>Chapter 5 Summary and Outcomes .....</b>	<b>149</b>
Bibliography .....	151

## List of Symbols, Abbreviations

### Term – definition

(NPr)<sub>2</sub>VCl<sub>2</sub> – 1,1'-Bis[3-(trimethylammonium)propyl]-4,4'-(1,4-phenylene) bipyridinium tetrachloride

2,6-DPPEAQ – [[(Anthraquinone-2,6-diyl)bis(oxy)]bis(propane-3,1-diyl)] bis(phosphonic Acid) 2,6-Bis(3-phosphonopropyl-1-oxy)anthraquinone [(9,10-Dioxo-9,10-dihydroanthracene-2,6-diyl)bis(oxy-3,1-propanediyl)] bis(phosphonic Acid)

4-amino-TEMPO – 4-amino-2,2,6,6-tetramethylpiperidine-1-oxyl

AST – Accelerated stress test

CE – Coulombic efficiency

DBMMB – 2,5-di-tert-butyl-1-methoxy-4-[2'-methoxyethoxy] benzene

ECSA – Electrochemical surface area

EE – Energy efficiency

ESG – Environmental, social, and corporate governance

ESS – Energy storage systems

FcNCl –(ferrocenylmethyl)trimethylammonium chloride

FL – 9-fluorenone

LCOS – Levelized cost of storage

LIB – Lithium-ion battery

MVCl<sub>2</sub> - 1,1'-Dimethyl-4,4'-bipyridinium dichloride

NiHCF – Sodium nickel hexacyanoferrate

OCV – Open circuit voltage

RFB – Redox flow battery

SEI – Solid-electrolyte interface

SIB – Sodium-ion battery

SOC – State of charge

SOH – State of health

TEMPO – 2,2,6,6-Tetramethylpiperidin-1-yl)oxyl

TEMPOL – 4-Hydroxy TEMPO

VE – Voltage efficiency

VRFB – Vanadium redox flow battery

ZBFB – Zinc-bromine flow battery

## List of Figures

Figure 1.1 Benefits of energy storage along the electricity value chain.....	15
Figure 1.2 Classification of storage technologies by energy type .....	16
Figure 1.3 Comparison of key-type energy storage technologies in sense of storage capacity and discharge power duration .....	17
Figure 1.4. A - scheme of Li-ion batteries operation principal; B – voltage-capacity chart of anode and cathode materials .....	26
Figure 1.5. Europe map with ESS based on RFB.....	32
Figure 1.6. Scheme of RFB single cell construction and a scaled catholyte cell compartment for illustration of cell components position and function .....	34
Figure 1.7. Time dependence of capacity utilization for an irreversible and reversible fade	35
Figure 1.8. A – Chart of key parameters compromise for different aqueous RFB; B - overview of selected organic redox-active compounds classified according to their proven stability and redox potential vs SHE.....	45
Figure 1.9. Structures and redox potential of catholyte (blue) and anolyte (orange) molecules used in organic solvent (1– 10) and water (11–29).....	46
Figure 1.10. Scheme of RFB stack of n single cells in series with internal components	61
Figure 1.11. The equivalent circuit of the single RFB cell with listed components, the generalized equivalent circuit used for fitting, and the Nyquist plot of a 5 cm <sup>2</sup> single cell with 1.6 M vanadium electrolyte at different SOCs .....	66
Figure 1.12. Schematic representation of the reactions during its charging and discharging processes .....	70
Figure 1.13. Classification of bipolar plate materials for PEMFC and RFB applications	72

## **List of Tables**

Table 1.1 Technical requirements for Grid Applications of Battery Energy Storage.....	18
Table 1.2. Technology input parameters for LCOS (with standard deviation) .....	22
Table 1.3. Summary of the most extensively studied inorganic-based RFBs .....	41
Table 1.4 Summary for organic RFB characteristics. The numbers of redox pairs correspond to the molecules in Fig. 1.9. ....	47
Table 1.5 Pairs of solid-booster and mediator with cell enhancement characteristics .....	51
Table 1.6 Characteristic parameters of electrolyte and RFB performance.....	56

## Chapter 1. Introduction

Reduction of CO<sub>2</sub> emission and introduction of ESG (Environmental, social, and corporate governance) approaches in most of the production areas is a global trend. Orientation to green energy production makes the whole stack of technologies in the market very demanded. Renewables have a 95% share of the net increase in global power capacity (290 GW renewable power generation in 2021), thus, playing a significant role in the sustainably-oriented energy market [1].

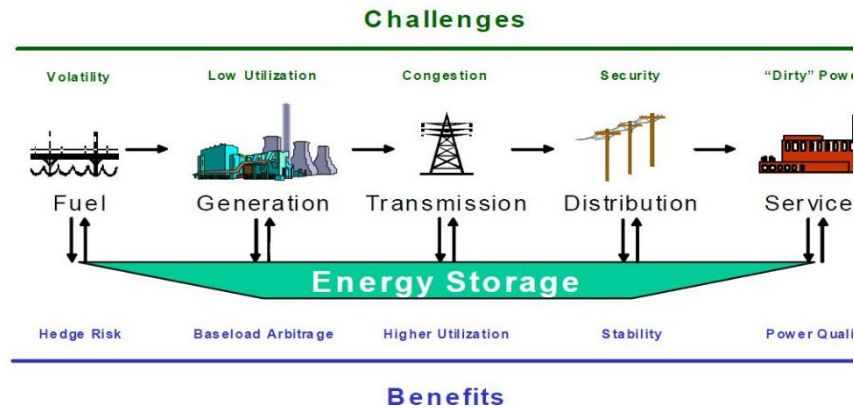


Fig. 1.1 Benefits of the energy storage along the electricity value chain. Reprinted with permission from [2]. Copyright 2022 Energy Storage Council.

New infrastructures are required for integrated and distributed renewables-based grid systems to maintain operational flexibility and durability in the energy supply. Hence, optimization of energy distribution and profitability from renewable energy sources requires a joint installation of Energy Storage Systems (ESS). Therefore, all components of the grid supply chain ESS implementation is seen to be beneficial (Fig. 1.1) [2,3]. That is why a significant growth in ESS installations is expected to create a market opportunity

for manufacturers worth a cumulative \$27 trillion through to 2050 [1]. Energy storage systems include a bench of various technologies, and the one is selected based on grid service required [4]. In the following chapter, the main ESS use cases and technologies will be overviewed. Particularly, battery systems will be discussed in more detail. Among the batteries, this thesis is devoted to the Redox Flow Battery (RFB) technology, which will be introduced with an advanced discussion of the technology, unsolved problems, and the state-of-art approaches for overcoming the limitations.

### 1.1 Energy Storage technologies

ESSs are divided firstly in terms of stored energy type into mechanical, thermal, electrochemical, electrical, and chemical (Fig. 1.2). Based on each type of energy different devices were developed. As the particular devices have specific ranges of power, capacity, and time response, the second classification of ESSs is based on matching technologies and applications (Fig. 1.3).

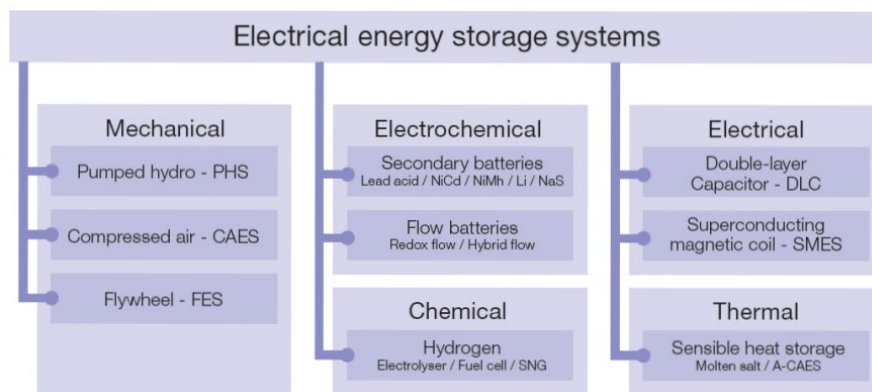


Figure 1.2 Classification of Storage Technologies by Energy Type. Reprinted with permission from [5]. Copyright 2022 Energy Regulators Regional Association.

In general, use cases of ESS dictate two main factors for the selection of technology: discharge time and power. Three power regions demonstrate a gradual drop in required power from generation to the end-user supply chain. Middle power applications with >1 min discharge time are recognized as the most demanded and searching for new solutions field, which includes a constantly updated list of applications.

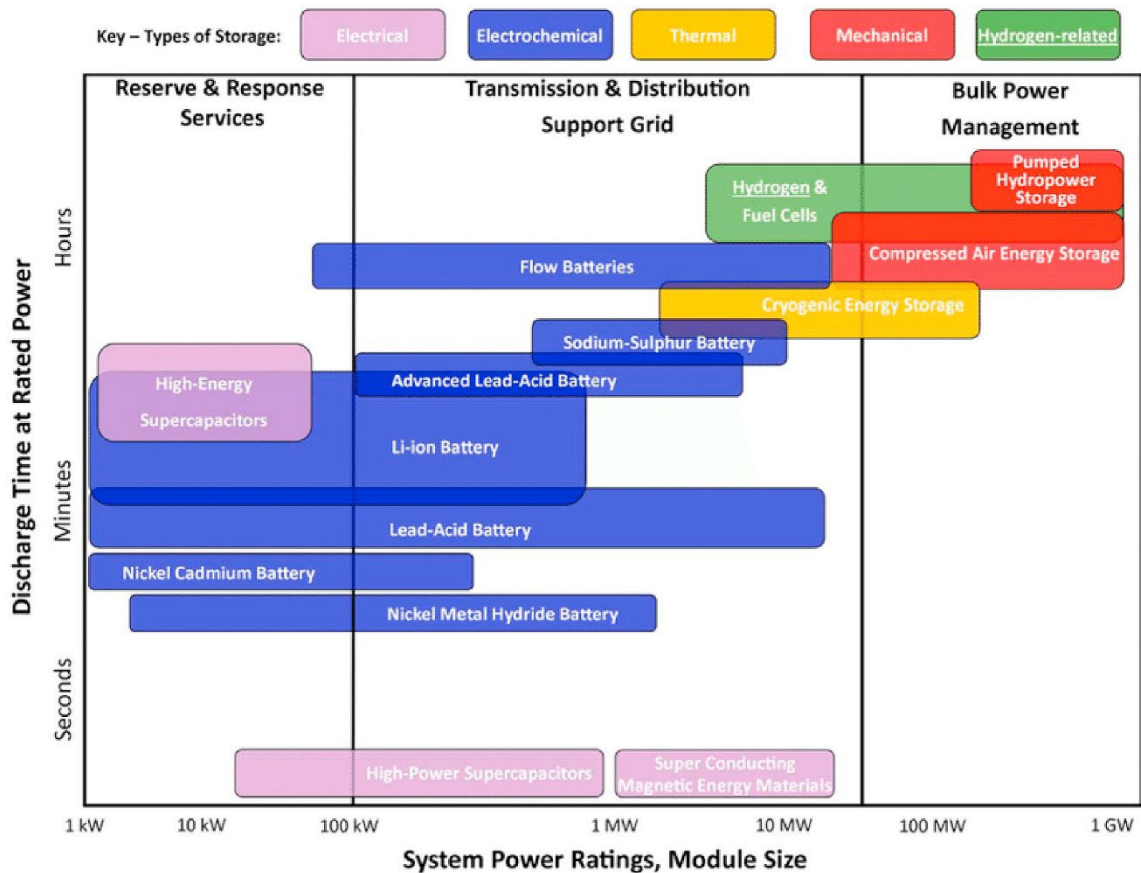


Fig. 1.3 Comparison of key-type energy storage technologies in sense of storage capacity and discharge power duration. Reprinted with permission from [6]. Copyright 2022

Elsevier.

A lot of pilot projects along with the development of legal basis, regulation procedures, and standardizations are ongoing around the world [7]. In practice, the realization of a single project of the device installation is performed by network owners, network operators, or “Behind-the-meter” customer services [8]. The extended list of ESS implementations with technical requirements is shown below

Table 1.1 Technical requirements for Grid Applications of Battery Energy Storage [7,9,10]

<b>Grid Application</b>	<b>Technical Considerations</b>
<p><b>Electric energy time-shift (arbitrage)</b> Purchasing inexpensive electric energy, stored during periods when prices or system marginal costs are low. Storage can provide similar time-shift duty by storing excess energy production from renewable sources.</p>	<p>Storage system size range: 1 – 500 MW</p> <p>Target discharge duration range: &lt; 1 hour</p> <p>Minimum cycles/year: 250 +</p>
<p><b>Electric supply capacity</b> Energy storage could be used to defer or reduce the need to buy new central station generation capacity in the wholesale electricity marketplace.</p>	<p>Storage system size range: 1–500 MW</p> <p>Target discharge duration range: 2–6 hours</p> <p>Minimum cycles/year: 5–100</p>
<p><b>Regulating reserve (Frequency control)</b> Automatically correct the continuous, fast, frequent changes in load or generation within the shortest applicable market interval</p>	<p>Storage system size range: 100 kW–200 MW</p> <p>Target discharge duration range: 10 seconds to 1 hour</p> <p>Minimum cycles/year: 250–2000</p>

<p><b>Spinning, non-spinning, and supplemental reserves</b> The operation of an electric grid requires reserve capacity that can be called on when some portion of the normal electric supply resources unexpectedly become unavailable. Generally, reserves are at least as large as the single largest generation unit.</p>	<p>Storage system size range: 10–100 MW</p> <p>Target discharge duration range: 15 minutes to 1 hour</p> <p>Minimum cycles/year: 20–50</p>
<p><b>Voltage support</b> Normally, designated power plants are used to generate reactive power (expressed in VAR) to offset reactance in the grid. These power plants could be displaced by strategically placed energy storage within the grid at central locations or by multiple VAR-support storage systems placed near large loads, following the distributed approach.</p>	<p>Storage system size range: 1–10 MW</p> <p>Target discharge duration range: Not applicable</p> <p>Minimum cycles/year: Not applicable</p>
<p><b>Black start</b> Storage systems provide an active reserve of power and energy within the grid and can be used to energize transmission and distribution lines and provide station power to bring power plants online after a catastrophic failure of the grid.</p>	<p>Storage system size range: 5–50 MW</p> <p>Target discharge duration range: 15 minutes to 1 hour</p> <p>Minimum cycles/year: 10–20</p>
<p><b>Transmission upgrade deferral</b> involves delaying utility investments in transmission system upgrades, by using relatively small amounts of storage. Consider a transmission system with peak electric loading that is approaching the system’s load-carrying capacity (design rating).</p>	<p>Storage system size range: 10–100 MW</p> <p>Target discharge duration range: 2–8 hours</p> <p>Minimum cycles/year: 10–50</p>
<p><b>Transmission congestion relief</b> When transmission capacity additions do not keep pace with the growth in peak electric demand, the transmission systems</p>	<p>Storage system size range: 1–100 MW</p>

<p>become congested. Electricity storage can be used to avoid congestion-related costs and charges, especially if the costs become onerous because of significant transmission system congestion.</p>	<p>Target discharge duration range: 1–4 hours Minimum cycles/year: 50–100</p>
<p><b>Power quality</b> The electric power quality service involves using storage to protect customer on-site loads downstream (from storage) against short-duration events that affect the quality of power delivered to the customer’s loads (variations in voltage magnitude, variations in the primary 60-hertz (Hz) frequency, low power factor (voltage and current excessively out of phase with each other), harmonics (the presence of currents or voltages at frequencies other than the primary frequency), interruptions in service)</p>	<p>Storage system size range: 100 kW–10 MW Target discharge duration range: 10 seconds to 15 minutes Minimum cycles/year: 10–200</p>
<p><b>Demand charge management</b> Electricity storage can be used by end-users (utility customers) to reduce their overall costs for electric service by reducing their demand during peak periods specified by the utility.</p>	<p>Storage system size range: 50 kW–10 MW Target discharge duration range: 1–4 hours Minimum cycles/year: 50–500</p>
<p><b>EV charging infrastructure</b> Energy storage that is used as an energy source for EV charging infrastructure, including in combination with an on-site PV system</p>	<p>Storage system size range: 50 kW–10 MW Target discharge duration range: 4–8 hours Minimum cycles/year: 150-500</p>

The most common use for battery storage in 2018 was a frequency regulation (50%), followed by reserve capacity (9%), bill management (8%), and energy time-shifting (8%) (percentage of total installed capacity) [9]. However, the shown classification does not include the market size for each use case, one can observe a significant share of batteries technology, which covers a sufficient list of use cases. The economic profitability of each technology for the use case is calculated by the Levelized Cost of Storage (LCOS), which summarizes power and energy-related capital and operational costs (\$/kW and \$/kWh), performance metrics for energy storage technologies [10]. The LCOS is calculated based on equation 1.1:

$$LCOS \left[ \frac{\$}{MWh} \right] = \frac{Investment\ cost + \sum_n^N \frac{O\&M\ cost}{(1+r)^n} + \sum_n^N \frac{Charging\ cost}{(1+r)^n} + \frac{End-of-life\ cost}{(1+r)^{N+1}}}{\sum_n^N \frac{Elec_{Discharged}}{(1+r)^n}} \quad Eq.1.1$$

Where  $r$  is the discount rate,  $n$  is a specific year of operation, and  $N$  is the lifetime of the technology. The lifetime is the minimum of cycle life including construction times. O&M is the operation and maintenance cost.  $Elec_{Discharged}$  is calculated discharged electricity, which considers annual cycles, nominal energy capacity depth-of-discharge, round-trip efficiency, cycle degradation, time degradation, self-discharge, and construction time of the technology.

Typical values of the LOCS for frequency regulation application with a power range of >50 MW are presented in Table 1.2 (data was reproduced from [10,11] and recalculated for the 2018 year). More recent information on economical profitability varies greatly depending on the source.

Based on the LOCS and the requirements of the project the ESS is selected. If the pumped-hydro is an established technology with dominated power share of 94 % (199.5 GW in 2021), its list of use cases is limited by > 1 GW power requirements, and continuous growth of distributed power grid (< 100 MW) promotes the development of other technologies [12]. The investments into the alternatives, like batteries and flywheels, are continuing to grow even though its global power share is small. Global investments in grid battery storage were estimated at roughly 4.7 billion U.S. dollars, with an increase of 34 % in comparison to the previous year [13]. Total power installation of grid energy storage achieved 12 GW in 2021, with a Russian share of 125 MW [14].

Table 1.2. Technology input parameters for LCOS (with standard deviation).

	<b>Units</b>	<b>Lithium-ion</b>	<b>Lead-acid</b>	<b>Vanadium RFB</b>
<b>LCOS</b>	<b>\$/MWh</b>	<b>251 (19%)</b>	<b>382 (10%)</b>	<b>328 (21%)</b>
Operation cost - Power	\$/kW-yr	10 (35%)	8 (31%)	12 (52%)
Operation cost - Energy	\$/MWh	3 (60%)	1 (60%)	1 (60%)
Replacement interval	cycles	3250	1225	8272
Discount rate	%	8	8	8
Round-trip efficiency	%	86 (7%)	84 (0%)	74 (9%)
Self-discharge	%/day	0	0	0

Lifetime (100% DoD)	cycles	3250 (38%)	1225 (35%)	8272 (13%)
Shelf life	years	13 (38%)	10 (50%)	13 (20%)
Time degradation	%/year	0.017 (5%)	2.2 (5%)	1.7 (5%)
Cycle degradation	%/cycle	0.0069 (5%)	0.0182 (5%)	0.0027 (7%)
Construction time	years	1	1	1

**To sum up, the LCOS trend, market growth, and listed above ESS use cases illustrate the profitability of battery technology for many applications. Existing battery technologies are discussed below in more details.**

## 1.2 Battery energy storage systems overview

Batteries convert the electric energy into the form of chemical energy by a specific electrochemical process. Throughout the thesis, I discuss rechargeable batteries (secondary batteries), which can undergo discharge-charge cycling many times. The main specific characteristics of battery technology are (1) power ratings: total electrical power required for a normal operation of a device; (2) discharge time at rated power; (3) volumetric energy density in Wh L<sup>-1</sup>; (4) gravimetric energy density in Wh kg<sup>-1</sup>. The power rating graph with listed battery types demonstrates a unique niche for different technologies (Fig. 1.3). The most common batteries, like lead-acid and lithium-ion, have less discharge time at rated power, than redox flow batteries. This fact is attributed to independent scaling of capacity and power in RFB, while these parameters are bounded for Li-ion and Lead-acid batteries. Below lithium-ion technology is briefly introduced showing the limitations and advantages as a reference technology in comparison with redox flow batteries.

### 1.2.1 Lithium-ion batteries (LIBs)

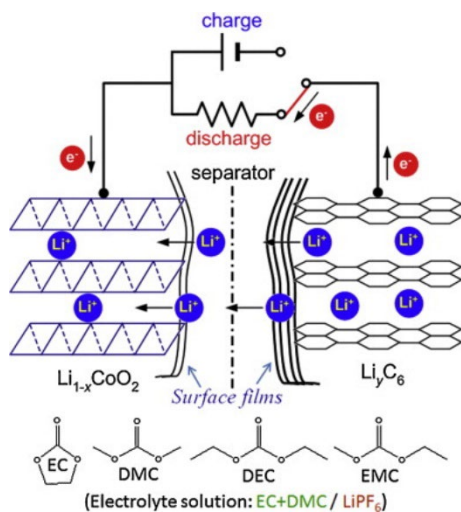
Lithium-ion batteries were introduced into the market in 1991 [15]. Due to its revolutionary high energy density this technology attracts huge investment and scientific interest, boosting the durability and economic profitability yearly [16].

The basic working principle is based on a reversible electron-ion coupled electrochemical reaction, called (de)intercalation, which happens inside the solid crystal material. Li<sup>+</sup> intercalates into the host matrix of the materials, while the electron is

transferred from the external electrical circuit to the host crystal's atom, maintaining electroneutrality (Fig. 1.4 A). The intercalation processes have different equilibrium potentials for each type of host matrix (Fig. 1.4 B). Materials, like graphite and lithium titanate, have a low potential for intercalation and are utilized as anodes in Li-ion batteries. High-voltage materials are used as cathodes, this list is represented by transition metal oxide materials, like lithium cobalt oxide, lithium iron phosphate, lithium manganese oxide, lithium-rich layered materials, and lithium nickel manganese cobalt oxides. Maintaining ion currents inside the battery is done by organic electrolytes, which are a mix of lithium salts and organic solvents [16]. Common lithium salts are lithium hexafluorophosphate, lithium tetrafluoroborate, and lithium perchlorate, which are dissolved in a mixture of ethylene carbonate, propylene carbonate, dimethyl carbonate, or/and diethyl carbonate.

Technically, the LIB is assembled from two metal foils covered with a thin film of mixed electroactive materials, carbon source, and binder (called anode and cathode slurries), which are sandwiched between the polymer separator and drenched in liquid electrolyte. Different forms of cells are manufactured, like pouches, coin-cells, cylindrical, and prismatic, depending on the packaging procedure of such sandwich-like roll of Li-ion battery components.

A



B

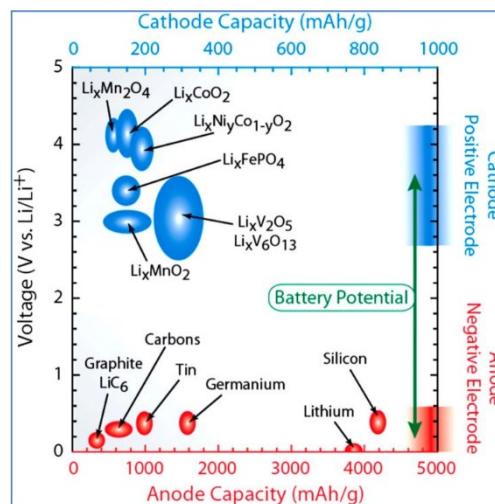


Fig. 1.4. A - scheme of Li-ion batteries operation principal; B – voltage-capacity chart of anode and cathode materials. These images are reprinted with permission from [16,17] Copyright 2022 Joint Research Centre (European Commission). Copyright 2022 Elsevier.

Economically driven research in LIBs implies solving problems with the most impact on price, which are (1) long cycle life and low-capacity fade; (2) high power density; (3) fast charging; (4) minimal impact on the environment; (5) production cost decrease; and (6) safety.

- 1) Long cycling and low-capacity fade are the most crucial parameters for the LCOS, as it predicts the total amount of stored energy. The batteries cycling and degradation speed depend on the depth of discharge and rate of discharge. In practice, manufacturers declare from 500 to 5000 cycles for 80% of discharge at a rated power of 1 C (battery discharge in one hour) [8]. The lifetime of LIB is dictated by degradation mechanisms

inside the cell. The main issues are the formation of a thick blocking layer on surfaces of anode and cathode slurries, called SEI – solid-electrolyte interface; detaching the slurry from the supporting foil, hence, loss of electron contact; and irreversible phase transformation in the structure of cathode materials [18]. Ongoing R&D for improving the lifecycles is focused on advanced charge-discharge protocols, boosting the cell stability, and minimizing the SEI growth [19].

- 2) An increase in gravimetric power density can be achieved by reducing the mass of non-electroactive components in the cell, or by enhancing the capacity and power of the materials. Tesla implements the first path from the manufacturing point of view by changing the form-factor of the battery from 18650 to 4680 [20]. On the other side, the scientific community proposes new perspective materials for the cathode side and new high-voltage electrolytes to enhance battery power and specific capacity [21].
- 3) Fast charging request from the electrical vehicle industry implies the development of advanced cells. Improvement in fast charging performance is a multiscale problem, thus, new approaches are needed from atomic to system level [22]. At the nanoscale level, materials with advanced morphology are developed, which are capable of fast and reversible redox processes, e.g. graphene-based ones.
- 4) Eco-friendly technology and the availability of raw materials are the high-risk points in the manufacturing process. Typically used cobalt, lithium and nickel are mined in certain regions; thus, control of the material source, mining methods, and distribution streams are controlled by the local governments. This issue forces battery manufacturers

to hedge risks by developing materials from available components (like  $\text{LiFePO}_4$ ) and creating a distributed suppliers' system [23]. Moreover, continuous improvement of assessment metrics of  $\text{CO}_2$  emission from mining and manufacturing is ongoing [8,24].

5) Overall, the ecological trend and the goal to reduce production costs lead to the development of circular economics, meaning the reuse of raw materials from spent batteries [25]. The recycling industry is growing rapidly these days and a lot of effective material recovery technologies were introduced [25,26].

6) Safety is always the main requirement for mass-production technology. LIBs have already come a long testing way; specialists accumulated a lot of experience by working with them and many critical issues were overcome. Still, the development of testing standards and tuning of technologies are continuing [27]. Moreover, special additives are used in the electrolyte to prevent overcharging, which is usually the reason for inflammation [28].

Proposed solutions to each problem, discussed above, can reduce the manufacturing cost of LIBs, and move the technology to a mass-production scale for electrical vehicles and ESS.

**Overall, the LIBs market is exponentially growing, exciding 286 GWh at 2021 [29]. The lithium-ion battery market is focused on the more marginal sector of electric cars. ESSs are a secondary market, usually for second-life batteries, since LIBs do not fully meet the requirements of LCOS due to a small number of cycles and discharge time at rated power [30]. Thus, the ESS niche is the main for flow batteries.**

**The protracted stage of pilot testing is the only reason for the not low LCOS yet (small production volumes). RFBs have a gap in these ten years to occupy their niche, otherwise then the market will be overflowing with used lithium-ion batteries from electric cars, which is already a great trend [30].**

### *1.2.2 Post Lithium-ion batteries*

**1) Sodium-ion batteries (SIBs).** Sodium ions, as well as lithium ions, can undergo the intercalation reaction into the host crystal structure despite bigger radius. While the production technology requires the same steps and manufacturing facilities, the main features lie in materials for cell production (anode, cathode, and electrolyte).

The development of sodium intercalation materials starts in the 90-s. Up to now, only several anode materials, like hard carbon and titan-based compounds, have reached a commercial stage of technology with demonstrated stable cycling over 1000 cycles [31]. Hard carbons are usually prepared by high-temperature carbonization of solid-phase polymer precursors as a carbon source. Sodium plating on hard carbon surfaces during fast charging (same as high overpotentials) is one of the safety concerns. The most critically unresolved issue, however, is the first cycle's irreversible capacity loss, which reduces the access charge. More advanced sodium metal anodes are still under development due to unstable surface passivation layer [32]. Titan-based components, like sulfides, NASICON-type  $\text{NaTi}_2(\text{PO}_4)_3$ , and anatase-type  $\text{TiO}_2$  have a sloping voltage profile that undermines the available energy density. Furthermore, low first-cycle coulombic efficiency leads to a

gravimetric capacity of less than 150 mAh g<sup>-1</sup>. Electrolyte selection is another challenge for SIBs which depends on the selected anode material. Stabilization of SEI and electrochemical stability at high voltages are the most critical points.

Cathode materials are represented by two major groups: layered metal oxides and polyanion compounds. The main challenges for cathodes are stability of crystal structure so that no irreversible phase transformation occurs. Moreover, the majority of proposed cathodes have a biphasic intercalation mechanism, leading to the characteristic stepwise voltage profiles. The most prominent materials for cathode materials are NASICON-type Na<sub>3</sub>V<sub>2</sub>(PO<sub>4</sub>)<sub>3</sub> and Na<sub>3</sub>V<sub>2</sub>(PO<sub>4</sub>)<sub>2</sub>F<sub>3</sub>, which have already reached the production level. These materials typically are cycled within two voltage plateaus. Both suffer from low electron conductivity, which can be treated by optimization of morphology and conductive additives, like carbon [31].

In summary, SIBs are now at the pilot stage of production with many testing sites around the world [33]. SIBs are seen to be competitive technology to RFBs in ESS applications for the next years as utilized materials are widespread and stable cycling life are already demonstrated [34].

**2) Rechargeable sodium-sulfur (Na-S) batteries** are a promising ESS technology due to their high energy density and low cost. High-temperature sodium-sulfur batteries with molten sodium and sulfur as cathode materials operating at 300-350 °C were proposed in 1966, and later successfully commercialized for utility-scale stationary energy storage [35].

Anode and cathode sides were separated by  $\text{Al}_2\text{O}_3$  based membrane, which conducts  $\text{Na}^+$ . The main disadvantage is a maintaining of constant high temperature, which resulted in high operating costs, materials degradation (corrosion), and severe safety issues. Moreover, polysulfides as the final discharge product deliver about a third of the sulfur's theoretical capacity.

Switching to new low-temperature Na-S batteries sufficiently decreases the LCOS and improved safety [36]. The battery works on a reversible reaction of  $\text{Na}^+ + \text{S}^{2-} = \text{Na}_2\text{S}$ , which has a multistage mechanism depending on the electrolyte (ether-based and carbonate-based). In general, these Na-S batteries face several common intrinsic obstacles in both electrolytes, which trigger performance deterioration in the form of high irreversible capacity, self-discharging, and poor cycle stability: (1) the uncontrollable growth of Na dendrites during cycling; (2) the shuttle effect of Na polysulfides; (3) slow kinetics of conversion from long-chain polysulfides to short-chain; (4) poor electronic conductivity of sulfur.

To sum up, Na-S technology is already presented in the market of utility-scale ESS, however, safety issues and performance deterioration require additional research and development for further distribution in other market segments.

**3) Two-electron batteries** based on the reaction of bivalent metal ions become an active development area, since the approaches of stabilization of metal anode interface were proposed. However, both technologies of magnesium and calcium rechargeable batteries

are at the laboratory level with some attempts to prepare small prototype cells. Stable cycling for high-performance cathodes and metal anodes remained the main bottleneck in the technology development. Even stable cycling of the half-cell was demonstrated for different graphite-based, polymer-based and intercalation-based systems, as well as high-voltage electrolytes with desolvation barriers mitigation of the cations at the electrode/electrolyte interfaces were proposed; reported full-cell cycling data demonstrated inappropriate coulombic efficiency. Nevertheless, research in this field is ongoing, because the high specific capacities up to  $300 \text{ Wh kg}^{-1}$  and  $600 \text{ Wh L}^{-1}$  can be achieved [37,38].

**Comparison of the post-lithium battery technologies with RFBs can be done in three different aspects: technology readiness level, LCOS and specific energy characteristics. The number of companies with ready-made products based on a flow battery and sodium-ion batteries is the same, but the share of installed power is five times greater for sodium-ion technology [39]. Despite the rapidly developing energy storage market, the growth of flow battery share was hindered due to poorly developed legislative framework and a system of standards and operation rules. The successful cooperation work of the leading companies has shifted the process, and the market is growing now. Sodium-sulfur-based and 2-electron batteries have not been distributed much due to the high LCOS at the moment. A comparison of the energy characteristics of existing technologies naturally shows the superiority by 5 to 10 times of solid-based energy solutions. However, this parameter remains less important than energy cost in the case of stationary applications.**

### 1.3 Redox flow batteries (RFBs)

Among all grid EESs, Redox Flow Batteries (RFBs) with long cycle life and low energy losses were recognized as a perfect solution for application with discharge time > one hour and cycle-life >10000. RFB is a rechargeable battery in which electrolyte flows through electrochemical cells from one or more tanks. An increase in the energy storage capacity is done by increasing the volume of electrolytes stored in the tanks. The electrochemical cells can be electrically connected in series or parallel, thus, determining the power. Decoupling of energy rating and power rating is the most prominent RFB feature.



Fig. 1.5. Europe map with ESS based on RFB. This image is reprinted from IFBF web page [40]. Copyright 2022 International Flow Battery Forum.

Flow batteries are already recognized technology with more than 150 installation sites over the world. We show the map of installations in Europe (Fig. 1.5) to illustrate the RFB use implementations: over 70% of installations for industrial applications and another part as pilot projects in research institutions. Despite the high readiness of RFB technologies, there are still unsolved issues in the development stage, limiting a wide spreading of RFBs: (1) enhancement of energy storage capacity; (2) cost reduction of the electrolytes; (3) development of stable and cheap electrolytes without high volatility price of components; (4) reduction of cell components cost; (5) RFB response modeling with high precision for battery management system controls [41–43]. As a result, research recently focuses on the designing new electrolytes synthesized from earth-abundant elements, optimization of cell materials manufacturing and development the control algorithms. Below, we discuss in detail the state-of-art of proposed solutions and the methods used for the investigation and comparison of different materials and compounds in the scope of RFB applications.

### *1.3.1 Working principle of RFBs*

In general, a flow battery consists of three major components: tanks with electrolytes, electrochemical cells, and a battery management system. Liquid electrolytes with redox-active components circulate between tanks and cells, where redox reactions occur. The design and utilized materials for cells mainly determine the RFB power profiles,



The battery management system controls the overall workflow of the battery and evaluates its State of Charge (SOC) and State of Health (SOH) [44,45]. Through RFBs, various chemistries have reached different levels of technology readiness. Vanadium Flow Battery (VFB) is the most developed and successfully commercialized, while organic-based RFBs are under the intensive development stage with several pilot projects [46,47].

### 1.3.2 General logic for the RFB system development

The ideal battery technology must have a high specific energy density and works close to the theoretical capacity limit for an infinite number of cycles. This is a general goal for the development of ESS. If well-established lithium-ion technology is approaching its capacity utilization to the theoretical one and continuous work for the reduction of capacity fade to  $0.001\% \text{ cycle}^{-1}$  is ongoing, the RFB technology does not achieve such a great performance. However, the technology is sold on the market, because its capacity can be restored back to the maximal capacity utilization, which is usually  $\sim 80\%$ , and the resulting capacity fade is low (Fig. 1.7).

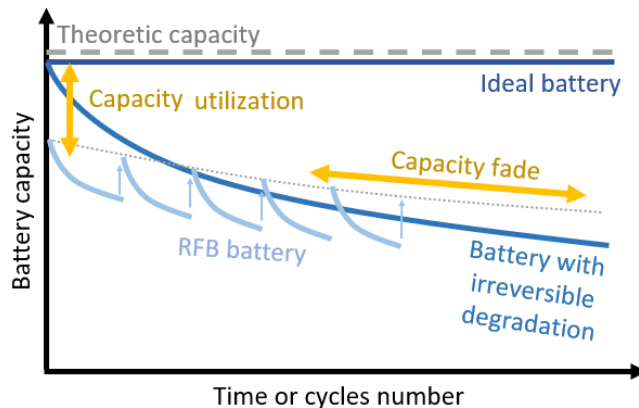


Fig. 1.7. Time dependence of capacity utilization for an irreversible and reversible fade.

Nevertheless, flattening of local capacity fade and enhancement in capacity utilization are the most economical drivers in RFB technology [48]. Capacity utilization at the  $n^{\text{th}}$  cycle depends on three main factors: available redox-active species capacity, its degradation rate, and the cell cycling conditions, which requires balancing power and capacity characteristics. Overall, the logic for a particular system development has several steps:

1. The pair of electrolyte compositions has to be evaluated in the scope of energy density, redox reaction rates, and reversibility [49]. The composition of the electrolyte is selected to maximize the capacity utilization and minimize the fade.
2. The cell components optimization is performed for the maximization of power output, capacity utilization, and cycling life. Tuning the materials and shape of battery internal components helps to reduce cell resistance and activation losses coming from ineffective kinetics. Prove-of-concept RFB tests are conducted at this stage with 10-200 cycles at different flow rates.
3. The next step is transferring the obtained data from prove-of-concept devices to the up-scaled prototypes with concentrated electrolytes. This step becomes a real technology threshold dividing economically viable projects and non-scalable scientific ones.
4. The development of a battery management system for grid integration requires building an accurate model of current battery parameters (SOC, SOH, and current, potential profiles) [50,51].

**Therefore, the level of RFB research and unsolved problems are directly dependent on target chemistries. For example, boosting the energy density of organic-**

based RFBs remains the open issue leading to a huge effort towards new chemistries generation [52–54]. For vanadium RFBs, target filling of gaps in the developed theory is required for tuning the model accuracy, benchmarking protocols for materials, cells, and reduction of capacity decay tests [55,56].

In the scope of this thesis, I am focusing on revealing the reasons for poor capacity utilization (1) in RFBs based on insoluble solid active materials, and (2) in vanadium RFB from the electrode and bipolar plate materials optimization point of view. Therefore, the literature review is constructed of two parts: (1) redox-active materials in RFB and its limitations in capacity utilization, and (2) cell components requirements for the efficiency maximization.

## 1.4 Electrolyte compositions for RFBs

Electrolytes in RFB consist of solvent, supporting salt, and redox-active species and are usually divided into water-based and organic ones. The main difference in solvents is an electrochemical stability window: water-based systems are limited by a water stability window ( $\sim -0.4 - 1.2$  V vs. SHE), while organic-based RFBs, using acetonitrile, DMSO, or PC, have a broader window up to 4 V. Therefore, chemicals utilized as a redox-active compound are selected in the range of electrolyte stability window. These compounds can be organic synthesized redox-active molecules, polymers, and inorganic compounds, typically metal ions.

### 1.4.1 Chemistry in industrialized RFBs

Several chemistries have reached a commercial-stage production:

- 1) **Vanadium RFB (VRFB)** is firstly commercialized in 90-s [57]. Up to date, over 10 companies around the world proposed their ESS solution, based on VRFBs [58]. The battery utilizes reversible vanadium reactions in four oxidation states:



Elimination of cross-contamination issues makes this type of battery preferable with long cycle life ( $>20000$  cycles). The battery operates with an energy efficiency of  $>75\%$  at current densities in the order of  $80\text{-}200 \text{ mA cm}^{-2}$ , which gives a  $100\text{-}280 \text{ mW cm}^{-2}$  power density. This value is smaller than for the same type of reactor, used as a proton

exchange membrane fuel cell, which has  $1 \text{ W cm}^{-2}$  working power [59]. However, the constant development of high-powerful stacks is ongoing and a  $370 \text{ W cm}^{-2}$  system has been already demonstrated [60].

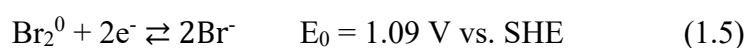
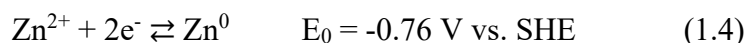
As VRFBs produce DC, grid operation of the device is done by a bidirectional d.c./a.c. inverter. Operational control, e.g. electrolyte flow rate, temperature sensing, and electrolyte balancing are performed by Battery Management System (BMS). As operation principals and voltage profiles differ from conventional LIBs systems, the need for an accurate prediction model of the RFBs system arises [42,61]. Actual State of Charge (SOC) prediction is restricted by constant change of volume, total concentration, and electrolyte degradation process [61,62].

In general, the present research aims to the reduction of LCOS [63] by the development of advanced membranes with higher conductivity and lower crossover [64], new materials for bipolar plates and porous electrodes with enhanced performance [65–67] effective stack designs [45], imbalance mitigation strategies [68], and BMS algorithm improvements [69–71]. Nevertheless, a fundamental bottleneck is a low energy density, which makes VRFB less attractive than conventional LIB system [72]. Coupled with the volatile price of vanadium, it caused shifting to the alternative chemistries for RFB technology.

**2) Zinc–bromine (ZBFB)** was scaled up into industrial systems [73]. It uses a zinc negative electrode and zinc bromine solutions as catholyte with a high OCV of 1.85 V. Companies, like ZBB technologies (now Ensync Energy systems), Redflow Ltd.,

and Primus Inc. successfully installed many systems in a range of 600 kWh – 2 MWh [74].

Zinc bromide aqueous solutions are stored in both tanks and used only selected ions react at each side:



The negative side reaction is (dis)solvation of Zn/Zn<sup>2+</sup> pair, which increases the risk of a short circuit due to the growth of dendrites. As a consequence, accurate monitoring of the battery condition and regular discharge is necessary [75]. Bromine is always dissolved, while solid zinc is deposited onto the negative carbon electrode, thus conferring the hybrid nature to the battery. Bromine is sequestered and stored in oily phase sedimentation. Additionally, expensive sequestering/complexing agents are needed to avoid toxic bromine vapor emissions. Search for the effective and low-cost additives to the bromine electrolyte is ongoing [76].

ZBFBs have no cycle life limitations because the electrolytes do not suffer aging effects and crossover [76]. Having a performance comparable to VRFBs, ZBFB can operate at current densities up to 80 mA cm<sup>-2</sup> [75]. Even though zinc and bromine are low-cost materials, ZBFB systems have comparable with VRFB energy costs [42,76,77].

3) Several companies in Europe (Kemiwatt, Jena Batteries, Green Energy Storage, and CMBlu) have introduced their pilot projects based on **organic chemistry on kW scale** (pyridine-based anolyte 20–100 kW and 400 kWh) [78]. Probably, Kemiwatt is working on quinone-based / ferrocyanide electrolyte [79], and Jena Batteries is employing pyridine-based anolyte and TEMPO-based catholyte [80] in their demonstrators. However, no official data with proven long cycle life of such system were not published.

#### *1.4.2 Inorganic-based and hybrid RFBs*

Other chemistries are in the development stage. Based on a number of patents and publications, one can conclude that new grid-scale projects based on advanced chemistries will be put into operation soon. Table 1.3 with developed inorganic water-based systems mostly is represented by a combination of already discussed ion pairs.

Table 1.3. Summary of the most extensively studied inorganic-based RFBs

<b>Name</b>	<b>Redox couples: Anode - Cathode</b>	<b>Support electrolyte</b>	<b>Performance</b>	<b>Ref</b>
<b>V-V</b>	$V^{3+} / V^{2+}$ $VO_2^+ / VO^{2+}$	H <sub>2</sub> SO <sub>4</sub> , HCl, H <sub>3</sub> PO <sub>4</sub>	Discussed above	[81]

<b>Zn-Br<sub>2</sub></b>	Zn <sup>2+</sup> / Zn <sup>0</sup> Br <sub>2</sub> <sup>0</sup> /2Br <sup>-</sup>	NaBr, Na <sub>2</sub> SO <sub>4</sub>	Discussed above	[82]
<b>V- Br<sub>2</sub></b>	V <sup>3+</sup> / V <sup>2+</sup> Br <sub>2</sub> <sup>0</sup> /2Br <sup>-</sup>	VBr <sub>3</sub> , HCl	VBr <sub>3</sub> in both half-cells.  The high solubility of 3–4 M, allowing for energy densities up to 50–70 Wh L.  Lab-scale cell cycling at 20 mA cm <sup>-2</sup> gives coulombic and energy efficiencies of 83% and 66%, respectively.	[83]
<b>Fe-Cr</b>	Cr <sup>3+</sup> /Cr <sup>2+</sup> Fe <sup>3+</sup> / Fe <sup>2+</sup>	HCl	Energy efficiency of 80% at 200 mA cm <sup>-2</sup> (65°C). The capacity decay is 0.6%/cycle.  A low capital cost of \$137.6 kWh for 8 h energy storage  Issues with crossover and side reactions.	[84,85]
<b>Fe-Fe</b>	Fe <sup>2+</sup> /Fe <sup>0</sup> Fe <sup>3+</sup> /Fe <sup>2+</sup>	NH <sub>4</sub> Cl, ascorbic acid	Coulombic efficiency of 97.9% at 100 mA cm <sup>-2</sup> (60°C)  Issues with reversibility of iron plating, pH drift during long cycle	[86]
<b>Zn-Fe</b>	Zn(OH) <sub>4</sub> <sup>2-</sup> / Zn <sup>0</sup>	KOH	OCV potential is 1.81 V, operation currents < 260 mA cm <sup>-2</sup>	[87]

	[Fe(CN) <sub>6</sub> ] <sup>3+</sup> / [Fe(CN) <sub>6</sub> ] <sup>4-</sup>		Capital cost under \$90/kWh  CE of ~ 99% and EE of ~ 86% at 80 mA cm <sup>-2</sup> for 100 cycles.  Issues with dendrites growth and membrane stability.  A new composite membrane based on poly(ether sulfone) and layered double hydroxides was tested.	
<b>Cu-Cu</b>	1) Cu <sup>+</sup> /Cu <sup>0</sup>  Cu <sup>2+</sup> /Cu <sup>+</sup>  2) CuCl <sub>y</sub> <sup>2-y</sup> / CuC <sub>x</sub> <sup>1-x</sup>  CuC <sub>x</sub> <sup>1-x</sup> / Cu <sup>0</sup>	HCl	Comparable energy density to vanadium RFB due to high solubility of copper (3 M).  Coulombic efficiency of 92% at 30 mA cm <sup>-2</sup> .  Issues with dendrites formation and the deposit growth close to the membrane, slow kinetics.	[88,89]
<b>POMs</b>	1) Li <sub>6</sub> [P <sub>2</sub> W <sub>18</sub> O <sub>62</sub> ]/ H <sub>n</sub> Li <sub>6</sub> [P <sub>2</sub> W <sub>18</sub> O <sub>62</sub> ]  HBr/Br <sub>2</sub>  2) [SiW <sub>12</sub> O <sub>40</sub> ] <sup>4-</sup> / [SiW <sub>12</sub> O <sub>40</sub> ] <sup>4+n-</sup>  [PV <sub>14</sub> O <sub>42</sub> ] <sup>9-</sup> / [PV <sub>14</sub> O <sub>42</sub> ] <sup>9+m-</sup>	LiCl, HCl	The capacity density was 42.6 Ah L <sup>-1</sup> for 0.1 M at 50 mA cm <sup>-2</sup> with a coulombic efficiency of 96%.  230Ah L <sup>-1</sup> can be achieved at 20 °C for 0.5M electrolytes with an energy efficiency of 76%.	[90,91]

			Capacity fade was 0.16% / cycle for 14 days test (155 cycles at 30 mA cm <sup>-2</sup> ).  Issues in a synthesis upscaling, degradation electrolyte rate.	
--	--	--	---	--

Moreover, several types of hybrid batteries with one gas-based redox reaction are actively investigated, such as vanadium–oxygen redox flow battery and hydrogen–bromine flow battery [42]. For both types of RFB, a catalytic layer has to be implemented for gas-phase reaction, thus, stability of the catalyst is one of the challenges. The layer degrades mainly due to contamination from opposite side species [92].

**Vanadium – oxygen flow battery** is based on oxygen reduction reaction and vanadium V<sup>3+</sup>/V<sup>2+</sup> pair. It operates under moderate current densities (< 50 mA cm<sup>-2</sup>), hence, the maximum reported power density was <100 mW cm<sup>-2</sup> [93]. Three main issues for the cell construction are a catalyst layer dissolution due to water uptake, oxygen crossover to the anode side, and a blocking layer formation on the membrane surface.

**Hydrogen–bromine flow battery** has a low cell voltage of 1.09 V, but it is supposed to have a high volumetric energy density (>200 Wh L<sup>-1</sup>) as an alternative benefit [94]. In practice, RFB cells suffer from bromine crossover, which leads to catalyst poisoning, and a highly corrosive environment due to bromine reactivity [95]. Therefore, safe operation and material selection, like gaskets and membranes, are still challenging tasks.

### 1.4.3 Organic-based RFBs

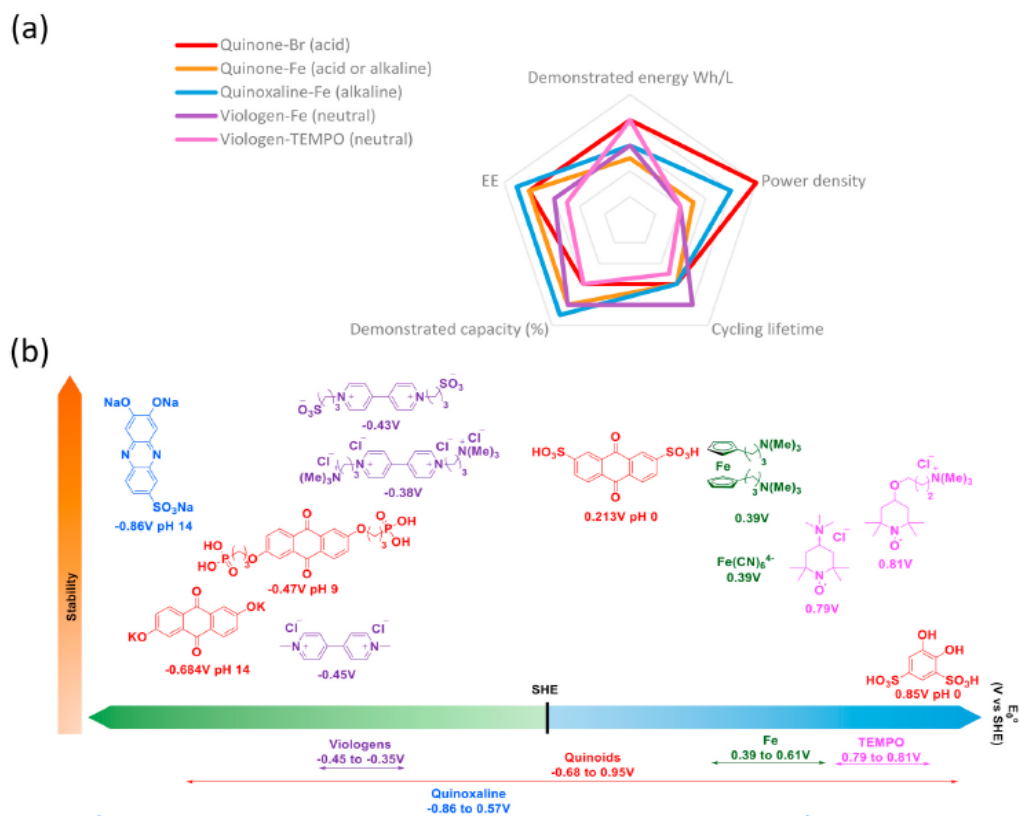


Fig. 1.8. A – Chart of key parameters compromise for different aqueous RFB; B - overview of selected organic redox-active compounds classified according to their proven stability and redox potential vs SHE (red: benzoquinone/anthraquinone, blue: phenazine, purple: viologens, green: iron complexes, pink: TEMPO derivatives). Reprinted with permission from [42]. Copyright 2022 Elsevier

The above works are based on available raw materials that only need to be purified. Thus, the contribution of the electrolyte to the price is predictable, as well as substitution or regeneration of the electrolyte is possible. Despite the fact that organic redox molecules

cannot be regenerated in most cases, they are still very promising due to flexible customization. Active research is directed to the development of cheap, stable, and highly soluble organic pairs.

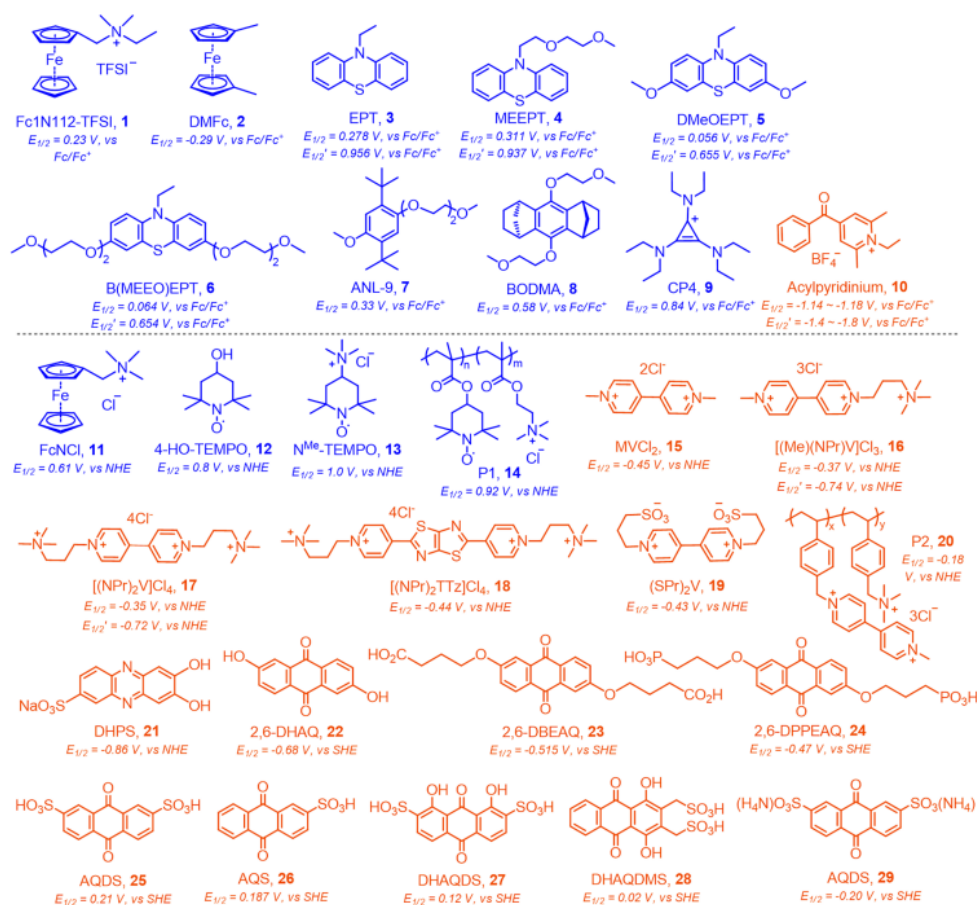


Fig. 1.9. Structures and redox potential of catholyte (blue) and anolyte (orange) molecules used in organic solvent (1– 10) and water (11–29). Reprinted with permission from [96]. Copyright 2022 American Chemical Society

In more detail, molecular engineering aimed to design the redox-active species for higher cell voltage, with higher solubility, reduced crossover, increased stability, and fast

kinetics. Molecules with improved characteristics serve as a proof of cost-effective organic electrolytes existence, even the up-to-date majority of synthesized molecules does not satisfy all requirements, and a compromise has to be accepted (Fig.1.8) [42,48,78].

In the scope of this work, we do not consider organic pairs in detail. In brief, the standard classification divides all molecules by active redox centers. Inside each type, there is a wide range of molecules, both for the anode and cathode sides, which are suitable for different types of solvents. These types of molecules are quinoids, quinoxalines, bipyridines, nitroxyl radicals, and ferrocenes (Fig. 1.9).

There is a benchmark molecule for each type and newly synthesized molecules are usually compared with it. We list only outstanding works with proven long-term cycles to show which problems remain unresolved and to estimate the available capacity of such compounds.

Table 1.4 Summary for organic RFB characteristics. The numbers of redox pairs correspond to the molecules in Fig. 1.9. The table is adopted from the review [96].

Copyright 2022 American Chemical Society

<b>Redox pairs</b>	<b>Electro-lyte</b>	<b>Energy density, Wh L<sup>-1</sup></b>	<b>Cycle number at current density</b>	<b>at</b>	<b>Coulombic (CE), Energy efficiency (EE), %</b>	<b>Capacity fade, % per cycle</b>	<b>Ref</b>
(NPr) <sub>2</sub> VCl <sub>2</sub>	0.5 M NaCl	9.2	500	at 60 mA cm <sup>-2</sup>	CE > 99%, EE 48%	0.005	[97]

#17 / #13 *	* See	Fig.1.9						
MVCl <sub>2</sub>	2 M	9.9	700	at 10	CE > 99%,	0.04	[98]	
FcNCl	NaCl			mA cm <sup>-2</sup>	EE 65%			
#11 / # 15								
AQDS(NH <sub>4</sub> ) <sub>2</sub>	0.75 M	12	300	at 60	CE > 99%,	0.0005	[99]	
I <sub>2</sub> / I <sub>3</sub> <sup>-</sup> #29	NH <sub>4</sub> I			mA cm <sup>-2</sup>	EE 70%			
2,6-DPPEAQ	1 M KCl	13	500	at 100	CE > 99%,	0.00036	[10	
K <sub>4</sub> [Fe(CN) <sub>6</sub> ]	pH 9			mA cm <sup>-2</sup>	EE 66%		0]	
#24								
DBMMB	1.0 M	15	100	at 15	CE 95%	0.2	[10	
FL	TEA-			mA cm <sup>-2</sup>	EE 70%		1]	
apr. #7 / #10	TFSI in MeCN							
DMFc+MVCl	1 M	16	4000	at 10	CE 99.8%	0.00005	[10	
One molecule	NaCl			mA cm <sup>-2</sup>	EE 60%		2]	
with 2 redox centers #2+#15								

It follows from the summary table 1.4 that the volumetric energy density so far does not exceed that in inorganic benchmarks, like VRFB with 35 Wh L<sup>-1</sup>, and this is a significant barrier to the transition to organic RFB in large-scale projects. Therefore, an additional increase in organic RFB capacity is needed [103].

#### *1.4.4 RFBs based on insoluble solid active materials*

Three approaches to solving increase specific capacity above solubility limit were proposed. (I) A cell can operate on immiscible redox electrolytes with high energy density without a membrane. Several electrolyte compositions were proposed for such a battery [43]. However, they suffered from low current densities. (II) Another way is an introduction of the solid materials for additional energy storage with high volumetric energy density. (III) Hybrid flow batteries, when one of the redox reactions involves solution/dissolution of the material were reviewed above. Here, we focused on suspension-based RFBs with redox-active particles in the electrolyte of two types: the chemical and the electrochemical reaction of solid.

Solid materials for energy storage in RFBs are represented by polymeric compounds with redox-active sides and inorganic particles with bulk or surface-based reaction. Each particle can undergo either a direct redox reaction inside the cell through an electrochemical process by collision with the electrode (semi-solid or slurry RFB) or an indirect process by chemical reaction with soluble redox mediators. Such systems are called redox-targeting RFB with a solid booster.

Several advanced systems were proposed as semi-solid RFBs, where the suspensions of particles were pumped through the cell. We included also the polymer solutions in the list, as high viscosity is a common feature for such systems.

One of the prominent works proposed to use of lithium-ion battery materials in suspension for advanced flow batteries:  $\text{LiCoO}_2$ ,  $\text{LiFePO}_4$ ,  $\text{LiNi}_{0.5}\text{Mn}_{1.5}\text{O}_4$ , and  $\text{Li}_4\text{Ti}_5\text{O}_{12}$ ,

which were mixed as a slurry with carbon black to get effective percolation network for effective redox conversion [104]. The main issues for inorganic suspension RFBs were charge flow out of the cell and slow kinetics limited by lithium intercalation reaction. Another RFB with  $\beta$ -Ni(OH)<sub>2</sub> nanoparticle suspension suffered from stochastic cycling behavior with fluctuated discharge capacity [105]. The problem was the formation of the unstable surface layer on the particles' surface during the redox reaction, thus, a search for the stabilization additives was required. To overcome these limitations, the next generation of polymer-based systems was proposed. Redox-active sites were anchored on polymer main chain, thus, problems with poor kinetics (organic species have fast kinetics) and crossover were solved. The prominent example of the RFB was based on TEMPO- and viologen- anchored polymers [106]. Capacity fade was 0.2% per cycle during the 100 cycles at 40 mA cm<sup>-2</sup>. This system had an energy density of 10 Wh L<sup>-1</sup>, and further capacity enhancement was limited by viscosity growth.

The next improvement was done by aggregating the polymeric molecules into clusters and micelles. Zn – polymer RFB with 'TEMPO Corona' was demonstrated with stable cycling only in a not-pumped cell (1000 cycles with 0.01% capacity decay) [107]. However, switching to the flow cell showed a drastic resistance of the system, which can be operated under 1-5 mA cm<sup>-2</sup> current densities. Another example of quinone copolymer particles as a slurry RFB demonstrated a similar trend in cycling: low current densities < 20 mA cm<sup>-2</sup> were used for cycling [108]. The capacity decay was 0.36% per cycle and total capacity utilization was 30 %. In further chapters, the nature of these losses will be discussed based on our publications.

Overall, the discussed redox systems are limited in the current densities range due to the high internal resistance of the cell, sluggish kinetics, the drastic difference in theoretical and practical capacities, still low energy density, and high viscosities [109]. As a next generation of RFBs, redox targeting RFBs with solid booster were designed to overcome these limitations [110].

Solid materials capable of reversible energy storage were placed in the tank. A chemical reaction between the solid booster and the mediator inside the tank passes effectively if the booster surface is accessible and the electrolyte can be freely pumped through the booster medium. From a thermodynamic point of view, the reaction is Nernst-driven, which implies matching the redox potential of the solid and soluble species. In table 1.5 we listed the pairs of solid-booster and mediator, which were described in the literature.

Table 1.5 Pairs of solid-booster and mediator with cell enhancement characteristics.

<b>Redox mediator (RM) / solid booster (SB)</b>	<b>RM capacity SB capacity theoretical</b>	<b>Capacity enhancement effect</b>	<b>Cycles with current density with coulombic and energy efficiencies (CE, EE)</b>	<b>Ref</b>
0.3 M Fe <sub>2</sub> (SO <sub>4</sub> ) <sub>3</sub> / Polyaniline	26 Ah L <sup>-1</sup> 64.8 mAh g <sup>-1</sup>	41.2 mAh L <sup>-1</sup> 84 Ah L <sup>-1</sup> teor	25 cycles at 200 mA cm <sup>2</sup> give CE 88%	[111]

0.1 M 10-methylphenothiazine as the cathodic and 9-fluorenone as the anodic mediator NASICON-type $\text{Na}_3\text{V}_2(\text{PO}_4)_3$ for both sides	8 Ah L <sup>-1</sup> Cathode 117 mAh g <sup>-1</sup> / 24 Ah L <sup>-1</sup> Anode 58.5 mAh g <sup>-1</sup>	Cathode 82, Anode 41 Ah L <sup>-1</sup> Cathode 137, Anode 81 Ah L <sup>-1</sup> teor	2 cycles at 0.20 mA cm <sup>-2</sup> give CE of 97% and EE of 82%	[112]
$\text{VO}_2^+/\text{VO}^{2+}$ Prussian blue analogue (VO) <sub>6</sub> [Fe(CN) <sub>6</sub> ] <sub>3</sub>	25 Ah L <sup>-1</sup> 135 Ah L <sup>-1</sup>	44.6 Ah L <sup>-1</sup> 135 Ah L <sup>-1</sup> teor	70 cycles at 30 mA cm <sup>-2</sup> give CE of 97% and EE of 82%	[113]
0.2 M ferrocene-grafted ionic liquid LiFePO <sub>4</sub>	38 Ah L <sup>-1</sup> 170 mAh g <sup>-1</sup>	96 Ah L <sup>-1</sup> 300 Ah L <sup>-1</sup> teor	50 cycles at 30 mA cm <sup>2</sup> give CE of 97% and EE of 92%	[114]
0.3 M K <sub>4</sub> [Fe(CN) <sub>6</sub> ] Ni(OH) <sub>2</sub>	8 Ah L <sup>-1</sup> 1180 Ah L <sup>-1</sup>	29 Ah L <sup>-1</sup> 60 Ah L <sup>-1</sup> teor	100 cycles at 20 mA cm <sup>-2</sup> give CE of 99% and EE of 79%	[115]
0.2 M K <sub>4</sub> [Fe(CN) <sub>6</sub> ] LiFePO <sub>4</sub> in H <sub>2</sub> O - DMSO mixture	5 Ah L <sup>-1</sup> 170 mAh g <sup>-1</sup>	10 Ah L <sup>-1</sup> 435 Ah L <sup>-1</sup> teor	1 cycle at 1 mA cm <sup>-2</sup> gives CE of 99%	[116]
0.25 M K <sub>4</sub> [Fe(CN) <sub>6</sub> ] Fe <sub>4</sub> [Fe(CN) <sub>6</sub> ] <sub>3</sub>	6.7 Ah L <sup>-1</sup> 124 mAh g <sup>-1</sup>	61.6 Ah L <sup>-1</sup> 222 Ah L <sup>-1</sup> teor	500 cycles at 20 mA cm <sup>-2</sup> give CE of 99.7% and EE of 87.5%	[117]

Anode:				
0.2 M 2,7-AQDS	5.36 Ah L <sup>-1</sup>	22 Ah L <sup>-1</sup>		
Polyimide	150 mAh g <sup>-1</sup>	97 Ah L <sup>-1</sup> teor		
Cathode:	8 Ah L <sup>-1</sup>	12 Ah L <sup>-1</sup>	500 cycles at 5 mA cm <sup>-2</sup> give CE of 95% and EE of 77%	[118]
0.6 M NaI	60 mAh g <sup>-1</sup>	31 Ah L <sup>-1</sup> teor		
NiHCF				

**One can conclude that demonstrated capacity enhancements are impressive, however, all are far below the theoretical limit. The main reasons are incomplete utilization of solid-booster capacity, as well as low concentrations of mediators. In case of semi-solid RFB, the utilized capacity of the solids must be increased, for that, it is essential to understand the limiting factors of such behavior. The methods of electrolyte diagnostics for different types of electrolytes will be discussed below.**

#### *1.4.5 Electrolyte characterization methods and RFB performance metrics*

The development of new electrolyte compositions with high energy density, which can give high efficiencies in flow battery tests remains a crucial task for the RFB research

field. New electrolyte is usually characterized in terms of thermodynamic and kinetic parameters out of the RFB cell, followed by under-flow tests.

Overall, several consecutive tests are performed to characterize the electrolyte. Firstly, the structural and chemical characterization of redox-active species is performed by a suitable set of physical-chemical methods, nuclear magnetic resonance (NMR), UV/vis, Infrared (IR) and Raman, mass spectroscopies; atomic absorption (AAS), and atomic emission spectroscopies (AES), Electron Spin Resonance, elemental analysis, X-ray diffraction and Energy-dispersive X-ray spectroscopy (EDX) [49]. As a result, the established formula, molecular weight, and structure allow researchers to evaluate the theoretical gravimetric capacity of the material.

The second step implies a thermodynamic and kinetic parameters extraction using well-developed classical electrochemistry approaches such as cyclic voltammetry, rotation disk electrode, and EIS for materials dissolved in low concentrations in three-electrode cell [119]. Additionally, spectroelectrochemical methods can be applied to investigate the reaction pathways and molecule transformation during the redox process [120,121]. One can conclude the preliminary redox potential of the studied species ( $E_0'$ ), estimates its impact on activation losses in case of slow electron transfer ( $k$  – the electrochemical rate constant), and get a raw estimation of maximal limiting currents ( $i_{lim}$ ), based on diffusion coefficient ( $D$ ) calculation. Usually, the values in a flow cell test differ from those derived by the *ex-situ* methods, as high concentration, porous electrodes, and forced convection regimes drastically influence the current-voltage response [122]. To sum up, the external

methods of electrolyte evaluation give information of formal potential and kinetics of redox reaction, while its stability needs to be assessed additionally as well as RFB performance.

Thirdly, tests in the static cell come to place providing an accelerated stability measurement. The degradation level of the material is controlled by specific physical-chemical methods of characterization, which are sensitive to the possible degradation changes in the solution [123]. In other words, capacity decay represents the maximum CE, that can be achieved, while an additional control method shows how the material degrades and which strategies can be applied to mitigate this fade.

Additionally, the solubility of the material is investigated to tune the supporting electrolyte and determine the maximal volumetric energy storage. Maximal volumetric filling of the solid material also characterizes the maximal available capacity. As a result, a balance between stability, viscosity, and energy density has to be achieved to get the representable data with effective power densities in the RFB tests.

Last, but not least, tests in the flow cell represent the real perspectives of the material. No universal protocols for the cell test are selected by the scientific community, thus, the comparison of literature data is complicated. However, several attempts in the unification of test protocols were done [49,78,124]. One of the works aim to introduce a representable degradation protocol test, utilizing a symmetric cell design (one electrolyte of 50% SoC) and a special cycling protocol [78]. Another work discusses in detail typical parameters, that characterize the cell performance [124]. I already used the terms for different chemistries in comparison above [125]. Here, I briefly introduce the typical

parameters used to describe the quality of the selected RFB (Table 1.6). The same notation is used throughout the thesis work.

Table 1.6 Characteristic parameters of electrolyte and RFB performance.

Short name	Formula	Notations
$q^V$ , $Ah L^{-1}$	$q^V = \frac{Q_E}{V_E}$	$q^V$ – volumetric electrolyte capacity $Q_E$ – total charge delivered by electrolyte portion of volume $V_E$
$q^m$ , $Ah g^{-1}$	$q^m = \frac{Q_E}{m_E}$	$q^m$ – gravimetric electrolyte capacity $Q_E$ – total charge delivered by electrolyte portion of mass $m_E$
$w^V$ , $Wh L^{-1}$	$w^V = \frac{Q_E * \overline{V}_{disch}}{V_E}$	$w^V$ – volumetric electrolyte energy density. $Q_E$ – total charge delivered by electrolyte portion of volume $V_E$ with an average cell potential $\overline{V}_{disch}$ during discharge.
$Q_{teor}$ , $Ah$	$Q_{teor} = \frac{\vartheta_E * n * F}{3600}$	$Q_{teor}$ – maximal charge that can be extracted from the electrolyte, based on $\vartheta_E$ mols of the active component with elementary redox reaction with $n$ electrons, $F$ – Faraday constant.
$CF$ , $\% / cycle$	$CF = \frac{1}{N} (100 - \frac{Q_{disch}}{Q_{teor}})$	$CF$ – capacity fade during $N$ cycles, which represents a loss of capacity due to the

		<p>degradation regarding the cycle number.</p> <p><math>Q_{disch}</math> is an extracted charge during one discharge cycle with respect to total <math>Q_{teor}</math></p> <p>*<math>CF</math> can be expressed in % / day to represent the time capacity decay.</p>
$CR, \%$	$CR = \frac{Q_{disch}}{Q_{teor}} * 100$	<p><math>CR</math> – capacity retention during one cycle, which represents a real extracted charge <math>Q_{disch}</math> during total discharging with respect to total <math>Q_{teor}</math>.</p>
$i,$ $mA\ cm^{-2}$	$i = \frac{I}{A_{cell}}$	<p><math>i</math> – current density for cycling tests, <math>I</math> – an applied current, <math>A_{cell}</math> – a geometrical area of the membrane in the cell.</p>
$CE, \%$	$CE = \frac{Q_{disch}}{Q_{charge}} * 100$	<p><math>CE</math> – coulombic efficiency is a ratio between the extracted charge <math>Q_{disch}</math> during total discharging of the cell and the total charge <math>Q_{charge}</math> inserted into the cell during charging within one cycle.</p>
$VE, \%$	$VE = \frac{\overline{V}_{disch}}{\overline{V}_{charge}} * 100$	<p><math>VE</math> – voltage efficiency is a ratio between the averaged cell potential <math>\overline{V}_{disch}</math> during discharge and the average potential <math>\overline{V}_{charge}</math> during charging.</p>

$EE, \%$	$EE = CE * VE$	$EE$ – energy efficiency represents the total efficiency per cycle in terms of energy loss. It is calculated by the multiplication of coulombic and voltage efficiencies for simplification. In general, EE is a ratio of total extracted energy and inserted energy into the battery within one cycle.
$SOC, \%$	$SOC = \frac{Q_{charge}(t)}{Q_{teor}} * 100$	$SOC$ – state of charge is a ratio of the charge stored in the battery at a specific time $Q_{charge}(t)$ and the total battery capacity $Q_{teor}$

Below a quick review of how the discussed research logic was applied to the insoluble solid class of redox-active materials is presented.

#### 1.4.6 Characterization of insoluble solid redox-active materials

Firstly, the structure and formal chemical composition of solid materials are characterized. Refined crystal structure parameters, microphotographs of morphology, and elemental analysis are a standard set of characteristics used for crystal redox-active materials [112,114]. The amorphous-based material, like congregated redox-active polymers, is characterized in terms of particle size, and molecular weight RFB [108]. Theoretic specific capacity is calculated based on chemical composition.

Then, formal potentials of redox transitions, and the number of electrons are determined using cyclic voltammetry. Standard dried slurry electrodes are usually used for the intercalating materials, which are tested in a half-cell [126]. Alternatively, glassy carbon electrodes can be covered with special inks, containing the solid material and binder [112,113]. Moreover, cyclic voltammetry from the concentrated suspension can be also applied [106]. The authors applied also a rotation disk electrode measurement to get a raw estimation of diffusion coefficients and apparent rate constants, despite the fact of colloidal solution, the equations were based on the model of pure diluted solution. Here, it is worth mentioning, that raw estimation of the real specific capacity of the material is possible, as the charge can be integrated from the experiment and the mass of the sample is known.

The compatibility of electrolyte components, like a solid booster/mediator pair, is checked by external characterization methods, like IR and XRD [108,116]. Changes in the structure during the deintercalation/deintercalation can be tracked, or changes in IR-bands intensities due to the reorganization of redox-active sites. Additionally, the viscosity of the slurry and pumping rate can be balanced before the RFB tests.

As the last step, materials are tested inside the flow battery and efficiencies and capacity fade are calculated. Static H-cell tests are used for fast degradation rate determinations, while cycling in flow battery usually lasts longer and shows the real available capacity and its fade. Up to 100 cycles under flow conditions is a required proof-of-concept demonstration. Achieved power and capacity characteristics are rarely discussed in terms of reasons for non-100% utilization (Table 1.5 showed that capacity utilization for most reviewed papers was below 50%). For example, prolonged cycling of

polymer suspension was demonstrated with a capacity fade of 0.01 % per cycle, however, the utilization capacity of the material was only 17 %, which equaled the volumetric capacity of a 9 Ah L<sup>-1</sup> [106].

**To sum up, the existing methods of electrolyte characterization show its power and energy parameters but do not reveal the reasons for the decrease or increase in the specified values. Advanced methods must be developed to track the reaction pathways investigate the degradation processes and elucidate the bottleneck of the redox processes of new materials.**

## 1.5 Main components in the electrochemical cell

### 1.5.1 Main function of cell components

Flow cells are the main part of the system responsible for energy conversion processes. Development of an effective cell/stack is an engineering challenge as special properties of the materials, complex electrolyte hydrodynamics, manufacturing restrictions, and economic availability have to be taken into the account. In the scope of this work, we will focus on materials' properties and requirements for them, without delving into stack engineering. In general, the electrochemical stack consists of end plates, current collectors, plastic frames, bipolar plates, porous electrodes, gaskets, and a separator (commonly, a membrane) (Fig. 1.10). All components are tightened together in a sandwich-like block by fastening elements. Below we discuss in detail the function of each basic component, main properties, and investigation methods for each of the components.

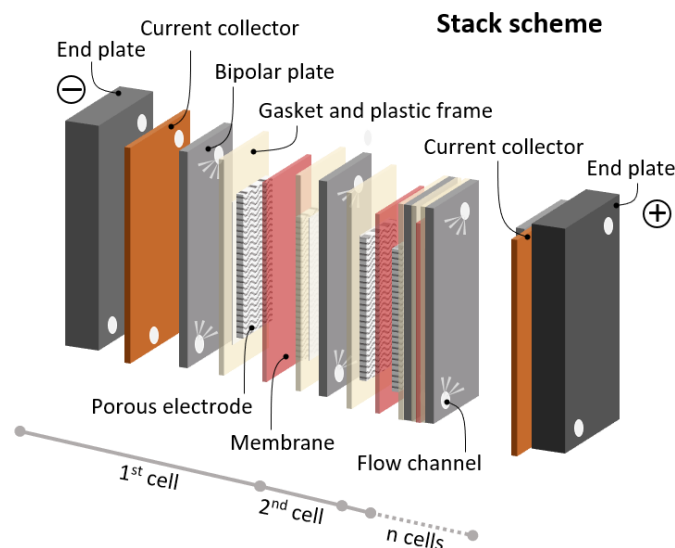


Fig.1.10 Scheme of RFB stack of  $n$  single cells in series with internal components.

When the electrolyte flow through the stack, each component plays a specific role in effective energy conversion processes:

- **End plates** are usually metal flat plates with specially designed inlet and outlet fittings for electrolytes. Moreover, they distribute the pressure evenly over the entire stack area and are the basis for fastening the tightening bolts.
- **Current collectors** serve for the accumulation of charge from the bipolar plates and delivery is into the power system. The plates are usually made of copper or gold-plated metal.
- **Bipolar plate** provides electron shortcuts from a porous electrode to a current collector. It serves as the electrode made of impermeable, dense material with high conductivity. Moreover, the plates allow a serial connection of the cells: one bipolar plate serves as a negative electrode for the first cell and as a positive electrode for the second cell [127] (Fig 1.9). A bipolar plate is made of inert conductive materials, such as carbon composites, titanium, or aluminum.
- **Plastic frame** provides a non-leakless connection of bipolar plate with porous electrodes and electrolyte channel. It distributes the catholyte through the one half-cells and the anolyte through opposite ones. The frame is designed for effective distribution of an electrolyte through the porous electrodes, prevention of shunt currents, and maintaining assembly tightness. The frames are usually produced from standard plastics like PP, PE, or PVC.

- **Gasket** is a flexible thin film, which prevents leakage between solid components of the stack. It protects the membrane from damage by protruding defects of bipolar plates and electrodes. This film is made of rubber.
- **Porous electrode** provides the main surface involved in heterogeneous redox reactions. The electrolyte flow through the porous media and the redox-active component diffuses to the electrode surface, oxidizes/reduces, and flows back to the flow channel. The electrode materials vary depending on the utilized electrolyte.
- **Membrane** is the key component that maintains electroneutrality inside the cell, conducting ionic current between two half-cells [128]. However, some specially designed electrolytes can work without the membrane due to immiscibility [42,129,130], majority of proposed electrolytes requires separation by the membrane [131,132]. Typically, the membrane conducts small size ions, like  $\text{H}_3\text{O}^+$ ,  $\text{Li}^+$ ,  $\text{Na}^+$  or  $\text{HSO}_4^-$ , as such structure configuration prevents redox-active molecules crossover, and small-sized ions have higher mobility. Membrane technology is developing extensively, and a lot of polymeric, ceramic, and composite materials were proposed.

### *1.5.2 Material requirements for each component*

Based on the role of each component, target values of material properties are formulated. General requirements for all components are (1) the mechanical durability; (2) the maintenance of form integrity of the part under constant pressure and electrolyte flow; (3) chemical and (4) electrochemical stability. The last two requirements imply that the

material must not react with electrolyte components and be oxidized/reduced under operation conditions. Long-duration tests for mechanical, chemical and electrochemical stability were not sufficiently developed, as RFB prototypes cycling usually last longer than a noticeable difference in material properties [133,134]. However, sometimes lack of investigation leads to the malfunction of installation [135]. We discuss several accelerated degradation tests in our papers devoted to bipolar plate materials.

Specific requirements for the material for each component are listed below:

- **End plates** are made of hard corrosion-resistant material.
- **Current collectors** are easy to polish metal plates with high conductivity.
- **Plastic frames** are made of nonporous plastic, which holds its shape steadily under load and is convenient in production.
- **Gasket** is a flexible thin film, which does not lose its elasticity over time and is guaranteed to be resistant to the effects of electrolyte and high overvoltage.
- **Membrane** has to conduct efficiently supporting electrolyte ions and block the penetration of redox-active species to another part of the cell. In other words, it must have low permeability toward active components. The selection of the material for the membrane depends on the chemistry of active materials, basic solvent, and pH. For example, the most widely used material for acid-based vanadium RFB is the Nafion membrane due to its chemical stability and high proton conductivity [136].
- **Porous electrodes** are made of stable well-conductive material with a high surface area. Ideally, the material has to be highly porous with open pores to reduce the pressure drop

through the stack. Tuning the electrode surface can sufficiently improve the kinetics of the reaction and boost the RFB power, that is why a lot of effort is done in this field for every type of RFBs [137,138].

- **Bipolar plates** are made of impermeable, dense materials with high electrochemical stability and high electronic conductivity.

To sum up, optimization of the cell components is performed for two reasons: to increase the durability of the stack by damping the capacity fade and to increase the nominal power by reduction of cell internal resistance. As each component and each interface can lead to system failure, it is essential to check each component individually [139]. We drew schematically the equivalent circuit for a single cell to illustrate the importance both of bulk and interfacial conductivities of each component (Fig. 1.11) as well as charge transfer resistances determined by the kinetics of redox reaction.

The sum of serial resistances from a current collector, bipolar plates and the membrane gives an Ohmic resistance of the cell, detected as a high-frequency intersection of the real axis, it is constant at any loads [140,141]. A parallel connection of the charge transfer resistance and constant phase element (CPE) represents a double layer in the electrode and averaged derivative overpotential by current, thus, it is variable for different loads. Total low-frequency response of the system can also include the diffusion term (for mHz range), but in general, the resulting resistance of the cell is equal to the sum of components and charge transfer ones.

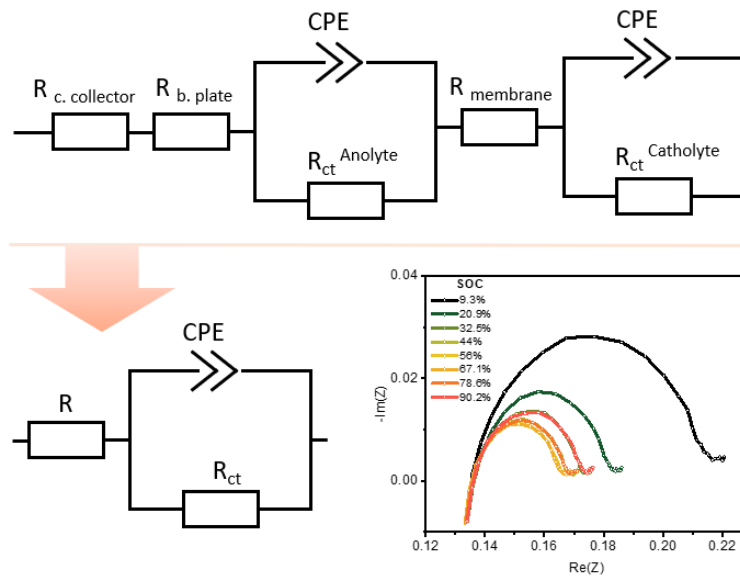


Fig. 1.11 The equivalent circuit of the single RFB cell with listed components, the generalized equivalent circuit used for fitting, and the Nyquist plot of a 5 cm<sup>2</sup> single cell with 1.6 M vanadium electrolyte at different SOCs. Voltage amplitude was 10 mV vs. OCV.

Figure 1.11 illustrates that conductivity and interfacial resistances are the main target parameters that scientists look at when designing the material. We discuss the electrode and bipolar plate materials and their characterization methods for example of vanadium RFB system in the next section. The focus on vanadium chemistry is for two reasons. Firstly, the use of vanadium as a raw material is quite profitable for Russia, meaning that the localization of the stack components production will make the technology economically viable. Secondly, the vanadium technology requires an increase in stack

power, which can be done by tuning components' properties, thus, an understanding of the improvement origins is needed for the target material design.

### *1.5.3 Benchmarks for electrode material for vanadium RFB*

Porous electrodes are based on carbon materials for almost all batteries, as cheap, well-conductive, and inert substrate [66]. Three main types are utilized for vanadium RFB: carbon felt, graphite felt, and carbon paper. These types differ by morphology and heat-treatment procedure during the manufacturing. Nevertheless, the materials have a large surface area, batteries performance with non-treated electrodes usually was poor [142]. Improvement of porous electrodes is a powerful method to enhance RFB power, especially for redox reactions with slow kinetics, like vanadium.

In general, there are two ways of electrode modification: either the material's surface is activated by special treatment, or it is decorated by additional electrocatalysts. Activation of the electrode surface by a different method (thermal, plasma, CO<sub>2</sub>) was reported as an effective way of performance enhancement [143–145]. In basics, the activation procedures changed the microstructure of the pristine surface and attached active sites, the oxygen-containing groups. As for additional surface decoration, over 70 scientific papers devoted to modification by electrode additives were reviewed recently [146]. The authors divided the modification into carbon-based (graphene, graphene oxide, carbon microspheres, carbon aerogel, carbon nanotubes) and metal-based (copper, nickel, bismuth, titanium, and tungsten) electrocatalysts. The comparison of the utilized capacity

at 100 mA/cm and the energy efficiency for different carbon felts and additives showed that metal-based additives are more efficient. In general, a typical pipeline of a new material investigation includes electrode modification method, morphology characterization, and tests in a single VRB cell to show the enhancement, without deep analysis of its origin.

However, for all reviewed papers there is no straightforward interpretation of enhancement origin, which can relate to hydrodynamic flow facilitation, new catalytic activity, increase in available electrochemical surface area (ECSA), wettability, or mass-transport improvements [146,147]. Several works looked through the correlations of different surface electrode characteristics and performance metrics and concluded that 1) wettability increases after the treatment, leading to the growth of ECSA [142]; 2) concentration of oxygen-surface groups improves kinetics up to some limit [148]; 3) mass transport through different electrodes morphologies plays a crucial role only for fast redox processes (like, for organic molecules) [149,150]; 4) introduction of active sites with the oxygen or nitrogen atoms, as well as metal nanoparticles improves the sluggish kinetics of vanadium [146]; 5) the degradation processes occur rapidly at electrodes with small ECSA and lead to the formation of sp<sup>3</sup> types of carbon on the surface [151]. However, elucidation of clear electrocatalysis mechanisms of different electrode modifications is complicated due to uncertainty in a real surface area and changing mass transport; thus, only integral enhancement effects are demonstrated in RFB prototypes.

The combination of electrochemical techniques with other characterization methods, like spectroscopies, allows scientists to track the reaction pathways in-situ.

However, the stability of the electrolytes itself was in the scope of the scientist's interest, but not the reaction pathways. For example, FTIR spectroelectrochemical tests were performed to track the solid-booster – mediator reaction for polyimide – 2,7-AQDS pair, showing the hydrogen-bonding mediated reaction mechanism [118]. Operando XRD experiments were conducted for MPTZ – NVP system to track the SOC at which the targeting redox reaction started [112]. UV-vis spectrometry in a specially made cell was used as an effective tool for electrolyte stability tests in organic RFB [152] and extraction of degradation mechanisms in metal-organic complexes (for example, chromium acetylacetonate) [153]. Operando studies of V(III) to V (IV) allow to distinguish different pathways of the reaction and decouple bulk pathway or a surface-catalyzed pathway, which depended on the state of the electrode surface [154]. A minor number of articles in the spectroelectrochemistry area for RFB applications is explained by the difficulty of conducting an experiment and interpretation. However, the research trend of the in-situ combination of methods is rising.

Moreover, in addition to reaction mechanisms deconvolution, the determination of the apparent rate constant of the reaction can also be a representative quantitative metric of electrocatalyst efficiency. These values are used in the modeling of the system and standard evaluation of these parameters allows the comparison of different electrode materials. Despite the fact that vanadium kinetics of both redox reactions has been studied intensively, data has significant variation in rate constants estimations and preferential mechanisms. As an illustration, the comprehensive review Roznyatovskaya et al. [155] highlights the four orders of magnitude difference in reported surface area-normalized rate constants.

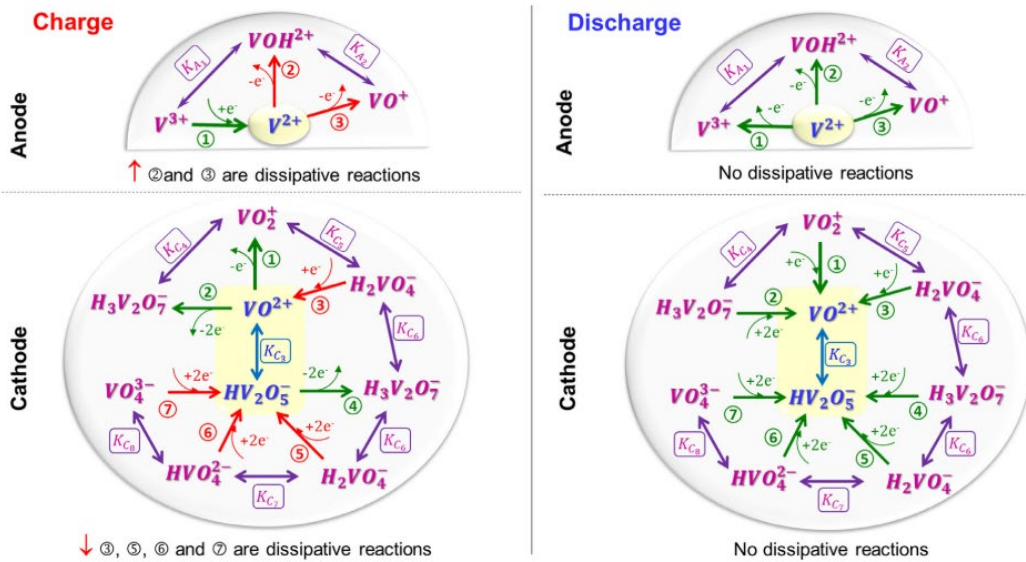


Fig. 1.12. Schematic representation of the reactions during its charging and discharging processes. Adverse and favorable events to the overall performance of the VRFB are highlighted with red and green arrows, respectively. Reproduced with permission from [156]. Copyright 2022 Elsevier

Classical techniques of rate constants determination, like RDE measurements, do not represent real conditions in the cell due to 1) high concentration of the electrolyte (1.6 M), 2) unknown ions activities, 3) forced convection of electrolyte through porous electrodes [123]. Therefore, a combination of new advanced setups and mass-transfer modeling is required for a more detailed determination of the rate constants. For example, the microfluidic cell was used to extract the rate constants under a forced convection regime for 1.7 M electrolyte. Resulted values of the constants were in the order of  $10^{-7}$  cm/s for

anolyte and  $10^{-5}$  for catholyte, however, the values were derived from Tafel slopes without considering a proton concentration. Advanced 0-D model extended for accounting the activation losses in a full cell design, using the Butler-Volmer formalism, showed that interpretation of the loss's origin is ambiguous, meaning that all losses can be assigned to any of half-cells, hence, direct extraction of kinetics parameters from the cell is not possible [157]. Moreover, the majority of the works treated the reaction mechanism as a single-step reaction for the simplification and reduction of fitting parameters, while the mechanisms are multi-step and the formal description of the stages is very complex in reality (Fig. 1.12) [156]. Therefore, a single-step approximation for extracting the apparent rate constants is one of the ways to derive useful and accurate values, excluding the consideration of mechanisms.

To sum up, the quantitative effect of electrode modification can be assessed by the determination of the electrochemical rate constant of the particular reaction. However, this approach does not distinguish the reason for the losses, which can be achieved by enhancing wettability, improving mass transport, increasing an active surface area, or changing the reaction mechanisms. These origins can be illustrated only with help of in-situ techniques, tracking the formation of new species on the electrode surface directly. At the end of this chapter, the questions in vanadium kinetics addressed by our research are listed.

#### 1.5.4 Benchmarks for bipolar plate material.

Bipolar plate materials were adopted for RFBs from polymer electrolyte membrane fuel cell (PEMFC) technology (Fig. 1.13) [158]. The selection of the particular materials is defined by the properties of utilized electrolytes and the stack designs. Carbon-polymer composites are standard materials for the vanadium RFB due to their chemical stability and low permeability [65].

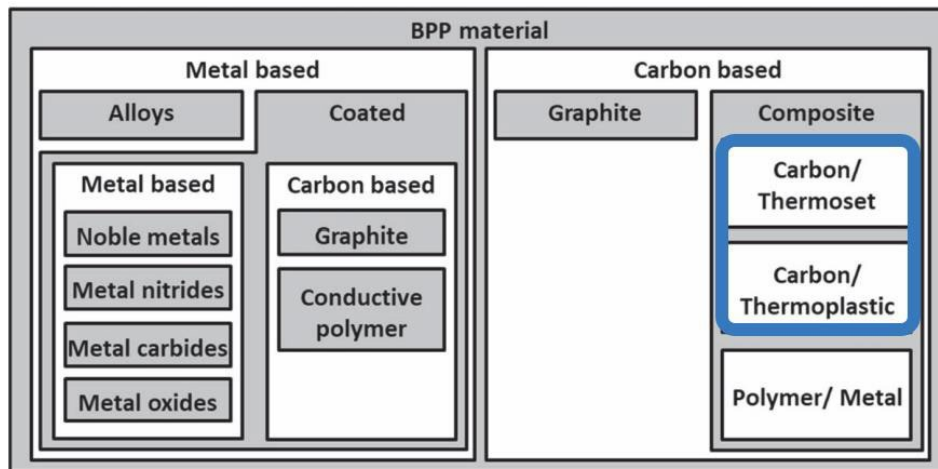


Fig. 1.13 Classification of bipolar plate materials for PEMFC and RFB applications. The blue frame represents suitable classes for vanadium RFB. This image is adopted from the work [158]. Copyright 2022 Electrochemical Society by IOP Publishing Limited

A comprehensive review is focused on carbon composite bipolar plates, listing the manufacturing procedures and the components: natural, spherical, and artificial graphite flakes, Ketjen black carbon, exfoliated graphite, and carbon fiber are used as carbon sources; and polyphenylene, various types of epoxy, polyvinylidene fluoride, etc. are used as a binder [158]. There are different manufacturing limitations for each material.

However, in general, manufacturers choose the economically profitable technology that suits the minimum acceptable requirements. Testing of the material includes several stages, discussed below.

The bipolar plate is a terminal for all electrons received on the porous electrodes to transport the external circuit. Therefore, the following requirements are crucial for the material selection: 1) a high electronic conductivity; 2) zero permeability to prevent battery self-discharge; 3) mechanical stability for convenient manufacturing process; 4) chemical and 5) electrochemical stability. The following methods are proposed to test the materials in the scope of the requirements.

Electronic conductivity is probed by a 4-probe test and by high-frequency EIS of an assembled cell. Sample of material is milled in shape, required for a cell assembling, then tested externally and in the cell with low-resistive membrane and symmetric electrolyte [158]. Moreover, additional attention was paid to the porous electrode – the plate contact, several specially designed additives were proposed to reduce this contact resistance: cactus-like carbon nanofibers effectively increased the contact area [159], adhesive conducting layer glued together the plate and the electrode [160].

The permeability is tested by applying a pressure difference across the bipolar plate sample, by estimating the area capacitance of the sample by cyclic voltammetry in the inert electrolyte, or by swelling of the sample in the electrolyte. The comparison with a known benchmark sample is required for reliable data interpretation for both methods. A pressure test is required for mechanically stable material and a specially designed setup, which is

usually used for commercial benchmarking. The electrochemical test is more accessible to perform, but it gives indirect proves permeability levels, operating the available surface for the electrolyte. Typically, the CV in 0.5-2 M H<sub>2</sub>SO<sub>4</sub> at different scan rates is used for accurate capacitance calculation [161]. The comparison of the samples is possible if the experimental parameters are fixed, and the geometric area of the studied bipolar plate is determined. A swelling test is performed before and after the cycling [158].

Mechanical stability is estimated by ultimate compressive strength tests, by assessment of time production, and by a number of defective units. The compression test is selected because it is a standard loading type for stack assembly [65].

The chemical stability of carbon materials can be crucial for catholyte components, as the most oxidative component of the electrolyte is the VO<sub>2</sub><sup>+</sup> ion. However, the formation of V<sub>2</sub>O<sub>3</sub><sup>2+</sup> dimers in the concentrated electrolyte limits quantitative analysis of degradation rate. This ion hinders the calculation of concentration change using UV-vis spectroscopy or electrochemical techniques, as calibrations are non-linear. Several methods were proposed to overcome the problem. Firstly, materials properties were monitored during aging in 0, 20, 80 and 100% SOC's anolyte and catholyte solutions [161]. Gradual oxidation of the surface was demonstrated as well as a significant increase in ECSA. Secondly, a comparative stability study of several samples can be done by the accelerated stress test (AST). After forced oxidation by anodic polarization in vanadyl solution, a visual, morphological, and surface group content were characterized [65,161]. Moreover, standard tests, developed for fuel cells materials are also applicable to the vanadium RFB [162]. For example, a protocol using Ce<sup>4+</sup> at 80 °C was proposed [163]. As a result, the

broad variety of ASTs does not allow numerical comparison of materials from different research groups.

Finally, the bipolar plates are tested in the RFB prototypes. Additionally, the flow field design can be tuned. The polarization slope, the maximum power density at fixed SOC, and electrolyte composition are standard characteristics of the cell quality assessment, which can be compared between the assemblies with flow fields, pump rates, and electrolyte composition.

**In conclusion, I want to point out that the development of materials is ongoing, despite the already large number of commercialized materials [158]. The main driver for the development of new materials is the desire of local manufacturers to reduce costs and localize bipolar plate production [164]. Thus, researchers continue to develop and test low-cost materials using reviewed algorithms.**

## **1.6 Summary from the literature review**

The literature review demonstrates the relevance of flow batteries in energy storage applications in comparison with other storage technologies. I have shown that the RFBs profit grows with prolonged cycle life when irreversible capacity loss becomes slower than in other storage systems. However, the low specific capacity of the RFBs and problems with incomplete capacity utilization make unprofitable RFB applications in many cases now. To reduce the energy cost, a detailed design, engineering, selection of materials and battery management systems development are necessary. Then, the roadmap for the development of a flow battery system was provided. Based on it, the problem of incomplete capacity utilization can be related either to chemical processes in the electrolyte, or to the stack construction features. In the case of low electrolyte capacity, the actual goal is a search for new stable compounds with increased and stable capacity. In the second case, target selection of materials that give the lowest internal resistance of the battery assembly is required. Systematic methodologies for the stack materials characterization and new redox active materials are only being formed. Thus, this thesis is devoted to characterization methods that allow choosing the material with optimal properties to maximize battery capacity and identify the reasons for low performance.

The first part of the literature review provides an overview of existing electrolytes: inorganic-, organic-, hybrid-based systems and the state-of-art approaches to enhance capacity. Up to date, the most promising direction in the development of the high-capacity electrolyte composition is the combined use of soluble and solid redox active components. However, significantly low practical capacities were demonstrated in all reviewed works.

Possible reasons for the incomplete utilization of capacity for advanced RFB with solid redox components and applied characterization methods for such systems were reviewed. However, most studies did not show or discuss reasons for the difference between theoretical and experimental specific capacities. It is even unclear whether the reason relates to the cell design or to the intrinsic properties of the redox colloids.

In the second part, the actual problems of stack materials development were analyzed in detail, showing the most prominent properties of the material, which contribute to the cell resistance. The vanadium-based system was chosen as a model RFB, due to a great accumulated scientific experience of this system and the VRFB suitability for a commercialization in Russia. The characterization methods of electrodes and bipolar plates materials were overviewed in detail, since these two components are key in reactions pathways. Substantial number of experimental approaches of the electrode modifications with the total cell efficiency improvement have been published. The application of the redox mechanisms' characterization methods and reaction modeling for a target development of electrode materials for efficient RFBs was observed. However, no systematic study of the enhancement reasons was done, and all works applied their own investigation protocol, so data comparison is hindered. The characterization methods review showed that the elucidation of the factor influence (e.g., hydrophobicity, real surface area or catalytic effect) on battery performance requires the material study outside the cell using specially designed characterization methods. Finally, the characterization methods of bipolar plate materials were reviewed. Special attention was paid to the stability

tests and degradation investigations, since the bipolar plate is often subjected to oxidation, and consequently, it increases the internal cell resistance.

In summary, all reviewed sections of the chapter were aimed to illustrate the significance of the problems discussed in the dissertation.

### **1.7 Goals and objectives of the Thesis**

The main goal of this thesis is the development of material characterization methods for the identification of kinetic limitations in different RFB electrolytes, as one of the main reasons for moderate practical capacities of these devices.

As it was discussed above, a low capacity utilization is attributed either to ineffective cell design or to sluggish kinetics of redox active species. As model systems, I chose a vanadium-based RFB and a promising class of composite electrolytes with enhanced theoretical capacity based on redox-active solid nanoparticles in suspensions. Thus, this work is aimed to solve the following objectives: 1) propose methods for the elucidation of the reaction mechanisms and their correlation with electrode material properties based on the vanadium model system; 2) identify the kinetics limitations that diminish the available capacity of redox-active colloids.

Three key questions should be answered in order to fulfil the first objective using the all-vanadium RFB as the test system: 1) how different carbon morphologies affect the redox reaction pathways for catholyte reaction during the formation  $\text{VO}_2^+$ ; 2) what electrokinetic parameters could be used and estimated for the VRFB with the industrial cell

design; 3) how strong the influence of bipolar plate morphology and electronic conductivity on the VFB performance is.

The second objective is addressed the problem: how to raise the practical capacity of the new type of electrolytes containing redox active colloids. Two methods of ex situ electrochemical methods were developed to characterize theoretic, experimental capacities of suspensions as well as to the reason for a low capacity utilization. Two materials are investigated: the redox-active polymer colloid with 4-amino-TEMPO sites and the composite of  $\text{LiMn}_2\text{O}_4$  nanoparticles with carbon nanotubes.

Overall, a set of new techniques for redox processes characterization is proposed. Solving the problem of low-capacity response from colloids can lead to the development of stable electrolytes based on a pair of solid and soluble redox active substances with a high specific capacity. Combination of such an electrolyte and a low-resistance stack will significantly improve the economic viability of the RFB technology.

## Chapter 2. Reaction mechanisms on porous electrodes in Vanadium RFB

### 2.1 Overview of the Chapter 2

Vanadium redox reactions in VRFB are multi-step processes, which depend on many aspects, like electrode morphology and surface-active group concentration. We developed the method to track the reaction pathways ( $\text{VO}^{2+}$  to  $\text{VO}_2^+$ ) on the electrode surface, combining Raman spectroscopy and cyclic voltammetry. Our initial hypothesis was that the spectroelectrochemical technique allows us to decompose the mechanisms into the elemental steps and elucidate the limiting one. This information could sufficiently simplify the models for VRFB kinetics and shed some light on ways to reduce the kinetics contribution into the cell resistance.

Deconvolution of Raman spectra revealed several mechanisms going in parallel, which depend on properties of surface and overpotential. We extracted similar patterns in the reaction pathways on different substates but were not able to distinguish the limiting step precisely. Moreover, we observed that dimerized vanadium ions are also involved in the reaction, which makes the real reaction mechanism more ambiguous. As a result, we proposed the descriptive scheme of the reaction pathways.

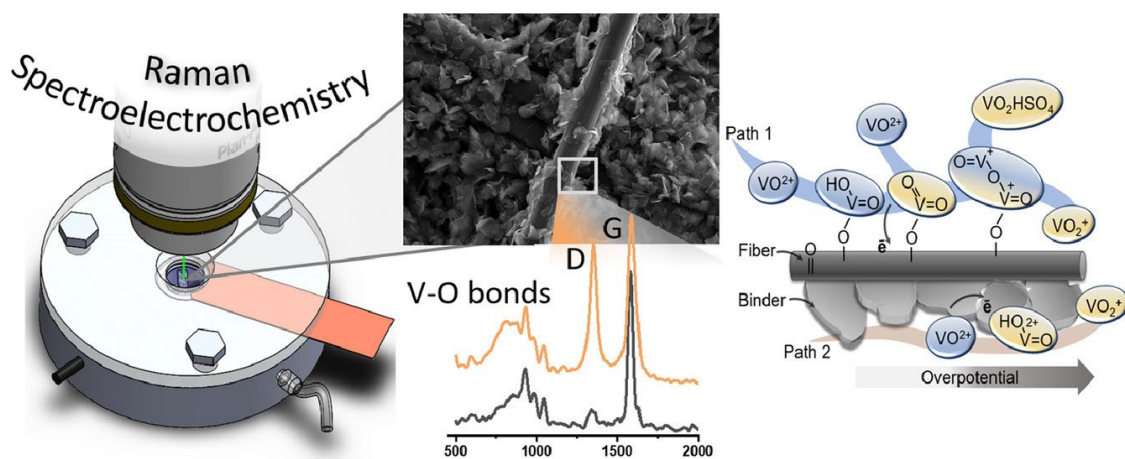
The method above showed a qualitative picture of the mechanisms but did not bring us closer to obtaining a simplified model of vanadium kinetics. Then we approached the problem from the other side. We treated the vanadium reactions as single-step ones with Butler-Volmer kinetics. We applied a specially designed model for fitting the polarization data from symmetric vanadium cells to estimate the apparent rate constants and charge

transfer coefficients. This approach isolated kinetic parameters for the real RFB system with a concentrated electrolyte, porous electrodes, and a constant electrolyte flow.

As the result, we proposed the catholyte reaction pathways and the set of kinetics parameters that characterizes vanadium redox processes in general, without considering the various mechanisms.

## 2.2 In situ spectroelectrochemical Raman studies of vanadyl-ion oxidation mechanisms on carbon paper electrodes for vanadium RFB

My contribution: Conceptualization, Methodology, Investigation, Software, Validation, Visualization, Writing - Original Draft.



Reprinted with permission from [165]. Copyright 2022 Elsevier



ELSEVIER

Contents lists available at ScienceDirect

Electrochimica Acta

journal homepage: [www.elsevier.com/locate/electacta](http://www.elsevier.com/locate/electacta)

# In situ spectroelectrochemical Raman studies of vanadyl-ion oxidation mechanisms on carbon paper electrodes for vanadium flow batteries



Nataliya A. Gvozdik\*, Keith J. Stevenson

Center for Energy Science and Technology, Skolkovo Institute of Science and Technology, Bolshoy Boulevard 30, bld. 1, Moscow, 121205, Russia

## ARTICLE INFO

### Article history:

Received 21 October 2020

Revised 16 March 2021

Accepted 31 March 2021

Available online 10 April 2021

### Keywords:

Vanadium flow battery

In-situ Raman spectroelectrochemistry

Carbon paper

## ABSTRACT

The elucidation of redox reaction mechanisms utilized in vanadium flow battery opens broad opportunities for targeted improvement of performance in specific power and energy efficiency. However, there is no unified agreement with regard to the catholyte reaction mechanism as common electrochemical methods such as cyclic voltammetry show general current-voltage response without distinguishing the various vanadium reaction intermediates involved in the redox reaction process. The literature describes several mechanisms that vary from electrode carbon composition, surface functionality, and electrolyte composition. Still, all proposed reaction pathways were derived from indirect models, and thus the introduction of an additional method for monitoring the speciation of vanadium moieties and for spatially resolving redox processes at the electrode/electrolyte interface is required for reliable validation of the reaction mechanism. Herein, we introduce a new spectroelectrochemical technique, which combines Raman spectroscopy with cyclic voltammetry as a powerful tool for deducing complex redox mechanisms at carbon paper electrodes. In particular, the vanadyl oxidation reaction mechanism was investigated on heated carbon paper with the help of in situ Raman Spectroelectrochemistry. Significant differences in the reactivity of carbon paper was found for electrodes activated at different temperatures and show that the fibers are more susceptible to oxidation, while the binder burns, which leads to a decrease in electrochemical active surface area. The monitoring of vanadyl oxidation showed two different reaction mechanisms on the fiber surface and the alternative one for the binder phase. Thus, this new spectroelectrochemical technique is an effective tool to track species transformation during redox reaction not only for catholyte in Vanadium Flow batteries but also for other systems.

© 2021 Elsevier Ltd. All rights reserved.

## 1. Introduction

The utilization of renewables is becoming a more pragmatic alternative with a global trend towards the implementation of environmental-friendly technologies [1,2]. The combination of renewables with energy storage devices having a capacity in the range 5 kW h–10 MW h drastically increase its rentability, and Redox Flow Batteries (RFB) are one of the most suitable technologies among the market options [3–5]. Their key features are independent scaling of capacity and power coupled with a long-cycle operation (20000 cycles), which comes from the utilization of stable redox-active soluble species, in particular, vanadium ions in different oxidation states that eliminates a crossover problem [6–8].

Typical vanadium electrolyte based RFB (1.5–2 M vanadium species in acidic solution) suffers from limited volumetric specific energy density coupled with incomplete electrolyte utiliza-

tion [9–12]. One of the straightforward approaches addressed to this problem is a decrease in cell resistance. The impact of activation losses coming from poor kinetics of vanadium redox reaction is usually estimated as 5–20% of cell resistivity [13,14]. Electrode improvement towards accelerated kinetics is considered as a preferable approach to overcome this limitation. Modification of carbon electrode surface was performed by various methods, such as alkaline, acid, oxidative treatment, ultra-sonification, CO<sub>2</sub> activation, catalytic particles impregnation, electrochemical oxidation, and heat treatment in the oxidative environment [14–20]. A significant improvement in VFB performance was demonstrated after modification in all these works. The origin of these strategies' effectiveness was an increase of wettability coupled with the acceleration of redox reaction rates [21]. However, the research to date has tended to focus on practical application rather than fundamental studies of the mechanisms that lead to improved kinetics of electron transfer of vanadyl ions at carbon electrodes.

\* Corresponding author.

E-mail address: [Nataliya.gvozdik@skoltech.ru](mailto:Nataliya.gvozdik@skoltech.ru) (N.A. Gvozdik).

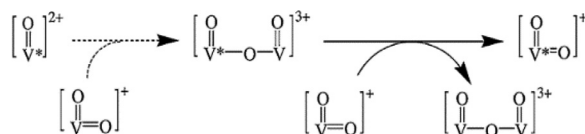


Fig. 1. Proposed reaction mechanisms of the  $\text{VO}_2^+/\text{VO}^{2+}$  redox couple studied via NMR spectroscopy [25,29,30].

A deep investigation of multi-stage reaction mechanisms has been mostly restricted to a limited amount of applied techniques (e.g., cyclic voltammetry). In particular, several-step mechanisms were suggested based on cyclic voltammetry and EIS, pointing out the importance of oxygen-containing groups as possible catalysts to accelerate vanadium redox reactions [22–24]. The hydroxyl, carbonyl, and carboxyl functional groups can act as active adsorption sites for vanadium ions (fixing ion's position on the electrode surface) and accelerate the electron transfer and the change of ion structure [15,25]. Moreover, a correct interpretation of the electrochemical data requires an accurate estimation of real electrochemical surface area (ECSA), as the introduction of hydrophilic groups on the surface leads to the growth of material wettability [21]. Greco and coauthors studied in detail thermally-treated carbon paper electrodes and demonstrated that overall oxygen content on the surface correlates with the growth of rate constant (data was normalized by ECSA). They also found that performance improved with the decay of ECSA, which was attributed to the combustion of the binder phase of the carbon paper [26]. So far, little attention has been paid to the role of morphology and local structure of the electrode material. It was shown that  $\text{sp}^2$  hybridized carbon content, as well as the  $\Delta E$  in  $\text{V(V)}/\text{V(IV)}$  reaction, decreased for amorphous carbons (Vulcan® XC72) during heating activation, while the tendency was vice-versa for more ordered structures (graphite and carbon paper) [27]. Hence, the activation treatment effect depends also on the material structure.

The extraction of different factors leading to change in the reactions' kinetics seems to be challenging, as complex electrochemical mechanisms are hard to trace and model; thus, the introduction of additional analytical techniques for species monitoring gives insights into the process [28]. For example, the electron exchange reaction  $\text{V(V)}/\text{V(IV)}$  in acidic solutions was examined by NMR spectroscopy. In the case of  $\text{V(V)}/\text{V(IV)}$  solution, an equilibrium of  $\text{V}_2\text{O}_3^{3+}$  complex,  $\text{VO}_2^+$ , and  $\text{VO}^{2+}$  ions was established, and electron transfer between the complex and free ion, following the scheme [29,30] (Fig. 1).

Based on this scheme, Wu and coauthors proposed that the surface oxygen plays the same role as complex formation in the solution: the reaction mechanism occurs via an inner-sphere species with C-O-V bond formation [25]. Further investigations have shown that the reaction mechanism is determined by the surface properties [31,32]. However, the proposed models were based on electrochemical measurements, and no detailed studies on the detection of intermediates were performed even at more standard electrode materials, such as the carbon paper or carbon felt.

This paper proposes a new methodology for the investigation of the  $\text{V(IV)}/\text{V(V)}$  reaction mechanism based on Raman spectroelectrochemistry. Spatially resolved detection of different vanadium species, as well as carbon material morphology, is possible with this technique. A specially designed electrochemical cell allowed us to combine cyclic voltammetry with a Raman microscopy and track the reaction at the electrode surface. Careful characterization of the materials was performed in order to track the properties change in tendency. The heat-treated carbon electrode with the best electrochemical performance was selected for deeper Raman microscopy investigation. The oxidation reaction of catholyte was studied in detail as the charging process ( $\text{VO}^{2+} + \text{H}_2\text{O} - \bar{e} \rightarrow \text{VO}_2^+ + 2\text{H}^+$ )

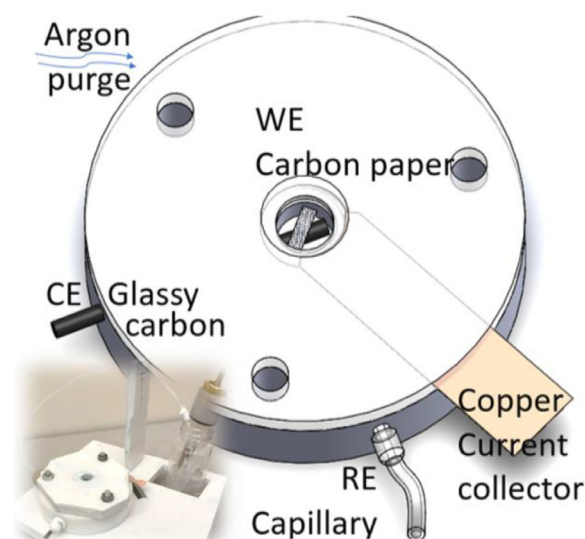


Fig. 2. Schematic model and a real cell for *in-situ* Raman voltammetry.

on thermally activated carbon paper. Analysis of Raman spectra revealed a drastic difference in Raman signal from two carbon paper components (fiber and binder), and different forms of vanadium species were detected. All in all, Raman spectroelectrochemical study of the reaction provided clear evidence of the existence of two different mechanisms in activated carbon paper.

## 2. Experimental

**Materials:** Carbon paper Sigracet SGL 28AA (Fuel Cell Store, USA) was used as pristine material for investigation.  $\text{VO}_2\text{SO}_4 \cdot x\text{H}_2\text{O}$  (Sigma-Aldrich, 97%) was used as a vanadium source. Carbon felt Sigracell GFD4.6 EA (Fuel Cell Store, USA) was used as a counter electrode in a 3-electrode *in-situ* Raman cell. Nafion® 115 as a membrane for the flow battery tests was conditioned before the tests.

**Carbon paper modification:** Series of carbon paper samples were heated under the air at different temperatures (400, 420, 440, 460, and 480 °C) for 20 h with 30 min of heating time and independent cooling in a muffle oven. The contact angle measurements were performed at Kruss DSA25 contact angle test stage. The microstructure of carbon paper was studied with FEI Quattro S Scanning Electron Microscope (the accelerating voltage was 15 kV with magnifications from  $\times 300$  to  $\times 5000$ ). X-ray Photoelectron Spectroscopy (XPS) measurements of carbon paper samples were performed using PHI 500 VersaProbe II spectrometers with spherical mirror analyzers. Al  $K\alpha$  monochromatic x-ray source with 1486.6 eV X-ray energy was utilized. Survey spectra were recorded with 1.0 eV step size, while high-resolution spectra were recorded with 0.1 eV step size. High-resolution XPS spectra were processed to obtain atomic concentration. First, photoelectron backgrounds were subtracted from the high-resolution spectra using Shirley function approximation. The resulting spectra were used for element quantifications. All the spectra were calibrated to the same C1s binding energy position 284.8 eV. Electrode capacitance was used as an approximate estimation of electrochemically active surface area (ECSA). Cyclic voltammetry with a weighted sample of the carbon paper as a working electrode was measured for scan rates 10, 20, 50, and 100 mV/s. The test was performed at 2.5 M  $\text{H}_2\text{SO}_4$  electrolyte. The capacitive current was used at the potential of 0.7V vs. Ag/AgCl 3 M KCl electrode. The same response from the polished glassy carbon electrode was used as the reference sample with a

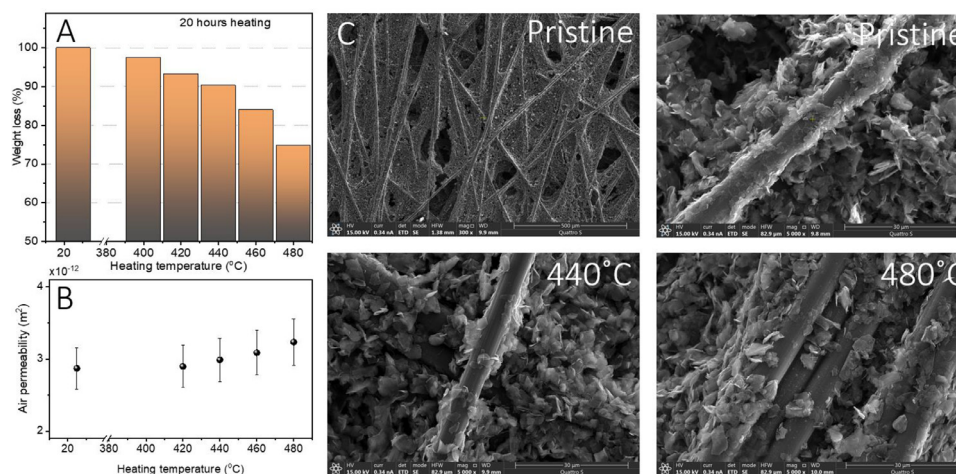


**Fig. 3.** A – mass loss of the samples after the activation treatment at different temperatures; B – Air permeability for the heated samples; C– SEM microphotographs of pristine and heated samples at 440 °C and 480 °C with magnification 300x and 5000x.

known area. The capacitance was calculated from a linear fit of the scan rate dependent capacitive current.

**Cyclic voltammetry:** A standard three-electrode cell filled with 2.5 M  $H_2SO_4$  was used with reference Ag/AgCl electrode in 3 M KCl connected to the cell by a salt bridge and graphite counter electrode for additional ex-situ measurements. A round piece of studied carbon paper sample with a 0.25 cm radius was used as working electrodes. Data was recorded with IR-correction deduced from the high-frequency intercept of Nyquist plots of EIS in the range 0–1.1 V and 0.6–1 V vs. reference with scan rates 5, 10, 20, 50, 100 mV/s using Biologic ST200 potentiostat. A linear fit of the scan rate dependence on capacitive current was performed to obtain the carbon electrode capacitance, which was normalized to the known specific capacitance of glassy carbon electrode and to the mass of the carbon paper electrode in order to get an electrochemically active surface area (ECSA). Air permeability was derived from the linear fit of pressure drop through the sample – flow rate dependence from Darcy's law. The test setup was discussed in details by A. Tamayol et al. [33].

**Vanadium RFB tests:** Single-cell flow battery assembly was done based on Brushett group design [34] with a 2.5 cm<sup>2</sup> electrode area. The battery contained three layers of carbon paper as electrodes and Nafion 115 as a membrane. The electrolyte consisting of 1.6 M of vanadium ions in 4 M total sulfates concentration (12 ml) was pumped through the cell with a 30 ml/min flow rate. Cycling was performed at 60, 100, 150, and 200 mA/cm<sup>2</sup> current densities with the cutoffs of 0.8 and 1.7 V. The polarization curve was determined by the following procedure: (a) battery was charged till 50% State of Charge (SoC) by 100 mA/cm<sup>2</sup>; (2) discharge current in the range [25–1100 mA/cm<sup>2</sup>] was applied for 20 s, and last 5 points were averaged; (3) the battery was charged back to 50% SoC by 150 mA/cm<sup>2</sup>; then steps 2 and 3 were repeated with another discharge current density. The EIS data were collected before and after tests in a range of 200kHz – 0.1Hz with 10 mV amplitude. All data were measured by Biologic ST200 potentiostat.

**In-situ Raman spectroelectrochemistry:** Specially designed three-electrode cell was made of Teflon (Fig. 1). The piece of carbon paper (0.2 × 1 cm) was placed on the copper tape as a working electrode. The contact was isolated by FKM O-ring compressed between the cell body and transparent acrylic frame. The disk of the felt (1 cm in diameter) was put on the bottom of the cell as a counter electrode and connected by a glassy carbon rod. The capillary was mounted in the body of the cell, filled by 3 M KCl, and covered by Nafion 117, similarly to the construction reported here [35]. The opposite end of the capillary was put

into the vessel with a reference Ag/AgCl electrode in the 3 M KCl solution. The electrochemical cell was placed in the working area of the DXRxi Raman Imaging Microscope (532 nm, 2 mW), which was focused on the working electrode covered by 25 μm of a 1 M  $VOSO_4$  solution in 2.5 M  $H_2SO_4$ . Cyclic voltammetry was performed in a range of 0.6–1.1 V with 5 mV/s scan rate with IR corrections using Autolab potentiostat. A microscope sample compartment was purged with argon. Raman spectra were collected during the forward (cathodic) process of the second cycle. Manual selection of the studied surface was done with alternate focusing on the surface of the fiber or binder during the experiment.

**Raman spectroscopy data processing:** Raman data were treated according to the following procedure: the baseline was subtracted using the algorithm [36]; the spectra were normalized to the maximum intensity of the G-band of the carbon (around 1590 cm<sup>-1</sup>). The region 700–1100 cm<sup>-1</sup> was subtracted and additionally normalized to the band 1040 cm<sup>-1</sup> attributed to the asymmetric stretching vibration of  $HSO_4^-$  ion as this band had a constant intensity in pretest reference solutions [37].

### 3. Results and discussion

#### 3.1. Carbon paper characterization

Material properties, in general, are connected to the manufacturing method, and some of the deduced features in this paper are also related to the way of carbon paper production. In general, carbon fibers are mixed with a sticky, low-cost polymer binder (a thermoset resin), which form a flake-like phase on the surface of the fibers after drying. The final step of heating leads to graphitization and carbonization processes, which change the structure of the resin to amorphous carbon and increase the crystallinity of carbon fibers providing high conductivity of carbon paper [38]. As annealing is done under the inert atmosphere, no additional functionalization of the material surface occurs. However, carbon itself is hydrophobic, and assistive treatment is required to change the wetting behavior. Therefore, air-exposed heating is one of the scalable methods of surface modification, taking into account that excess activation can be accompanied by partial destruction of the material.

Heating of carbon paper samples under different temperatures (25 °C or pristine, 400, 420, 440, 460, and 480 °C) in the air for 20 hours revealed significant morphology and structure changes. Samples' weight loss was in proportion to the heating temperature from 2.5% for 400 °C to 25.2% for 480 °C (Fig. 3A). A notice-

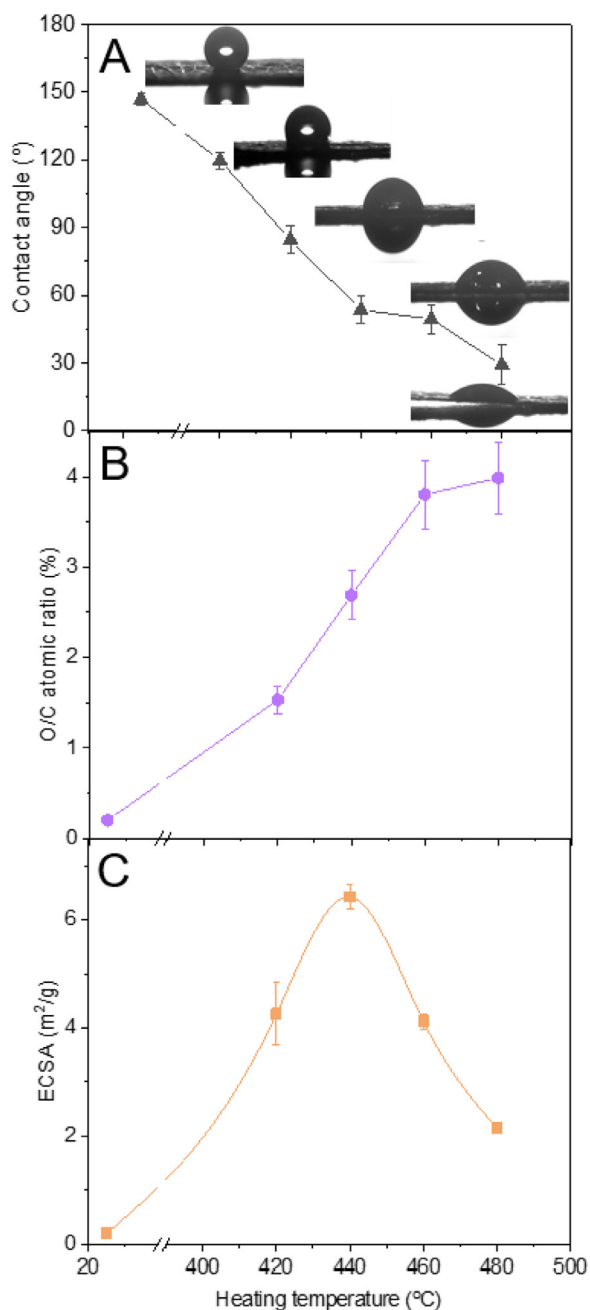


**Fig. 4.** A – water contact angle measurement for carbon paper samples; B – oxygen to carbon ratio derived from XPS spectra integration; C – the specific electrochemically active surface area of samples obtained from the capacitive current at 0.7 V vs. Ag/AgCl.

able degradation in mechanical properties began from 460 °C, and the sample heated up to 480 °C almost lost its integrity. However, the material remained its continuity, and only minor growth in gas permeability was observed with the increase of the activation temperature (Fig. 3B). This observation is attributed to the gradual burning of less structured and more sensitive to oxidation parts of the material, in particular the binder phase of carbon paper. This macroscopic phase content change was also proved by SEM microphotographs (Fig. 3C). Carbon fibers in pristine material were almost fully covered by flakes of the binder. A higher fraction of the carbon fiber surface was opened through the set of the studying samples, where the surface of the fibers was released by burning binder flakes. No statistical changes in fiber diameter were de-

tected. This process automatically was accomplished by oxidation of the material surface.

The wettability of the carbon paper significantly increased with the growth of treatment temperature (Fig. 4A). The hydrophilicity of carbon paper occurred at 420 °C and higher. The optimum contact angle, which provided a prompt wetting of material, was below 60°, which matched the data for samples heated above 440 °C. Surface oxygen content derived from XPS spectra correlated with an observed wetting enhancement: the surface became gradually saturated with oxygen as temperature increased (Fig. 4B) and reached 4% level. The collected XPS data provided a local integrated analysis representing the surface composition, which mainly consisted of carbonyl and hydroxyl oxygen types.

In addition to the wettability and local composition of the surface, a real electrochemically active surface area of the electrodes was calculated based on double-layer capacitance to get insight into the surface involvement in the reactions (Fig. 4C). ECSA was in close agreement with the contact angle measurements as the material's hydrophilicity increased, the ECSA also grew, unless the point where the amount of annihilated material exceeded the oxygen impact. The sample, which was selected for further investigation, had the maximum ECSA of 6.4 m<sup>2</sup>/g.

Furthermore, CV test at a relatively low scan rate of 5 mV/s demonstrated the presence of a surface Faradaic reaction, that was attributed to the hydroquinone–quinone redox reaction and phenol-carbonyl redox reaction in acid media (Fig. 5A) [39,40]. This observation clearly showed that carbon paper surface usually is covered with carbonyl groups at the battery operating potentials. Moreover, this characteristic current peak was pronouncing only below the 5 mV/s scan rates, which implied slow kinetics of this process and its minor intensity, which made the effect masked by double-layer currents at higher scan rates. Intensification of this reaction was observed for samples with low-temperature activation till 440 °C. In contrast, further increase of temperature treatment led to a gradual decay of the peak, which was due to the overall decrease of sample mass and surface area. However, normalization of charge that passed during the oxidation process to ECSA of the samples showed that surface concentration of the redox-active oxygen gradually grew with activation temperature rise, which correlates with the XPS data (Fig. 5B). Overall, received trends of ECSA and oxygen content were in agreement with literature data [26]. It was shown above that a larger area of fibers could be involved in the process, and a progressive drop in ECSA occurred during the heating. These findings suggested that fibers tend to allocate more oxygen functional groups on their surface, meaning a spatial heterogeneity of the reaction in the material, the same results were demonstrated for N-doping carbon paper [41].

Based on the discussed above material properties evolution, the optimal temperature for the carbon paper activation was 440 °C, as such treatment balanced the surface oxidative functionalization and the mass reduction making the sample with the highest ECSA. This sample was used for further investigation.

### 3.2. Carbon paper electrode performance in vanadium flow battery

A single-cell vanadium prototype with carbon paper electrodes activated at 440°C was tested to prove the material suitability in the real device (Fig. 6). The polarization curve at 50% SoC had a slope of 0.81 Ω/cm<sup>2</sup> at the initial linear part, further deviation from linearity corresponded to the gradual increase of a mass-transport impact. Calculated resistance is a total cell resistance that summarizes the contribution of all elements of the system (membrane, mass-transport, charge transfer, cable resistances). A maximum power density of 525 mW/cm<sup>2</sup> was achieved at 620 mA/cm<sup>2</sup>, which is in agreement with the literature data [42]. Cycling per-

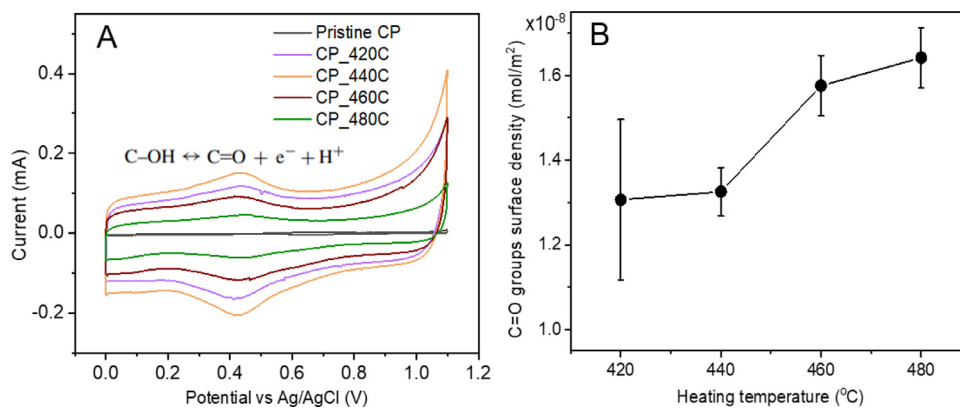


**Fig. 5.** A - CVs of carbon paper samples (5 mm-diameter disk) in range of 0–1.1 V in 2.5 M H<sub>2</sub>SO<sub>4</sub> solution with 5 mV/s scan rate, all data were normalized in proportion to the relative mass change of the samples; B - the surface concentration of electroactive quinone groups estimated from the current anodic peak integration normalized by ECSA.

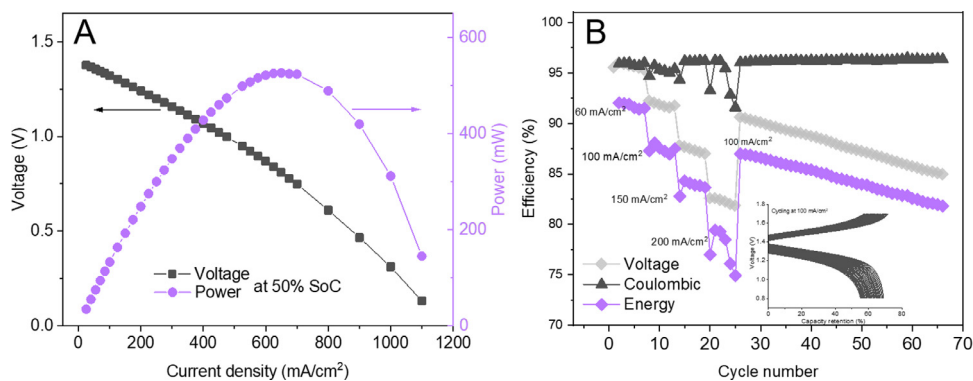


**Fig. 6.** A - Battery polarization and power density at 50% State of Charge (SoC); B - Voltage, Coulombic, and Energy efficiencies during cycling at different current densities; inserted graph - charge-discharge curves for cycling at 100 mA/cm<sup>2</sup>.

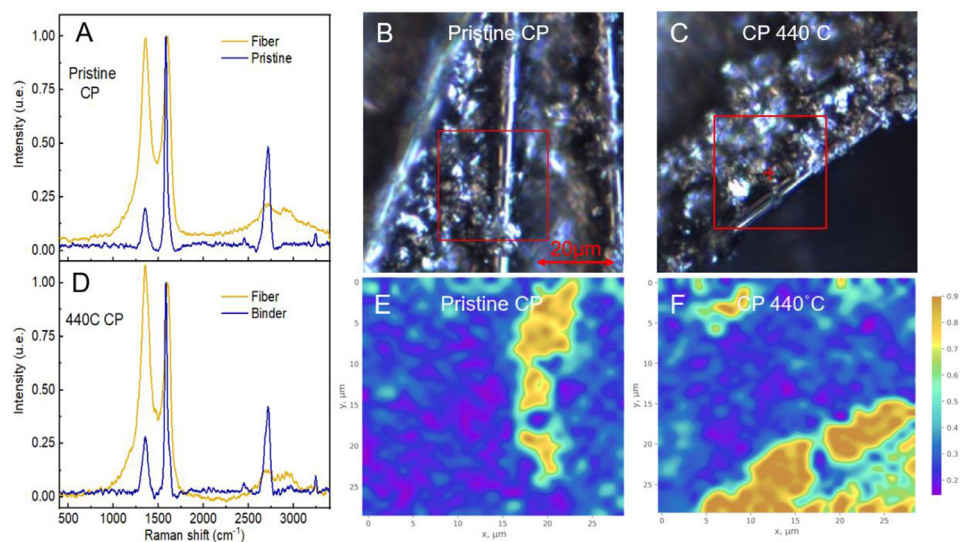


**Fig. 7.** A and D - Raman spectra of pristine and activated at 440 °C carbon paper, respectively; B and C - an optical confocal photograph from Raman spectroscopy of pristine and activated at 440 °C carbon paper, respectively; E and F - mapping of selected areas (red squares) using I<sub>D</sub>/I<sub>G</sub> ratio as an analytical signal of pristine and activated at 440 °C carbon paper, respectively (red color corresponds to I<sub>D</sub>/I<sub>G</sub> ratio more than 0.9).

formance data was measured at different current densities: an insignificant drop in Coulombic efficiency during the first cycling as well as after the current density change was observed as a common feature of such tests, which is usually attributed to the presence of oxygen and other impurities. Coulombic efficiency stabilized and remained constant at the level of 96.3% with a deviation

of only 0.16%. This stability, along with a constant gradual drop of the voltage efficiency, is attributed to the relative concentration change in the compartments, clearly demonstrated no presence of degradation inside the cell. In total, the energy efficiency of the battery at current densities below 150 mA/cm<sup>2</sup> was higher than 80%, which is a general target for RFB systems. Therefore, in-

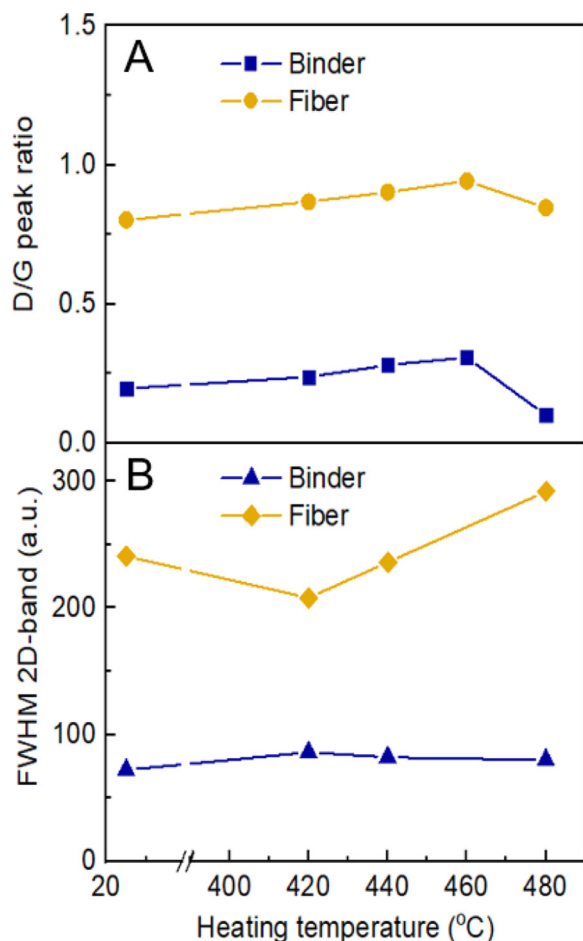


**Fig. 8.** A –  $I_D/I_G$  ratio dependence for the binder and fiber phases on the treatment temperature; B – the 2D-band FWHM for the binder and fiber phases on the treatment temperature.

vestigated material was well suited as an electrode material for VFB.

### 3.3. Carbon paper Raman mapping

Preliminary studies of carbon paper structure revealed a drastic difference in Raman signal from fibers and the binder of the carbon paper that distinguishes two phases of the material (Fig. 7).

Here, the mapping of pristine and activated at 440 °C samples represents the ratio of D and G bands as one of the characteristic differences of the spectra depending on the phase (Fig. 7 E, F). The D-band located at 1350  $\text{cm}^{-1}$  corresponds to defects and lattice disorder in the structure, while the peak at around 1590  $\text{cm}^{-1}$  is attributed to the G-band, which relates to the  $\text{sp}^2$  carbon [43]. The relative intensity of D band to G band ( $I_D/I_G$ ) can be used to reflect the disorder degree of the graphite. Fibers had a higher  $I_D/I_G$  ratio indicating the presence of turbostratic carbon and disordered surface structures. Particular D/G profiles are common for the carbonized but not graphitized carbon fibers [44]. While the binder phase had a moderate  $I_D/I_G$  ratio, that means the enhancement in graphitization and more regular structure (Fig. 7 A, D).

$I_D/I_G$  ratio increased with activation temperature growth for both phases with the same slope, even if the values were different. (Fig. 8 A). That implied constant accumulation of oxygen groups on the surfaces of both phases, as any surface functionalization disturbs the layer structure and causes D-band growth [43]. More importantly, a drastic difference in 2D-bands at around 2700  $\text{cm}^{-1}$  of two phases was observed (Fig. 7 A, D). 2D-band is sensitive to the charge carrier interactions and a full-wave half maximum (FWHM) of the 2D-band for carbon materials, especially for the graphene-based, related in direct proportion to the Fermi level. A high value of the 2D peak FWHM, representing a wider intense 2D-band, indicates a more exchangeable charge carrier and a lower energy barrier for charge transfer at the interface [41,45]. Therefore, the probability of redox process event is higher as different forms of species can react, overcoming the activation barrier. Here we demonstrate that with an increase of activation temperature, the opposite trends of FWHM for fiber and binder fraction occurred (Fig. 8B). Moderate oxidation of carbon fibers at 420 °C led to a decrease of FWHM, attributed to a decrease in electron density, compared with the pristine sample, but a further increase of activation temperature recovered and exceeded the initial level, meaning that the Fermi level of the studied sample (440 °C) was the same as the pristine one's. Even the existence of a sharp 2D-band in the binder spectra further confirmed its well-ordered layered structure; this fraction tends to be less electroactive, as its FWHM was significantly lower than for the fibers.

It can be concluded based on Raman data that a binder had more structured morphology than fiber, but it had a lower Fermi level and electronic conductivity than fibers, which led to low electrochemical activity [38]. Although well-studied carbon fibers are known for their highly ordered structure, which is responsible for their high electric conductivity, fiber's outer layer's structure is less ordered. Taking into account previously discussed carbon pa-

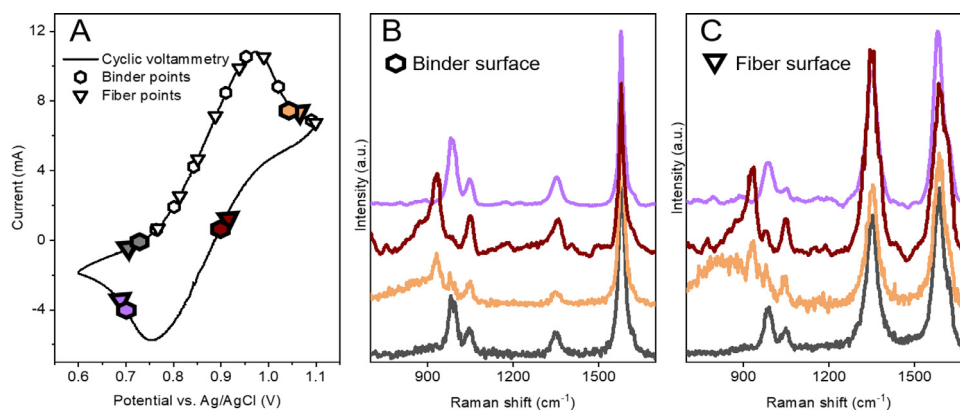


**Fig. 9.** A – Cyclic voltammetry of a 1M  $\text{VOSO}_4$  solution in 2.5 M  $\text{H}_2\text{SO}_4$  with the carbon paper heated at 440 °C as a working electrode. The scan rate was 5 mV/s. Triangular signs correspond to the points of spectra collection on the fiber surface; hexagonal symbols correspond to the points of spectra collection on the binder. Colored symbols refer to potentials at which Raman spectra were obtained. B – Raman spectra measured at a certain potential on the binder surface. C – Raman spectra measured at a certain potential on the fiber surface.

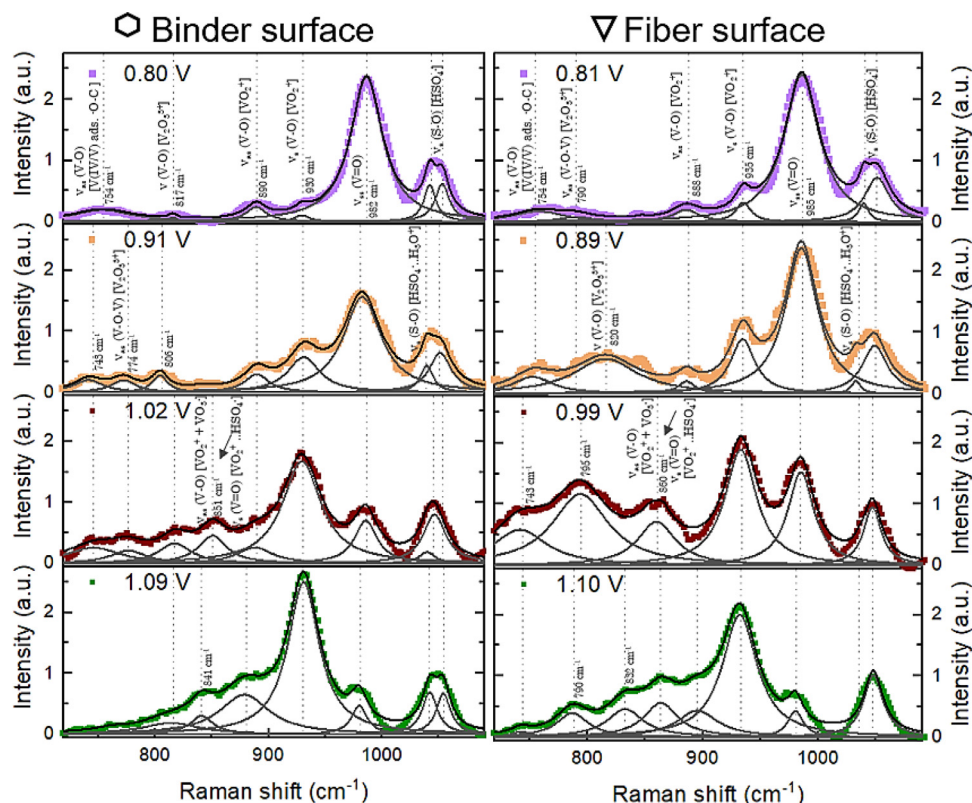


Fig. 10. Spectral evolution with the growth of applied potential collected on the binder and the fiber surface.

per properties, such as mass loss via binder fraction illumination and preferential oxygen functional groups formation on fibers, one could infer that the studied material is heterogeneous with two distinguishing phases that have different electrochemical activity.

### 3.4. In-situ Raman voltammetry

We designed a special three-electrode cell, which can be installed inside the Raman spectroscope for a more in-depth investigation of reaction mechanisms on oxygen-enriched and depleted surface areas of the carbon paper (Fig. 2). We chose the oxidation process of vanadium catholyte to have assured the known initial concentration of vanadium species ( $\text{VO}^{2+} + \text{H}_2\text{O} - \bar{e} \rightarrow \text{VO}_2^+ + 2\text{H}^+$ ). We were able to track a surface concentration of the vanadium species during the cyclic voltammetry by focusing directly on the carbon paper surface (Fig. 9). Additional tests were done before selecting a suitable vanadium concentration, minimum immersion depth of the working electrode, and the regime of Raman spectra recording. Manual focusing on different fractions of the material during voltammetry was required to be aware of surface concentration probing. We used  $I_D/I_C$  ratio of each spectrum was a marker of belonging to an exact fraction; examples of raw data for binder and fiber surfaces are presented on figure 9B, C.

The deconvolution of Raman spectra was based on the preliminary measurements of reference solutions and the literature data [37,46–48]. As studied vanadium species were in the solution, significant peak broadening occurred (Fig. 10). Characteristic pronounced peaks attributed to the  $\text{HSO}_4^-$  and  $\text{HSO}_4^- \cdot \text{H}_3\text{O}^+$  stretching vibration of S–O around  $1047 \text{ cm}^{-1}$ , and  $1035 \text{ cm}^{-1}$  were detected for all spectra. The peak at  $990 \text{ cm}^{-1}$  corresponded to the V=O stretching vibration had a noticeable decrease in intensity moving from V(IV) solutions to V(V). Symmetric vibrations of oxy-

gen in  $\text{VO}_2^+$  ion occurred around  $935 \text{ cm}^{-1}$ , and extensive growth was observed with an increase of potential. A less intensive band of asymmetric stretching in  $\text{VO}_2^+$  ion at  $\sim 890 \text{ cm}^{-1}$  had the same tendency on both surfaces. With the growth of potential, the peak intensity of the V=O stretching band gradually decreased on both surfaces; simultaneously, the appearance of a new band attributed to different V(V) species were observed, and these bands varied depending on the surface. Additional integration of  $\text{HSO}_4^-$  or  $\text{SO}_4^{2-}$  into the  $\text{VO}_2^+$  coordination sphere caused a shift and a broad vibration band at the range of  $830\text{--}860 \text{ cm}^{-1}$ . Thus, the main peak of  $\text{VO}_2^+$  ( $930\text{--}935 \text{ cm}^{-1}$ ) had a shoulder formed by asymmetric mode and additional mode from  $\text{VO}_2\text{HSO}_4$ , as it can be clearly seen at the high potentials. Distinguishing intensities of these modes and potential dependence gave one of the keys to understanding the reaction mechanism. Further low-frequency modes of spectra had noticeable differences depending on the studied surface. Asymmetric stretching mode from V–O–V in dimers ( $\text{V}_2\text{O}_3^{3+}$ ,  $\text{HV}_2\text{O}_3^{3+}$ ,  $\text{HV}_2\text{O}_5^-$ ) was found at the range of  $780\text{--}820 \text{ cm}^{-1}$ . The intensity of the dimer peak grew with the SoC and was significantly greater at the fiber surface. Moreover, its relative intensity raised sufficiently compared to the reference solutions and the literature data [48]. An additional unidentified peak at  $\sim 743 \text{ cm}^{-1}$  was detected preferentially on the fiber surface at low overpotentials. No presence of the same peak was detected in the reference solutions. This band was attributed to the asymmetric bonding in V–O in dimers or in the C–O–V structure, as  $\text{VO}^{2+}$  were chemisorbed at the oxygen-functional groups on the fiber surface, as a depolarization of the V–O bond by surface oxygen predominately causes a low-frequency shift of the antisymmetric vibrations [49].

We visualized changes in the intensity of the most important bands for the binder and the fiber spectra to facilitate the mechanism interpretation (Fig. 11). We deduced the following features of vanadyl oxidation:

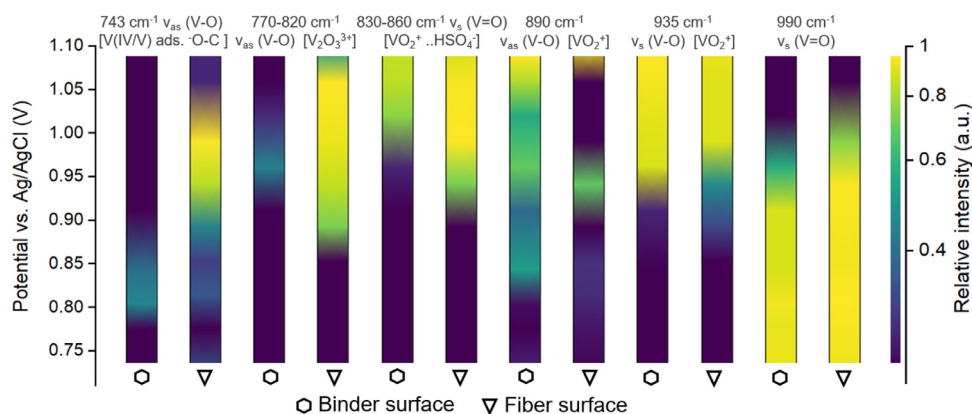


**Fig. 11.** Relative intensity changes depending on applied potential and examined surface. The data were normalized by the maximum of both spectra sets (binder and fiber surfaces) for each band.

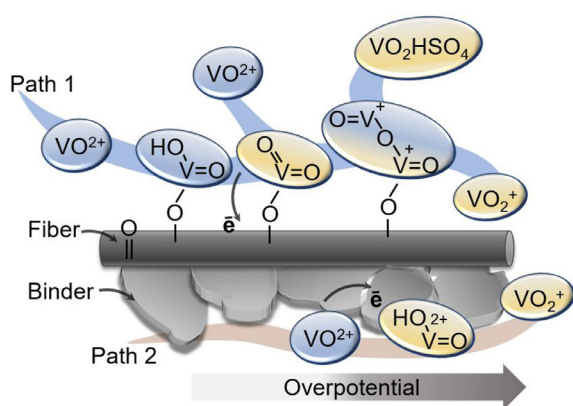


**Fig. 12.** Different reaction pathways of vanadyl oxidation.

- 1) Growth of V(V) bands intensity for the fiber started from 0.86 V vs. Ag/AgCl, which coincided with an  $E_{1/2}$ , while the start of the reaction was shifted to 0.9 V for the binder surface.
- 2) The formation of the dimers was observed preferentially on the fiber surface. The band growth may be interpreted as an accumulation of the dimers near the electrode.
- 3) In addition, adsorbed vanadium species were observed at moderate overpotentials, while  $\text{VO}_2\cdot\text{HSO}_4$  ions were more likely formed at high overpotentials.
- 4) As the binder surface was oxygen-depleted and the adsorbed intermediates were diminished, so the transformation into the pure  $\text{VO}_2^+$  ions started firstly, while the incorporation of  $\text{HSO}_4^-$  into the coordination sphere was detected at higher overpotentials. These observations coincided with the proposed and hypothesized mechanisms in the literature [32,50].

As we tracked the appearance of different species with the growth of potential, we were able to propose an illustrative scheme of prevailing mechanisms during the reaction. The electrode surface functionalization significantly influences the reaction pathways.

**Path 1.** The oxygen-enriched surface reduces the required energy barrier for the start of the reaction (Fig. 12. Path 1). Vanadyl ion was chemisorbed on the carbonyl oxygen forming inner-sphere complex [50]. A certain amount of  $\text{VO}_2^+$  ions was formed by sequential addition of the  $-\text{OH}$  from  $\text{H}_2\text{O}$  in the ion coordination sphere and the electron transfer coupled with  $\text{H}^+$  desorption in the  $-\text{OH}$ . Accumulated  $\text{VO}_2^+$  ions formed dimers with vanadyl ions straight on the electrode surface. Additionally, the observed delay in reducing the  $990\text{ cm}^{-1}$  peak and the appearance

of the  $935\text{ cm}^{-1}$  peak showed that the redox reaction was going through the dimer formation at low overpotentials. We assumed that the electron transfer occurs on the adsorbed dimer, as a similar scheme was proposed for the V(V) reduction [32]. With the growth of overpotential, the straight formation of  $\text{VO}_2^+$  adsorbed ions was observed, meaning partial decomposition of the dimers in the form of pure  $\text{VO}_2^+$  or  $\text{VO}_2\cdot\text{HSO}_4$ . Therefore, this transition through the adsorbed forms implies a high activation barrier for the desorption from the surface after electron transfer.

**Path 2.** The pathway for the oxygen-depleted surfaces shows no significant changes for low and high overpotentials (Fig. 12. Path 2). Sufficiently low effect of dimer formation was presented on the oxygen-depleted surfaces at moderate overpotentials. The direct transformation of the vanadyl ion to  $\text{VO}_2^+$  at moderate overpotentials shifted to the formation of  $\text{VO}_2\cdot\text{HSO}_4$  with the growth of overpotential. No species accumulation was detected on the surface. The gradual rise of the asymmetric band at  $888\text{ cm}^{-1}$  indirectly indicates the formation of  $\text{VOOH}^{2+}$  ions, which can be the intermediate in  $\text{VO}_2^+$  formation. The same pathway variability was discussed in the literature [28]. In summary, we proposed the following scheme of the reaction mechanism.

#### 4. Conclusions

This paper investigated the vanadyl oxidation reaction mechanism at activated carbon paper electrodes. In situ Raman spectroscopy was combined with cyclic voltammetry to monitor the reaction pathway in 1 M sulfuric acid electrolyte. Raman mapping revealed the presence of two different surfaces in the electrode: fibers of the carbon paper had a turbostratic carbon structure with the partially oxidized surface, while binder flakes remained their graphitic structure without oxygen enrichment. The vanadyl redox reaction proceeds through two different pathways on these surfaces that depend upon the applied overpotential. Deconvolution of the potential dependent Raman spectra of vanadium species indicated that: (i) oxygen-enriched electrode surface decreased the overpotential at which the reaction started and promoted the formation of dimers under moderate overpotentials; (ii) preferential formation and  $\text{HSO}_4^-$ -associated  $\text{VO}_2^+$  ions rather than free  $\text{VO}_2^+$  ions were characteristic at overpotentials on the fiber surface. Furthermore, the oxygen-depleted binder surface proceeded via one pathway at all overpotentials, which consisted of two undistinguishable steps: formation of  $\text{VOOH}^+$  and the electron transfer converting this species into  $\text{VOOH}^{2+}$ ; and further formation of free and  $\text{HSO}_4^-$ -associated  $\text{VO}_2^+$  ions. On this basis, we were able to provide clear evidence of dimers incorporation into the electrochemical reactions of catholyte in VFB and get insights into the

surface modification role in the real electrode material. Furthermore, we believe that the demonstrated *In Situ* Raman spectro-electrochemical approach for redox mechanism study can be implemented in other complex redox systems associated with electrochemical energy storage technologies.

### Declaration of Competing Interest

The authors declare that they have no known competing financial interests or personal relationships that could have appeared to influence the work reported in this paper.

### Credit authorship contribution statement

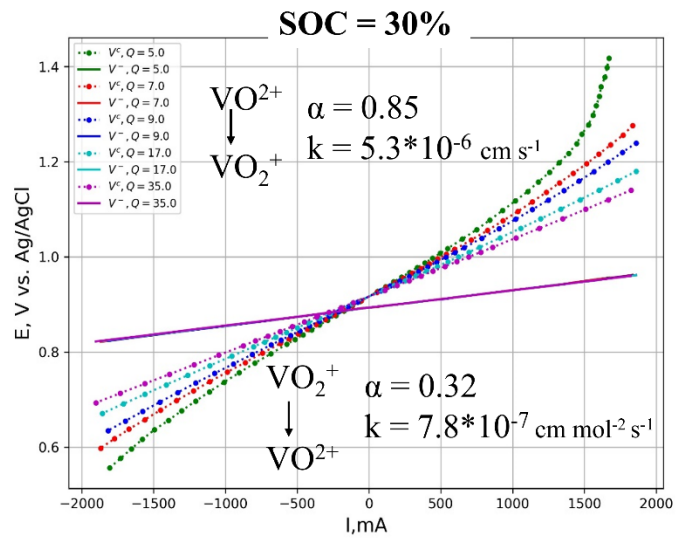
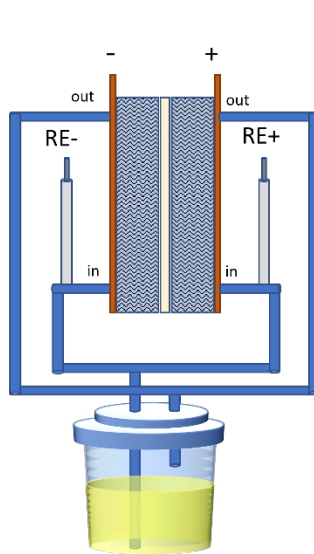
**Nataliya A. Gvozdik:** Conceptualization, Methodology, Software, Validation, Formal analysis, Investigation, Resources, Writing - original draft, Visualization. **Keith J. Stevenson:** Conceptualization, Resources, Writing - review & editing, Supervision, Project administration, Funding acquisition.

### References

- [1] J. Leadbetter, L.G. Swan, Selection of battery technology to support grid-integrated renewable electricity, *J. Power Sources*. 216 (2012) 376–386, doi:10.1016/j.jpowsour.2012.05.081.
- [2] A.D. International Renewable Energy Agency, Demand-side flexibility for power sector transformation, (2019).
- [3] A. Pullikkas, A comparative overview of large-scale battery systems for electricity storage, *Renew. Sustain. Energy Rev.* 27 (2013) 778–788, doi:10.1016/j.rser.2013.07.017.
- [4] C. Minke, T. Turek, Technology cycle analysis for emerging technologies on the example of the vanadium redox flow battery, 2014 World Autom. Congr. (2014) 382–387, doi:10.1109/WAC.2014.6935957.
- [5] B. Battke, T.S. Schmidt, D. Grosspietsch, V.H. Hoffmann, A review and probabilistic model of lifecycle costs of stationary batteries in multiple applications, *Renew. Sustain. Energy Rev.* 25 (2013) 240–250, doi:10.1016/j.rser.2013.04.023.
- [6] T. Shigematsu, The development and demonstration status of practical flow battery systems, *Curr. Opin. Electrochem.* 18 (2019) 55–60, doi:10.1016/j.coelec.2019.10.001.
- [7] C. Minke, T. Turek, Economics of vanadium redox flow battery membranes, *J. Power Sources*. 286 (2015) 247–257, doi:10.1016/j.jpowsour.2015.03.144.
- [8] K. Yano, S. Hayashi, T. Kumamoto, T. Shibata, Development and Demonstration of Redox Flow Battery System FEATURED TOPIC, (n.d.).
- [9] K.J. Kim, M.-S. Park, Y.-J. Kim, J.H. Kim, S.X. Dou, M. Skyllas-Kazacos, A technology review of electrodes and reaction mechanisms in vanadium redox flow batteries, *J. Mater. Chem. A*. 3 (2015) 16913–16933, doi:10.1039/C5TA02613J.
- [10] C. Choi, S. Kim, R. Kim, Y. Choi, S. Kim, H. young Jung, J.H. Yang, H.T. Kim, A review of vanadium electrolytes for vanadium redox flow batteries, *Renew. Sustain. Energy Rev.* 69 (2017) 263–274, doi:10.1016/j.rser.2016.11.188.
- [11] W. Lu, X. Li, H. Zhang, The next generation vanadium flow batteries with high power density-A perspective, *Phys. Chem. Chem. Phys.* 20 (2017) 23–35, doi:10.1039/c7cp07456e.
- [12] N. Roznyatovskaya, J. Noack, H. Mild, M. Fühl, P. Fischer, K. Pinkwart, J. Tübke, M. Skyllas-Kazacos, Vanadium electrolyte for all-vanadium redox-flow batteries: The effect of the counter ion, *Batteries* 5 (2019) 1–16, doi:10.3390/batteries5010013.
- [13] T. Liu, X. Li, H. Zhang, J. Chen, Progress on the electrode materials towards vanadium flow batteries (VFBs) with improved power density, *J. Energy Chem.* (2018), doi:10.1016/j.jechem.2018.07.003.
- [14] A.M. Pezeshki, J.T. Clement, G.M. Veith, T.A. Zawodzinski, M.M. Mench, High performance electrodes in vanadium redox flow batteries through oxygen-enriched thermal activation, *J. Power Sources*. 294 (2015) 333–338, doi:10.1016/j.jpowsour.2015.05.118.
- [15] L. Yue, W. Li, F. Sun, L. Zhao, L. Xing, Highly hydroxylated carbon fibres as electrode materials of all-vanadium redox flow battery, *Carbon N. Y.* 48 (2010) 3079–3090, doi:10.1016/j.carbon.2010.04.044.
- [16] A. Bourke, M.A. Miller, R.P. Lynch, J.S. Wainright, R.F. Savinell, D.N. Buckley, Effect of cathodic and anodic treatments of carbon on the electrode kinetics of VIV/VV oxidation-reduction, *J. Electrochem. Soc.* 162 (2015) A1547–A1555, doi:10.1149/2.0671508jes.
- [17] T. Liu, X. Li, C. Xu, H. Zhang, Activated carbon fiber paper based electrodes with high electrocatalytic activity for vanadium flow batteries with improved power density, *ACS Appl. Mater. Interfaces*. 9 (2017) 4626–4633, doi:10.1021/acsami.6b14478.
- [18] Z. He, Y. Jiang, Y. Li, J. Zhu, H. Zhou, W. Meng, L. Wang, L. Dai, Carbon layer-exfoliated, wettability-enhanced, SO<sub>3</sub>H-functionalized carbon paper: a superior positive electrode for vanadium redox flow battery, *Carbon N. Y.* 127 (2018) 297–304, doi:10.1016/j.carbon.2017.11.006.
- [19] H. Jiang, L. Wei, X. Fan, J. Xu, W. Shyy, T. Zhao, A novel energy storage system incorporating electrically rechargeable liquid fuels as the storage medium, *Sci. Bull.* 64 (2019) 270–280, doi:10.1016/j.scib.2019.01.014.
- [20] A. Forner-Cuenca, F.R. Brushett, Engineering porous electrodes for next-generation redox flow batteries: recent progress and opportunities, *Curr. Opin. Electrochem.* 18 (2019) 113–122, doi:10.1016/j.coelec.2019.11.002.
- [21] M.A. Goulet, M. Skyllas-Kazacos, E. Kjeang, The importance of wetting in carbon paper electrodes for vanadium redox reactions, *Carbon N. Y.* 101 (2016) 390–398, doi:10.1016/j.carbon.2016.02.011.
- [22] W. Zhang, J. Xi, Z. Li, H. Zhou, L. Liu, Z. Wu, X. Qiu, Electrochemical activation of graphite felt electrode for VO<sup>2+</sup>/VO<sup>2+</sup> redox couple application, *Electrochim. Acta*. 89 (2013) 429–435, doi:10.1016/j.electacta.2012.11.072.
- [23] L. Cao, M. Skyllas-Kazacos, D.W. Wang, Effects of surface pretreatment of glassy carbon on the electrochemical behavior of V(IV)/V(V) redox reaction, *J. Electrochem. Soc.* 163 (2016) A1164–A1174, doi:10.1149/2.0261607jes.
- [24] M.A. Goulet, M. Eikerling, E. Kjeang, Direct measurement of electrochemical reaction kinetics in flow-through porous electrodes, *Electrochem. Commun.* 57 (2015) 14–17, doi:10.1016/j.elecom.2015.04.019.
- [25] X.W. Wu, T. Yamamura, S. Ohta, Q.X. Zhang, F.C. Lv, C.M. Liu, K. Shirasaki, I. Satoh, T. Shikama, D. Lu, S.Q. Liu, Acceleration of the redox kinetics of VO<sup>2+</sup>/VO<sup>2+</sup> and V<sup>3+</sup>/V<sup>2+</sup> couples on carbon paper, *J. Appl. Electrochem.* 41 (2011) 1183–1190, doi:10.1007/s10800-011-0343-7.
- [26] K.V. Greco, A. Forner-cuenca, A. Mularczyk, J. Eller, F.R. Brushett, Elucidating the Nuanced Effects of Thermal Pretreatment on Carbon 2 Paper Electrodes for Vanadium Redox Flow Batteries, 2018, doi:10.1021/acsami.8b15793.
- [27] A. Nefedov, H. Sezen, C. Wöll, J. Melke, P. Jakes, J. Langner, L. Riekehr, Z. Zhokarger, A. Nefedov, H. Sezen, Carbon Materials for the positive electrode in all-Vanadium Redox Flow Batteries, *Carbon N. Y.* (2014), doi:10.1016/j.carbon.2014.06.075.
- [28] N. Roznyatovskaya, J. Noack, K. Pinkwart, J. Tübke, Aspects of electron transfer processes in vanadium redox-flow batteries, *Curr. Opin. Electrochem.* 19 (2020) 42–48, doi:10.1016/j.coelec.2019.10.003.
- [29] P. Blanc, C. Madic, J.P. Launey, Spectrophotometric identification of a mixed-valence cation-cation complex between aquadioxovanadium(V) and aquaioxovanadium(IV) ions in perchloric, sulfuric, and hydrochloric acid media, *Inorgan. Chem.* 21 (1982) 2923–2928, doi:10.1021/ic00138a003.
- [30] K. Okamoto, J. Woo-Sik, H. Tomiyasu, H. Fukutomi, Vanadium-51 NMR line-broadening in the mixture of dioxovanadium(V) and oxovanadium(IV) ions in perchloric acid solution, *Inorganica Chim. Acta*. 143 (1988) 217–221, doi:10.1016/S0020-1693(00)83692-0.
- [31] Z. He, Y. Jiang, Y. Wei, C. Zhao, F. Jiang, L. Li, H. Zhou, W. Meng, L. Wang, L. Dai, N,P co-doped carbon microsphere as superior electrocatalyst for VO<sub>2</sub><sup>+</sup>/VO<sub>2</sub><sup>+</sup> redox reaction, *Electrochim. Acta*. 259 (2018) 122–130, doi:10.1016/j.electacta.2017.10.169.
- [32] W. Wang, X. Fan, Y. Qin, J. Liu, C. Yan, C. Zeng, The reduction reaction kinetics of vanadium(V) in acidic solutions on a platinum electrode with unusual difference compared to carbon electrodes, *Electrochim. Acta*. 283 (2018) 1313–1322, doi:10.1016/j.electacta.2018.07.071.
- [33] A. Tamayol, F. McGregor, M. Bahrami, Single phase through-plane permeability of carbon paper gas diffusion layers, *J. Power Sources*. 204 (2012) 94–99, doi:10.1016/j.jpowsour.2011.11.084.
- [34] J.D. Milshtein, J.L. Barton, R.M. Darling, F.R. Brushett, 1,4-acetamido-2,2,6,6-tetramethylpiperidine-1-oxyl as a model organic redox active compound for nonaqueous flow batteries, *J. Power Sources*. 327 (2016) 151–159, doi:10.1016/j.jpowsour.2016.06.125.
- [35] G. Hinds, E. Brightman, In situ mapping of electrode potential in a PEM fuel cell, *Electrochem. Commun.* 17 (2012) 26–29, doi:10.1016/j.elecom.2012.01.007.
- [36] P.H.C. Eilers, H.F.M. Boelens, Baseline Correction with Asymmetric Least Squares Smoothing, *Life Sci* (2005) 1–26, doi:10.1021/ac034173t.
- [37] N. Kausar, R. Howe, M. Skyllas-Kazacos, Raman spectroscopy studies of concentrated vanadium redox battery positive electrolytes, *J. Appl. Electrochem.* 31 (2001) 1327–1332, doi:10.1023/A:1013870624722.
- [38] S. Simaafrookhteh, R. Taherian, M. Shakeri, Stochastic microstructure reconstruction of a binder/carbon fiber/expanded graphite carbon fiber paper for PEMFCs applications: mass transport and conductivity properties, *J. Electrochem. Soc.* 166 (2019) F3287–F3299, doi:10.1149/2.0331907jes.
- [39] Y.J. Oh, J.J. Yoo, Y. Il Kim, J.K. Yoon, H.N. Yoon, J.H. Kim, S. Bin Park, Oxygen functional groups and electrochemical capacitive behavior of incompletely reduced graphene oxides as a thin-film electrode of supercapacitor, *Electrochim. Acta*. 116 (2014) 118–128, https://doi.org/10.1016/j.electacta.2013.11.040.
- [40] Y. Shao, G. Yin, J. Zhang, Y. Gao, Comparative investigation of the resistance to electrochemical oxidation of carbon black and carbon nanotubes in aqueous sulfuric acid solution, *Electrochim. Acta*. 51 (2006) 5853–5857, doi:10.1016/j.electacta.2006.03.021.
- [41] A.K. Singh, N. Yasri, K. Karan, E.P.L. Roberts, Electrocatalytic activity of functionalized carbon paper electrodes and their correlation to the fermi level derived from Raman spectra, *ACS Appl. Energy Mater.* 2 (2019) 2324–2336, doi:10.1021/acsami.9b00180.
- [42] J. Charvát, P. Mazúr, J. Dundálek, J. Pociedič, J. Vrána, J. Mrlík, J. Kosek, S. Dinter, Performance enhancement of vanadium redox flow battery by optimized electrode compression and operational conditions, *J. Energy Storage*. 30 (2020) 101468, doi:10.1016/j.est.2020.101468.
- [43] J. Bin Wu, M.L. Lin, X. Cong, H.N. Liu, P.H. Tan, Raman spectroscopy of graphene-based materials and its applications in related devices, *Chem. Soc. Rev.* 47 (2018) 1822–1873, doi:10.1039/c6cs00915h.
- [44] S.K. Martha, N.J. Dudney, J.O. Kiggans, J. Nanda, Electrochemical stability of carbon fibers compared to aluminum as current collectors for lithium-ion batteries, *J. Electrochem. Soc.* 159 (2012) A1652–A1658, doi:10.1149/2.041210jes.

- [45] H. Xu, L. Xie, H. Zhang, J. Zhang, Effect of graphene Fermi level on the Raman scattering intensity of molecules on graphene, *ACS Nano* (2011) 5338–5344, doi:[10.1021/nn103237x](https://doi.org/10.1021/nn103237x).
- [46] M.B. Smirnov, E.M. Roginskii, K.S. Smirnov, R. Baddour-Hadjean, J.P. Pereira-Ramos, Unraveling the structure-Raman spectra relationships in  $V_2O_5$  Polymorphs via a comprehensive experimental and DFT study, *Inorg. Chem.* 57 (2018) 9190–9204, doi:[10.1021/acs.inorgchem.8b01212](https://doi.org/10.1021/acs.inorgchem.8b01212).
- [47] E.R. Malinowski, R.A. Cox, U.L. Haldna, Factor analysis for isolation of the Raman spectra of aqueous sulfuric acid components, *Anal. Chem.* 56 (1984) 778–781, doi:[10.1021/ac00268a043](https://doi.org/10.1021/ac00268a043).
- [48] C. Sun, K. Vezzù, G. Pagot, A. Nale, Y.H. Bang, G. Pace, E. Negro, C. Gambaro, L. Meda, T.A. Zawodzinski, V. Di Noto, Elucidation of the interplay between vanadium species and charge-discharge processes in VRFBs by Raman spectroscopy, *Electrochim. Acta.* 318 (2019) 913–921, doi:[10.1016/j.electacta.2019.06.130](https://doi.org/10.1016/j.electacta.2019.06.130).
- [49] K. Kanamori, Y. Ookubo, K. Ino, K. Kawai, H. Michibata, Raman spectral study on the structure of a hydrolytic dimer of the aquavanadium(III) ion, *Inorg. Chem.* 30 (1991) 3832–3836, doi:[10.1021/ic00020a012](https://doi.org/10.1021/ic00020a012).
- [50] Z. Jiang, K. Klyukin, V. Alexandrov, Ab initio metadynamics study of the  $VO_2^+/VO_2^+$  redox reaction mechanism at the graphite edge/water interface, *ACS Appl. Mater. Interfaces.* 10 (2018) 20621–20626, doi:[10.1021/acsami.8b05864](https://doi.org/10.1021/acsami.8b05864).

### 2.3 Determination of kinetics parameters in Vanadium RFB with reference electrodes



## **Determination of Kinetics Parameters in Vanadium RFB with Reference Electrodes.**

*The work was presented in the 241st ECS Meeting conference.*

*The paper is under preparation.*

### **Introduction**

The efficiency of the redox process is connected to the current density and the power of the battery. Vanadium RFB has two reactions, which have poor kinetics and complicated mechanisms [156]. To fix it porous electrodes with an enlarged surface are used. Additionally, a lot of effort was done to develop advanced electrodes with catalytic effect [146]. Such works usually demonstrate the improved performance but do not discuss its reasons and provide numerical data.

The available experimental data for VRFBs is usually limited by open-circuit voltage (OCV) and potential (OCP), charge/discharge voltage profiles at constant load current, full cell polarization curves at the fixed state of charge (SOC), and internal stack ohmic resistances. This complicates the decoupling and accessing of the voltage loss sources, with the prevailing ones usually classified as ohmic, concentration, and activation overpotentials. The decoupling of overpotentials at positive and negative half-cells requires the half-cell potentials measurements with reference electrodes (RE) in addition to full cell data [155,166,167]. Therefore, the development of a self-consistent experimental setup is crucial for understanding and decoupling internal losses in VRFB.

We proposed an alternative way for electrode materials characterization with numerical metrics of reaction rate. The vanadium redox reaction was treated as a single-step reaction without consideration of mechanisms. Such an engineering approach generates effective apparent kinetics parameters (charge transfer coefficients and apparent rate constants). This method can be applied to any electrode material and allow the comparison of the electrocatalysis effect of different materials.

The developed approach is corroborated by the numerical study to decouple the losses between the half-cells by extracting the effective kinetic and mass transfer parameters in a real vanadium RFB equipped with reference electrodes. Firstly, we made a calibration for the SOC vs the OCP for the symmetrical setup. Then, we generated data for the modeling from symmetric cell design. Finally, we validated the model on the full cell data.

As a result, we refined reliably the order of the apparent rate constants for vanadium redox reactions and showed that charge transfer coefficients significantly differ from 0.5 for both catholyte and anolyte reactions.

### **Model development**

We apply the 0-D model based on general mass and charge conservation principles. The key feature of the model is the approach for the determination of the integral mass-transfer coefficient on the electrode-electrolyte interface that allows a describing non-linear polarization behavior at high currents. The model is derived within the continuous stirred-

tank reactor approximation and isothermal conditions. The model is discussed in more detail in the works of our group [51,157].

In the presence of the electrical current, additional losses change a cell potential ( $U$ ) relative to the cell equilibrium potential ( $U_{eq}$ ). Such losses are constituted by activation ( $\eta_{act}$ ), Ohmic ( $R_{ce}I$ ), and concentration overpotentials ( $\eta_{con}$ ), and cell voltage can be calculated as:

$$U = U_{eq} \pm (R_{ce}I + \eta_{con\&act}) \quad (2.1)$$

Cell losses are represented as the sum of terms, attributed to different physical processes. Activation losses are caused by activation energy barriers of redox reactions and sluggish kinetics; Ohmic losses are caused by the finite electrical resistance of the cell; concentration losses are caused by mass transport limitations of reactants from the bulk solution in the cell to the surface of the electrode.

Concentration losses are represented as:

$$\eta_{con}(t) = \frac{GT}{F} \ln \left( 1 - \frac{I(t)}{I_{lim}(t)} \right) \quad (2.2)$$

Limiting currents depend on the electrodes area ( $A_e$ ) and surface concentration ( $C_{react}$ ), and can be evaluated as:

$$I_{lim} = k_m A_e F C_{react}^{hc} \quad (2.3)$$

$k_m$  is an empirical mass transfer coefficient that should be tuned for the particular setup. This value represents the joint effect of diffusion and convection of the reacting species on the electrode-electrolyte interface and can be further approximated as function 2.4, where  $u$  is a flow rate, and  $\alpha, \beta$  are experimental coefficients.

$$k_m = \alpha u^\beta \quad (2.4)$$

Ohmic losses are derived from the EIS of the cell with the assumption, that cell resistance ( $R_{ce}$ ) is constant during the experiments.

Additionally, the model was expanded using Butler-Volmer formalism for the simulation of the activation losses (Eq. 2.5). Each reaction was treated with respect to directions and thermodynamic restrictions. We used the thermodynamically consistent single-step mechanisms for the reaction going in opposite directions at both parts of a symmetric cell.

Single-step mechanism

Butler-Volmer formalism for reaction kinetics and mass-balance equations:

$$r_{c,a}^{pe} = k_{0,a,c}^{pe} c_{VO_2^+} c_{H^+}^2 \exp\left(-\frac{\alpha_{a,c}^{pe} F(E^{pe} - E_0^{pe})}{RT}\right) - k_{0,a,c}^{pe} c_{VO^{2+}} \exp\left(\frac{(1 - \alpha_{a,c}^{pe}) F(E^{pe} - E_0^{pe})}{RT}\right)$$

$$r_{c,a}^{ne} = k_{0,a,c}^{ne} c_{V^{3+}} \exp\left(-\frac{\alpha_{a,c}^{ne} F(E^{ne} - E_0^{ne})}{RT}\right) - k_{0,a,c}^{ne} c_{V^{2+}} \exp\left(\frac{(1 - \alpha_{a,c}^{ne}) F(E^{ne} - E_0^{ne})}{RT}\right)$$

$$\left(\frac{dc_{VO_2^+}}{dt}\right)_{x=0} = 0 \approx k_m (c_{VO_2^+}^* - c_{VO_2^+}) - r_{c,a}^{pe}$$

$$\left(\frac{dc_{VO^{2+}}}{dt}\right)_{x=0} = 0 \approx k_m (c_{VO^{2+}}^* - c_{VO^{2+}}) + r_{c,a}^{pe}$$

$E_0^{pe,ne}$  - standard potential for pe, ne half-cell reactions  
\* - bulk concentrations

$$\frac{I_{load}}{A_{electrode} F} + r_{c,a}^{pe} = 0$$

$$-\frac{I_{load}}{A_{electrode} F} + r_{c,a}^{ne} = 0$$

$k_m = \alpha_{MT} u^{\beta_{MT}}$

$U_{battery} = U_{eq} + IR_{ce} + N(E^{pe,eq} - E^{pe}) + N(E^{ne,eq} - E^{ne})$

$\eta_{con\&act}$

(2.5)

As a model result, we derived 6 parameters for each experiment in the symmetric cell: two mass transfer confinements ( $\alpha, \beta$ ), pairs of apparent rate constants and charge transfer coefficients for anodic and cathodic reactions ( $\alpha_{c,a}, k_{c,a}$ ). Below we present the

derivation of the equations used for modeling (Eq.2.5). Detailed explanation and formula derivation can be found in [157].

## Experimental section

Setup construction: We adopted a 5 cm<sup>2</sup> flow-through cell with a Nafion 115 membrane and thermally-activated carbon felt electrodes (Sigracell GFD4.65 EA felt, 500°C for 10 h). Two leakless Ag/AgCl electrodes are placed in both inlets of the cell at a 1.5 cm distance from the bipolar plate (Fig. 2.1). Testing is performed by BioLogic potentiostat VMP-3 with 10A booster.

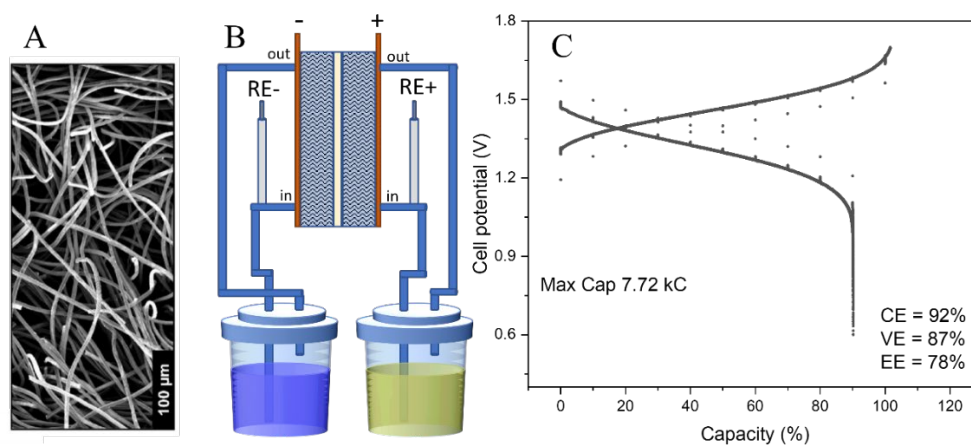


Fig. 2.1 A – SEM of carbon felt electrode; B – scheme of full cell experimental setup with two reference electrodes; C – cell cycling for the SOC determination test.

SOC calibration: The calibration experiment is done to estimate the real SOC of the system for both anolyte (NE) and catholyte (PE). The calibration curve is constructed as SOC vs OCP dependence for PE and NE. As it was measured at open-circuit conditions after sufficient time to equilibrate the system, this experimental setup provides the same data as the separate OCP cell connected in parallel with the cell under the load conditions.

The 60 ml of electrolyte was charged by passing 500 mA through the cell. OCP of both bipolar plates vs. the nearest reference electrode was simultaneously measured. Every 10% SOC, charging was interrupted for 30 sec to record the OCP of the half-cell (Fig.2.1C). Assuming that crossover does not affect significantly on SOC due to the sufficient volume of electrolyte, we built the calibration curve using the coulometry and compared it with the Nernst equation. Proton activity(concentration) was included in the equation for catholyte. The resulting calibration curves are then used to determine SOC in our experiments using the interpolation of the calibration curve.

This approach is supported by the low estimated rate of crossover ( $0.00008 \text{ mol/h cm}^2$ ) for the Nafion 115. Indeed, for the charging for 5 hours the crossover brings a rather low error of 2.1 % into the SOC determination.

Symmetric cell testing protocol:

1. 50 ml of commercial electrolyte solution (1.6M of vanadium ions (V(III/IV) in 3M  $\text{H}_2\text{SO}_4$ ) is used each time with constant Argon purging of the solutions.
2. Preparation of anolyte or catholyte sample with the target SOC is done by potentiostatic charging at 1.6 V with coulometric control.

3. 50 ml of charged electrolyte (anolyte or catholyte) is placed in a single tank, from which the electrolyte is pumped to both sides.
4. One of the bipolar plates is connected as a working electrode, and the counter is another one. The reference electrode is connected to the Ag/AgCl electrode and placed near the counter bipolar plate so that potential control is done through the whole cell.
5. OCP of both bipolar plates was recorded simultaneously with a testing procedure by additional potentiostat channels.
6. The flow rate was controlled by a peristaltic pump and changed automatically after the potentiostatic titration procedure is finished.
7. The OCP is recorded vs. Ag/AgCl electrode. The stability of OCP is a marker for the absence of side reactions.
8. Two-point EIS is recorded for further calculation, the reference electrode is connected to the counter electrode for this step.
9. Potentiostatic titration with steps of 25 mV vs. OCP for 40 sec followed by 80 sec relaxation time at OCV was done with the current cutoff of 4A.
10. Firstly, the procedure is done for positive overpotentials, then for negative ones. Secondly, the flow rate of the pump is changed and the procedure is repeated.
11. Ohmic resistance of the cell was determined by 2-points EIS measurements.

Full cell testing protocol:

We used the same configuration of the experiment as for symmetric cells. Reference electrodes are connected as OCP sensors to the nearest bipolar plate. The cell is tested in

two-point mode with simultaneous OCP of negative and positive bipolar plate tracking. The polarization is done on current steps mode with steps of 100 mA and voltages cutoffs 0.2 - 1.75 V.

1. Charging at 500 mA was done for the selected time to ensure the change of SOC by 10%.
2. Then the procedure was interrupted by polarization measurement. It consists of an alternation of a charge current step for 40 sec, relaxation on the OCV, a discharge current of the same magnitude, and again OCV.
3. After reaching the cutoff, further charging for (+10% SOC) was performed by 500 mA, and the polarization measurements were repeated.
4. A new electrolyte was used for the same experiment at different flow rates.

## **Results**

The cell was charged with  $100 \text{ mA cm}^{-2}$  current density. OCV of both bipolar plates vs. the nearest reference electrode was simultaneously measured. Every 10% SOC, charging was interrupted for 30 sec to record the OCV of the cell. Assuming the error of 2% from a crossover, we derived the SOC calibration curve and checked it by the Nernst equation. Proton concentration was included in the equation for catholyte [168]. SOC's for all other experiments were determined using the interpolation of a calibration curve.

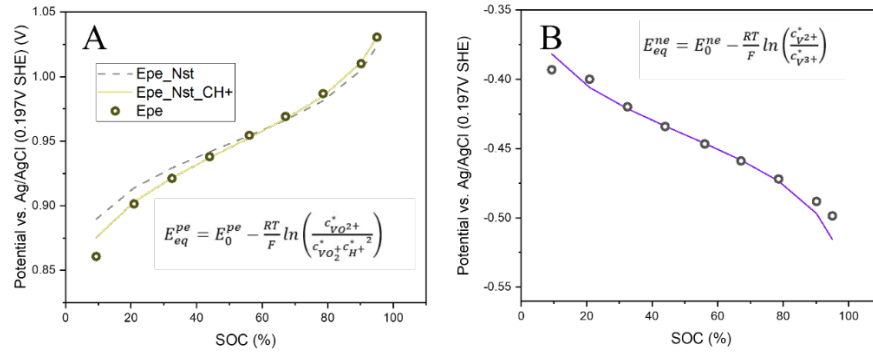


Fig. 2.2 A – catholyte calibration curve for SOC vs. OCP modeled by Nernst equations with/without considering proton concentration; B – anolyte calibration curve for SOC vs. OCP.

The next important experimental finding was in the place of the reference electrode. Placing the reference in the outlet resulted in unstable potential control and overestimated potential losses. Hence, we placed two reference electrodes in the inlet of the symmetric cell and measure three signals. Polarization was carried out in a 3-point cell in the potentiostatic mode and simultaneously detect the OCP of the plates (marked as blue arrows in Fig.2.3). We take steps of potentials vs. OCP, measure the current transients, and calculate its average after they reach steady-state; thus, obtaining the quasi-steady state polarization curve. The flow rate is varied for each SOC under study.

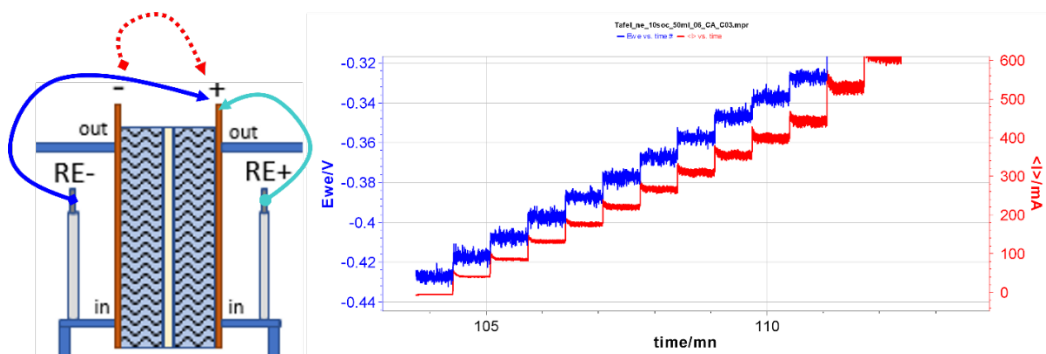


Fig. 2.3 Symmetric cell test connections and an example of raw data. The blue arrow and the blue curve represent the same voltage signal; the red arrow and curve represent the current.

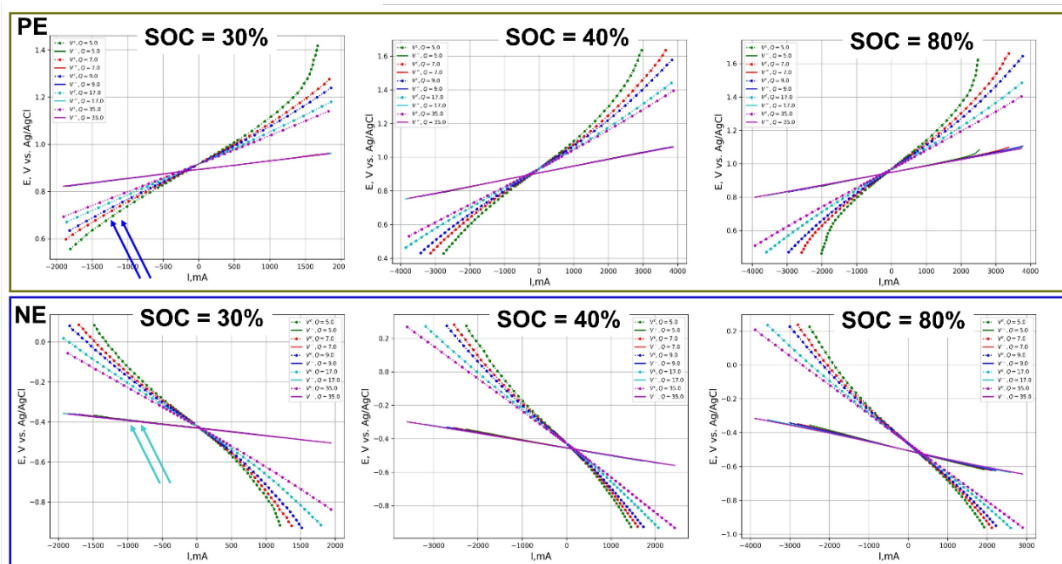


Fig. 2.4. Polarization data for different flow rates, SOC, and OCP of the working electrode. PE – a catholyte-based symmetric cell, NE – an anolyte-based symmetric cell.

Blue arrows correspond to the connection type from figure 2.3.

During the voltage steps, the overpotential gradient through the symmetric cell looks like in figure 2.3. After the data processing, we derived the set of polarization curves. We show the raw data for several SOC for anolyte (NE) and catholyte (PE) in figure 2.4. Voltage control through the cell gives a drastic slope (blue arrows in figure 2.4), compared with OCP measured from the same bipolar plate vs. nearest reference. The mass transfer effect is noticeable at high currents: the curves spreading become noticeable for different flow rates.

The data for the modeling was overpotentials vs. current dependence at different flow rates. OCV of the symmetric cell was subtracted from each data point. Here we demonstrated again that the experimental setup cannot sense the real losses inside the cell without the modeling. If we proposed that no potential distribution occurs inside the cell, ideally, a difference of  $V^+ - V^-$  (difference between OCPs of bipolar plates) should give the same value as a V cell (Fig. 2.5). Whereas the V cell has a larger slope than  $V^+ - V^-$ . That means that potential drop inside the cell cannot be accessed by the reference electrode on the inlet-outlet of the cell. Reference electrodes should be introduced inside the cell as close to the membrane as possible for direct measurements of losses [169].

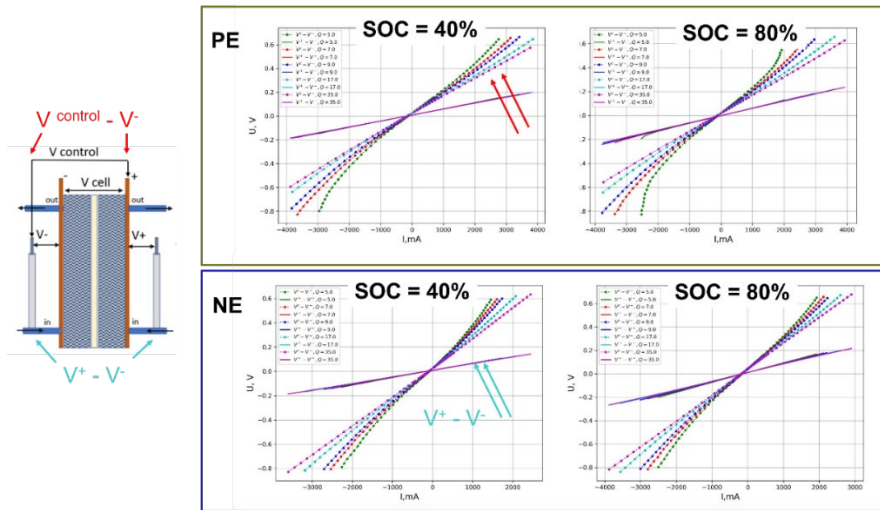


Fig. 2.5. Overpotential vs. current data for different flow rates, SOC, and OCP of the working electrode, used for modeling.

## Discussion

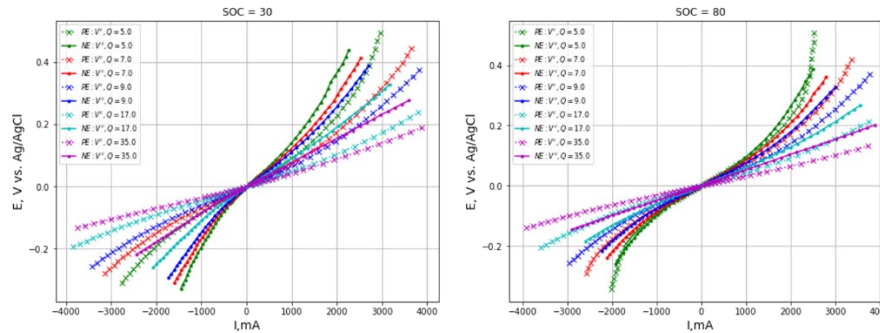


Fig. 2.6 Overpotentials comparison for analyte (NE) and catholyte (PE).

The main experimental outcome was that all losses inside the cell cannot be sensed by reference electrodes placed outside the current lines. On contrary, the polarization tests with potential control across the cell give reasonable estimations of total losses in the cell

(See Fig. 2.6 and 2.7). Higher losses were observed systematically for anolyte reaction, which is in an agreement with literature data [143,167].

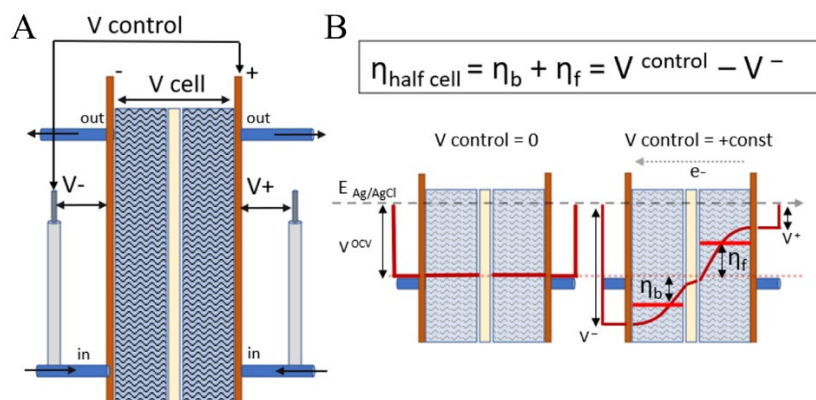


Fig. 2.7. A - Symmetric cell setup with data collection scheme; B – potential distribution profile across the cell for the experiments.

We fitted the data with the developed model. The main model assumptions are 1) averaged the gradients, 2) one-step reaction mechanisms, and 3) backward/forward reaction has different mechanisms. The overpotential gradient through the symmetric cell is presented in figure 2.7 B. The reaction is going forward in the right half-cell, and backward in the left half-cell. We averaged the potential drop through each of half-cells, as accurate distribution was unknown. Moreover, we assume that membrane potential is constant, and it can be neglected since its value is within the measurement errors [170].

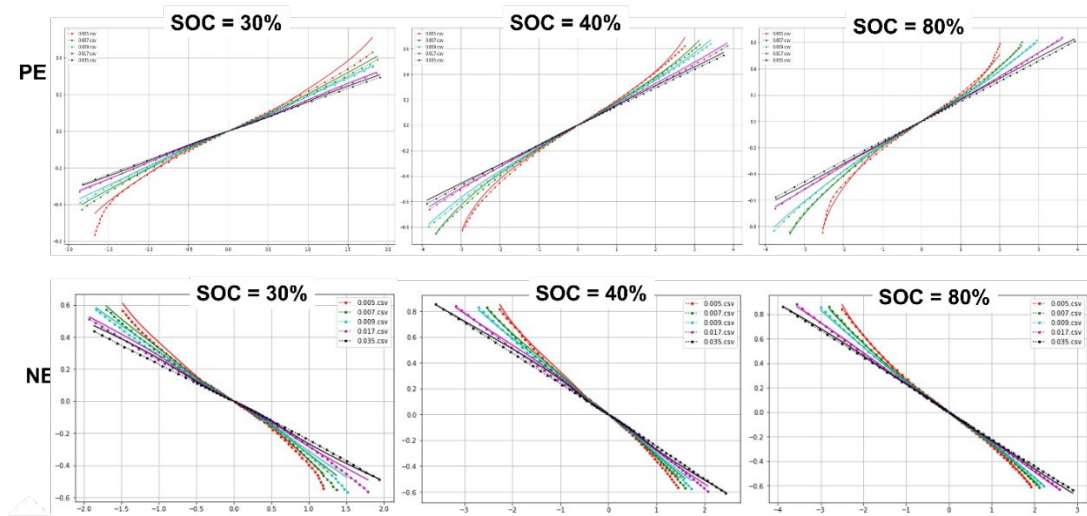


Fig. 2.8 The example of the fitting data from a symmetrical cell.

We fitted the data with our model with high accuracy (Fig. 2.8). As a result, we obtained sets of  $k_{a,c}$  and  $\alpha_{a,c}$ . They are derived for each SOC independently for both cathodic and anodic directions. These parameters can be further used as the lookup table in the dynamic simulations. Importantly, charge transfer coefficients were never 0.5, which points out the complex nature of the reaction mechanism and the geometry of the porous electrode. Looking at the unsymmetric behavior of the errors, one can conclude that it is not possible to uniquely split the forward and backward reaction impact into the overpotential. Nevertheless, averaging constants from values with errors below 100% allows us to accurately estimate the order of the rate constants. One can notice that charging is expected to have fewer losses ( $k_a$  for PE and  $k_c$  for NE in figure 2.9). The rate constants are in the range of  $8 \cdot 10^{-7}$  to  $8 \cdot 10^{-6}$ . Importantly, the  $k_c$  for the catholyte reaction has a different dimension, as proton concentration is included in the consideration.

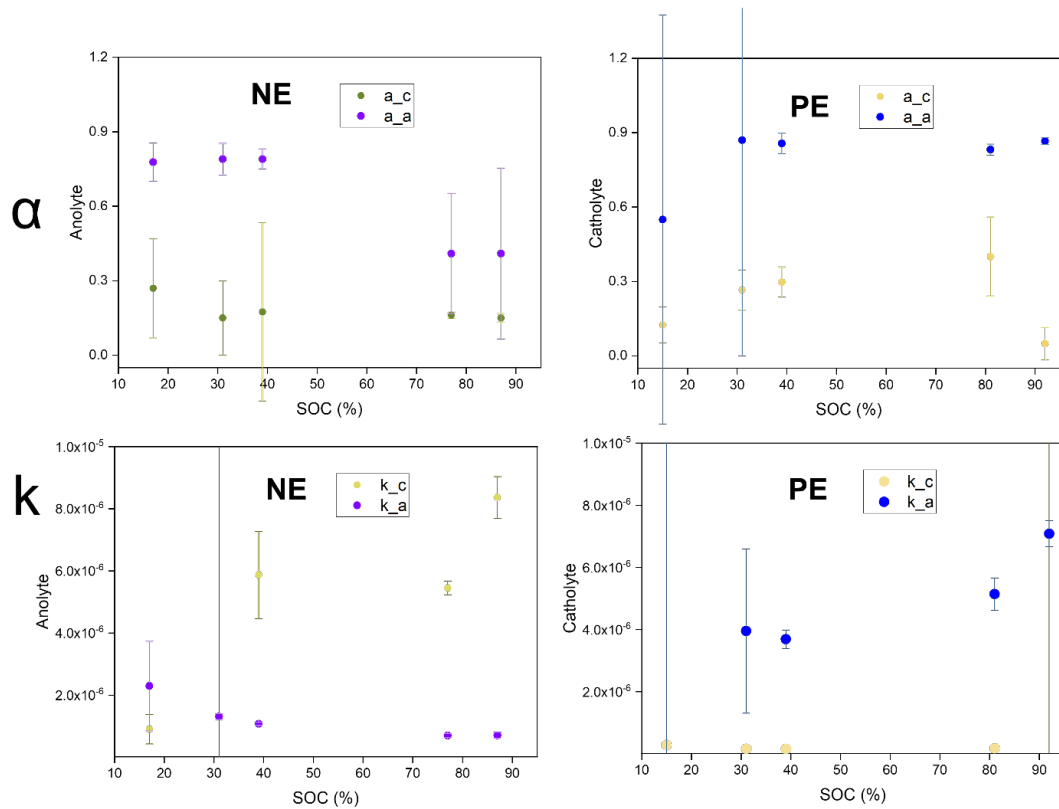


Fig. 2.9 Kinetic parameters for catholyte (PE) and anolyte (NE) at different SOC levels.

Local sensitivity analysis shows that even in a simple symmetric experimental design, we can use only parameters either for a cathodic or anodic net reaction. That means, for example, if the alpha cathodic fitted well, an anodic is unfixed and can vary in a broad range between 0 and 1, without an increase of fitting error, same for rate constants. Sensitivity analysis represents a deviation for the parameters in symmetric cells (green and cyan areas in figure 2.10 A), and as a reference for full cell fit without the parameter restrictions (red areas). Pronounced red area means that model accuracy for the symmetric design is much high and allows extracting exact values.

A full cell test was done for model validation by recording the charging curve with an interruption for current-control polarization. Fitting in the range of parameter errors from a symmetric cell, gave an acceptable fit with divergence for high currents (Fig. 2.10 B). This deviation probably relates to ineffective mass-transport coefficients fit. Moreover, there was a sufficient increase in the total error for high SOC as a pronounced area of mass-transport influence in polarization curves decreased at high SOC. Thus, the fit precision was also reduced toward high SOC.

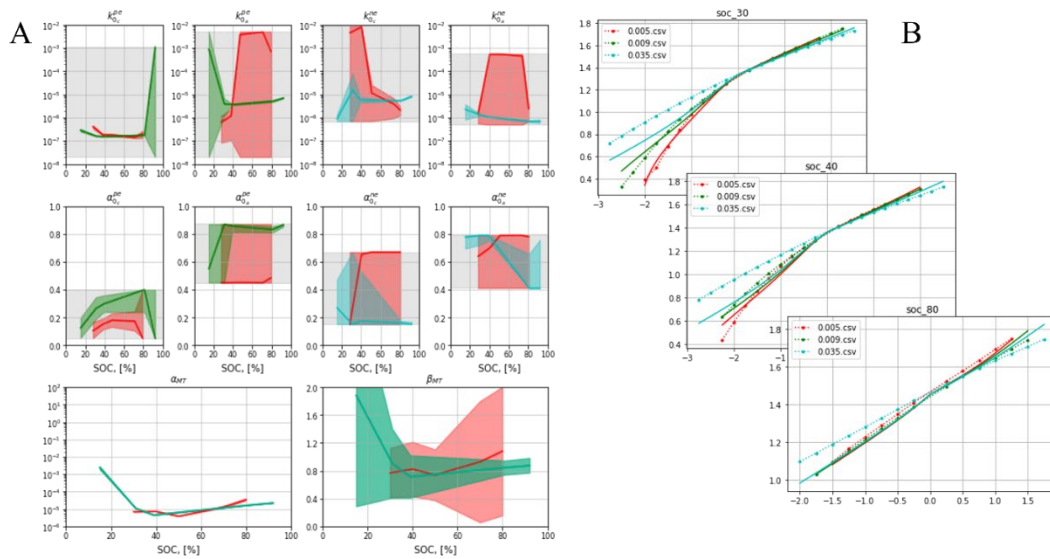


Fig. 2.10 A – sensitivity analysis for symmetric cells in different SOC and full cells fitted with approximate parameters restrictions, taken from the literature (red area). Green and cyan areas correspond to the uncertainties in kinetic parameters for catholyte and anolyte, respectively. B – a full cell fitting with parameters restrictions, derived from symmetric cell fit. Dots represent the experimental data; the lines are the fitting curves for different flow rates.

## Conclusion

We proposed a method of the apparent rate constant determination in the flow conditions of RFB. The main challenge of decoupling losses was done by using the symmetric cell design and the extended model, which consider the activation losses in detail.

The effective thermodynamically consistent single-step reaction mechanisms were considered at both half cells, thus decreasing the number of free kinetic parameters. The proposed approach demonstrated the importance of correct reference electrode placement. The application of symmetric cell reduced the number of unknown parameters in the model, hence, decreasing the fitting errors. Thus, the rate constant's order of magnitude is established exactly.

Averaged values for the kinetics parameters showed the difference in the rate of charging and discharging reactions.  $V^{2+} \rightarrow V^{3+}$  reaction goes slower than the  $V^{3+} \rightarrow V^{2+}$  with  $k = 9.5 \cdot 10^{-7} \text{ cm s}^{-1}$ , while the charge transfer coefficient for this reaction was higher and equal to 0.79. The complex reaction of  $V(V) \rightarrow V(IV)$  goes slower than the  $V(IV) \rightarrow V(V)$  with  $k = 7.8 \cdot 10^{-7} \text{ cm mol}^{-2} \text{ s}^{-1}$ , the charge transfer coefficient for  $VO_2^+ \rightarrow VO^{2+}$  is lower too and equal to 0.32.

To sum up, the extracted apparent rate constants for vanadium pairs were in the range between  $0.8 \cdot 10^{-6}$  and  $8 \cdot 10^{-6} \text{ cm s}^{-1}$ , and the charge transfer coefficient varies significantly and were lower for reduction processes. Based on polarization data, we can propose that the limiting process is the anolyte reaction.

Thus, the extracted apparent rate constants under conditions of a real flow battery provide important insights for developing reliable and efficient VRFBs applicable for energy storage systems. We showed the method of kinetics parameters evaluation for oxidized carbon felt electrodes, but the method can be applied easily for new electrode materials.

## 2.4 Conclusions from the Chapter 2

The chapter is devoted to the characterization of vanadium redox kinetics from two different points of view: elucidation of the limiting step in complex reaction of catholyte and extraction of apparent kinetic parameters for the reactions by fitting the polarization data.

Firstly, the mechanism of vanadyl oxidation was studied by a new spectroelectrochemical technique. The vanadyl redox reaction has two different pathways that depend on the applied overpotential and electrode surface. Deconvolution of the Raman spectra of vanadium species indicated that the oxygen-enriched electrode surface decreased the overpotential at which the reaction started and promoted the formation of vanadium complexes under moderate overpotentials. The oxygen-depleted binder surface enabled a single pathway at all overpotentials, which consisted of two undistinguishable steps: 1) formation of  $\text{VOOH}^+$  and the electron transfer converting this species into  $\text{VOOH}^{2+}$ , and 2) further formation of free and  $\text{HSO}_4^-$ -associated  $\text{VO}_2^+$  ions. Clear evidence of dimerized vanadium species incorporation into the electrochemical reactions was provided and a scheme of possible reaction pathways was developed. The method of redox

reaction tracking with Raman spectroscopy is suitable for any soluble redox-active species with only requirements of distinguishable Raman signals from oxidized and reduced forms.

Secondly, we proposed a method of apparent kinetic parameters determination in the operation conditions of VRFB. Decoupling of losses was done by a combination of modeling and a special setup with reference electrodes. Derived values for apparent rate constants were among the lowest of the reported in the literature. The order of all constants was below  $10^{-5} \text{ cm s}^{-1}$ . Moreover, noticeable asymmetry was observed in charge transfer coefficient values with lower values for cathodic reactions in both anolyte and catholyte.

To sum up, both developed methods are useful tools for the elucidation of the problems with sluggish kinetics of any redox-active species at different electrode materials utilized in RFB. In the case of vanadium RFB, additional improvements imply boosting of the  $\text{V}^{3+/2+}$  pair kinetics. Selection of the optimal electrode material is based on balancing of several factors: high active electrochemical surface area with many active sites and good transport properties for the electrolyte flow. Based on Raman studies, it occurs that high surface conductivity is an essential element for reaction rate acceleration. Therefore, a carbon material, like carbon paper or felt, modified by nanoparticles with pronounced catalytic effect, good stability in under operation conditions of the battery and high conductivity seems to be the best choice. Moreover, the additional attention must be paid to the suppression of hydrogen evolution reaction and stability of active sites on the anolyte side of the cell. Furthermore, balancing of the electrolyte flow rate, internal resistance of the cell, and the real surface area of the electrodes can effectively extend the operation regimes without kinetics limitations.

## **Chapter 3. Material selection protocol of bipolar plate for Vanadium RFB**

### **3.1. Overview of the Chapter 3**

As discussed in the Introduction, requirements of economic viability and defined threshold values for target parameters must be balanced for each material in the cell. Bipolar plate material is profitable to produce locally as it does not require complex equipment. This chapter is devoted to the search for locally manufactured conducting materials suitable for bipolar plate applications.

The implementation of carbon materials as bipolar plates provides low-resistance contacts and chemical stability toward the vanadium electrolyte components. The following requirements are crucial for the material selection: 1) a high electronic conductivity; 2) zero permeability to prevent battery self-discharge; 3) mechanical stability for a convenient manufacturing process; 4) chemical and 5) electrochemical stability. We investigated two manufacturing approaches for materials with a scalable manufacturing facility in Russia.

Firstly, the carbonized elastomer composite filled with hybrid carbon fillers (carbon black, carbon fibers, and graphite powder) was used as this material has certainly zero permeability. The key problem of the investigation was balancing the conductivity and toughness, as the addition of fillers at the same time improved conductivity and fragility.

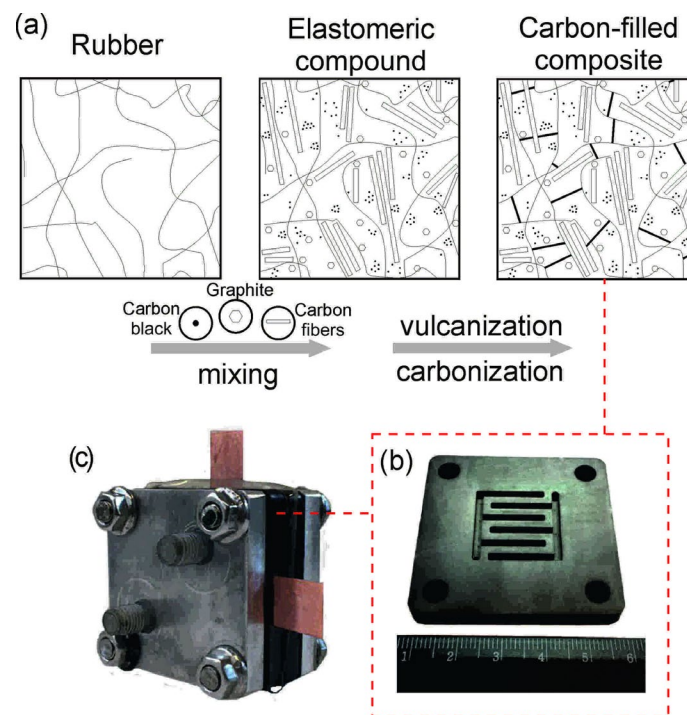
The second material was a graphite foil impregnated with fluoropolymer. The foil has a layered structure with high electric conductivity. It has non-zero permeability due to

the formation of open pores, which were fulfilled by the polymer during the material preparation. Special attention was paid to the investigation of material to electrochemical stability and the contact resistances in the cell.

As the result, a special set of testing methods was proposed for carbon material benchmarking for bipolar plates, with numerical values for conductivity, and mechanical and electrochemical stability tests.

### 3.2 Carbonized elastomer composite filled with hybrid carbon fillers for vanadium RFB bipolar plates

My contribution: Methodology, Investigation (cell design, degradation tests, RFB tests), Visualization, Writing – Original Draft.



Reprinted with permission from [171]. Copyright 2022 Elsevier



# Carbonized elastomer composite filled with hybrid carbon fillers for vanadium redox flow battery bipolar plates

E. Ruban<sup>a,b</sup>, A. Stepashkin<sup>c</sup>, N. Gvozdik<sup>d</sup>, D. Konev<sup>a</sup>, N. Kartashova<sup>a</sup>, A. Antipov<sup>a,e</sup>,  
M. Lyange<sup>b</sup>, A. Usenko<sup>a,b,c,\*</sup>

<sup>a</sup> Institute of Problems of Chemical Physics RAS, Acad. Semenov av., 1, 142432, Chernogolovka, Moscow Region, Russia

<sup>b</sup> Inenergy LLC, 2-nd Kotlyakovskiy lane 18, 115201, Moscow, Russia

<sup>c</sup> National University of Science and Technology MISIS, Leninsky av. 4, 119049, Moscow, Russia

<sup>d</sup> Skolkovo Institute of Science and Technology, Bolshoy Boulevard 30, bld 1, 121205, Moscow, Russia

<sup>e</sup> Mendeleev University of Chemical Technology of Russia, Miusskaya sq. 9, 125047, Moscow, Russia

## ARTICLE INFO

### Keywords:

Vanadium redox flow battery  
Bipolar plate  
Elastomer composite  
Carbon fiber  
Electrical conductivity

## ABSTRACT

New composite materials based on carbonized elastomers were investigated as a bipolar plate material for all-vanadium redox flow battery to substitute conventional graphite. The key material advantage is shifting from milling processing to straight forming of the final product during the synthesis. The final sintered composite demonstrated enhanced mechanical properties along with zero electrolyte permeability. Carbon fillers' influence on electrical and mechanical properties of the composite was studied. The assembled flow battery with new bipolar plates had a resistance of  $0.20 \Omega/\text{cm}^2$ , elusive permeability, suitable mechanical properties and proved suitability of the material in the current densities range of  $50\text{--}150 \text{ mA}/\text{cm}^2$  which meets the requirements for industrial vanadium flow batteries.

## 1. Introduction

Decrease of the wind and solar electricity cost and growing importance of climate change activities highlight the stationary energy storage systems' role for a sustainable and reliable energy economy. Redox flow battery (RFB) is a promising electrochemical technology for renewable energy integration due to its flexibility and scalability [1]. The most mature RFBs are based on vanadium salts (VRFB). Over dozens of projects have already been installed around the world, and the integration into grids is continuing [2].

Many significant achievements were made in the optimization of energy storage technology since pioneer works in the mid-1980s [3,4]. Cell component material improvement, a comprehensive understanding of fundamental working principles, and obtained experience of pilot projects allowed technology to become economically feasible. However, cost optimization and localization of component production are required for the extension of the RFB market.

One of the main components of the battery is a bipolar plate that makes electrical contact between the internal solutions and the connected wires. Bipolar plates possessing both high electrical conductivity

and mechanical strength has been urgently required for redox flow batteries and fuel cells. Typical material for the bipolar plate is dense graphite which, despite an excellent conductivity and chemical stability, has two drawbacks: noticeable permeability and complexity of batch processing [5]. In comparison with the graphite, the carbon-filled polymer composite materials also can be easily produced by the formation process; but a combination of sufficient mechanical properties, high conductivity, and chemical resistivity is challenging [6]. A high-quality carbon-filled composites were prepared for bipolar plates by B. Caglar et al. fabricated by introducing synthetic graphite and carbon nanotube (CNT) to polymer matrix [7]. However, the cost of the materials (fluoroelastomer) and a multi-steps production and permeability in operating conditions of VRFB remains disputable [8].

In this work we demonstrated the application of carbonized elastomer composite filled with hybrid carbon fillers as material for the bipolar plate. The material analogues of nitrile butadiene resin based on carbonized composites was successfully tested in petroleum fluids and acidic environments [9]. The ability to vary electrical and mechanical properties by changing the filler ratio alongside excellent formability makes the composites promising candidates for VRFB. Here we showed

\* Corresponding author at: Institute of Problems of Chemical Physics RAS, Acad. Semenov av., 1, 142432, Chernogolovka, Moscow region, Russia.

E-mail addresses: [e.ruban@inenergy.ru](mailto:e.ruban@inenergy.ru) (E. Ruban), [a.stepashkin@yandex.ru](mailto:a.stepashkin@yandex.ru) (A. Stepashkin), [n.gvozdik@inenergy.ru](mailto:n.gvozdik@inenergy.ru) (N. Gvozdik), [dkfrvzh@gmail.com](mailto:dkfrvzh@gmail.com) (D. Konev), [kartashova9natali@gmail.com](mailto:kartashova9natali@gmail.com) (N. Kartashova), [m.lyange@inenergy.ru](mailto:m.lyange@inenergy.ru) (M. Lyange), [a.usenko@inenergy.ru](mailto:a.usenko@inenergy.ru) (A. Usenko).

<https://doi.org/10.1016/j.mtcomm.2020.101967>

Received 2 September 2020; Received in revised form 4 December 2020; Accepted 9 December 2020

Available online 14 December 2020

2352-4928/© 2020 Elsevier Ltd. All rights reserved.

the first results of the material test in a VRFB prototype accomplished with material characterization.

## 2. Experimental

Experimental bipolar plates were fabricated by LLC “Elastocarb technologies”. The preparation of composite materials was carried out using rubber mixing rollers to obtain a highly filled elastomeric mixture based on nitrile butadiene rubber (BNR-18), discrete carbon fibers Toray T700 (length of 20 mm), crushed artificial graphite and carbon black grade N220. The mixture of rubber and fillers was vulcanized, followed by carbonization at argon atmosphere at 340 °C for 12 h (Fig. 1a). Electrical conductivity was measured on bars  $2 \times 4 \times 15$  mm by a transport measuring system Cryotel. Microstructure of the samples was investigated by a TESCAN VEGA 3 SBH scanning electron microscope. Elastic modulus and ultimate compressive strength were examined by a universal testing machine Zwick/Roell Z202 according to ISO 604:2002 on samples  $10 \times 10 \times 4$  mm and  $50 \times 10 \times 4$  mm on the hard pressure plates at traverse speed 2 mm/min. Every set of experiments contains 12 samples. Charge/discharge cycle was hold on Potentiostat-galvanostat P-40 × .

The stability test was conducted via soaking of the samples (ca. 2.5 g) in 1 M V(V) solution in 2 M H<sub>2</sub>SO<sub>4</sub> (15 mL) at 40 °C. The changes in mass and UV–vis spectra of the solution (processed according [10] to obtain V(V)/V(IV) ratio) were recorded for one month. A single cell VRFB with 4 cm<sup>2</sup> active area and interdigitated flow field were assembled with bipolar plates made of sample EC-FC-3 and the graphite (Carbotech 2231) as a reference sample. The setup included Nafion 117 membrane, 4 sheets of heat-treated carbon paper Sigracet SGL 39AA electrodes, 1.5 M vanadium electrolyte in 2.5 M H<sub>2</sub>SO<sub>4</sub> was pumped with flow rate of 60 mL/min. The electrolyte was prepared via preliminary electrolysis of VOSO<sub>4</sub> under constant current (400 mA) and further constant voltage regimes (1.7 V) with charge control to obtain V(III) solution. Polarization data at 50 % State of Charge (SoC) were collected by sequentially the change of the applied current with opposite polarities every 30 s with growing amplitude and 0.2 V and 1.7 V cutoffs. The electrolyte permeability of both materials was investigated before the test by a homemade test system that supplied the electrolyte under pressure of 3

atm onto the plate. No leaks were detected.

## 3. Results and discussion

The main properties and composition of the samples are presented in Table 1. Composites consisted of hybrid carbon fillers with different dimensions such as graphite, carbon black, and carbon fiber. A structure of percolating clusters in random clustered networks was formed by fillers, as presented in Fig. 1a. The total content of zero-dimensional fillers (graphite, carbon black) was 75 wt. %, one-dimensional carbon fiber ratio was 0, 6.25 wt. % and 12.25 wt. % for EC-FC-1, EC-FC-2, and EC-FC-3 samples, respectively. The gradual decay of conductivity with the growth of carbon fiber content was observed, which was related to the porosity increase and the appearance of less conductive new interfaces. However, the addition of carbon fibers significantly improved the mechanical properties of the material by enhancing the crack resistance and improving its milling stability.

The microstructure of carbonized elastomeric composites was homogenous with uniformly distributed fillers (Fig. 2). The average size of carbon flakes varied between 200–300 μm. The length of carbon fibers (Fig. 2 b, c) was about 150–300 μm that drastically decreased during the mixing stage due to the brittle nature of carbon. Although the porosity of the samples seemed to increase with the filler introduction, its permeability was undetectable, and therefore the porosity had a closed type. Besides, voids appearance can be explained by the changing from brittle fracture to ductile fracture mechanism in the presence of carbon fibers that led to revealing tracks.

The stress-strain compressive diagrams of carbonized composites demonstrated linear behavior for up to 75–80 MPa (Fig. 3a). The elastic modulus was calculated by applying 50 MPa load (Fig. 3b). Deformation limit during fracture was 0.8 %, which was higher than a typical value for graphite. The ultimate compressive strength and the elastic modulus of the proposed materials were 25 % higher than for graphite. The hardest sample EC-FC-3 was selected for the further test as the typical load on a bipolar plate is compression in a flow battery.

Additionally, the electrochemical stability test was performed to prove the suitability of the designed materials in the harsh conditions in the VRFB. The standard test of soaking the samples in the oxidative environment (Vanadium (V) in acid media) under 40 °C to accelerate the degradation process. No changes in mass were detected after one month of edging. However, a gradual decrease in V(V) concentration was observed with 90 % remained V(V) concentration after the test (Fig. 4). That was attributed to the partial surface oxidation of material as 0.7 mass% of the sample was involved in the reaction (calculation was based on the molar ratio).

Finally, the material EC-FC-3 was tested in the VRFB prototype and compared with the standard reference graphite sample (Fig. 1b, 1c). Polarization curves at 50 % SoC were measured as the average representation of the system (Fig. 5). Cell resistances extracted from the data as a slope of the current density vs. potential at low current densities were 0.20 Ω/cm<sup>2</sup> and 0.17 Ω/cm<sup>2</sup> for EC-FC-3 and the graphite,

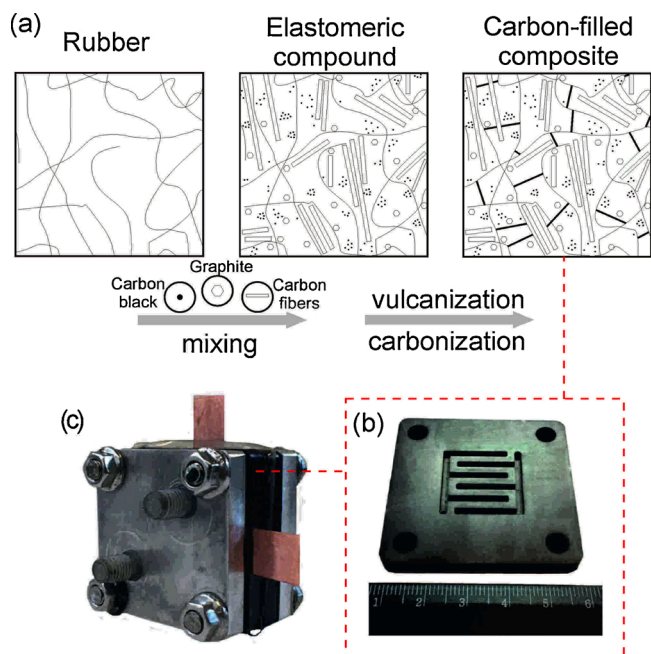


Fig. 1. Scheme of fabrication process (a); bipolar plate fabricated by using EC-FC-3 sample (b); VRFB prototype (c).

Table 1

Transport and mechanical properties of investigated composite samples with their designations and typical graphite for RFB bipolar plates.

Sample	EC-FC-1	EC-FC-2	EC-FC-3	Graphite reference
Density, g/cm <sup>3</sup>	1.71 ± 0.01	1.60 ± 0.01	1.55 ± 0.01	184 ± 0.01
Carbon fiber, Wt. % of	0	6.25	12.25	0
Electrical conductivity, S/cm	7.93 ± 0.16	7.52 ± 0.16	6.13 ± 0.12	93.4 ± 1.87
Elastic modulus, MPa	14.51 ± 0.47	13.7 ± 0.29	15.54 ± 0.39	11.8 ± 0.3
Ultimate compressive strength, MPa	94.8 ± 4.3	94.6 ± 9.5	104.2 ± 9.8	74.5 ± 7

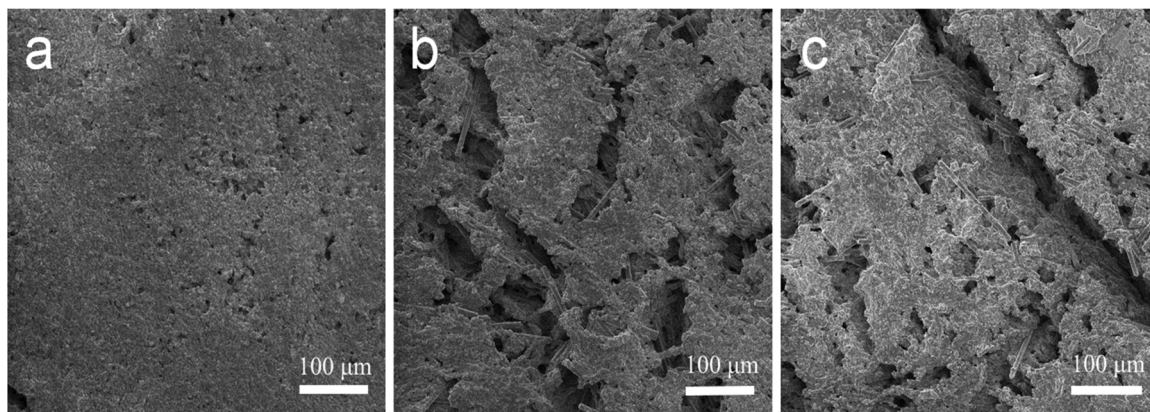


Fig. 2. SEM images of fabricated bipolar plates fractured with liquid nitrogen: EC-FC-1 (a), EC-FC-2 (b), EC-FC-3 (c).

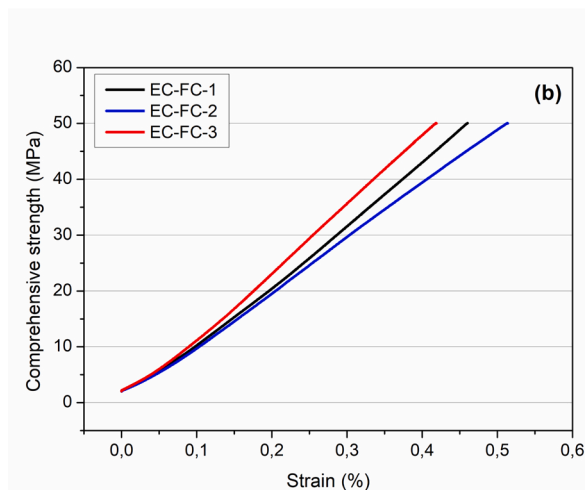
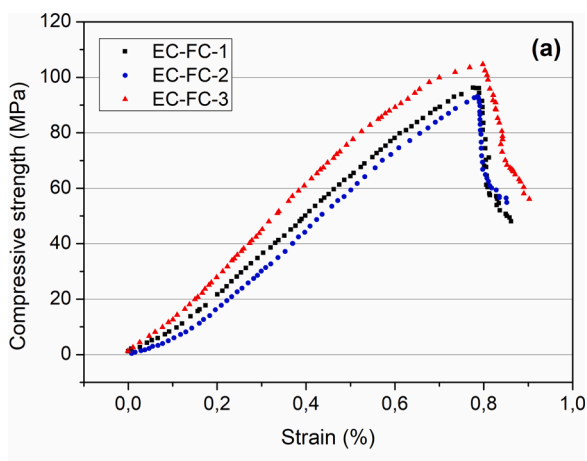


Fig. 3. Stress-strain compressive diagrams for ultimate compressive strength test (a) and for elastic modulus independent test (b).

respectively. Under fixed SoC, the same set of materials obtained difference in the cell resistances corresponded to the less effective contact resistance between the electrodes and studied bipolar plate material. This comparison gives indirect estimation of the contact resistance, which was a bit higher in case of new material, but sufficient enough to test the cell under standard current densities region up to 200 mA/cm<sup>2</sup>. However, the difference for EC-FC-3 and reference graphite samples is negligible for the current range 50–150 mA/cm<sup>2</sup> that is typically used in commercial VRFB. The same tendency referred to the power density

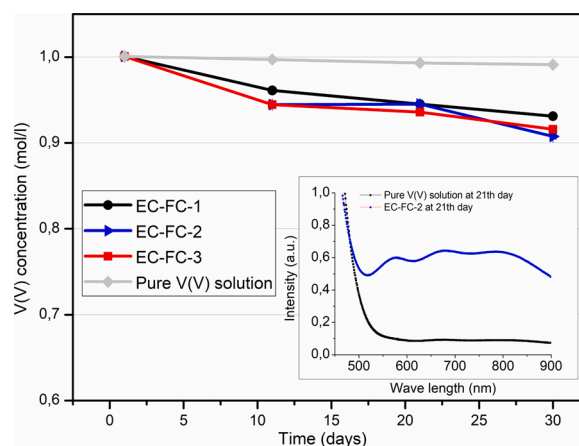


Fig. 4. Stability study of the samples in V(V) solution for one month. The change of V(V) concentration corresponded to the degradation rate; inserted UV-vis spectra – the examples of raw data.

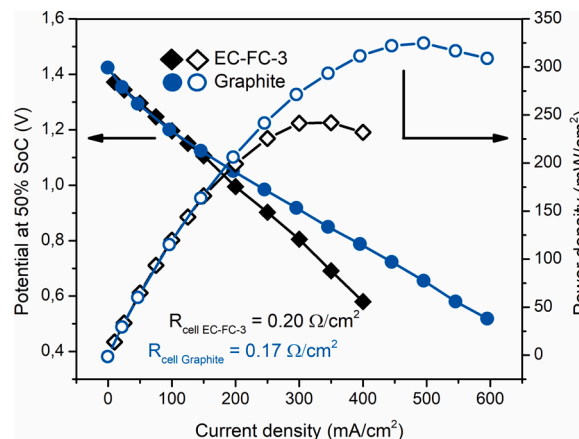


Fig. 5. Potential and power density as a function of current density for VRFB at 50 % SoC with bipolar plates made of EC-FC-3 composite and standard graphite as a reference.

profiles: the power for both cells matched at initial current densities. Significant degradation of the characteristics at high current densities associated with the insufficient conductivity of the sample.

#### 4. Conclusion

Developed materials had a uniform morphology, elusive permeability, excellent mechanical properties, and high enough conductivity (up to 7.9 S/cm) to be suitable for the flow battery applications at current densities used in commercial VRFB, which are up to 150 mA/cm<sup>2</sup>. Therefore, the formability of elastomers before the carbonization stage makes the composites attractive for large scale production of bipolar plates with complicated flow field architecture.

#### Declaration of Competing Interest

The authors declare that they have no known competing financial interests or personal relationships that could have appeared to influence the work reported in this paper.

#### Acknowledgments

This work is supported by the Russian Science Foundation (grant № 19-79-00334).

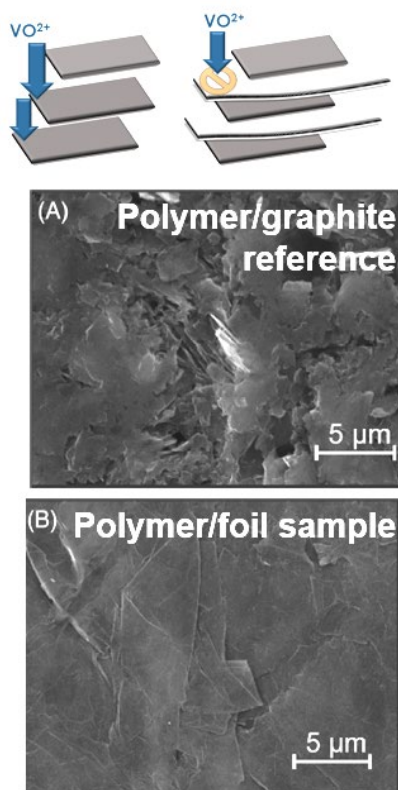
#### References

- [1] K. Lourenssen, J. Williams, F. Ahmadpour, R. Clemmer, S. Tasnim, Vanadium redox flow batteries: a comprehensive review, *J. Energy Storage*. 25 (2019), <https://doi.org/10.1016/j.est.2019.100844>.
- [2] K.F.K. Yano, S. Hayashi, K. Takahiro, T. Shibata, K. Yamanishi, Development and demonstration of redox flow battery system, *SEI Tech. Rev.* 84 (2017) 22–28.
- [3] M. Skyllas-Kazacos, Efficient vanadium redox flow cell, *J. Electrochem. Soc.* 134 (1987), <https://doi.org/10.1149/1.2100321>, 2950.
- [4] L.F. Arenas, C. Ponce de León, F.C. Walsh, Engineering aspects of the design, construction and performance of modular redox flow batteries for energy storage, *J. Energy Storage*. 11 (2017) 119–153, <https://doi.org/10.1016/j.est.2017.02.007>.
- [5] X. Ke, J.M. Prah, I.J.D. Alexander, J.S. Wainright, T.A. Zawodzinski, R.F. Savinell, Rechargeable redox flow batteries: flow fields, stacks and design considerations, *Chem. Soc. Rev.* 47 (2018) 8721–8743, <https://doi.org/10.1039/c8cs00072g>.
- [6] M. Park, Y.J. Jung, J. Ryu, J. Cho, Material selection and optimization for highly stable composite bipolar plates in vanadium redox flow batteries, *J. Mater. Chem. A*. 2 (2014) 15808–15815, <https://doi.org/10.1039/c4ta03542a>.
- [7] B. Caglar, P. Fischer, P. Kauranen, M. Karttunen, P. Elsner, Development of carbon nanotube and graphite filled polyphenylene sulfide based bipolar plates for all-vanadium redox flow batteries, *J. Power Sources* 256 (2014) 88–95, <https://doi.org/10.1016/j.jpowsour.2014.01.060>.
- [8] C. Minke, T. Hickmann, A.R. Dos Santos, U. Kunz, T. Turek, Cost and performance prospects for composite bipolar plates in fuel cells and redox flow batteries, *J. Power Sources* 305 (2016) 182–190, <https://doi.org/10.1016/j.jpowsour.2015.11.052>.
- [9] D.I. Chukov, A.A. Stepashkin, A.I. Salimon, S.D. Kaloshkin, Highly filled elastomeric matrix composites: structure and property evolution at low temperature carbonization, *Mater. Des.* 156 (2018) 22–31, <https://doi.org/10.1016/j.matdes.2018.06.034>.
- [10] C. Petchsingh, et al., Spectroscopic measurement of state of charge in vanadium flow batteries with an analytical model of V(IV)-V(V) absorbance, *Electrochem. Soc.* 163 (2016) A5068–A5083.

### 3.3 Fluoropolymer impregnated graphite foil as a bipolar plates of vanadium

#### RFBs

My contribution: Conceptualization, Formal Analysis, Visualization, Writing - Original Draft.



Reprinted with permission from [172]. License #52912490276123. Copyright

2022 John Wiley & Sons Ltd.

# Fluoropolymer impregnated graphite foil as a bipolar plates of vanadium flow battery

Pavel Loktionov<sup>1,2</sup> | Natalia Kartashova<sup>1,3</sup> | Dmitry Konev<sup>2</sup> | Lilia Abunaeva<sup>1</sup> | Anatoly Antipov<sup>1,4</sup> | Eugeny Ruban<sup>2,5</sup> | Alexander Terent'ev<sup>5,6</sup> | Natalia Gvozdik<sup>7</sup> | Maria Lyange<sup>5</sup> | Andrey Usenko<sup>5,8</sup>  | Keith Stevenson<sup>7</sup>

<sup>1</sup>Scientific-Educational Laboratory "Electroactive Materials and Chemical Power Sources, Mendeleev University of Chemical Technology of Russia, Moscow, Russia

<sup>2</sup>Department of Functional Materials for Chemical Energy Sources, Institute of Problems of Chemical Physics RAS, Moscow, Russia

<sup>3</sup>Faculty of Fundamental Physical and Chemical Engineering, Lomonosov Moscow State University, Moscow, Russia

<sup>4</sup>Faculty of Chemistry, Moscow Institute of Physics and Technology, Dolgoprudny, Russia

<sup>5</sup>Energy Storage Systems Department, Inenergy LLC, Moscow, Russia

<sup>6</sup>Laboratory of Plasma Processes in Metallurgy and Metal Processing, Baikov Institute of Metallurgy and Materials Science RAS, Moscow, Russia

<sup>7</sup>Center of Energy Science and Technology, Skolkovo Institute of Science and Technology, Moscow, Russia

<sup>8</sup>Functional Nano Systems and High Temperature Materials Department, National University of Science and Technology MISIS, Moscow, Russia

## Correspondence

Andrey Usenko, Energy Storage Systems Department, Inenergy LLC, 2-nd Kotlyakovskiy lane 18, 115201 Moscow, Russia.  
Email: a.usenko@inenergy.ru

## Funding information

Russian Science Foundation, Grant/Award Number: grant №19-79-00334

## Summary

Renewable energy in recent years plays an increasingly important role in the energy industry. Therefore, the problem of inventing efficient and affordable energy storage devices is of current importance. Vanadium redox flow battery stands out between a wide range of various chemical sources of electric energy. Discovering the way for optimizing the price of energy storage is one of the most important questions of the mentioned battery. New graphite-polymer composite materials study shows that they may become a replacement for commonly used brittle graphite. The current article presents the study of graphite foil (or flexible graphite) filling with a copolymer of tetrafluoroethylene and vinylidene fluoride F-42 properties. The article uses an implementation approach of putting the fluoropolymer into the pores of graphite foil, which shows a slight decrease in electrical conductivity, while a significant increase in its electrochemical stability in comparison with untreated graphite foil. Testing results of such material as current collectors (or bipolar plates) in a single membrane-electrode assembly of vanadium redox flow battery cell show peak value of discharge power density of 843 mW/cm<sup>2</sup>, energy efficiency of 78%-79% during cycling at 200 mA/cm<sup>2</sup> allowing us to assume the possibility of its successful application in redox flow battery stacks.

## KEYWORDS

bipolar plates, current collectors, flexible graphite, fluoropolymer, graphite foil, vanadium flow battery

## 1 | INTRODUCTION

Demand for long-term energy storage devices is growing for applications in alternative energy and power grid technologies. Among stationary electrochemical devices, redox flow batteries (RFBs) are considered to be promising systems with independent scaling of the capacity and discharge power.<sup>1</sup> Such systems employ two “electrolyte tanks” and electrochemical cell “stack,” where the charge/discharge reactions occur. The construction features and characteristics of the materials used in the cells “stack” determine the efficiency of the system. The most studied RFBs with vanadium electrolyte have reached a sufficient level of development, energy storage devices based on RFBs of various capacities and power are available in the marketplace.<sup>2</sup>

One of the key elements of RFB stacks is current collectors, in other words, bipolar plates (BP). BPs provide electrical contact of individual cells (membrane electrode assemblies, called MEA) in the stack and with an external circuit, separate the electrode spaces of the unit cells in the stack, ensure uniform distribution of electrolyte in the electrode region and heat distribution in the stack. Thereby materials for BP fabrication should possess high electrical conductivity, good mechanical and electrochemical stability, and high corrosion resistivity.<sup>3</sup> It is worth noting that 19%–28% RFB price comes to BPs, thus its production ought to be economically feasible.<sup>4</sup>

Materials for the manufacturing of BP can be divided into three types: (a) highly filled graphite materials; (b) carbon-polymer composites; (c) metals and alloys.<sup>5</sup> The first two groups differ from others with electrochemical stability and are often used for RFB applications.<sup>6</sup>

Carbon-polymer materials appear to be the most promising group for manufacturing affordable and efficient BPs, in contrast to graphite materials.<sup>3</sup> Indeed, a combination of a carbon-based conductive filler and inert polymer as binder results in good electrical conductivity, compactness, and soft mechanical processing. Graphite and its modified types, including expanded graphite,<sup>7</sup> synthetic anisotropic graphite,<sup>8</sup> mineral graphite,<sup>9,10</sup> compressed expanded graphite,<sup>11,12</sup> graphite and graphene mixture,<sup>13</sup> graphite foil,<sup>14</sup> carbon in different forms, such as carbon nanotubes,<sup>8</sup> carbon fabric,<sup>15,16</sup> carbon and carbon fibers mixture,<sup>17</sup> are used in the capacity of carbon-containing raw material. Thermoplastics polymers (polyvinylidene fluoride,<sup>18</sup> polypropylene,<sup>9,19,20</sup> etc.) and thermosets (epoxy,<sup>11,12</sup> phenolic,<sup>7</sup> and other resins) were applied as a binder. Such composites can be prepared by injection molding, compression molding, hot-compression of different layers, soft-layer method, polymer solution (or melt) impregnation with hot compression, etc. Available on the market materials own a

standard shape, not high mechanical properties for prototyping and high price. The study of new material for BPs is still an actual question. Earlier our group proposed a new concept of fast-prototyping of RFB MEA individual cells<sup>21,22</sup> or stacks<sup>23</sup> utilizing a series of laser-cut graphite foil (GF) sheets. BPs made of GF with laser-cut channels allow fast prototyping RFB with various flow field designs to optimize battery efficiency. However, the issue of residual porosity has not been solved, which led to gradual decay in the capacity due to the absorption of electrolyte into the pores of the GF.<sup>24</sup>

In this paper, we proposed an approach to improving the properties of BP made out of GF. We demonstrate a significant improvement of its electrochemical stability without a decline of RFB performance by impregnation of fluorinated polymer into the pores of GF followed by hot-pressing. The article proposes the method of impregnation and presents the investigation of morphology, electrical conductivity, electrochemical stability, and performance of bipolar plates.

## 2 | EXPERIMENTAL

### 2.1 | Chemicals

Graphite foil (GF) “Graflex” (GC Unichimtek, Moscow, Russia) is made from purified flake graphite by special chemical and heat treatment followed by rolling without binder.<sup>25</sup> Graflex graphite foil with a thickness of 1 mm (Unihimtek, Russia), graphite Carbotech 2231, and graphite-polymer composite (Liaoning Grepalofu New Energy Co., Ltd.) were used as carbon-based bipolar plates. Fluoropolymer F-42 (Ftoroplast-42, HaloPolymer, Russia; GOST 25428-82) and acetone (Sigmatech, Russia) were used for impregnation of GF. Proton-exchange membrane GP-IEM-103 (Liaoning Grepalofu New Energy Co., Ltd.) was pretreated before the use by sequential change of the solutions: (a) boiling in water for one hour; (b) boiling in a 3%-solution of hydrogen peroxide (97%, Reachim, Russia); and (c) boiling in 2 M sulfuric acid 97% (Sigmatech, Russia). Carbon felt (Sigracell GFD 4.6 EA, SGL group, Germany) was used as electrodes in a single vanadium RFB.  $\text{VOSO}_4 \cdot 3\text{H}_2\text{O}$  (97%, Reachim, Russia) and sulfuric acid are utilized as electrolyte precursors.

### 2.2 | Fabrication of BPs

A series of 1 mm thick graphite foils with different content of F-42 polymer were fabricated. First, impregnation of fluoropolymer was performed by filling the full

vacuum vial with GF samples with acetone solution F-42 (Figure S1). When the grains are filled with the solution, the pressure is gradually equalized to atmospheric level. After this procedure the samples are hold in solution for specified time. The upper level of concentration for saturation is limited by polymer solution viscosity, lower level - by insignificance of expected effect in case of full grains saturation. The samples were taken out of the solution after exposure time and left for 12 hours at room temperature to remove the solvent from the GF pores. Second, obtained samples undergo hot pressing at 165°C under the load of 280 kg/cm<sup>2</sup> for 1 minute. Laser-cutting process gives a required shape to samples (Figure S2). To characterize the degree of impregnation the difference in weight of untreated and impregnated GF was measured. The density difference was taken as a measure of the volume of GF potentially filled by the component introduced by impregnation (GF was considered as a carbon substrate with graphite density and pores, filled with the solution of the component):

$$\Delta m_{\max} = m_0 \omega_{\text{sol}} \rho_{\text{sol}} (\rho_{\text{GF}}^{-1} - \rho_{\text{G}}^{-1}) \quad (1)$$

where  $\Delta m_{\max}$  is the maximum possible mass gain for account of polymer [g];  $m_0$  is the sample mass before impregnation [g];  $\rho_{\text{GF}}$  is the density of GF [g/cm<sup>3</sup>];  $\rho_{\text{G}}$  is the density of mineral graphite [g/cm<sup>3</sup>];  $\rho_{\text{sol}}$  is the density of the impregnating solution F-42 [g/cm<sup>3</sup>]; and  $\omega_{\text{sol}}$  is the mass fraction of F-42 in solution [% wt.].

## 2.3 | Electrical resistivity measurement

*In-plane electrical resistivity* was measured by the four-point technique (Figure S3). The sample was tightly pressed in a rectangle device with four copper electric contacts, located at the same distance relative to each other, and an insulating gasket covered the sample top for pressing. The current value from 1 to 100 mA was passed through the cell, and the voltage between the internal contacts of the device was measured. The resistance of the cell was determined from the voltage-current slope dependence.

In-plane resistivity was calculated from Equation (2):

$$R_{i.p.} = R_{i.p.}^0 \cdot w \cdot \frac{h}{l} \quad (2)$$

where  $R_{i.p.}$  is the in-plane electrical resistivity [ $\Omega \cdot \text{m}$ ];  $R_{i.p.}^0$  is the resistivity of the sample [ $\Omega$ ];  $w$  is the sample width [m];  $h$  is the sample height [m]; and  $l$  is the length between the contacts of the measuring cell [m].

*Through-plane electrical resistivity* was measured in a homemade setup with a 4 cm<sup>2</sup> active area (Figure S3). The device was placed between the press plates with the sample pressed in the Teflon gasket. Then the voltage was measured during a linear sweep of the current from 1 to 100 mA with various values of compression—from 2.5 to 25 kg/cm<sup>2</sup>. Resistivity was determined based on the obtained series of voltage dependence of current. The obtained load dependence of resistivity was extrapolated to obtain resistance at zero load. The target resistance of the sample was obtained by subtraction of the empty cell resistance from the total one. Through-plane resistivity was calculated from Equation (3):

$$R_{t.p.} = (R_{t.p.}^0 - R'_{t.p.}) \cdot A \quad (3)$$

where  $R_{t.p.}$  is the sample through-plane electrical resistivity [ $\Omega \cdot \text{cm}^2$ ];  $R_{t.p.}^0$  is the resistivity of the sample [ $\Omega$ ];  $R'_{t.p.}$  is the resistivity of the empty cell [ $\Omega$ ]; and  $A$  is the area of the sample [cm<sup>2</sup>].

## 2.4 | The surface morphology of the graphite foils

The microscopic studies of the surface morphology were conducted with a Vega 3 Tescan equipped with an EDX. The degree of degradation after electrochemical experiments was evaluated by microphotographs obtained by a metallographic microscope Micromed MET with the camera UCMOS 14000 KPA.

## 2.5 | Electrochemical potential window

A specially designed three-electrode cell was used for electrochemical stability tests (Figure S4). The studied sample was used as a working electrode, which was pressed against the flange connection with known area using a connecting plate and screws; a silver chloride reference electrode (KCl sat.), and a platinum foil counter electrode were used in a solution of 1 M H<sub>2</sub>SO<sub>4</sub>. The working range of potentials for the electrochemical potential window was determined as follows. Cyclic voltammetry (CV) data at a scan rate of 25 mV/s was measured till the positive or negative current values exceeded 2 mA/cm<sup>2</sup> (besides the capacitive current). This value of current was chosen according to the following argumentation. The distribution of electrolytes between an individual cell in the RFB stack is carried out using common electrolyte lines. In addition to the electrical contact of individual cells through bipolar plates, an ionic

contact of electrolytes of neighboring cells is also created. As a result, shunt currents—current leaks occur in the process of charging or discharging the RFB along the paths of these ionic contacts. Shunting currents in Vanadium redox flow battery (VRFB) stacks not only reduce the battery efficiency but also cause electrochemical degradation, especially for the bipolar plate.<sup>26,27</sup> The value of shunting currents is in the order of one to a tenth of mA/cm<sup>2</sup>, and it is dictated by geometrical profiles of channels for electrolyte distribution and electrolytes conductivity.<sup>26,27</sup> The selection of optimal channel configuration can mitigate this problem, resulting in the maximum shunt current value of 2 mA cm<sup>2</sup> or less.<sup>28</sup> Therefore, the same current density was chosen as a cut-off for the determination of electrochemical window stability. Thus, the potential range at which the oxygen and hydrogen evolution currents were 2 mA/cm<sup>2</sup> was extracted. Then, the CV data in the selected potential range was recorded again and taken as the initial ones before the accelerated aging tests.

## 2.6 | Electrochemical aging test

The sample was inserted into the three-electrode cell as discussed above. Sample was polarized under current density of 2 mA/cm<sup>2</sup> (or −2 mA/cm<sup>2</sup>) for 10 minutes under constant stirring. CV was recorded during the test every 10 minutes to deduce the capacitance change (magnetic stirrer was turned off). The values of current corresponding to the potential 0.5 V vs Ag/AgCl (sat.) were derived from the CV data in the forward and reverse scans. The capacity of the sample was determined according to Equation (4):

$$C = \frac{I_m}{V} \quad (4)$$

where  $I_m = \frac{I_c + I_a}{2}$  is the a mean value of cathodic and anodic current at 0.5 V vs Ag/AgCl (sat.) [A] and  $V$  is the scan rate [V/s].

Then the described sequence of actions was repeated several times. After performing these tests, the surface of the material was analyzed using a metallographic microscope.

## 2.7 | Testing the modified GFs in vanadium RFB as bipolar plates

The single-cells of vanadium RFB based on GP-IEM-103 proton-exchange membrane were assembled with different bipolar plate materials: graphite/polymer composite,

untreated GF, and GF modified with F-42 (Figure 1). The active geometric area of the electrodes was 4 cm<sup>2</sup> with flow-through configuration, and a 30% degree of compression for the carbon felt electrodes was used. Vanadium electrolyte contained 1 M VOSO<sub>4</sub> with 4 M H<sub>2</sub>SO<sub>4</sub>. The generation of V<sup>2+</sup> anolyte solution was performed electrochemically by complete electrolysis of the initial solutions with a volume ratio of 1:2. Half of the catholyte electrolyte was removed from the tank at the end of the electrolysis, thus obtaining a fully charged RFB cell. Catholyte and anolyte were 30 mL volume each. The flow rate of the electrolyte was 100 mL/min.

**Polarization curves.** Alternating values of the charge/discharge current density was superimposed for the cell with fixed time intervals to register the polarization data under 50% State of Charge (SoC) in the step mode. The duration of each galvanostatic stage of polarization was 30 seconds. The maximum charge current  $I_{charge}$  was limited with 125 mA/cm<sup>2</sup>. Levelized value on the voltage dependence on time was used as the cell voltage for a given  $I$ . The power dependence on current density was constructed according to the received polarization curve. Additionally, the impedance spectra were recorded for the 100% and 50% SoC in the frequency range of 50-0.1 kHz with a voltage amplitude of 20 mV.

**Cycling** was carried out at the current densities of 200, 150, or 100 mA/cm<sup>2</sup> for six times with the voltage cutoffs of 0.8-1.7 V. Then, a cell was adjusted to 50% SoC in the potentiostatic mode to get the impedance spectra after the cycling.

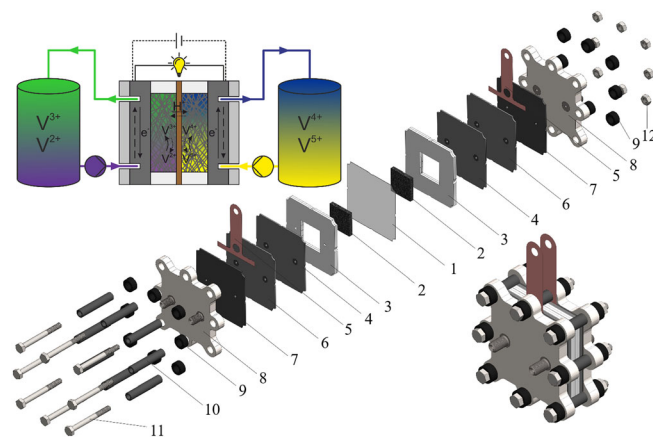


**FIGURE 1** Scheme of RFB in the disassembled (centered) and assembled (bottom right) and scheme of VRFB (top left): 1 - proton-exchange membrane; 2 - carbon felt electrodes; 3 - electrode gaskets; 4, 6 - current collector's plates made of graphite materials (test samples); 5 - copper foil contacts; 7 - sealing gaskets; 8 - metal end plates with fittings; 9 - insulating washers; 10 - insulating sleeves; 11 - bolts; 12 - nuts [Colour figure can be viewed at [wileyonlinelibrary.com](http://wileyonlinelibrary.com)]

### 3 | RESULTS AND DISCUSSIONS

#### 3.1 | Impregnation of GF with F-42 solutions

Graphite foil has a twice lower density than crystalline graphite (Table S5); hence, the excess volume must be filled by a polymer. The fluoropolymer F-42 was chosen as a polymer pores filler because it has excellent stability in concentrated acidic, alkaline, and oxidizing solutions. The main characteristics of F-42 fluoropolymer are given in Table S6. Accumulation of the filler inside the pores was investigated for three polymer solution concentrations (Figure 2). 5% polymer solution penetrated the pores of the GF faster than 10% and 15% solutions. Exposure for 100 hours led to at least 70% of the pore volume of the GF filled, while for more viscous solutions with an F-42 concentration of 10% and 15% reached only 30%-40% of the whole volume. Nevertheless, the absolute mass gain turns out to be noticeably higher when using the solution with the highest polymer content. In this evidence, the impregnation of the following samples was carried out with a 15% solution of the polymer in acetone during 80 hours and all subsequent measurements were carried out on samples GF impregnated with 1.8% wt. F-42.

#### 3.2 | In-plane and through-plane resistivity of impregnated GFs

Polymer impregnation does not affect the transport properties of the samples, as the basic graphitic structure remains the same. No significant increases in the in-plane (a) and through-plane (b) electrical resistivity were detected depending on the F-42 content (Figure S7). In-plane and through-plane resistivity of impregnated GFs changed insignificantly at the level of  $(2.4 \pm 0.1) \cdot 10^{-5} \Omega \cdot \text{m}$  and  $(2.7 \pm 1.3) \cdot 10^{-5} \Omega \cdot \text{m}^2$  respectively. In comparison, the commercial graphite-polymer composite has

the in-plane resistivity of  $8.0 \cdot 10^{-5} \Omega \cdot \text{m}$ , and through-plane resistivity equal to  $0.5 \cdot 10^{-5} \Omega \cdot \text{m}^2$ . The in-plane resistivity of untreated GF equals to  $(2.4 \pm 0.1) \cdot 10^{-5} \Omega \cdot \text{m}$ , and its through-plane resistivity equals to  $(2.5 \pm 1.9) \cdot 10^{-5} \Omega \cdot \text{m}^2$ . Therefore, the reported material obtains less pronounced anisotropy in transport properties and comparable values of resistivity.

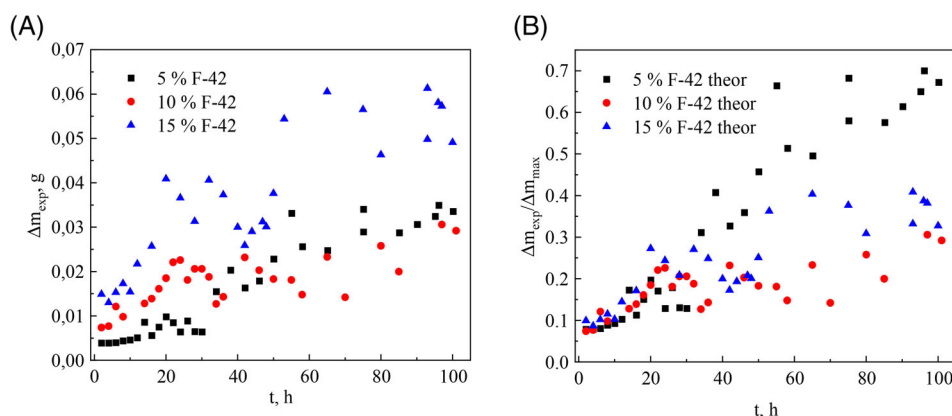
#### 3.3 | Morphology of graphite foil filled with fluoropolymer

Microphotographs of the commercial graphite-polymer composite, untreated GF, and GF modified with F-42 fluoropolymer are presented in Figure 3. A disordered distribution of graphite flakes in a commercial graphite/polymer composite showed a rough surface. At the same time, an untreated GF had a flat, dense surface layer of graphite foil formed by hot pressing of thermally expanded graphite powder. The expanded graphite flakes at the surface layer of the GF are mainly oriented. Even the surface layer of GF has a higher density than the inner layer due to the technological peculiarities; its porosity remains high enough for an effective polymer impregnation. The applied impregnation procedure and subsequent sample processing allow achieving a sufficiently high polymer content ( $\sim 8\%$  of the mass of fluorine, see Figure S8), while its distribution over the surface is uniform (Figure S9). The morphology of the sample did not change noticeably.

#### 3.4 | Determination of electrochemical potential window

We studied materials stability by cyclic voltammetry in acid solution in a standard three-electrode cell (Figures 4 and S4). As graphite (line 1) and GF (line 3) samples have a similar structure, their electrochemical window

**FIGURE 2** Time dependences of the mass gain of the GF samples due to F-42 A, and the portion of the mass gain from the maximum of the impregnated samples B, in solutions of F-42 of different concentrations in acetone [Colour figure can be viewed at [wileyonlinelibrary.com](http://wileyonlinelibrary.com)]



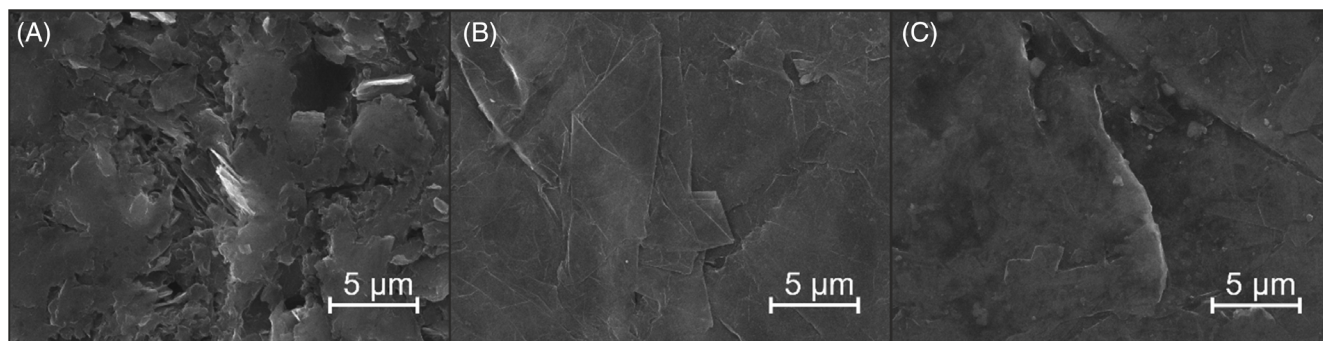


FIGURE 3 Surfaces of A, graphite composite, B, untreated GF, and C, GF impregnated with 1.8% wt. F-42

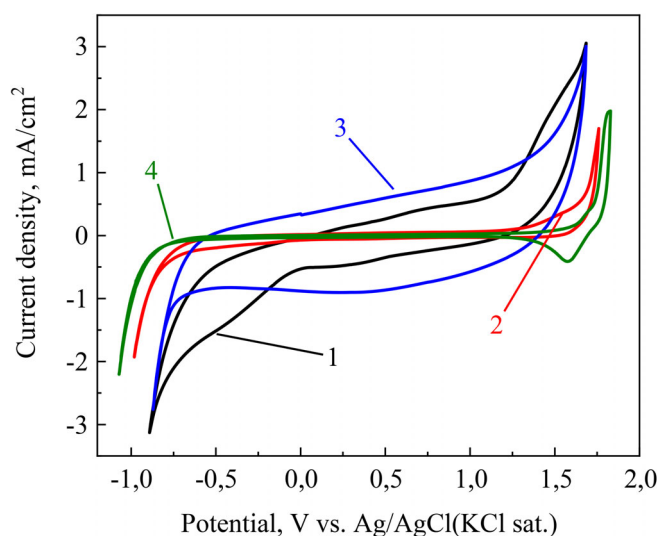


FIGURE 4 Cyclic voltammetry with scan rate 25 mV/s in 1 M  $\text{H}_2\text{SO}_4$  using studied samples as working electrodes: 1 - untreated graphite, 2 - graphite/polymer composite, 3 - untreated GF, and 4 - GF + F-42 (1.8%) [Colour figure can be viewed at [wileyonlinelibrary.com](http://wileyonlinelibrary.com)]

stability almost matched and was  $-0.89$ – $1.68$  V vs Ag/AgCl sat. for graphite and  $-0.87$ – $1.68$  V vs Ag/AgCl sat. for GF.<sup>29</sup> The graphite sample (line 1) had twice lower double-layer capacitance than the graphite foil (8.1 mF and 19.4 mF, respectively).<sup>30</sup> Moreover, graphite-polymer composite (line 2) showed a much lower double-layer capacitance of 1.1 mF and had a broader stability window from  $-0.98$  to 1.73 V vs Ag/AgCl sat. Sample of GF modified with polymer (line 4) shifted hydrogen evolution reaction to  $-1.06$  V vs Ag/AgCl sat., while the positive onset of the current remained around 1.73 V vs Ag/AgCl sat. Further increase of the potential gave rise to quasi-reversible reaction with reduction peak at 1.56 V vs Ag/AgCl sat. Among all samples, the F-42 modified GF (line 4) showed the lowest capacity: its capacity was 2.33 times lower than the capacity of the graphite-polymer composite (line 2). Therefore, it provided a significant increase in the

electrochemical stability window, which was from  $-1.07$  to 1.839 V; thus, the proposed material had improved electrochemical window stability comparing with commercial samples.

### 3.5 | Electrochemical aging in galvanostatic mode

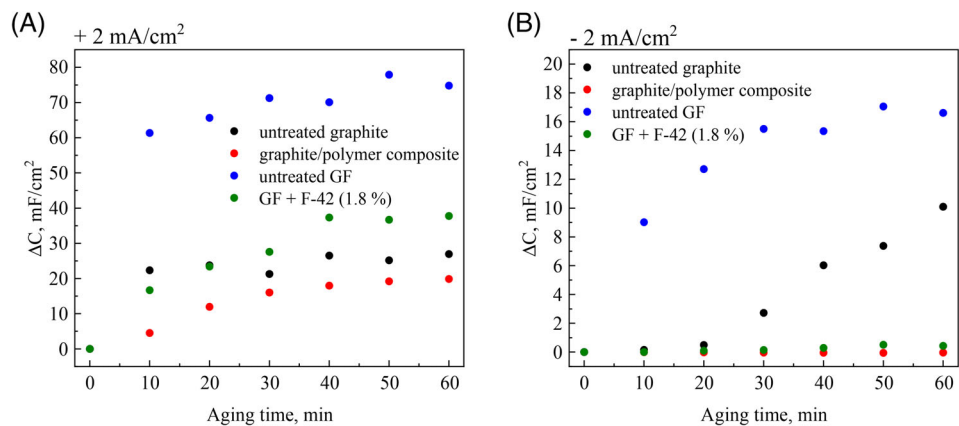
We selected a current density of  $2 \text{ mA/cm}^2$  for accelerated stability tests as this value matches shunting currents in stacks. Positive and negative currents were applied for one hour to imitate charge and discharge conditions in VRFB. The gradual growth of sample capacitance was observed during the test (Figure 5).

Oxidation under positive current (Figure 5A) revealed a drastic increase of capacitance for graphite and pure GF samples, while a lesser effect was observed for graphite/polymer composite and modified GF. The rough surface of graphite and composite did not change significantly at the microscale level during the test, while the flat surface of the GF underwent decomposition with sufficient morphology change (Figure S10). However, modification of GF allowed reducing the degradation rate twice. Such a drastic effect on morphology was attributed to the partial detachment of the surface graphite flakes, which degraded faster due to charge accumulation. A similar tendency was observed for the negative current (Figure 5b): the GF was unstable under these conditions, and modification noticeably stabilized it. The overall intensity of the capacitance change was gradually slower comparing with the positive current, which oxidizes and decomposes carbon.<sup>31</sup>

### 3.6 | Sample testing of various graphite materials in a single cell VRFB

The suitability of the designed material for bipolar plates was proved in a single cell vanadium RFB. Three cells were assembled with different bipolar plates made of

**FIGURE 5** Time dependence of samples capacity change related to initial capacitance on aging time for graphite, graphite-polymer composite, untreated GF, and modified GF under A, 2 mA/cm<sup>2</sup> and B, -2 mA/cm<sup>2</sup> current densities [Colour figure can be viewed at [wileyonlinelibrary.com](http://wileyonlinelibrary.com)]



graphite-polymer composite, untreated GF, and GF modified with F-42 fluoropolymer (1.8 wt%). First, the polarization curve (Figure 6) was measured, and then accelerated galvanostatic cycling was performed at three current densities (200, 150, and 100 mA cm<sup>2</sup>) to evaluate efficiencies of such cells (Figure 7).

Based on the polarization curves of the cells obtained in this work (Figure 6), it is possible to establish the ohmic control of the RFB operation range. The total resistance of the cell, derived from the polarization slope, was lower for the cells based on the GF bipolar plates, comparing to the composite bipolar plate, which was in agreement with previous works.<sup>21,22</sup>

Since the specific surface area of the pressed GF is significantly higher than the specific surface area of graphite (the value varies from 17 to 68 m<sup>2</sup>/g for GF different materials, while for natural graphite this value is about 0.6 m<sup>2</sup>/g<sup>30</sup>), one can assume that the value of the contact resistivity of the GF/porous electrode is slightly less than that for the graphite/electrode contact. As a result, the ohmic resistivity of the cell on the GF was reduced compared to the assembly on the graphite material (Table 1), which led to an increase in the specific power of the RFB from 780 to 860 mW/cm<sup>2</sup>. Although the total ohmic resistivity of the RFB assembly with impregnated bipolar plates was slightly higher than other assemblies in the series, the cell demonstrated a high discharge power density of 843 mW/cm<sup>2</sup>, which was significantly higher than the power of the assembly on a commercial graphite/polymer composite.

Comparison of the charge-discharge curves for the three studied RFB assemblies at a current density of 200 mA/cm<sup>2</sup> showed 4.7% higher capacity utilization for GF-based cells, comparing to the graphite-polymer composite (83.1% and 79.4%, respectively) (Figure 7A). It demonstrated the influence of total ohmic cell resistance on RFB performance: GF-based cells had slightly less resistance than the one of the graphite/polymer cell (0.107 vs 0.111 Ω). The use of bipolar plates impregnated

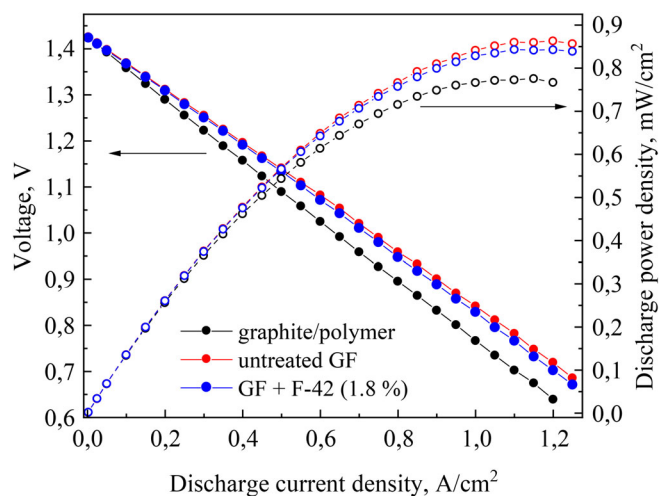


**FIGURE 6** Polarization at 50% SoC and power density profiles for the RFB cells with different bipolar plates [Colour figure can be viewed at [wileyonlinelibrary.com](http://wileyonlinelibrary.com)]

with F-42 (1.8 wt%) slightly increased the total ohmic resistance of the RFB cell compared to the cell on the GF (0.115 vs 0.107 Ω), resulting in 82.1% of the electrolyte utilization.

The cycling performance of three investigated cells at different current densities is presented in Figure 7B. The values of the voltaic efficiency for the assembly on graphite/polymer composite range from 80% to 90%, while this value ranged from 84% to 92% for the cell with untreated GF, which may be due to the lower ohmic resistivity of the cell with GF. However, the coulombic efficiencies for all cells decreased when moving from higher to lower current densities. This effect can be explained by increasing the cycle time at lower current rates, and since the accelerated cycling was carried out sequentially, the degree of imbalance of the electrolytes becomes more pronounced in the transition to subsequent current densities. The coulombic efficiency values for the assembly with GF are less than for the assembly on graphite/

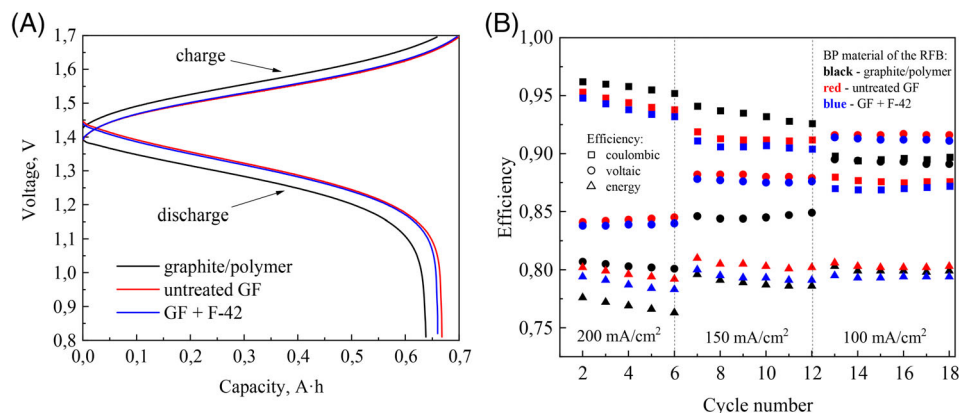


**FIGURE 7** A, Charge-discharge curves for three RFB on the second cycle, current density  $200 \text{ mA/cm}^2$  in the potential range 0.8–1.7 V; B, Relation of the coulombic, voltaic, and energy efficiencies on the cycle number of charge-discharge tests of three RFB cells for different cycling current densities [Colour figure can be viewed at [wileyonlinelibrary.com](http://wileyonlinelibrary.com)]

**TABLE 1** Cell characteristics during polarization and cycling

	Untreated GF	Impregnated GF by F-42	Graphite-polymer composite
Peak current density, $A/cm^2$	1.2	1.2	1.15
Peak power density, $mW/cm^2$	862	843	776
Cell resistance from polarization curve, $\Omega$	0.148	0.151	0.164
High-frequency cell resistance at 100% SoC before cycling, $\Omega$	0.114	0.120	0.118
High-frequency cell resistance at 50% SoC before cycling, $\Omega$	0.107	0.115	0.11
High-frequency cell resistance at 50% SoC after cycling, $\Omega$	0.112	0.120	0.112

polymer composite: from 88% to 95% for GF compared to 90% to 96% for graphite/polymer composite due to a greater degree of electrolyte utilization. In addition, the electrolyte volume can be permanently lost due to the absorption into the pores of the GF. Despite the low values of the coulombic efficiency of the GF-based cells, the energy efficiencies were higher than that of the graphite/polymer composite assembly (79%–81% vs 76%–80%). Due to the increase in the ohmic resistivity of the cell with bipolar plates modified by F-42, in comparison with the resistivity of the cell on the untreated GF, the coulombic efficiency decreased slightly in comparison with the GF (no more than 1%). The values of the voltaic efficiency also decreased slightly, but they are still significantly higher than the voltaic efficiency of the graphite/polymer cell (higher by 2%–3%). As a result, energy efficiency values ranging from 78.3% to 79.4% were obtained.

## 4 | CONCLUSIONS

In this work, the possibility of creating an electrochemically stable material based on an available and easy-to-process graphite foil was demonstrated. The electrical conductivity characteristics after the impregnation of the

GF with a fluoropolymer following by pressing the material during hot pressing decreased insignificantly compared to the compacted untreated GF. This factor is the main advantage of this graphite-polymer composites production method.

Modification of the GF by fluoropolymers was allowed to significantly increase the most important characteristic of the materials for RFB bipolar plates and extending by 12.6% electrochemical potential window comparing with the untreated GF. A significant increase of electrochemical potential window due to the compaction of the pores of the GF fluoropolymers also made it possible to significantly increase the electrochemical stability of such material under conditions simulating the effect of shunt currents occurring in the RFB stacks.

Unique morphology of the proposed material results in the lower contact resistance of the GF/electrode in comparison with the graphite/electrode contact due to the significant difference in the surface areas of these materials. In this paper, bipolar plates made of GF modified with F-42 were tested in a single cell of vanadium RFB in comparison with samples of untreated GF and commercial graphite/polymer composite. It was demonstrated that the method of volumetric filling of the GF pores allows maintaining a low value of the contact

resistance of the bipolar plate, which affects the power density of the RFB cell. The power density of fluoropolymer-modified GF cell only slightly decreased compared to the cell on the untreated GF (843 vs 862 mW/cm<sup>2</sup>), but this value was still significantly higher than the power density of the battery on commercial graphite/polymer composite (843 vs 776 mW/cm<sup>2</sup>). The cell demonstrated a high energy efficiency values of 78.3%–79.4% during cycling at 200 mA/cm<sup>2</sup>, which is slightly higher than the results obtained on the cell with a commercial graphite/polymer composite -76.3%–77.6% (under 200 mA/cm<sup>2</sup>), while the electrolyte utilization in the first case is about 2.7% higher.

High energy efficiency and power density of the cell based on the modified GF, combined with its improved electrochemical stability allowing us to conclude that such material can be successfully used as the bipolar plates in vanadium RFB.

## DATA AVAILABILITY STATEMENT

Data openly available in a public repository that issues datasets with DOIs.

## ORCID

Andrey Usenko  <https://orcid.org/0000-0002-4119-5292>

## REFERENCES

- Petrov MM, Modestov AD, Konev DV, et al. Redox flow batteries: importance in modern electrical energy industry and comparative characteristics of the main types. *Russ Chem Rev.* 2021;90(6):677-702. <https://doi.org/10.1070/RCR4987>
- Schlachtberger DP, Brown T, Schäfer M, Schramm S, Greiner M. Cost optimal scenarios of a future highly renewable European electricity system: exploring the influence of weather data, cost parameters and policy constraints. *Energy.* 2018;163:100-114. <https://doi.org/10.1016/j.energy.2018.08.070>
- Antunes RA, De Oliveira MCL, Ett G, Ett V. Carbon materials in composite bipolar plates for polymer electrolyte membrane fuel cells: a review of the main challenges to improve electrical performance. *J Power Sources.* 2011;196:2945-2961. <https://doi.org/10.1016/j.jpowsour.2010.12.041>
- Minke C, Kunz U, Turek T. Techno-economic assessment of novel vanadium redox flow batteries with large-area cells. *J Power Sources.* 2017;361:105-114. <https://doi.org/10.1016/j.jpowsour.2017.06.066>
- Hermann A, Chaudhuri T, Spagnol P. Bipolar plates for PEM fuel cells: a review. *Int J Hydrogen Energy.* 2005;30:1297-1302. <https://doi.org/10.1016/j.ijhydene.2005.04.016>
- Antunes RA, Oliveira MCL, Ett G, Ett V. Corrosion of metal bipolar plates for PEM fuel cells: a review. *Int J Hydrogen Energy.* 2010;35:3632-3647. <https://doi.org/10.1016/j.ijhydene.2010.01.059>
- Li W, Jing S, Wang S, Wang C, Xie X. Experimental investigation of expanded graphite/phenolic resin composite bipolar plate. *Int J Hydrogen Energy.* 2016;41(36):16240-16246. <https://doi.org/10.1016/j.ijhydene.2016.05.253>
- Caglar B, Fischer P, Kauranen P, Karttunen M, Elsner P. Development of carbon nanotube and graphite filled polyphenylene sulfide based bipolar plates for all-vanadium redox flow batteries. *J Power Sources.* 2014;256:88-95. <https://doi.org/10.1016/j.jpowsour.2014.01.060>
- Satola B, Kirchner CN, Komsysiaka L, Wittstock G. Chemical stability of graphite-polypropylene bipolar plates for the vanadium redox flow battery at resting state. *J Electrochem Soc.* 2016;163(10):A2318-A2325. <https://doi.org/10.1149/2.0841610jes>
- Wang M, KDo W, Kim DK, Lou T, Huang Z. Study on impregnation of polytetrafluoroethylene in graphite for use as fuel cell collector. *Int J Hydrogen Energy.* 2005;30(9):1027-1030. <https://doi.org/10.1016/j.ijhydene.2004.12.013>
- Du C, Ming P, Hou M, et al. The preparation technique optimization of epoxy/compressed expanded graphite composite bipolar plates for proton exchange membrane fuel cells. *J Power Sources.* 2010;195(16):5312-5319. <https://doi.org/10.1016/j.jpowsour.2010.03.005>
- Du C, Ming P, Hou M, et al. Preparation and properties of thin epoxy/compressed expanded graphite composite bipolar plates for proton exchange membrane fuel cells. *J Power Sources.* 2010;195(3):794-800. <https://doi.org/10.1016/j.jpowsour.2009.08.033>
- Liao W, Zhang Y, Zhou X, et al. Low-carbon-content composite bipolar plates: a novel design and its performance in vanadium redox flow batteries. *ChemistrySelect.* 2019;4(8):2421-2427. <https://doi.org/10.1002/slct.201900521>
- Kim S, Yoon Y, Narejo GM, Jung M, Kim KJ, Kim YJ. Flexible graphite bipolar plates for vanadium redox flow batteries. *Int J Energy Res.* 2021;45:11098-11108. <https://doi.org/10.1002/er.6592>
- Kim KH, Kim BG, Lee DG. Development of carbon composite bipolar plate (BP) for vanadium redox flow battery (VRFB). *Compos. Struct.* 2014;109(1):253-259. <https://doi.org/10.1016/j.compstruct.2013.11.002>
- Nam S, Lee D, Lee DG, Kim J. Nano carbon/fluoroelastomer composite bipolar plate for a vanadium redox flow battery (VRFB). *Compos. Struct.* 2017;159:220-227. <https://doi.org/10.1016/j.compstruct.2016.09.063>
- Ruban E, Stepashkin A, Gvozdk N, et al. Carbonized elastomer composite filled with hybrid carbon fillers for vanadium redox flow battery bipolar plates. *Mater Today Commun.* 2020;26:101967. <https://doi.org/10.1016/j.mtcomm.2020.101967>
- Liu Z, Wang B, Yu L. Preparation and surface modification of PVDF-carbon felt composite bipolar plates for vanadium flow battery. *J Energy Chem.* 2018;27(5):1369-1375. <https://doi.org/10.1016/j.jechem.2018.04.010>
- Satola B, Komsysiaka L, Wittstock G. Bulk aging of graphite-polypropylene current collectors induced by electrochemical cycling in the positive electrolyte of vanadium redox flow batteries. *J. Electrochem. Soc.* 2017;164(12):A2566-A2572. <https://doi.org/10.1149/2.1261712jes>
- Rzeczkowski P, Krause B, Pötschke P. Characterization of highly filled PP/graphite composites for adhesive joining in fuel cell applications. *Polymers.* 2019;11(3):462. <https://doi.org/10.3390/polym11030462>
- Pichugov RD, Konev DV, Petrov MM, et al. Electrolyte flow field variation: a cell for testing and optimization of membrane electrode assembly for vanadium redox flow batteries.

- ChemPlusChem*. 2020;85(8):1919-1927. <https://doi.org/10.1002/cplu.202000519>
22. Petrov MM, Pichugov RD, Loktionov PA, et al. Test cell for membrane electrode assembly of the vanadium redox flow battery. *Dokl Phys Chem*. 2020;491(1):19-23. <https://doi.org/10.1134/S0012501620030021>
23. Glazkov AT, Antipov AE, Konev DV, et al. Dataset of a vanadium redox flow battery 10 membrane-electrode assembly stack. *Data Brief*. 2020;31:105840. <https://doi.org/10.1016/j.dib.2020.105840>
24. SGL Carbon Sigraflex Datasheet. June 21, 2021. <https://www.sglcarbon.com/pdf/SGL-Datasheet-SIGRAFLEX-APX2-APX-E-C-Z-Foil-EN.pdf/>.
25. Unihimtek company. June 2, 2021. <https://www.graflex.ru/#>.
26. Yin C, Guo S, Fang H, Liu J, Li Y, Tang H. Numerical and experimental studies of stack shunt current for vanadium redox flow battery. *Appl Energy*. 2015;151:237-248. <https://doi.org/10.1016/j.apenergy.2015.04.080>
27. Darling RM, Shiau H-S, Weber AZ, Perry ML. The relationship between shunt currents and edge corrosion in flow batteries. *J Electrochem Soc*. 2017;164:E3081-E3091. <https://doi.org/10.1149/2.0081711jes>
28. Pilinski N, Käding C, Dushina A, Hickmann T, Dyck A, Wagner P. Investigation of corrosion methods for bipolar plates for high temperature polymer electrolyte membrane fuel cell application. *Energies*. 2020;13(1):235. <https://doi.org/10.3390/en13010235>
29. Yakovlev AV, Finaenov AI, Zabud'kov SL, Yakovleva EV. Thermally expanded graphite: synthesis, properties, and prospects for use. *Russ J Appl Chem*. 2006;79(11):1741-1751. <https://doi.org/10.1134/S1070427206110012>
30. Shornikova ON, Kogan EV, Sorokina NE, Avdeev VV. The specific surface area and porous structure of graphite materials. *Russ. J. Phys. Chem*. 2009;83(6):1022-1025. <https://doi.org/10.1134/S0036024409060260>
31. Gallagher KG, Fuller TF. Kinetic model of the electrochemical oxidation of graphitic carbon in acidic environments. *Phys Chem Chem Phys*. 2009;11(48):11557-11567. <https://doi.org/10.1039/b915478g>

## SUPPORTING INFORMATION

Additional supporting information may be found online in the Supporting Information section at the end of this article.

**How to cite this article:** Loktionov P, Kartashova N, Konev D, et al. Fluoropolymer impregnated graphite foil as a bipolar plates of vanadium flow battery. *Int J Energy Res*. 2021;1-10. <https://doi.org/10.1002/er.7088>

### 3.4 Conclusions from the Chapter 3

Two materials were examined as bipolar plates in vanadium RFB. A set of special techniques was proposed for studying the stability issues of materials. Specially developed AST in vanadium (V) solution was used for the chemical stability assessment of materials. Additionally, ECSA determination measurements were adopted for the electrochemical stability tests as ECSA represents the area accessible to the solution due to open pores. Both methods derive their unique characteristic values for the stability assessment, which can be used to compare different materials. The samples of commercial bipolar plate materials were tested in the same conditions as a reference. As a result, materials were comprehensively analyzed before the RFB testing.

The papers proposed two different methods for creating the impermeable well-conducting material. A comparison of two technologies revealed that reduction of porosity for well-conducting material is a better strategy than carbonization of amorphous materials with carbon fillers as conductive additives. The requirement for high conductivity is crucial as insufficient conductivity leads to high contact resistance between electrodes and current collectors, and, hence, to poor battery performance.

Based on materials tests we can select the following nominal parameters for the bipolar plate materials. The methods are listed in the importance and time costs order. The consistent selection of materials according to the list of requirements will allow rapid screening and optimization of materials: 1) electric conductivity  $> 200 \text{ S cm}^{-1}$ ; 2) capacitance derived from CV test  $< 10 \text{ mF cm}^{-2}$ ; 3) elastic modulus  $> 13 \text{ MPa}$  and an

ultimate compressive strength  $> 9$  MPa; 4) potential window is broader than operation RFB voltage cutoffs; 5) chemical stability test in  $V^{5+}$  with degradation rate  $< 0.25$  % per day.

## **Chapter 4. Suspensions investigation as redox-active compounds for RFB**

### **4.1 Overview of the Chapter 4**

Despite unlimited opportunities in organic redox molecule design, highly concentrated solutions usually rapidly degrade and have high viscosities. Immobilization of organic molecules in the solid matrix was recognized as one of the approaches to overcome this limitation. The second approach, called solid-booster, implies the addition of solid particles able to store the energy with the same potential as soluble species (mediators). Overall, these materials are nanoparticles in aqueous media, for which redox reaction is going either as a spontaneous collision with an electrode in the cell or reacts as a homogeneous reaction without the electrode surface in the tank. Theoretical volumetric capacity of such systems significantly exceeds standard values of soluble species. However, both cases require understating of limiting reaction stages for further system development. Here, we propose several methods for sensing electrochemical responses for such systems. We studied two materials, related to different approaches, and elucidated a similar pattern related to the problem of incomplete capacity utilization.

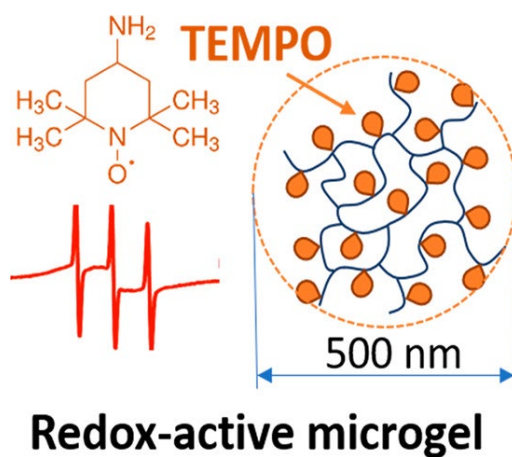
Firstly, we investigated the electrochemical properties of the material made of polymers mixture with redox-active groups in the form of sub-micron size globules. TEMPO molecules were used as a redox-active center.

Secondly, we studied the delithiation reaction of  $\text{LiMn}_2\text{O}_4$  as a model material for solid boosters. We used a single particle collision experiment to sense the behavior of suspension without constant contact with the electrode.

As a result, we determine the maximum capacity utilization for each material and proposed that low local conductivity causes localization of redox reaction on part of the particle, which is close to the electrode. Therefore, to maximize the capacity for such a class of redox-active species tuning electric conductivity is needed.

## 4.2 Redox-Active Aqueous Microgels for Energy Storage Applications

My contribution: Methodology, Investigation (electrochemical characterization),  
Visualization, Writing – Part of original draft



Reprinted with permission from [173]. Copyright 2022 American Chemical Society

# Redox-Active Aqueous Microgels for Energy Storage Applications

Elena Yu. Kozhunova,\* Natalia A. Gvozdik, Mikhail V. Motyakin, Oxana V. Vyshivannaya, Keith J. Stevenson, Daniil M. Itkis, and Alexander V. Chertovich



Cite This: *J. Phys. Chem. Lett.* 2020, 11, 10561–10565



Read Online

ACCESS |



Metrics & More

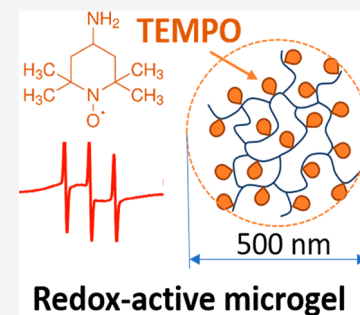


Article Recommendations



Supporting Information

**ABSTRACT:** The search for new environmental-friendly materials for energy storage is ongoing. In the presented paper, we propose polymer microgels as a new class of redox-active colloids (RACs). The microgel stable colloids are perspective low-viscosity fluids for advanced flow batteries with high volumetric energy density. In this research, we describe the procedure for the anchoring of 4-amino-2,2,6,6-tetramethylpiperidine-1-oxyl (4-amino-TEMPO) redox-active sites to the polymeric chains of water-soluble microgels based on poly(*N*-isopropylacrylamide)–poly(acrylic acid) interpenetrating networks. Using cyclic voltammetry and EPR spectroscopy, we show that ca. 14% of 4-amino-TEMPO groups retain electroactive properties and demonstrate the reversible redox response. It allows achieving a stable capacity of 2.5 mAh/g, enabling the low-viscous catholyte with a capacity of more than 100 mAh/L.



The scalability and cost-efficiency of redox flow batteries mark them as an attractive choice for large stationary energy storage systems. The trend of switching from typical inorganic redox couples (e.g., vanadium- or zinc-based) to advanced organic-based or hybrid semisolid ones is now observed in the field.<sup>1–3</sup> The interest in organic redox-active molecules rapidly increases.<sup>4–6</sup> Using such species instead of expensive and often toxic metal-based systems can enable the development of cheaper, eco-friendly, and safe redox flow systems.

Unfortunately, the involvement of low-molecular redox-active components forces the use of expensive ion-exchange membranes to prevent the battery self-discharge due to the species crossover. High-molecular systems, i.e., polymers, nowadays draw increasing attention for energy storage applications.<sup>7,8</sup> Employment of polymers with anchored redox-active groups<sup>9,10</sup> in redox-flow batteries simplifies the membrane's requirements and enables using the dialysis membranes with submicron- or even microsized pores. The main drawback of such an approach is the polymeric solution's high viscosity, even at low concentrations. Macromolecular aggregates, such as block copolymer micelles,<sup>11,12</sup> can tackle the problem; however, their energy efficiency remains unclear. The viologen-based RACs for flow batteries comprising redox-active polymer spheres were also presented.<sup>13</sup> Moreover, most of the reported systems were based on organic solvents, while aqueous-based electrolytes would be preferable due to their availability, stability, and high conductivity.<sup>14</sup>

Here, we suggest an approach combining the strength of colloids, micelles, and linear redox-active polymers. We propose using weakly cross-linked submicron-sized polymer meshes, called microgels, schematically shown in Figure 1. Such systems possess low viscosity typical for micellar or colloidal solutions, while the concentration of redox-active

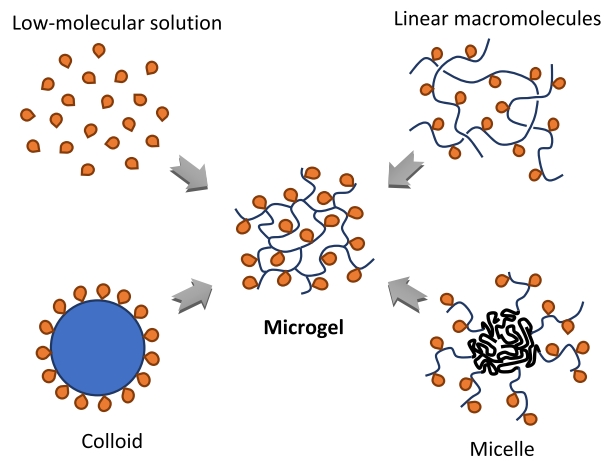


**Figure 1.** Structure of various redox-active systems. Orange drops represent the redox-active sites, and black lines represent the polymer main chains. Microgels simultaneously incorporate features from all other systems: high volume concentration of redox-active groups, solution stability, high molecular mass, and low viscosity.

groups can be as high as that for linear polymer-based systems. The internal structure of a microgel can be represented as a three-dimensional cross-linked polymeric swelled mesh. The microgels form stable suspensions of the microparticles with a

**Received:** October 19, 2020

**Accepted:** November 25, 2020

**Published:** December 9, 2020



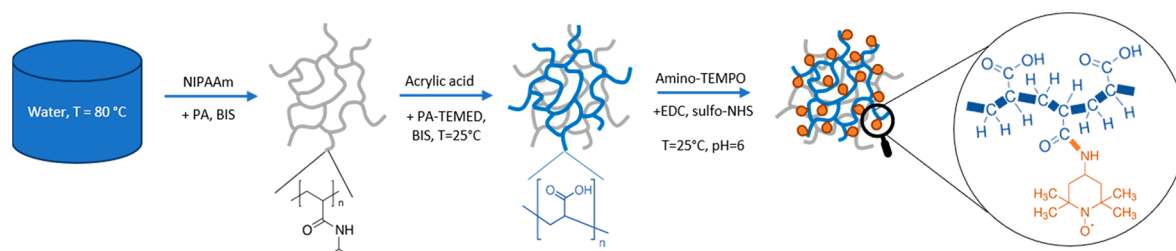


**Figure 2.** Scheme of the synthesis of redox-active IPN microgels.

narrow particle size distribution and can undergo a conformation change in response to the environmental variation. The synthesis of microgels is relatively easy and scalable.<sup>15,16</sup>

Very recently, the redox-active supramolecular microgels on the base of poly(hydroquinone) were reported,<sup>17,18</sup> although electrochemical characterization was not done, and energy storage application was not proposed for such objects yet. In the present study, we characterize the electrochemical response of redox-active microgels and prove the possibility of using the 4-amino-TEMPO-modified samples comprising poly-*N*-isopropylacrylamide and poly(acrylic acid) as active materials for electrochemical energy storage.

Interpenetrating network (IPN) microgels were chosen as polymeric carriers of redox-active TEMPO groups. Each IPN microgel particle consisted of two interpenetrating networks—the first network was based on poly-*N*-isopropylacrylamide (PNIPAAm), and the second network was based on poly(acrylic acid) (PAA). The reasons for such an architecture were the following. There is a robust procedure that allows modification of PAA chains with TEMPO groups in aqueous media;<sup>2,19</sup> thus, a microgel candidate should have a high content of PAA (i). For convenience and easy reproduction on a larger scale, microgels-carriers' synthesis should proceed in water and be governed by self-assembly mechanisms such as precipitation polymerization, which means using PNIPAAm-like components (ii). P(NIPAA-AA) copolymer microgels could be easily synthesized, but the achievable acrylic acid concentration in these particles is relatively low—about 10–15% of the total mass. At the same time, template-like synthesis of the PAA network inside the PNIPAAm microgel network—leading to the formation of IPN structure (see Figure 2)—allows increasing the PAA content up to 30–35%.<sup>20</sup> Among other benefits of PNIPAAm-PAA IPN microgel is the increased stability of colloid solution under different conditions and thermoresponsive qualities, allowing for further particle morphology adjustment.<sup>21</sup> That said, for our research, we decided to use PNIPAAm-PAA IPN microgels. The detailed synthetic procedure and characterization methods can be found in the Supporting Information. A single microgel particle's molecular weight could be roughly estimated as 100 M by combining static light scattering and calculation based on the particle diameter and density.

For attaining redox properties, the PNIPAAm-PAA IPN microgels were modified by 4-amino-TEMPO using an EDC-mediated process (last panel in Figure 2). As a reference for further electrochemical studies, linear PAA with two different molecular weights ( $M_w$   $400 \times 10^3$  and  $3 \times 10^6$  Da) was modified with TEMPO by the same protocol. The procedure allowed us to anchor the amino groups of 4-amino-TEMPO to carboxyl groups of PAA, forming amide groups (see the Supporting Information for FTIR spectra, Figure S1, and

commentary). The degree of substitution of PAA –OH groups after modification with amino-TEMPO was evaluated by pH-metric titration and found to be ca. 21%; see Figure S2 and the commentary in the Supporting Information. The modification of IPN microgel aqueous dispersions proceeded at room temperature in the air; the solution pH was kept at 6 during the whole process. After the dialysis, the resulting solution appeared semitransparent with a yellowish hue, typical for TEMPO-bearing moieties. The dispersion was found to be stable for at least six months under standard conditions.

Dynamic light scattering studies of the obtained TEMPO-IPN microgels showed the particles with a monodisperse size distribution with a mean hydrodynamic radius  $R_h$  equal to 270 nm, which was smaller than the mean  $R_h$  of non-modified IPN microgels ( $R_h = 370$  nm) measured under the same pH and temperature conditions ( $T = 23$  °C and pH 5.5) (Figure 3a). These results are supported by TEM microscopy; see Figure S3. That signified the changes in the particle structure attributed to the addition of TEMPO groups.

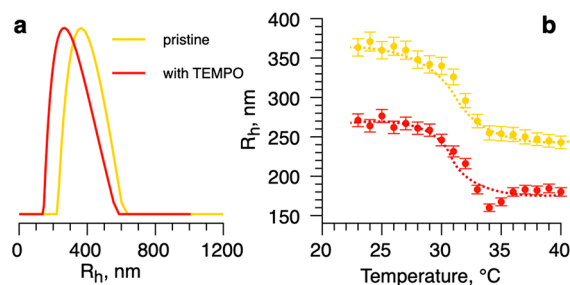


**Figure 3.** (a) Hydrodynamic radius distribution and (b) dependence of the hydrodynamic radius  $R_h$  on temperature for IPN microgel and TEMPO-IPN microgel in water (pH 5.5). The scattering angle is 90°.

The  $R_g/R_h$  value of pristine and TEMPO-modified microgels was found to be 0.5 at room temperature, which corresponds to the “soft sphere” structure with a denser core and a “fuzzy” particle surface with weakly cross-linked or dangling polymer chains.<sup>21</sup> It should be noted that the modified IPN microgels retained their thermosensitivity (Figure 3b), which could be further used for the enhancement of the solution viscosity. The  $R_g/R_h$  value was close to 0.78 (the theoretical values for a hard sphere) at high temperature, indicating a dense structure due to the collapse of the PNIPAAm subchains.

The concentration of active radicals in the samples was estimated using electron paramagnetic resonance (EPR) spectroscopy. The EPR spectra of TEMPO-modified PAA polymers are shown in Figure 4a. They revealed a typical motionally narrowed triplet indicating a fast oscillation ( $\sim 10^{11}$  Hz) of radical groups in solution.<sup>22</sup> The concentrations of the active radical groups in both TEMPO-PAA polymers were

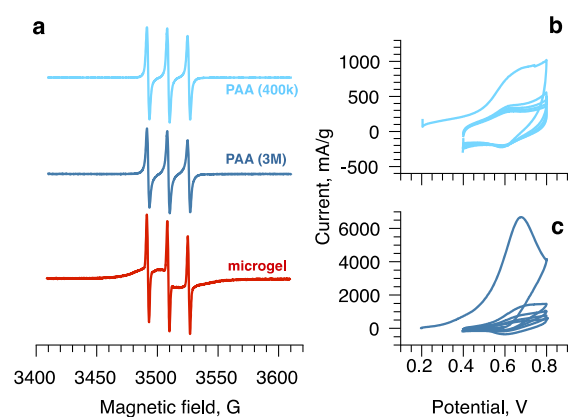


**Figure 4.** EPR spectra of the TEMPO-modified PAA polymers and IPN microgel at 293 K (a) and cyclic voltammograms of TEMPO-modified linear PAA with  $M_w$   $400 \times 10^3$  (b) and  $3 \times 10^6$  (c) Da.

found to be approximately the same:  $2.1 \times 10^{-3}$  M in PAA with  $M_w$   $400 \times 10^3$  and  $1.9 \times 10^{-3}$  M in PAA with  $M_w$   $3 \times 10^6$ .

For the TEMPO-modified IPN microgel EPR spectrum showed the presence of two different components. It should be noted that the non-modified IPN microgels had no features in the EPR spectrum, so we attributed the observed signals of the modified samples to TEMPO groups. The first component is a motionally narrowed triplet (the same as in TEMPO-PAA), typical for fast oscillating radical groups. The second consists of a broad unresolved line and can be assigned to the TEMPO radicals located in the polymer region with restricted molecular motion. A similar broadening of EPR spectra caused by the motion restriction of the nitroxide radicals was observed, for instance, in poly(*N*-isopropylacrylamide) gel and PAA polymer.<sup>19,23</sup> Thereby, the EPR data pointed to the existence of at least two different locations of TEMPO groups in IPN microgel: inside the network structure and attached to loosely cross-linked corona. Double integration of the spectrum indicated that the concentration of free oscillating TEMPO groups was approximately  $6.3 \times 10^{-5}$  M, while the total concentration of TEMPO groups in IPN microgel was  $1.2 \times 10^{-3}$  M.

Cyclic voltammetry confirmed the redox activity of the TEMPO-modified polymers and microgels, which were mixed with carbon conductive additive and drop-casted onto the glassy carbon electrode. Both TEMPO-modified linear PAA polymers were found to be redox-active, showing a strong oxidation peak at ca. 0.56 V vs Ag/AgCl (see Figure 4b,c) in the first cycle. However, the cathodic current at the reverse cycle was much lower than anodic revealing poor reversibility.

Further cycling led to the rapid peak current fade, especially for a longer chain PAA. Such a drastic fade might be attributed to the partial blocking of the interaction of oxoammonium cation by near-sited acidic groups of linear PAA.<sup>24</sup>

In contrast, TEMPO-modified microgels demonstrated a reversible response; however, the significant irreversible oxidative current was registered during the first cycle. The cyclic voltammogram of such a sample is plotted in Figure 5a. Although the oxidation current in the first cycle was ca. 70% higher, the voltamperometric response quickly stabilized and demonstrated the reversible behavior for further cycles. The gravimetric capacity estimated from the galvanostatic voltage profiles was ca. 2.5 mA/g with the Coulombic efficiency over 90% (Figure 5b). The redox response stabilization might be attributed to the microgel structure, which hindered PAA molecular motion, preventing the recombination of the oxoammonium cation and acidic group. Besides, the pronounced capacitance for the samples detected at different scan rates indicated the lack of electrical contact for the bulk of the material, which is a typical problem for such systems.<sup>25</sup> Further increase of capacity can be achieved by tuning the microgel architecture with a conductive filler. Summarizing the discussed findings, the immobilization of PAA inside the microgels provided the stable redox response corresponding to the activity of about 14% of the anchored 4-amino-TEMPO groups (the total concentration was estimated as 1.2 mM by EPR).

In addition to a stable electrochemical response, the microgel sample demonstrated lower viscosity compared to reference linear polymers, as can be expected. The viscosity measurements, which were performed by measuring the quartz crystal resonant frequency shift in the solutions, revealed that 1.2 cP solution could contain about 10 g/L of 400k PAA, 2.5 g/L of longer 3 M linear PAA, or about 40 g/L of cross-linked spherical IPN microgel particles. Therefore, proposed materials are potential candidates for the low-viscosity polymer catholyte for aqueous flow batteries.

To summarize, we proposed a new class of RACs—redox-active microgels—as a prospective candidate for the next generation of flow batteries. For the first time, we modified the PNIPAAm-PAA polymer microgel particles with redox-active 4-amino-TEMPO groups. The described synthetic approach was easily scalable and undemanding. The developed microgels showed the redox response at 0.56 V vs Ag/AgCl with 2.5 mAh/g capacity. In contrast to linear polymers modified with 4-amino-TEMPO groups, the synthesized microgels showed a stable redox response in cyclic voltammetry experiments. It was found that 14% of TEMPO sites from the total

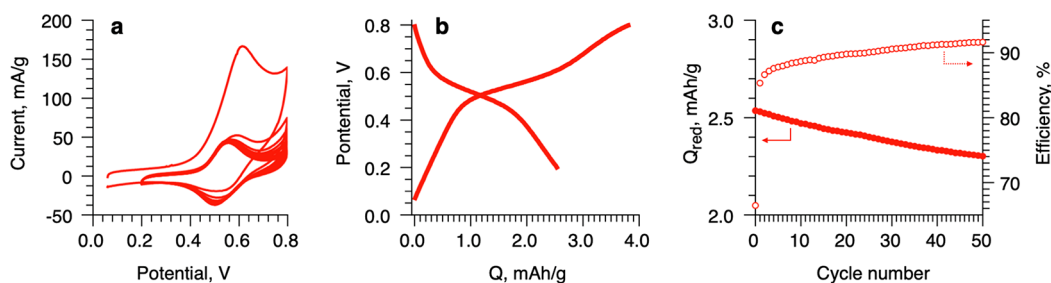


**Figure 5.** Electrochemical characterization of redox-active TEMPO-IPN microgels. (a) Cyclic voltammogram with 10 mV/s scan rate. (b) Charge/discharge profile at 50 mA/g current density. (c) Dependence of the specific capacity and Coulombic efficiency estimated from galvanostatic cycling on the cycle number.

concentration of the anchored redox-active groups contribute to electrochemical reactions.

Further tuning of the material with conductive species can significantly improve the capacity. Moreover, the proposed redox-active microgels can form low-viscosity aqueous solutions at even high concentrations. Thus, the proposed material is a promising candidate for the advanced flow battery electrolytes. Several other applications, such as redox mediators and nanoreactor systems, might also benefit from using the redox-active microgel particles. The redox response sensitivity to pH, temperature, and other factors and testing the solutions in redox-flow prototypes require further research and are out of this short Letter's scope.

## ■ ASSOCIATED CONTENT

### Supporting Information

The Supporting Information is available free of charge at <https://pubs.acs.org/doi/10.1021/acs.jpcllett.0c03164>.

The list of the used materials, detailed synthetic procedure, and characterization methods (PDF)

## ■ AUTHOR INFORMATION

### Corresponding Author

Elena Yu. Kozhunova – Department of Physics, M. V. Lomonosov Moscow State University, 119991 Moscow, Russian Federation; [orcid.org/0000-0003-2062-004X](https://orcid.org/0000-0003-2062-004X); Email: [kozhunova@poly.phys.msu.ru](mailto:kozhunova@poly.phys.msu.ru)

### Authors

Natalia A. Gvozdik – Center for Energy Science and Technology, Skolkovo Institute of Science and Technology, 121205 Moscow, Russia

Mikhail V. Motyakin – N.N. Semenov Federal Research Center for Chemical Physics, 119991 Moscow, Russia; Emanuel Institute of Biochemical Physics, Russian Academy of Sciences, Moscow 119334, Russia

Oxana V. Vyshivannaya – A.N. Nesmeyanov Institute of Organoelement Compounds of Russian Academy of Sciences, 119991 Moscow, Russia

Keith J. Stevenson – Center for Energy Science and Technology, Skolkovo Institute of Science and Technology, 121205 Moscow, Russia; [orcid.org/0000-0002-1082-2871](https://orcid.org/0000-0002-1082-2871)

Daniil M. Itkis – N.N. Semenov Federal Research Center for Chemical Physics, 119991 Moscow, Russia; Department of Chemistry, M. V. Lomonosov Moscow State University, 119991 Moscow, Russian Federation; [orcid.org/0000-0002-6363-6669](https://orcid.org/0000-0002-6363-6669)

Alexander V. Chertovich – Department of Physics, M. V. Lomonosov Moscow State University, 119991 Moscow, Russian Federation; N.N. Semenov Federal Research Center for Chemical Physics, 119991 Moscow, Russia

Complete contact information is available at:

<https://pubs.acs.org/doi/10.1021/acs.jpcllett.0c03164>

### Notes

The authors declare no competing financial interest.

## ■ ACKNOWLEDGMENTS

This work was supported by RFBR (No. 19-33-70052) and the Ministry of Science and Higher Education of the Russian Federation. The authors thank the senior researcher of the

Faculty of Physics of MSU, Dr. Elena P. Kharitonova, for FTIR measurements.

## ■ REFERENCES

- (1) Gentil, S.; Reynard, D.; Girault, H. H. Aqueous Organic and Redox-Mediated Redox Flow Batteries: A Review. *Curr. Opin. Electrochem.* **2020**, *21*, 7–13.
- (2) Chen, R.; Bresser, D.; Saraf, M.; Gerlach, P.; Balducci, A.; Kunz, S.; Schröder, D.; Passerini, S.; Chen, J. A Comparative Review of Electrolytes for Organic-Material-Based Energy-Storage Devices Employing Solid Electrodes and Redox Fluids. *ChemSusChem* **2020**, *13* (9), 2205–2219.
- (3) Zhong, F.; Yang, M.; Ding, M.; Jia, C. Organic Electroactive Molecule-Based Electrolytes for Redox Flow Batteries: Status and Challenges of Molecular Design. *Front. Chem.* **2020**, *8*, 451.
- (4) Winsberg, J.; Stolze, C.; Muench, S.; Liedl, F.; Hager, M. D.; Schubert, U. S. TEMPO/Phenazine Combi-Molecule: A Redox-Active Material for Symmetric Aqueous Redox-Flow Batteries. *ACS Energy Lett.* **2016**, *1* (5), 976–980.
- (5) Janoschka, T.; Martin, N.; Hager, M. D.; Schubert, U. S. An Aqueous Redox-Flow Battery with High Capacity and Power: The TEMPTMA/MV System. *Angew. Chem., Int. Ed.* **2016**, *55* (46), 14427–14430.
- (6) Kim, J.; Kim, J. H.; Ariga, K. Redox-Active Polymers for Energy Storage Nanoarchitectonics. *Joule* **2017**, *1* (4), 739–768.
- (7) Wu, Z.; Xie, J.; Xu, Z. J.; Zhang, S.; Zhang, Q. Recent Progress in Metal-Organic Polymers as Promising Electrodes for Lithium/Sodium Rechargeable Batteries. *J. Mater. Chem. A* **2019**, *7* (9), 4259–4290.
- (8) Mohd Abdah, M. A. A.; Azman, N. H. N.; Kulandaivalu, S.; Sulaiman, Y. Review of the Use of Transition-Metal-Oxide and Conducting Polymer-Based Fibres for High-Performance Supercapacitors. *Mater. Des.* **2020**, *186*, 108199.
- (9) Sukegawa, T.; Masuko, I.; Oyaizu, K.; Nishide, H. Expanding the Dimensionality of Polymers Populated with Organic Robust Radicals toward Flow Cell Application: Synthesis of TEMPO-Crowded Bottlebrush Polymers Using Anionic Polymerization and ROMP. *Macromolecules* **2014**, *47* (24), 8611–8617.
- (10) Janoschka, T.; Martin, N.; Martin, U.; Friebe, C.; Morgenstern, S.; Hiller, H.; Hager, M. D.; Schubert, U. S. An Aqueous, Polymer-Based Redox-Flow Battery Using Non-Corrosive, Safe, and Low-Cost Materials. *Nature* **2015**, *527* (7576), 78–81.
- (11) Winsberg, J.; Muench, S.; Hagemann, T.; Morgenstern, S.; Janoschka, T.; Billing, M.; Schacher, F. H.; Hauffman, G.; Gohy, J. F.; Hoepfner, S.; et al. Polymer/Zinc Hybrid-Flow Battery Using Block Copolymer Micelles Featuring a TEMPO Corona as Catholyte. *Polym. Chem.* **2016**, *7* (9), 1711–1718.
- (12) Burgess, M.; Moore, J. S.; Rodríguez-López, J. Redox Active Polymers as Soluble Nanomaterials for Energy Storage. *Acc. Chem. Res.* **2016**, *49* (11), 2649–2657.
- (13) Montoto, E. C.; Nagarjuna, G.; Hui, J.; Burgess, M.; Sekerak, N. M.; Hernández-Burgos, K.; Wei, T. S.; Kneer, M.; Grolman, J.; Cheng, K. J.; et al. Redox Active Colloids as Discrete Energy Storage Carriers. *J. Am. Chem. Soc.* **2016**, *138* (40), 13230–13237.
- (14) Wang, X.; Chai, J.; Jiang, J. Redox Flow Batteries Based on Insoluble Redox-Active Materials. A Review. *Nano Mater. Sci.* **2020**, DOI: 10.1016/j.nanoms.2020.06.003.
- (15) Plamper, F. A.; Richtering, W. Functional Microgels and Microgel Systems. *Acc. Chem. Res.* **2017**, *50*, 131–140.
- (16) Karg, M.; Pich, A.; Hellweg, T.; Hoare, T.; Lyon, L. A.; Crassous, J. J.; Suzuki, D.; Gumerov, R.; Schneider, S.; Potemkin, I.; et al. Nanogels and Microgels: From Model Colloids to Applications, Recent Developments, and Future Trends. *Langmuir* **2019**, *35* (19), 6231–6255.
- (17) Li, H.; Mergel, O.; Jain, P.; Li, X.; Peng, H.; Rahimi, K.; Singh, S.; Plamper, F. A.; Pich, A. Electroactive and Degradable Supramolecular Microgels. *Soft Matter* **2019**, *15* (42), 8589–8602.
- (18) Jung, S. H.; Schneider, S.; Plamper, F.; Pich, A. Responsive Supramolecular Microgels with Redox-Triggered Cleavable Crosslinks. *Macromolecules* **2020**, *53* (3), 1043–1053.

(19) Fu, Q.; Gray, Z. R.; Van Der Est, A.; Pelton, R. H. Phase Behavior of Aqueous Poly(Acrylic Acid-g-TEMPO). *Macromolecules* **2016**, *49* (13), 4935–4939.

(20) Grinberg, V.; Burova, T.; Grinberg, N.; Buyanovskaya, A.; Khokhlov, A.; Kozhunova, E.; Vyshivannaya, O.; Nasimova, I. Functionalized Thermoresponsive Microgels Based on N-Isopropylacrylamide: Energetics and Mechanism of Phase Transitions. *Eur. Polym. J.* **2020**, *133*, 109722.

(21) Kozhunova, E. Y.; Vyshivannaya, O. V.; Nasimova, I. R. "Smart" IPN Microgels with Different Network Structures: Self-Crosslinked vs Conventionally Crosslinked. *Polymer* **2019**, *176*, 127–134.

(22) Pilař, J.; Labský, J. EPR Study of Chain Rotational Dynamics in Dilute Aqueous Solutions of Spin-Labeled Poly(Acrylic Acid) at Different Degrees of Neutralization. *Macromolecules* **1994**, *27* (14), 3977–3981.

(23) Vesterinen, E.; Dobrodumov, A.; Tenhu, H. Spin-Labeled Polyelectrolyte Gels Based on Poly(N-Isopropylacrylamide). Effects of the Network Structure and the Gel Collapse on the EPR Spectra. *Macromolecules* **1997**, *30* (5), 1311–1316.

(24) Hansen, K. A.; Blinco, J. P. Nitroxide Radical Polymers-A Versatile Material Class for High-Tech Applications. *Polym. Chem.* **2018**, *9* (13), 1479–1516.

(25) Zanzola, E.; Gentil, S.; Gschwend, G.; Reynard, D.; Smirnov, E.; Dennison, C. R.; Girault, H. H.; Peljo, P. Solid Electrochemical Energy Storage for Aqueous Redox Flow Batteries: The Case of Copper Hexacyanoferrate. *Electrochim. Acta* **2019**, *321*, 134704.

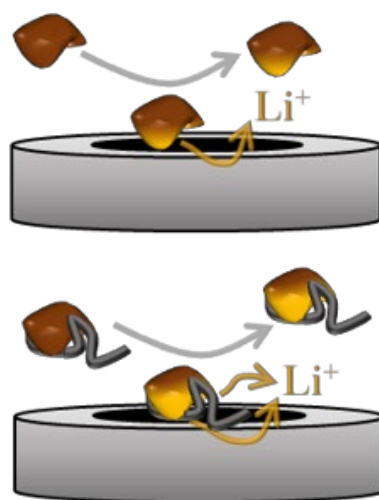
#### NOTE ADDED AFTER ISSUE PUBLICATION

A production error resulted in incorrect page numbers. The page numbers were revised, and the Letter was posted with the correct page range (10561–10565) on January 11, 2021.

### 4.3 Influence of Conductive Additives for Nano-impact Electrochemistry

#### Study of Single $\text{LiMn}_2\text{O}_4$ Particles

My contribution: Conceptualization, Methodology, Investigation, Software, Validation, Visualization, Writing - Original Draft



Reprinted with permission from [174]. Copyright 2022 Elsevier



## Influence of conductive additives in a nano-impact electrochemistry study of single $\text{LiMn}_2\text{O}_4$ particles

Nataliya A. Gvozdik<sup>a,\*</sup>, Anna A. Kurbatova<sup>a</sup>, Nikolay A. Ovsyannikov<sup>a</sup>, Mariam A. Pogossova<sup>a</sup>, Keith J. Stevenson<sup>a</sup>

<sup>a</sup> Skolkovo Institute of Science and Technology, Bolshoy Boulevard 30, bld 1, 121205 Moscow, Russia

### ARTICLE INFO

#### Keywords:

Nano impacts  
Solid boosters  
 $\text{LiMn}_2\text{O}_4$   
Conductivity  
Conductive additives

### ABSTRACT

The application of traditional cathode materials for metal-ion batteries in suspensions is recognized as an effective way of enhancing the volumetric energy density of flow batteries. These additives are called solid boosters. We have studied the influence of conducting additives on the rate-limiting steps (i.e. ion or electron transfer) for intercalating  $\text{LiMn}_2\text{O}_4$  materials in suspensions. We analyzed the charge distribution and the maximum current resulting from a single particle of  $\text{LiMn}_2\text{O}_4$  colliding with an electrode (i.e. nano-impact electrochemistry) and compared the results to studies with added carbon nanotubes in the water to ensure fast mixed ion/electron transfer.  $\text{LiMn}_2\text{O}_4$  nanoparticles 76 nm in size were synthesized via a solution combustion method, then mixed with 30 wt% carbon nanotubes as a composite suspension. Electron transfer from the  $\text{LiMn}_2\text{O}_4$  particle to the electrode was found to be the critical factor affecting the response during the single-particle collision. With an increase in the potential, the average charge observed for deintercalation from the composite particles increased nonlinearly and reached 47 % deintercalation at 1.1 V vs. Ag/AgCl. At the same time, only 5 % of lithium can be extracted from  $\text{LiMn}_2\text{O}_4$  particles when no carbon nanotube additive is present. Therefore, the addition of a conductive component is essential for the effective investigation of intercalation materials in suspensions and in nano-impact electrochemistry studies.

### 1. Introduction

Redox flow batteries (RFBs) represent a promising technology for large-scale energy storage due to their independent power and capacity scaling, and long lifetime [1]. However, the energy density of RFBs remains a critical problem and requires large amounts of electrolyte to achieve the required capacities [2]. This limitation results in a non-scalable implementation for many organic redox molecules as the maximum energy density of a classical RFB is limited by the solubility of the active species [3]. To bypass these limitations, an innovative approach was proposed by Wang's group in 2013 [4]. Solid materials, which were indirectly charged/discharged via a soluble redox mediator, were used to store extra energy in tanks. In other words, the solid materials (or solid boosters) potentially enhance the volumetric capacity, decreasing the required volume of expensive soluble organic compounds [5,6].

Almost all proposed solid-booster materials are solids in which the redox reaction is coupled with ion transfer (intercalation/

deintercalation) [7]. The most popular are well-known cathode materials for metal-ion batteries, such as  $\text{LiFePO}_4$ , Prussian blue, and  $\text{Na}_3\text{V}_2(\text{PO}_4)_3$  [5,6,8,9]. The intercalation process has been studied in connection with battery applications, where the material particles are in constant contact with a current collector and mixed with conductive carbon additives [10,11]. At the same time, the processes of spontaneous reaction between the solid booster and the organic mediator in the solution have not yet been investigated in detail. The electrochemical behavior of independent particles which are not in constant contact with the electrode surface is little understood [12]. One of the techniques used to detect a single particle collision with a potentiostatted electrode surface, known as nano-impact electrochemistry, makes it possible to probe the electrochemical response of electroactive particles in suspension [13]. There are several works demonstrating nano impacts on intercalation materials, such as  $\text{LiFePO}_4$ ,  $\text{LiCoO}_2$ ,  $\text{LiMn}_2\text{O}_4$ , and Prussian blue [14–17]. The experiments were conducted in an aqueous electrolyte, and the required overpotentials for starting deintercalation were usually > 100 mV [14,16,18].

\* Corresponding author.

E-mail address: [nataliya.gvozdik@skoltech.ru](mailto:nataliya.gvozdik@skoltech.ru) (N.A. Gvozdik).

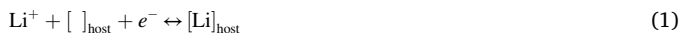
<https://doi.org/10.1016/j.elecom.2022.107304>

Received 14 May 2022; Received in revised form 4 June 2022; Accepted 7 June 2022

Available online 8 June 2022

1388-2481/© 2022 The Authors. Published by Elsevier B.V. This is an open access article under the CC BY-NC-ND license (<http://creativecommons.org/licenses/by-nc-nd/4.0/>).

More detailed investigations of the limiting step for the (de)intercalation process during collisions on  $\text{TiO}_2$ ,  $\text{LiCoO}_2$ , and  $\text{LiMn}_2\text{O}_4$  have been carried out [19–21]. For the general case of metal-ion deintercalation into an oxide-type matrix in aqueous media, the process involves the following steps: (I) ion solid-state diffusion in the host lattice; (II) adion formation; (III) ion transfer across the particle/electrolyte interface; (IV) electron transfer across the particle/electrode interface; (V) solvation of the ion at the electrode/electrolyte interface; and (VI) ion diffusion in the electrolyte [11]. Stages II–V can be generalized within the framework of Butler–Volmer kinetics, representing the charge transfer mechanism as:



Exponential behavior of nano-impact transients – overpotential dependence would be expected on treating the reaction mechanism in such a way. However, Butler–Volmer dependence of nano-impact responses was not observed for all materials studied. This suggests the need to elucidate the limiting steps for nano impacts by treating each reaction step individually. In particular, the transfer of ions across the solid/solution interface and poor host electron conductivity have been indicated as the limiting steps [19,21]. Additionally, no comparison of different materials and composites has been performed within one paper using the same experimental setup. We propose that the addition of conducting additives can facilitate electron/ion transfer and enhance the total charge extracted from particles while decreasing the required overpotential. Since the transfer of  $\text{Li}^+$  and an electron across the interface are connected, the surface conductivity increase should lead to an increase in current (and integrated charge passed). A more detailed comparison of the shape of transients can give information on the nature of the limiting step. During stage (I) of bulk diffusion, the current attenuation will be proportional to  $\sim \text{time}^{-0.5}$ , or  $\ln(i)$  will be proportional to time according to Fick's law, depending on a time constant [22]. The slow stages (II, III, and V) will lead to current decay in proportion to  $\sim \text{time}^{-1}$  as for reactions taking place exclusively near the surface, like surface-confined species [19]. The slow stage IV should have the same trend as diffusion unless the surface conductivity increases. This implies that the amount of deintercalated lithium ions is determined by the number of electrons, due to the electroneutrality principle.

In this paper, we synthesized nanoparticles of  $\text{LiMn}_2\text{O}_4$  as a model of the most conductive cathode material [23]. We collected data from nano-impacts at different potentials for pristine particles and from suspensions with carbon nanotubes. Analysis of the total charge and maximum current distributions, and the forms of the transients, provide clear support for our hypothesis that electron transfer plays a crucial role.

## 2. Experimental

### 2.1. Materials synthesis and characterization

$\text{LiMn}_2\text{O}_4$  nanoparticles were synthesized via solution combustion method involving calcination at  $700^\circ\text{C}$  in an air-filled muffle furnace for 8 h [24]. A composite material containing 30 wt% of carbon nanotubes was prepared from 0.4 wt% suspensions with 0.2 wt% PVP (Tuball™, OsSiAl, Russia). The suspension with the material was ball-milled and dried at  $70^\circ\text{C}$ . The samples were denoted LMO and LMO/CNT for pristine particles and the composite, respectively. Powder X-ray diffraction analysis (XRD) was used to identify the phase and structural features using a Bruker D8 Advance diffractometer (Bragg-Brentano geometry;  $\text{CuK}_{\alpha 1,2}$ ). Micrographs were obtained using a Helios G4 two-beam scanning electron microscope at 1 kV. Electrochemical characterization of LMO was performed for a film electrode. The composite electrode was made of LMO powder mixed with carbon black and PVDF and then cast on a platinum foil. Electrochemical tests were carried out

in a three-electrode cell with a 3 M KCl Ag/AgCl reference electrode using a VMP3 Multichannel Potentiostat (Biologic, France). The upper cutoff of the potential was 1.05 V vs. 3 M Ag/AgCl due to water electrolysis (see [supplementary information \(SI 1\)](#))

### 2.2. Nano-impact experiment

All measurements were carried out using an NPI (Germany) setup consisting of a reading head (differential (3-electrode) headstage), an amplifier (amplifier for voltammetry and amperometry VA-10) connected to an ADC with software written in our lab. The head of the device was in a Faraday cage. A three-electrode cell with a homemade platinum working microelectrode (10  $\mu\text{m}$  diameter) and a 3 M KCl Ag/AgCl reference electrode was used with 2 mM  $\text{Li}_2\text{SO}_4$  and  $\sim 50$  pM of the studied particles (see [supplementary information \(SI 2\)](#)). The baseline for the supporting electrolyte was measured before testing each sample; the current was recorded at a fixed potential; then, the test sample was added, and the dataset was recorded at the same potential. An example of recorded data is presented in Fig. 1. The data were processed using a Python script. Additionally, the quality of the microelectrode surface was controlled by cyclic voltammetry with 5 mM potassium ferrocyanide to check the limiting current and 0.5 M sulfuric acid to check the pronounced hydrogen UPD area (see [supplementary information \(SI 3\)](#)).

## 3. Results

### 3.1. Characterization of the nanoparticles

The structure and morphology of the obtained LMO nanoparticles were studied prior to the nano-impact tests. Fig. 2(A) shows the experimental, refined, and differential powder XRD patterns – one can observe the presence of pure  $\text{LiMn}_2\text{O}_4$  with no admixture phases detectable. The widened appearance of the reflexes is in agreement with the small size of the particles analyzed (about 70 nm). The good match between theoretical and experimental patterns (selected error coefficients:  $R_p = 1.35$ ,  $R_{wp} = 3.05$ ,  $R_{Ball} = 3.77$ ) demonstrates that the compound's chemical composition and structural features generally correspond well to those nominally expected. The unit cell dimension  $a$  is 8.1725(2) Å, which indicates a slightly lower lithium content in the structure [25]. Minor initial delithiation of the sample is in accordance with the synthesis route, especially for nano-scale particles at high temperatures in an oxidative environment [26]. The LMO nanoparticles had an average size of 76 nm (Fig. 2B).

The electrochemical properties of the material were tested in aqueous media. An aqueous electrolyte was selected for two reasons: (1)

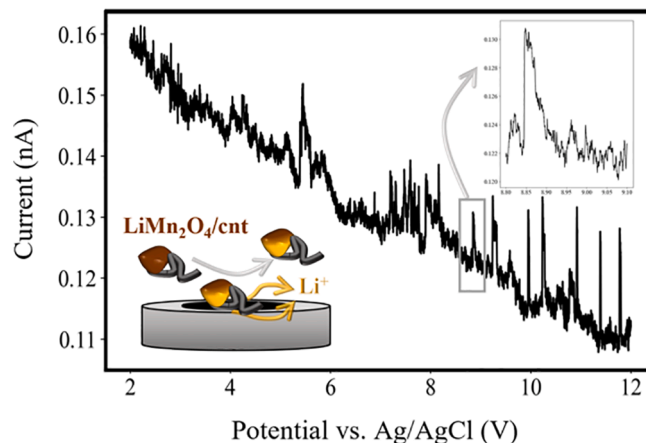
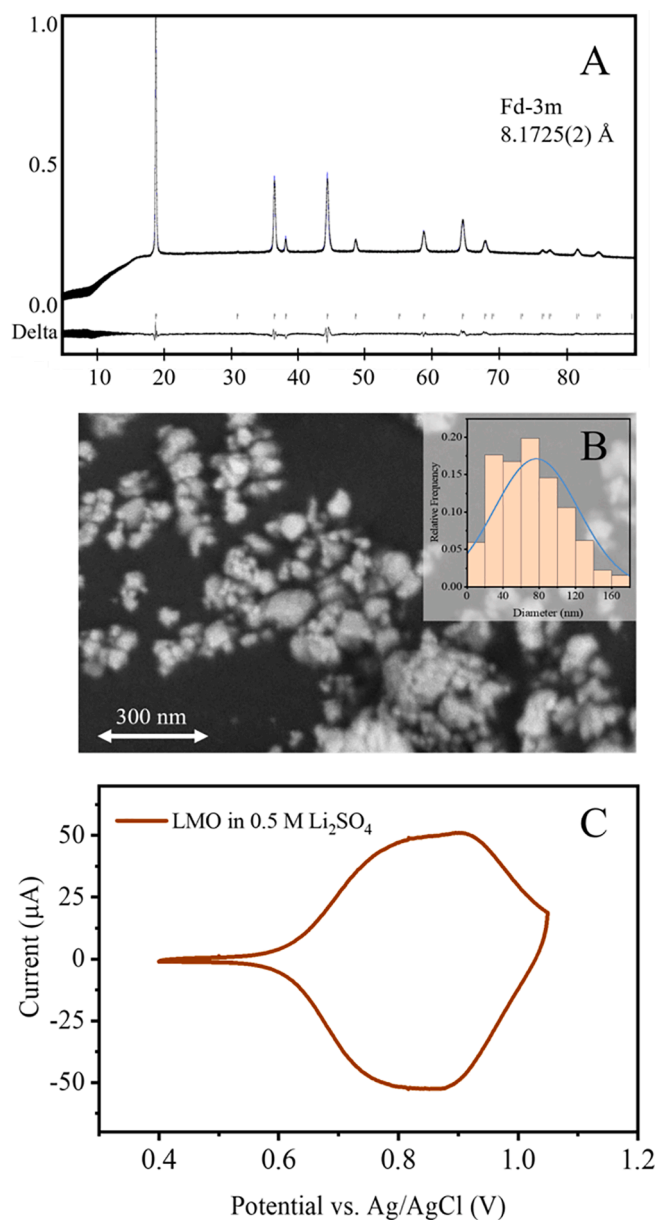


Fig. 1. Current profile for LMO/CNT composite at 1 V vs. Ag/AgCl and a scheme showing the collision of a LMO/CNT nanoparticle with the electrode for deintercalation.



**Fig. 2.** (A) XRD pattern and profile refinement of LMO; (B) micrograph and particle size distribution for LMO; (C) cyclic voltammetry with a scan rate of 0.2 mV/s for the composite electrode with LMO in 0.5 M  $\text{Li}_2\text{SO}_4$  aqueous electrolyte.

to eliminate the formation of blocking layers on the surface of the particles; (2) for fast diffusion of lithium ions in water; (3) for rapid solvation of  $\text{Li}^+$  in water [11,27,28]. The cyclic voltammetry showed a reversible redox process, which was limited by the water electrochemical stability window. Due to the high impact of the surface reaction from nanoparticles of LMO and their high dispersion, the fusion (or convolution) of two peaks typical of LMO was observed [29]. The average half-wave potentials of the peaks were 0.77 V and 0.88 V vs. Ag/AgCl, respectively. Moreover, CVs of a similar shape were observed for LMO in a lithium half-cell and for the LMO/CNT composite in 0.5 M  $\text{Li}_2\text{SO}_4$  (see supplementary information (SI 1,4,5)). The material had a capacity of 80 mAh/g in water (calculated by integrating the deintercalation charge and knowing the mass of the material).

### 3.2. Analysis of nano-impact experiments

A statistical analysis was performed on nano-impact datasets for LMO and LMO/CNT suspensions at different potentials. Prior to the test, the baselines of the supporting electrolyte and the suspension of nanotubes were measured to ensure that no parasitic processes occur at the potential of interest (see supplementary information (SI 7)). We studied the deintercalation process by assessing the charge distribution, the duration of impacts, and the distribution of maximum currents (Fig. 3).

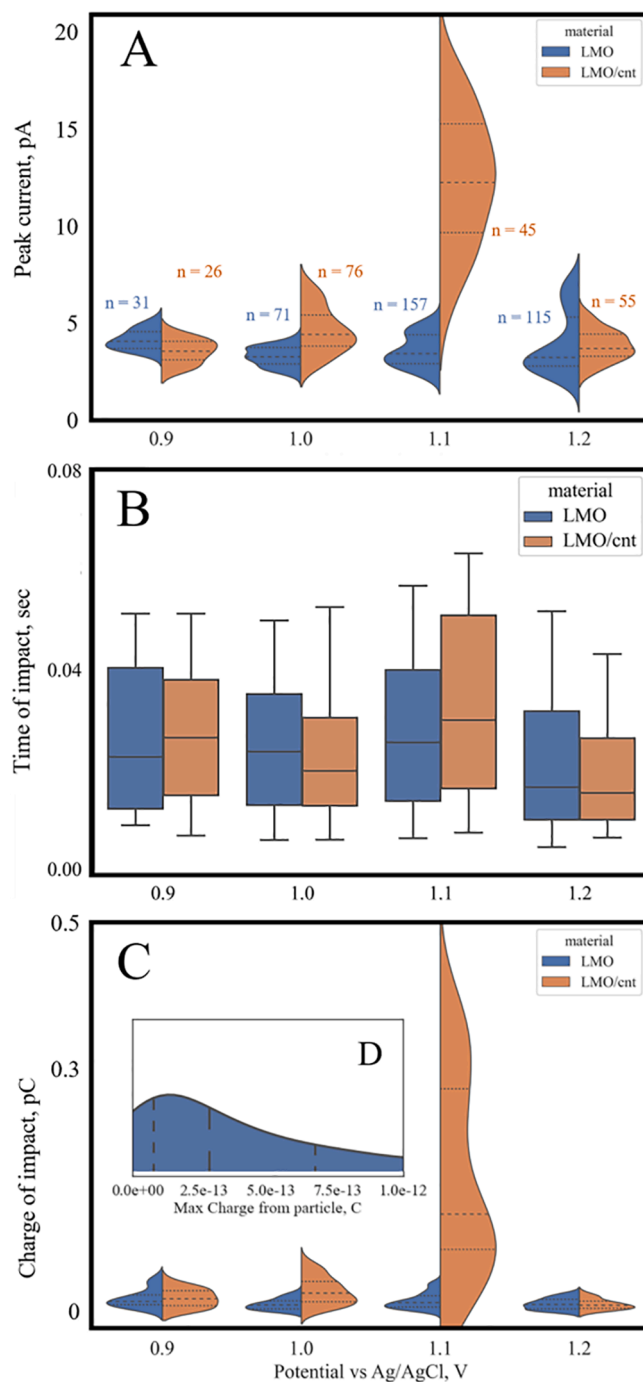


**Fig. 3.** (A) charge, (B) duration, and (C) maximum current distributions for transients during deintercalation at different potentials for the pristine material (LMO) and the composite (LMO/CNT). (D) Maximum charge distribution extracted from the particle, calculated based on the particle size distribution. The long-dashed lines show the median values; the short-dashed lines show the location of 25% and 75% of data points.

The two studied materials have a statistically significant difference in the maximum transient currents: there was a stable mean value of 3.7 pA at any potential for pristine LMO nanoparticles with increasing deviations from 0.9 V to 1.1 V, while a nonlinear rise from 3.5 pA at 0.9 V to 12 pA at 1.1 V was observed for the composite material (Fig. 3A). The average duration of the nano-impacts was 27 ms for both materials regardless of the applied potential (Fig. 3B).

In addition, we should point out that the number of impacts involved in the statistical analysis deviates with the potential as the frequency of collisions decreased drastically for low (0.9 V) and high (1.2 V) potentials (Fig. 3C) (see the supplementary information (SI 6)). We assumed that there was a low signal/noise ratio for impacts at low overpotentials (50 mV), thus, a small number of events were detected. G. Zampardi demonstrated a significant amount of collisions starting only from 400 mV of overpotential with the same material, probably due to the larger particle size (200 nm) [16]. By contrast, nano-impacts from LiCoO<sub>2</sub> nanoparticles were reported at an overpotential of 100 mV [20]. At a potential of 1.2 V vs. Ag/AgCl a platinum oxide blocking layer started to form, which reduced the conductivity of the electrode surface, leading to a decrease in the total current and charge [30]. We intentionally included the data for the higher potential to illustrate the impact of surface conductivity.

#### 4. Discussions

The total charge distribution showed the same trend as the peak current: the deintercalation in the composite was more efficient than in the pristine material. The broad distribution of charge for the LMO/CNT composite relates to the fact that the binding of nanotubes with nanoparticles varies significantly, and their contact with the electrode also had great variability. As less than 25% of sampling intersects for the LMO and LMO/CNT sets, we can deduce that this difference is meaningful. The maximum charge distribution is presented in Fig. 3(D), calculated from the particle size distribution. One can conclude that incomplete deintercalation occurs during collisions. The averaged statistical data for the deintercalation ratio and maximum currents are presented in Fig. 4(A) and are discussed below.

The maximum transient currents grow nonlinearly with the increase in overpotential for the composite, however, the study of this behavior with the selected function was not possible due to high statistical errors. Consequently, the analysis of the average charge had the same trend as the time of impact and was the same for both materials and any potential. The ratio of average charge and the total maximum charge of the particle gives the deintercalation degree, which represents the percentage of lithium extracted from the particles. The deintercalation degree for LMO particles remained the same at a level of 4 % for all potentials, while the LMO/CNT particles had a deintercalation degree which increased from 5 % to 47 % with growing overpotential (Fig. 4A).

In the scheme of the deintercalation reaction stages discussed in the introduction, it was stated that transient forms and their dependence on overpotential can elucidate the limiting step. Firstly, we demonstrated that addition of carbon nanotubes significantly changes the resulting currents, which strongly suggests that electron transfer from particle to the electrode is the limiting step. Moreover, nanotubes increase the contact area between the particle and the electrode. Secondly, they reduce the energy barrier for electron transfer by creating additional intermediate levels between the metal of the electrode and the particles, which are semiconductors [31]. As electron transfer takes place between the surfaces of the electrode and the particle, the real effective area of contact determines the admissible number of electrons, while the lithium deintercalation process is slow and sets the shape of the transient [32]. We prepared a dataset with a high signal-to-noise ratio at 1.1 V for transient approximation by diffusion-controlled models. The diffusion coefficient and characteristic diffusion length determined from fitting using a spherical model shows whether the deintercalation happens near the electrode surface or uniformly across the particle.

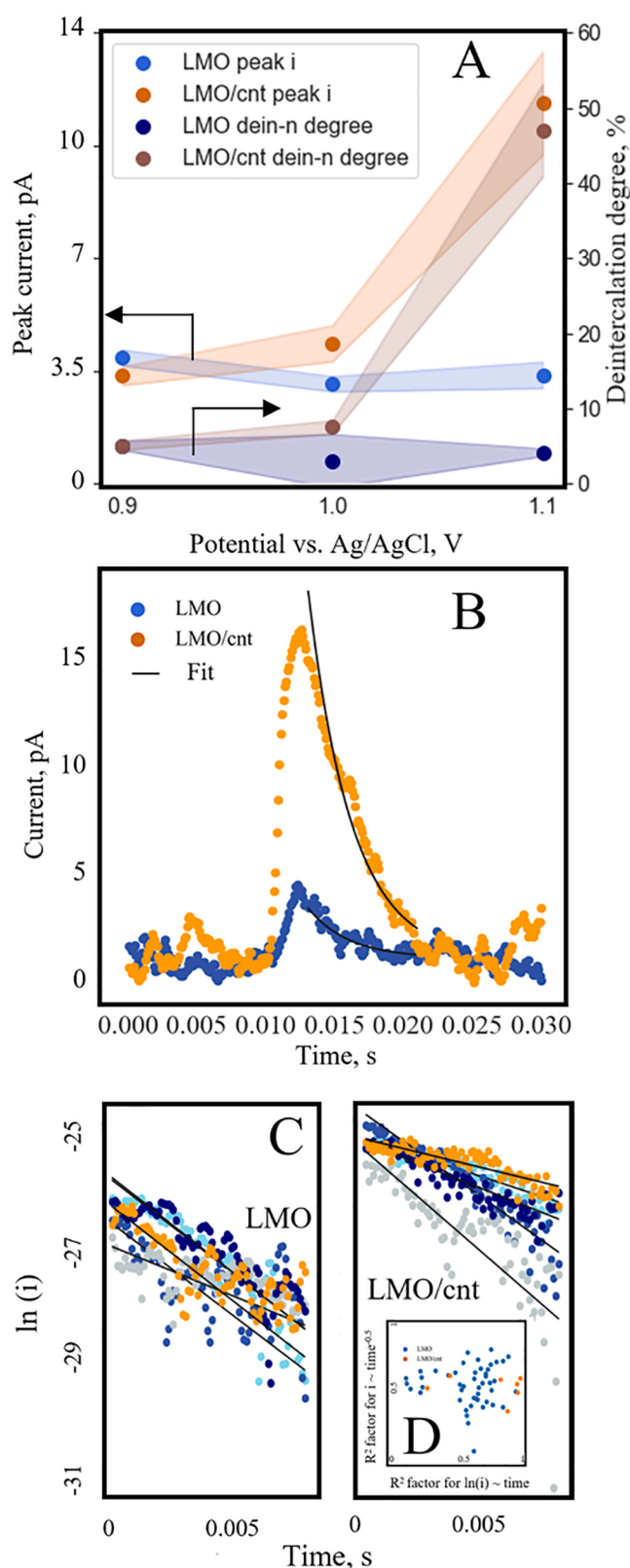


**Fig. 4.** (A) Mean values with standard deviations for peak transient current and deintercalation degree with respect to the particle size distribution (standard deviations are shown as colored areas). (B) Examples of transients fitted by a diffusion limiting model for LMO and LMO/CNT samples. (C) Semi-logarithmic scale of transients (points) and linear fit (lines); (D)  $R^2$  factor comparison for two models for bulk diffusion.

We utilized two models from PITT measurements, fitting the transients as a line in (1)  $i \sim \text{time}^{-0.5}$  scale (as a Cottrell equation) or in (2)  $\ln(i) \sim \text{time}$  scale, typical of the case with a prolonged time exposure [22]. It happens that the  $R$ -factor for the second type of fitting was higher, and hence we used it to estimate the reaction parameters (Fig. 4D). A comparison of  $R$ -factors for both approximation models and examples of fitting data are shown in Fig. 4 (B,C). Better fitting for the semi-logarithmic model was also reported for LiCoO<sub>2</sub> nano-impacts transients [20]. The form of the peak was described based on the radial uniform diffusion model for simplicity:

$$i(t) = i_{\text{peak}} e^{-\left(\frac{Dt}{r^2}\right)} \quad (2)$$

where  $t$  is the time (starting time of each transient was set to 0),  $D$  is the diffusion coefficient of Li<sup>+</sup> in the host material, and  $i_{\text{peak}}$  is a pre-exponential factor independent of time,  $r$  is the characteristic length, which is the radius of the particle in the case of full deintercalation. Derived from fitting, the exponential factor  $\left(\frac{Dt}{r^2}\right)$  was equal to  $336 \pm 152$  for the LMO material and  $232 \pm 98$  for the LMO/CNT sample. Recalculation of  $r$  from this equation using  $D$  in the range  $10^{-12}$ – $10^{-10}$  cm<sup>2</sup>/s showed that  $r$  was in the range 0.1 – 10 nm for LMO and 0.2 – 20 nm for LMO/CNT, resulting in a maximum deintercalation degree of 4 %, which was not correct according to the measurements. Therefore, the radial diffusion model cannot be applied to the whole particle, only to the area near the electrode region of the particle involved in the reaction (Fig. 1A).

## 5. Conclusions

The influence of a conductive carbon additive was demonstrated for the model cathode material LiMn<sub>2</sub>O<sub>4</sub> in aqueous suspension, where the nanoparticles stayed suspended without a constant electrode contact. Synthesized nanoparticles of LiMn<sub>2</sub>O<sub>4</sub> (76 nm in size) were mixed with carbon nanotubes to make a conductive composite suspension. The charge and peak current distributions changed differently with applied overpotential: the average charge and peak currents grew nonlinearly for the composite but were constant for the pristine material. The resulting deintercalation degree for the composite reached 49 % at a potential of 1.1 V vs. Ag/AgCl, while only 4 % of the lithium was extracted from the pristine LiMn<sub>2</sub>O<sub>4</sub> particles. The current transients were analyzed to deduce the limitation stage. The difference in the maxima and form of the transients shows that electron transfer is the rate-determining step for LiMn<sub>2</sub>O<sub>4</sub>. Deintercalation occurs only near the contact between the particle and the electrode – carbon nanotubes increase the contact area, involving a larger part of the particle in the deintercalation. Therefore, we suggest that the use of conductive additives in nano-impact experiments with intercalating systems is a useful tool for signal boosting and enhancing redox flow battery performance (energy density and efficiency).

## Declaration of Competing Interest

The authors declare that they have no known competing financial interests or personal relationships that could have appeared to influence the work reported in this paper.

## Acknowledgment

This work was supported by RFBR, project number 20-33-90305. The work was funded by Skoltech-MIT Next Generation Program “Energy-dense and Durable Nonaqueous Redox Flow Batteries enabled by Flowing Solid-state Capacity Boosters”

## Appendix A. Supplementary data

Supplementary data to this article can be found online at <https://doi.org/10.1016/j.elecom.2022.107304>.

## References

- [1] X.Z. Yuan, C. Song, A. Platt, N. Zhao, H. Wang, H. Li, K. Fatih, D. Jang, *Int. J. Energy Res.* 43 (2019) 6599–6638.
- [2] J. Luo, B. Hu, M. Hu, Y. Zhao, T.L. Liu, *ACS Energy Lett.* 4 (2019) 2220–2240.
- [3] E. Sánchez-Díez, E. Ventosa, M. Guarnieri, A. Trovò, C. Flox, R. Marcella, F. Soavio, P. Mazur, E. Aranzabe, R. Ferret, *J. Power Sources* 481 (2021), 228804.
- [4] Q. Huang, H. Li, M. Grätzel, Q. Wang, *Phys. Chem. Chem. Phys.* 15 (2013) 1793–1797.
- [5] J. Yu, L. Fan, R. Yan, M. Zhou, Q. Wang, *ACS Energy Lett.* 3 (2018) 2314–2320.
- [6] Y. Chen, M. Zhou, Y. Xia, X. Wang, Y. Liu, Y. Yao, H. Zhang, Y. Li, S. Lu, W. Qin, X. Wu, Q. Wang, *Joule* 3 (2019) 2255–2267.
- [7] S. Gentil, D. Reynard, H.H. Girault, *Curr. Opin. Electrochem.* 21 (2020) 7–13.
- [8] M. Zhou, Y. Chen, Q. Zhang, S. Xi, J. Yu, Y. Du, Y. Hu, Q. Wang, *Adv. Energy Mater.* 9 (2019) 1970116.
- [9] E. Zanzola, S. Gentil, G. Gschwend, D. Reynard, E. Smirnov, C.R. Dennison, H. H. Girault, P. Peljo, *Electrochim. Acta* 321 (2019), 134704.
- [10] A.R. Iarchuk, V.A. Nikitina, E.A. Karpushkin, V.G. Sergeev, E.V. Antipov, K. J. Stevenson, A.M. Abakumov, *ChemElectroChem* 6 (2019) 5090–5100.
- [11] S.Y. Vassiliev, V.V. Sentyurin, E.E. Levin, V.A. Nikitina, *Electrochim. Acta* 302 (2019) 316–326.
- [12] W. Xu, G. Zou, H. Hou, X. Ji, W. Xu, G. Zou, H. Hou, X. Ji, *Small* 15 (2019) 1804908.
- [13] K.J. Stevenson, K. Tschulik, *Curr. Opin. Electrochem.* 6 (2017) 38–45.
- [14] W. Xu, Y. Zhou, X. Ji, *J. Phys. Chem. Lett.* 9 (2018) 4976–4980.
- [15] L. Sun, D. Jiang, M. Li, T. Liu, L. Yuan, W. Wang, H.Y. Chen, *Anal. Chem.* 89 (2017) 6050–6055.
- [16] G. Zampardi, C. Batchelor-Mcauley, E. Kätelhön, R.G. Compton, *Angew. Chemie* 129 (2017) 656–659.
- [17] G. Zampardi, S.V. Sokolov, C. Batchelor-McAuley, R.G. Compton, *Chem. – A Eur. J.* 23 (2017) 14338–14344.
- [18] S.V. Sokolov, S. Eloul, E. Kätelhön, C. Batchelor-McAuley, R.G. Compton, *Phys. Chem. Chem. Phys.* 19 (2016) 28–43.
- [19] T. Löffler, J. Clausmeyer, P. Wilde, K. Tschulik, W. Schuhmann, E. Ventosa, *Nano Energy* 57 (2019) 827–834.
- [20] S. Rano, C. Laberty-Robert, K. Ngo, C.M. Sánchez-Sánchez, V. Vivier, *Phys. Chem. Chem. Phys.* 21 (2019) 5416–5423.
- [21] G. Zampardi, C. Batchelor-McAuley, E. Kätelhön, R.G. Compton, *Angew. Chem. Int. Ed.* 56 (2017) 641–644.
- [22] Y. Zhu, T. Gao, X. Fan, F. Han, C. Wang, *Acc. Chem. Res.* 50 (2017) 1022–1031.
- [23] R. Zhao, S. Zhang, J. Liu, J. Gu, *J. Power Sources* 299 (2015) 557–577.
- [24] Q. Zhang, J. Mei, X. Wang, J. Guo, F. Tang, W. Lu, *J. Alloys Compd.* 617 (2014) 326–331.
- [25] E. Andrade, A. Romero Núñez, A. Ibarra Palos, J. Cruz, M.F. Rocha, C. Solis, O. G. De Lucio, E.P. Zavala, *Nucl. Instruments Methods Phys. Res. Sect. B: Beam Interact. with Mater. Atoms* 269 (2011) 440–443.
- [26] S. Sharifi-Asl, J. Lu, K. Amine, R. Shahbazian-Yassar, *Adv. Energy Mater.* 9 (2019) 1–19.
- [27] G. Zampardi, F. La Mantia, *Batter. Supercaps* 3 (2020) 672–697.
- [28] K. Xu, *Chem. Rev.* 114 (2014) 11503–11618.
- [29] J. Fan, L.L. Yu, G.D. Fan, W.L. Xu, J.J. Xing, J.T. Zhao, *J. Materiomics* 7 (2021) 488–497.
- [30] S. Prass, J. St-Pierre, M. Klingele, K.A. Friedrich, N. Zamel, *Electrocatalysis* 12 (2021) 45–55.
- [31] M. Moghaddam, S. Sepp, C. Wiberg, A. Bertei, A. Rucci, P. Peljo, *Mol.* 26 (2021) 2111.
- [32] H. Le, C. Lin, E. Kätelhön, R.G. Compton, *Electrochim. Acta* 298 (2019) 778–787.

#### 4.4 Conclusions from the Chapter 4

Microgels with 4-amino-TEMPO redox-active sites have stable cycling with capacity up to 100 mAh/L, that corresponded to 14 % of capacity utilization. The material was investigated by drop-casting the thin film on a flat surface of the electrode. An unfortunate loss of > 70% initial capacity at the first irreversible oxidation process was observed. This fade is caused by the reorganization of the micro-gel structure due to the inability to compensate for the charge. The insufficient electronic conductivity of 500 nm globulus led to the localization of the reaction in the near-electrode area.

Similar localization of the reaction we demonstrated by nano-impact technique. Suspension of  $\text{LiMn}_2\text{O}_4$  as a solid-booster was studied with and without the addition of carbon nanotubes. The statistical analysis showed that total capacity utilization during the collision has grown from 5 to 47 % with the addition of carbon nanotubes. The conductive additives provided additional intermediate energy levels for the electron transfer and increased the contact area between the particle and the electrode. Thus, the application of conductive additive accelerates the deintercalation reaction.

In summary, we demonstrated that redox-active suspensions need effective electronic conductivity to achieve maximum capacity. The introduction of the conductive additives that are closely connected to the nanoparticles is one of the useful approaches.

## Chapter 5 Summary and Outcomes

This thesis was devoted to the development of tools that can be applied for materials characterization in the scope of RFB applications. In a conclusion, I discuss how the methods can be used on other materials and which problems can be addressed.

1) I developed the method of in-situ Raman monitoring of vanadyl oxidation reaction on the carbon paper electrode. A specially designed three-electrode cell can be utilized for any chemistries, stable in air, and any electrode materials. In general, tracking species transformation on the electrode surface during the redox process is a powerful tool for the investigation of degradation processes of the redox-active components or electrode surface. Moreover, this method can be used to prove the presence of a catalytic effect of electrode additives.

2) A new method was proposed for kinetic parameters identification, which utilized experimental data corroborated by the numerical model with activation losses. Numerical evaluation of redox reaction rates is an important issue for reliable RFB modeling and electrode materials comparison. In particular, it is the useful tool for the comparison of vanadium reaction rates for different electrode materials.

3) I determined the set of essential parameters for bipolar plate materials. The developed benchmarking protocol allows fast screening of materials, starting with the target value of electronic conductivity. Moreover, the influence of bipolar plate morphology on chemical and electrochemical stability was demonstrated.

4) I characterized two redox-active colloids in terms of available capacity. The effect of the carbon nanotubes addition to the colloid was demonstrated by the nano-impact technique, demonstrating the necessity of electronic conductivity to achieve maximum capacity. The conductive additives provided additional intermediate energy levels for the electron transfer and increased the contact area between the particle and the electrode. Therefore, the application of conductive additive accelerates the redox reaction and the conversion level for dielectric redox-active nanoparticles.

Overall, this thesis proposes the state-of-the-art framework of material characterization methods, which are effective and industry applicable tools for diagnostic RFB problems. In particular, this work opens up many future perspectives regarding the carbon materials selection for vanadium RFB, like porous electrodes and bipolar plates. Developed stability tests and kinetics characterization methods allow targeted development of durable and powerful vanadium stack. Additionally, investigation of solid redox-active materials as a new RFB electrolyte class using proposed methods elucidated the reason of their incomplete capacity utilization. Overcoming this bottleneck will facilitate the development of advanced organic RFB and bring them to the energy market.

## Bibliography

- [1] L. (International E.A. Cozzi, T. (International E.A. Gould, World Energy Outlook 2021, 2021.
- [2] J. Makansi, J. Abboud, Energy Storage. The Missing Link in the Electricity Value Chain. An ESC White Paper, 2002.
- [3] D. Kim, H. Kim, D. Won, Operation strategy of shared ESS based on power sensitivity analysis to minimize PV curtailment and maximize profit, IEEE Access. 8 (2020) 197097–197110. <https://doi.org/10.1109/ACCESS.2020.3034339>.
- [4] Z. (Gary) Yang, Electrochemical Energy Storage for Green Grid: Status and Challenges, ECS Meeting Abstracts. MA2011-02 (2011) 155–155. <https://doi.org/10.1149/ma2011-02/4/155>.
- [5] I. Táczai, G. Szörényi, Energy Regulators Regional Association Secretariat Overview of the Energy Storage Possibilities to Support the Electrical Power System Overview of the Energy Storage Possibilities to Support the Electrical Power System, (2016).
- [6] C. Rae, S. Kerr, M.M. Maroto-Valer, Upscaling smart local energy systems: A review of technical barriers, Renewable and Sustainable Energy Reviews. 131 (2020) 110020. <https://doi.org/10.1016/j.rser.2020.110020>.
- [7] McKenzie Baker, Battery Storage - a global enabler of the Energy Transition, 2022.
- [8] D.K. Kim, S. Yoneoka, A.Z. Banatwala, Y.-T. Kim, K.-Y. Nam, Handbook on Battery Energy Storage System, 2018.
- [9] D.M.R. Abbas A. Akhil, Georgianne Huff, Aileen B. Currier, Benjamin C. Kaun, and W.D.G. Stella Bingqing Chen, Andrew L. Cotter, Dale T. Bradshaw, DOE / EPRI 2013 Electricity Storage Handbook in Collaboration with NRECA, Sandia National Laboratories, 2014.

- [10] O. Schmidt, S. Melchior, A. Hawkes, I. Staffell, Projecting the Future Levelized Cost of Electricity Storage Technologies, *Joule*. 3 (2019) 81–100. <https://doi.org/10.1016/j.joule.2018.12.008>.
- [11] Lazard' s levelized cost of storage analysis – version 4.0, 2018.
- [12] I. Grand View Research, Energy Storage Systems Market Size, Share & Trends Report Energy Storage Systems Market Size, Share & Trends Analysis Report by Technology (Pumped Hydro, Electrochemical Storage, Electromechanical Storage, Thermal Storage), By Region, And Segment Forecast, 2022.
- [13] Global grid battery storage investments 2015-2021 | Statista, (n.d.). <https://www.statista.com/statistics/1301517/grid-battery-storage-investments-worldwide/#statisticContainer> (accessed May 5, 2022).
- [14] Д. Холкин, Ю. Удальцов, Рынок систем накопления электроэнергии в россии: потенциал развития, 2018.
- [15] M. V. Reddy, A. Mauger, C.M. Julien, A. Paoella, K. Zaghbi, Brief History of Early Lithium-Battery Development, *Materials*. 13 (2020). <https://doi.org/10.3390/MA13081884>.
- [16] D.; T.I.; Tarvydas, Li-ion batteries for mobility and stationary storage applications - Publications Office of the EU, 2018.
- [17] H.D. Yoo, E. Markevich, G. Salitra, D. Sharon, D. Aurbach, On the challenge of developing advanced technologies for electrochemical energy storage and conversion, *Materials Today*. 17 (2014) 110–121. <https://doi.org/10.1016/J.MATTOD.2014.02.014>.
- [18] C.R. Birkl, M.R. Roberts, E. McTurk, P.G. Bruce, D.A. Howey, Degradation diagnostics for lithium ion cells, *J Power Sources*. 341 (2017) 373–386. <https://doi.org/10.1016/j.jpowsour.2016.12.011>.

- [19] Q. Wang, B. Mao, S.I. Stolarov, J. Sun, A review of lithium ion battery failure mechanisms and fire prevention strategies, *Prog Energy Combust Sci.* 73 (2019) 95–131. <https://doi.org/10.1016/j.pecs.2019.03.002>.
- [20] Born Ontario, Tesla Impact report 2020, 2020.
- [21] P. Kumar Nayak, E.M. Erickson, F. Schipper, T. Rao Penki, N. Munichandraiah, P. Adelhelm, H. Sclar, F. Amalraj, B. Markovsky, D. Aurbach, P.K. Nayak, E.M. Erickson, F. Schipper, T.R. Penki, H. Sclar, F. Amalraj, B. Markovsky, D. Aurbach, P. Adelhelm, N. Munichandraiah, Review on Challenges and Recent Advances in the Electrochemical Performance of High Capacity Li- and Mn-Rich Cathode Materials for Li-Ion Batteries, *Adv Energy Mater.* 8 (2018) 1702397. <https://doi.org/10.1002/AENM.201702397>.
- [22] A. Tomaszewska, Z. Chu, X. Feng, S. O’Kane, X. Liu, J. Chen, C. Ji, E. Endler, R. Li, L. Liu, Y. Li, S. Zheng, S. Vetterlein, M. Gao, J. Du, M. Parkes, M. Ouyang, M. Marinescu, G. Offer, B. Wu, Lithium-ion battery fast charging: A review, *ETransportation.* 1 (2019) 100011. <https://doi.org/10.1016/J.ETRAN.2019.100011>.
- [23] A. Mayyas, D. Steward, M. Mann, The case for recycling: Overview and challenges in the material supply chain for automotive li-ion batteries, *Sustainable Materials and Technologies.* 19 (2019) e00087. <https://doi.org/10.1016/j.susmat.2018.e00087>.
- [24] K. Mongird, V. Viswanathan, P. Balducci, J. Alam, V. Fotedar, V. Koritarov, B. Hadjerioua, Energy Storage Technology and Cost Characterization Report | Department of Energy, US Department of Energy. (2019).
- [25] H.E. Melin, State-of-the-art in reuse and recycling of lithium-ion batteries – A research review, *Circular Energy Storage.* 1 (2020) 1–57.
- [26] W. Lv, Z. Wang, H. Cao, Y. Sun, Y. Zhang, Z. Sun, A Critical Review and Analysis on the Recycling of Spent Lithium-Ion Batteries, *ACS Sustain Chem Eng.* 6 (2018) 1504–1521. <https://doi.org/10.1021/acssuschemeng.7b03811>.

- [27] Y. Chen, Y. Kang, Y. Zhao, L. Wang, J. Liu, Y. Li, Z. Liang, X. He, X. Li, N. Tavajohi, B. Li, A review of lithium-ion battery safety concerns: The issues, strategies, and testing standards, *Journal of Energy Chemistry*. 59 (2021) 83–99. <https://doi.org/10.1016/J.JECHEM.2020.10.017>.
- [28] K. Kim, H. Ma, S. Park, N.S. Choi, Electrolyte-Additive-Driven Interfacial Engineering for High-Capacity Electrodes in Lithium-Ion Batteries: Promise and Challenges, *ACS Energy Lett.* 5 (2020) 1537–1553. [https://doi.org/10.1021/ACSENERGYLETT.0C00468/SUPPL\\_FILE/NZ0C00468\\_SI\\_001.PDF](https://doi.org/10.1021/ACSENERGYLETT.0C00468/SUPPL_FILE/NZ0C00468_SI_001.PDF).
- [29] Global Passenger xEV Battery Market Doubled In 2021: 286 GWh, (n.d.). <https://insideevs.com/news/566626/global-xev-battery-market-2021/> (accessed May 7, 2022).
- [30] E. Martinez-Laserna, I. Gandiaga, E. Sarasketa-Zabala, J. Badeda, D.I. Stroe, M. Swierczynski, A. Goikoetxea, Battery second life: Hype, hope or reality? A critical review of the state of the art, *Renewable and Sustainable Energy Reviews*. 93 (2018) 701–718. <https://doi.org/10.1016/j.rser.2018.04.035>.
- [31] M.D. Slater, D. Kim, E. Lee, C.S. Johnson, Sodium-Ion Batteries, *Adv Funct Mater.* 23 (2013) 947–958. <https://doi.org/10.1002/ADFM.201200691>.
- [32] K. Chayambuka, G. Mulder, D.L. Danilov, P.H. L Notten, K. Chayambuka, G. Mulder VITO, D.L. Danilov, P.H. L Notten, Sodium-Ion Battery Materials and Electrochemical Properties Reviewed, *Adv Energy Mater.* 8 (2018) 1800079. <https://doi.org/10.1002/AENM.201800079>.
- [33] S. Lilley, Sodium-ion Batteries: Inexpensive and Sustainable Energy Storage, *Farady Insights*. (2022). <https://doi.org/10.1039/D1TA00376C>.
- [34] C. Vaalma, D. Buchholz, M. Weil, S. Passerini, A cost and resource analysis of sodium-ion batteries, *Nature Reviews Materials* 2018 3:4. 3 (2018) 1–11. <https://doi.org/10.1038/natrevmats.2018.13>.

- [35] Y. Wang, D. Zhou, V. Palomares, D. Shanmukaraj, B. Sun, X. Tang, C. Wang, M. Armand, T. Rojo, G. Wang, Revitalising sodium–sulfur batteries for non-high-temperature operation: a crucial review, *Energy Environ Sci.* 13 (2020) 3848–3879. <https://doi.org/10.1039/D0EE02203A>.
- [36] D. Kumar, S.K. Rajouria, S.B. Kuhar, D.K. Kanchan, Progress and prospects of sodium-sulfur batteries: A review, *Solid State Ion.* 312 (2017) 8–16. <https://doi.org/10.1016/J.SSI.2017.10.004>.
- [37] R. Dominko, J. Bitenc, R. Berthelot, M. Gauthier, G. Pagot, V. di Noto, Magnesium batteries: Current picture and missing pieces of the puzzle, *J Power Sources.* 478 (2020). <https://doi.org/10.1016/j.jpowsour.2020.229027>.
- [38] M.E. Arroyo-De Dompablo, A. Ponrouch, P. Johansson, M.R. Palacín, Achievements, Challenges, and Prospects of Calcium Batteries, *Chem Rev.* 120 (2020) 6331–6357. <https://doi.org/10.1021/acs.chemrev.9b00339>.
- [39] M.Y. Worku, Recent Advances in Energy Storage Systems for Renewable Source Grid Integration: A Comprehensive Review, *Sustainability (Switzerland).* 14 (2022). <https://doi.org/10.3390/su14105985>.
- [40] RFB Installations Map, (n.d.). <https://flowbatteryforum.com/wp-content/uploads/2020/07/200701-FB-World-Map.pdf> (accessed May 11, 2022).
- [41] H.F. Gibbard, Redox flow batteries for energy storage, 28th International Battery Seminar and Exhibit 2011. 2 (2011) 998–1029. <https://doi.org/10.1016/b978-0-12-819723-3.00049-4>.
- [42] E. Sánchez-Díez, E. Ventosa, M. Guarnieri, A. Trovò, C. Flox, R. Marcilla, F. Soavi, P. Mazur, E. Aranzabe, R. Ferret, Redox flow batteries: Status and perspective towards sustainable stationary energy storage, *J Power Sources.* 481 (2021). <https://doi.org/10.1016/j.jpowsour.2020.228804>.

- [43] J. Winsberg, T. Hagemann, T. Janoschka, M.D. Hager, U.S. Schubert, Redox-Flow Batteries: From Metals to Organic Redox-Active Materials, *Angewandte Chemie - International Edition*. 56 (2017). <https://doi.org/10.1002/anie.201604925>.
- [44] R. Xiong, B. Xiong, Q. Zhang, S. Shi, Y. Su, D. Zhang, Capacity Fading Model of Vanadium Redox Flow Battery Considering Water Molecules Migration, *Int J Green Energy*. 00 (2022) 1–10. <https://doi.org/10.1080/15435075.2021.2015599>.
- [45] M. Guarnieri, A. Trovò, F. Picano, Enhancing the efficiency of kW-class vanadium redox flow batteries by flow factor modulation: An experimental method, *Appl Energy*. 262 (2020) 114532. <https://doi.org/10.1016/j.apenergy.2020.114532>.
- [46] M. Park, J. Ryu, W. Wang, J. Cho, Material design and engineering of next-generation flow-battery technologies, *Nat Rev Mater*. 2 (2016). <https://doi.org/10.1038/natrevmats.2016.80>.
- [47] C. Zhang, L. Zhang, Y. Ding, S. Peng, X. Guo, Y. Zhao, G. He, G. Yu, Progress and Prospects of Next-Generation Redox Flow Batteries, *Energy Storage Mater*. 15 (2018) 324–350. <https://doi.org/10.1016/j.ensm.2018.06.008>.
- [48] D.G. Kwabi, Y. Ji, M.J. Aziz, Electrolyte Lifetime in Aqueous Organic Redox Flow Batteries: A Critical Review, *Chem Rev*. (2020). <https://doi.org/10.1021/acs.chemrev.9b00599>.
- [49] O. Nolte, I.A. Volodin, C. Stolze, M.D. Hager, U.S. Schubert, Trust is good, control is better: A review on monitoring and characterization techniques for flow battery electrolytes, *Mater Horiz*. 8 (2021) 1866–1925. <https://doi.org/10.1039/d0mh01632b>.
- [50] Q. Liu, A. Turhan, T.A. Zawodzinski, M.M. Mench, In situ potential distribution measurement in an all-vanadium flow battery, *Chemical Communications*. 49 (2013) 6292–6294. <https://doi.org/10.1039/c3cc42092b>.

- [51] M. Pugach, M. Kondratenko, S. Briola, A. Bischi, Numerical and experimental study of the flow-by cell for Vanadium Redox Batteries, *Energy Procedia*. 142 (2017) 3667–3674. <https://doi.org/10.1016/j.egypro.2017.12.260>.
- [52] E.C. Montoto, G. Nagarjuna, J.S. Moore, J. Rodríguez-López, Redox Active Polymers for Non-Aqueous Redox Flow Batteries: Validation of the Size-Exclusion Approach, *J Electrochem Soc.* 164 (2017) A1688–A1694. <https://doi.org/10.1149/2.1511707jes>.
- [53] Y. Chen, M. Zhou, Y. Xia, X. Wang, Y. Liu, Y. Yao, H. Zhang, Y. Li, S. Lu, W. Qin, X. Wu, Q. Wang, A Stable and High-Capacity Redox Targeting-Based Electrolyte for Aqueous Flow Batteries, *Joule*. 3 (2019) 2255–2267. <https://doi.org/10.1016/j.joule.2019.06.007>.
- [54] Y. Ding, C. Zhang, L. Zhang, Y. Zhou, G. Yu, Pathways to Widespread Applications: Development of Redox Flow Batteries Based on New Chemistries, *Chem*. 5 (2019) 1964–1987. <https://doi.org/10.1016/j.chempr.2019.05.010>.
- [55] S. Corcuera, M. Skyllas-Kazacos, State-of-Charge Monitoring and Electrolyte Rebalancing Methods for the Vanadium Redox Flow Battery, *European Chemical Bulletin*. 1 (2012) 511–519. <https://doi.org/10.17628/ECB.2012.1.511>.
- [56] X.Z. Yuan, C. Song, A. Platt, N. Zhao, H. Wang, H. Li, K. Fatih, D. Jang, A review of all-vanadium redox flow battery durability: Degradation mechanisms and mitigation strategies, *Int J Energy Res.* (2019) 1–40. <https://doi.org/10.1002/er.4607>.
- [57] M., Development of redox flow batteries. A historical bibliography, *J Power Sources*. 27 (1989) 219–234. [https://doi.org/10.1016/0378-7753\(89\)80037-0](https://doi.org/10.1016/0378-7753(89)80037-0).
- [58] VANADIUM REDOX FLOW BATTERY COMPANIES | Vanitec, (n.d.). <https://www.vanitec.org/vanadium-redox-flow-battery-vrfb-companies> (accessed May 12, 2022).

- [59] V. Mehta, J.S. Cooper, Review and analysis of PEM fuel cell design and manufacturing, *J Power Sources*. 114 (2003) 32–53. [https://doi.org/10.1016/S0378-7753\(02\)00542-6](https://doi.org/10.1016/S0378-7753(02)00542-6).
- [60] M. Guarnieri, A. Trovò, G. Marini, A. Sutto, P. Alotto, High current polarization tests on a 9 kW vanadium redox flow battery, *J Power Sources*. 431 (2019) 239–249. <https://doi.org/10.1016/J.JPOWSOUR.2019.05.035>.
- [61] M. Skyllas-Kazacos, M. Kazacos, State of charge monitoring methods for vanadium redox flow battery control, *J Power Sources*. 196 (2011) 8822–8827. <https://doi.org/10.1016/j.jpowsour.2011.06.080>.
- [62] X.Z. Yuan, C. Song, A. Platt, N. Zhao, H. Wang, H. Li, K. Fatih, D. Jang, A review of all-vanadium redox flow battery durability: Degradation mechanisms and mitigation strategies, *Int J Energy Res*. 43 (2019) 6599–6638. <https://doi.org/10.1002/ER.4607>.
- [63] V. Viswanathan, A. Crawford, D. Stephenson, S. Kim, W. Wang, B. Li, G. Coffey, E. Thomsen, G. Graff, P. Balducci, M. Kintner-Meyer, V. Sprenkle, Cost and performance model for redox flow batteries, *J Power Sources*. 247 (2014) 1040–1051. <https://doi.org/10.1016/j.jpowsour.2012.12.023>.
- [64] Y. Shi, C. Eze, B. Xiong, W. He, H. Zhang, T.M. Lim, A. Ukil, J. Zhao, Recent development of membrane for vanadium redox flow battery applications: A review, *Appl Energy*. 238 (2019) 202–224. <https://doi.org/10.1016/j.apenergy.2018.12.087>.
- [65] R.K. Gautam, A. Kumar, A review of bipolar plate materials and flow field designs in the all-vanadium redox flow battery, *J Energy Storage*. 48 (2022) 104003. <https://doi.org/10.1016/j.est.2022.104003>.
- [66] M.H. Chakrabarti, N.P. Brandon, S.A. Hajimolana, F. Tariq, V. Yufit, M.A. Hashim, M.A. Hussain, C.T.J. Low, P. V. Aravind, Application of carbon materials in redox flow batteries, *J Power Sources*. 253 (2014) 150–166. <https://doi.org/10.1016/j.jpowsour.2013.12.038>.

- [67] R. Wang, Y. Li, Carbon electrodes improving electrochemical activity and enhancing mass and charge transports in aqueous flow battery: Status and perspective, *Energy Storage Mater.* 31 (2020) 230–251. <https://doi.org/10.1016/j.ensm.2020.06.012>.
- [68] T. Jirabovornwisut, A. Arpornwichanop, A review on the electrolyte imbalance in vanadium redox flow batteries, *Int J Hydrogen Energy.* 44 (2019) 24485–24509. <https://doi.org/10.1016/j.ijhydene.2019.07.106>.
- [69] A. Trovò, Battery management system for industrial-scale vanadium redox flow batteries: Features and operation, *J Power Sources.* 465 (2020) 228229. <https://doi.org/10.1016/J.JPOWSOUR.2020.228229>.
- [70] A. Trovo, M. Guarnieri, Battery management system with testing protocols for kW-class vanadium redox flow batteries, *Proceedings - 2020 2nd IEEE International Conference on Industrial Electronics for Sustainable Energy Systems, IESES 2020.* (2020) 33–38. <https://doi.org/10.1109/IESES45645.2020.9210697>.
- [71] A. Clemente, R. Costa-Castelló, Redox flow batteries: A literature review oriented to automatic control, *Energies (Basel).* 13 (2020) 1–31. <https://doi.org/10.3390/en13174514>.
- [72] L. da Silva Lima, M. Quartier, A. Buchmayr, D. Sanjuan-Delmás, H. Laget, D. Corbisier, J. Mertens, J. Dewulf, Life cycle assessment of lithium-ion batteries and vanadium redox flow batteries-based renewable energy storage systems, *Sustainable Energy Technologies and Assessments.* 46 (2021) 101286. <https://doi.org/10.1016/J.SETA.2021.101286>.
- [73] H. Zhang, W. Lu, X. Li, Progress and Perspectives of Flow Battery Technologies, *Electrochemical Energy Reviews.* 2 (2019) 492–506. <https://doi.org/10.1007/S41918-019-00047-1/FIGURES/13>.
- [74] A. Khor, P. Leung, M.R. Mohamed, C. Flox, Q. Xu, L. An, R.G.A. Wills, J.R. Morante, A.A. Shah, Review of zinc-based hybrid flow batteries: From

- fundamentals to applications, *Mater Today Energy*. 8 (2018) 80–108. <https://doi.org/10.1016/J.MTENER.2017.12.012>.
- [75] Z. Xu, Q. Fan, Y. Li, J. Wang, P.D. Lund, Review of zinc dendrite formation in zinc bromine redox flow battery, *Renewable and Sustainable Energy Reviews*. 127 (2020) 109838. <https://doi.org/10.1016/J.RSER.2020.109838>.
- [76] S. Biswas, A. Senju, R. Mohr, T. Hodson, N. Karthikeyan, K.W. Knehr, A.G. Hsieh, X. Yang, B.E. Koel, D.A. Steingart, Minimal architecture zinc–bromine battery for low cost electrochemical energy storage, *Energy Environ Sci*. 10 (2017) 114–120. <https://doi.org/10.1039/C6EE02782B>.
- [77] S. Weber, J.F. Peters, M. Baumann, M. Weil, Life Cycle Assessment of a Vanadium Redox Flow Battery, *Environ Sci Technol*. 52 (2018) 10864–10873. [https://doi.org/10.1021/ACS.EST.8B02073/SUPPL\\_FILE/ES8B02073\\_SI\\_001.PDF](https://doi.org/10.1021/ACS.EST.8B02073/SUPPL_FILE/ES8B02073_SI_001.PDF).
- [78] F.R. Brushett, M.J. Aziz, K.E. Rodby, On Lifetime and Cost of Redox-Active Organics for Aqueous Flow Batteries, *ACS Energy Lett*. 5 (2020) 879–884. [https://doi.org/10.1021/ACSENERGYLETT.0C00140/ASSET/IMAGES/LARGE/NZ0C00140\\_0005.JPEG](https://doi.org/10.1021/ACSENERGYLETT.0C00140/ASSET/IMAGES/LARGE/NZ0C00140_0005.JPEG).
- [79] Discover Our Technology - KEMIWATT | Your Energy Bank, (n.d.). <https://kemiwatt.com/technology/> (accessed May 13, 2022).
- [80] Technology - Jena Batteries, (n.d.). <https://jenabatteries.de/en/technology#c191> (accessed May 13, 2022).
- [81] S.R. Narayan, A. Nirmalchandar, A. Murali, B. Yang, L. Hooper-Burkhardt, S. Krishnamoorthy, G.K.S. Prakash, Next-generation aqueous flow battery chemistries, *Curr Opin Electrochem*. 18 (2019) 72–80. <https://doi.org/10.1016/J.COEELEC.2019.10.010>.

- [82] G.P. Rajarathnam, M. Schneider, X. Sun, A.M. Vassallo, The Influence of Supporting Electrolytes on Zinc Half-Cell Performance in Zinc/Bromine Flow Batteries, *J Electrochem Soc.* 163 (2016) A5112–A5117. <https://doi.org/10.1149/2.0151601JES/XML>.
- [83] C. Ponce de León, A. Frías-Ferrer, J. González-García, D.A. Szánto, F.C. Walsh, Redox flow cells for energy conversion, *J Power Sources.* 160 (2006) 716–732. <https://doi.org/10.1016/J.JPOWSOUR.2006.02.095>.
- [84] Y.K. Zeng, X.L. Zhou, L. An, L. Wei, T.S. Zhao, A high-performance flow-field structured iron-chromium redox flow battery, *J Power Sources.* 324 (2016) 738–744. <https://doi.org/10.1016/J.JPOWSOUR.2016.05.138>.
- [85] V. Jalan, H. Stark, J. Giner, Requirements for optimization of electrodes and electrolyte for the iron/chromium Redox flow cell, n.d.
- [86] B.S. Jayathilake, E.J. Plichta, M.A. Hendrickson, S.R. Narayanan, Improvements to the Coulombic Efficiency of the Iron Electrode for an All-Iron Redox-Flow Battery, *J Electrochem Soc.* 165 (2018) A1630–A1638. <https://doi.org/10.1149/2.0451809JES/XML>.
- [87] L. Zhi, Z. Yuan, X. Li, Recent development and prospect of membranes for alkaline zinc-iron flow battery, *Advanced Membranes.* 2 (2022) 100029. <https://doi.org/10.1016/J.ADVMEM.2022.100029>.
- [88] L. Sanz, D. Lloyd, E. Magdalena, J. Palma, K. Kontturi, Description and performance of a novel aqueous all-copper redox flow battery, *J Power Sources.* 268 (2014) 121–128. <https://doi.org/10.1016/J.JPOWSOUR.2014.06.008>.
- [89] L. Faggiano, G. Lacarbonara, W.D. Badenhorst, L. Murtoimäki, L. Sanz, C. Arbizzani, Short thermal treatment of carbon felts for copper-based redox flow batteries, *J Power Sources.* 520 (2022) 230846. <https://doi.org/10.1016/J.JPOWSOUR.2021.230846>.

- [90] J.J. Chen, M.D. Symes, L. Cronin, Highly reduced and protonated aqueous solutions of [P<sub>2</sub>W<sub>18</sub>O<sub>62</sub>]<sup>6-</sup> for on-demand hydrogen generation and energy storage, *Nature Chemistry* 2018 10:10. 10 (2018) 1042–1047. <https://doi.org/10.1038/s41557-018-0109-5>.
- [91] J. Friedl, M. V. Holland-Cunz, F. Cording, F.L. Pfanschilling, C. Wills, W. McFarlane, B. Schricker, R. Fleck, H. Wolfschmidt, U. Stimming, Asymmetric polyoxometalate electrolytes for advanced redox flow batteries, *Energy Environ Sci.* 11 (2018) 3010–3018. <https://doi.org/10.1039/C8EE00422F>.
- [92] K. Saadi, P. Nanikashvili, Z. Tatus-Portnoy, S. Hardisty, V. Shokhen, M. Zysler, D. Zitoun, Crossover-tolerant coated platinum catalysts in hydrogen/bromine redox flow battery, *J Power Sources.* 422 (2019) 84–91. <https://doi.org/10.1016/J.JPOWSOUR.2019.03.043>.
- [93] M. Risbud, C. Menictas, M. Skyllas-Kazacos, J. Noack, Vanadium Oxygen Fuel Cell Utilising High Concentration Electrolyte, *Batteries* 2019, Vol. 5, Page 24. 5 (2019) 24. <https://doi.org/10.3390/BATTERIES5010024>.
- [94] K.T. Cho, P. Ridgway, A.Z. Weber, S. Haussener, V. Battaglia, V. Srinivasan, High Performance Hydrogen/Bromine Redox Flow Battery for Grid-Scale Energy Storage, *J Electrochem Soc.* 159 (2012) A1806–A1815. <https://doi.org/10.1149/2.018211JES/XML>.
- [95] A.D. Modestov, D. V Konev, O. V Tripachev, A.E. Antipov, Y. V Tolmachev, M.A. Vorotyntsev, A.D. odestov, D. V Konev, O. V Tripachev, A.E. Antipov, D. V Tolmachev, M.A. Vorotyntsev, A Hydrogen–Bromate Flow Battery for Air-Deficient Environments, *Energy Technology.* 6 (2018) 242–245. <https://doi.org/10.1002/ENTE.201700447>.
- [96] J. Luo, B. Hu, M. Hu, Y. Zhao, T.L. Liu, Status and Prospects of Organic Redox Flow Batteries toward Sustainable Energy Storage, *ACS Energy Lett.* 4 (2019) 2220–2240. <https://doi.org/10.1021/acsenerylett.9b01332>.

- [97] B. Hu, Y. Tang, J. Luo, G. Grove, Y. Guo, T.L. Liu, Improved radical stability of viologen anolytes in aqueous organic redox flow batteries, *Chemical Communications*. 54 (2018) 6871–6874. <https://doi.org/10.1039/c8cc02336k>.
- [98] B. Hu, C. Debruler, Z. Rhodes, T.L. Liu, Long-Cycling aqueous organic Redox flow battery (AORFB) toward sustainable and safe energy storage, *J Am Chem Soc*. 139 (2017) 1207–1214. <https://doi.org/10.1021/JACS.6B10984>.
- [99] J. Winsberg, C. Stolze, S. Muench, F. Liedl, M.D. Hager, U.S. Schubert, TEMPO/Phenazine Combi-Molecule: A Redox-Active Material for Symmetric Aqueous Redox-Flow Batteries, *ACS Energy Lett*. 1 (2016) 976–980. <https://doi.org/10.1021/ACSENERGYLETT.6B00413>.
- [100] Y. Ji, M.A. Goulet, D.A. Pollack, D.G. Kwabi, S. Jin, D. De Porcellinis, E.F. Kerr, R.G. Gordon, M.J. Aziz, A Phosphonate-Functionalized Quinone Redox Flow Battery at Near-Neutral pH with Record Capacity Retention Rate, *Adv Energy Mater*. 9 (2019). <https://doi.org/10.1002/AENM.201900039>.
- [101] X. Wei, W. Xu, J. Huang, L. Zhang, E. Walter, C. Lawrence, M. Vijayakumar, W.A. Henderson, T. Liu, L. Cosimbescu, B. Li, V. Sprenkle, W. Wang, Radical Compatibility with Nonaqueous Electrolytes and Its Impact on an All-Organic Redox Flow Battery, *Angewandte Chemie - International Edition*. 54 (2015) 8684–8687. <https://doi.org/10.1002/ANIE.201501443>.
- [102] Y. Zhu, F. Yang, Z. Niu, H. Wu, Y. He, H. Zhu, J. Ye, Y. Zhao, X. Zhang, Enhanced cyclability of organic redox flow batteries enabled by an artificial bipolar molecule in neutral aqueous electrolyte, *J Power Sources*. 417 (2019) 83–89. <https://doi.org/10.1016/J.JPOWSOUR.2019.02.021>.
- [103] and S.-H.M. Sung-Hee Shin, Sung-Hyun Yun, A review on current development of non-aqueous redox flow batteries for perspective design of their membranes with characterization methods, *RSC Adv*. (2014) 10–15. <https://doi.org/10.1039/C4RA00230J>.

- [104] M. Duduta, B. Ho, V.C. Wood, P. Limthongkul, V.E. Brunini, W.C. Carter, Y.M. Chiang, Semi-solid lithium rechargeable flow battery, *Adv Energy Mater.* 1 (2011) 511–516. <https://doi.org/10.1002/aenm.201100152>.
- [105] Y. Li, C. He, E. V Timofeeva, Y. Ding, J. Parrondo, C. Segre, V. Ramani,  $\beta$ -Nickel hydroxide cathode material for nano-suspension redox flow batteries, (2017). <https://doi.org/10.1007/s11708-017-0496-0>.
- [106] T. Janoschka, N. Martin, U. Martin, C. Friebe, S. Morgenstern, H. Hiller, M.D. Hager, U.S. Schubert, An aqueous, polymer-based redox-flow battery using non-corrosive, safe, and low-cost materials, *Nature.* 527 (2015) 78–81. <https://doi.org/10.1038/nature15746>.
- [107] J. Winsberg, S. Muench, T. Hagemann, S. Morgenstern, T. Janoschka, M. Billing, F.H. Schacher, G. Hauffman, J.F. Gohy, S. Hoepfener, M.D. Hager, U.S. Schubert, Polymer/zinc hybrid-flow battery using block copolymer micelles featuring a TEMPO corona as catholyte, *Polym Chem.* 7 (2016) 1711–1718. <https://doi.org/10.1039/C5PY02036K>.
- [108] W. Yan, C. Wang, J. Tian, G. Zhu, L. Ma, Y. Wang, R. Chen, Y. Hu, L. Wang, T. Chen, J. Ma, Z. Jin, All-polymer particulate slurry batteries, *Nat Commun.* 10 (2019) 1–11. <https://doi.org/10.1038/s41467-019-10607-0>.
- [109] G. Di Florio, I. Pucher, P. Todeschi, M.C. Baratto, R. Basosi, E. Busi, Assessment of semi-organic electrolytes for redox flow battery: Life cycle assessment as a tool to steer industry toward green chemistry, *J Clean Prod.* 343 (2022) 130899. <https://doi.org/10.1016/J.JCLEPRO.2022.130899>.
- [110] R. Yan, Q. Wang, R. Yan, Q. Wang, Redox-Targeting-Based Flow Batteries for Large-Scale Energy Storage, *Advanced Materials.* 30 (2018) 1802406. <https://doi.org/10.1002/ADMA.201802406>.
- [111] E. Zanzola, C.R. Dennison, A. Battistel, P. Peljo, H. Vrabel, V. Amstutz, H.H. Girault, Redox Solid Energy Boosters for Flow Batteries: Polyaniline as a Case

- Study, *Electrochim Acta.* 235 (2017) 664–671.  
<https://doi.org/10.1016/j.electacta.2017.03.084>.
- [112] M. Zhou, Y. Chen, Q. Zhang, S. Xi, J. Yu, Y. Du, Y.Y.-S.S. Hu, Q. Wang, M. Zhou, Y. Chen, J. Yu, Q. Wang, Q. Zhang, Y.Y.-S.S. Hu, S. Xi, Y. Du, Na<sub>3</sub>V<sub>2</sub>(PO<sub>4</sub>)<sub>3</sub> as the Sole Solid Energy Storage Material for Redox Flow Sodium-Ion Battery, *Adv Energy Mater.* 9 (2019) 1901188. <https://doi.org/10.1002/AENM.201901188>.
- [113] Y. Cheng, X. Wang, S. Huang, W. Samarakoon, S. Xi, Y. Ji, H. Zhang, F. Zhang, Y. Du, Z. Feng, S. Adams, Q. Wang, Redox Targeting-Based Vanadium Redox-Flow Battery, *ACS Energy Lett.* 4 (2019) 3028–3035. <https://doi.org/10.1021/ACSENERGYLETT.9B01939>.
- [114] M. Zhou, Q. Huang, T.N. Pham Truong, J. Ghilane, Y.G. Zhu, C. Jia, R. Yan, L. Fan, H. Randriamahazaka, Q. Wang, Nernstian-Potential-Driven Redox-Targeting Reactions of Battery Materials, *Chem.* 3 (2017) 1036–1049. <https://doi.org/10.1016/J.CHEMPR.2017.10.003>.
- [115] T. Páez, A. Martínez-Cuezva, J. Palma, E. Ventosa, Mediated alkaline flow batteries: From fundamentals to application, *ACS Appl Energy Mater.* 2 (2019) 8328–8336. <https://doi.org/10.1021/ACSAEM.9B01826>.
- [116] J.F. Vivo-Vilches, A. Nadeina, N. Rahbani, V. Seznec, D. Larcher, E. Baudrin, LiFePO<sub>4</sub>-ferri/ferrocyanide redox targeting aqueous posolyte: Set-up, efficiency and kinetics, *J Power Sources.* 488 (2021) 229387. <https://doi.org/10.1016/j.jpowsour.2020.229387>.
- [117] Y. Chen, M. Zhou, Y. Xia, X. Wang, Y. Liu, Y. Yao, H. Zhang, Y. Li, S. Lu, W. Qin, X. Wu, Q. Wang, A Stable and High-Capacity Redox Targeting-Based Electrolyte for Aqueous Flow Batteries, *Joule.* 3 (2019) 2255–2267. <https://doi.org/10.1016/J.JOULE.2019.06.007>.
- [118] M. Zhou, Y. Chen, M. Salla, H. Zhang, X. Wang, S.R. Mothe, Q. Wang, Single-Molecule Redox-Targeting Reactions for a pH-Neutral Aqueous Organic Redox

Flow Battery, *Angewandte Chemie - International Edition*. 59 (2020) 14286–14291. <https://doi.org/10.1002/ANIE.202004603>.

- [119] H. Wang, S.Y. Sayed, E.J. Lubner, B.C. Olsen, S.M. Shirurkar, S. Venkatakrisnan, U.M. Tefashe, A.K. Farquhar, E.S. Smotkin, R.L. McCreery, J.M. Buriak, Redox Flow Batteries: How to Determine Electrochemical Kinetic Parameters, *ACS Nano*. 14 (2020) 2575–2584. <https://doi.org/10.1021/acsnano.0c01281>.
- [120] C. Ding, X. Ni, X. Li, X. Xi, X. Han, X. Bao, H. Zhang, Effects of phosphate additives on the stability of positive electrolytes for vanadium flow batteries, *Electrochim Acta*. 164 (2015) 307–314. <https://doi.org/10.1016/J.ELECTACTA.2015.02.187>.
- [121] T. Köhler, J. Hanzig, V. Koroteev, Optical spectroscopy as a tool for battery research, *Physical Sciences Reviews*. 4 (2019). <https://doi.org/10.1515/PSR-2017-0154>.
- [122] T. Liu, X. Wei, Z. Nie, V. Sprenkle, W. Wang, A Total Organic Aqueous Redox Flow Battery Employing a Low Cost and Sustainable Methyl Viologen Anolyte and 4-HO-TEMPO Catholyte, *Adv Energy Mater*. 6 (2016). <https://doi.org/10.1002/AENM.201501449>.
- [123] M. Skyllas-Kazacos, L. Cao, M. Kazacos, N. Kausar, A. Mousa, Vanadium Electrolyte Studies for the Vanadium Redox Battery—A Review, *ChemSusChem*. 9 (2016) 1521–1543. <https://doi.org/10.1002/cssc.201600102>.
- [124] Y. Yao, J. Lei, Y. Shi, F. Ai, Y.C. Lu, Assessment methods and performance metrics for redox flow batteries, *Nat Energy*. 6 (2021) 582–588. <https://doi.org/10.1038/s41560-020-00772-8>.
- [125] Q. Xu, Y.N. Ji, L.Y. Qin, P.K. Leung, F. Qiao, Y.S. Li, H.N. Su, Evaluation of redox flow batteries goes beyond round-trip efficiency: A technical review, *J Energy Storage*. 16 (2018) 108–115. <https://doi.org/10.1016/j.est.2018.01.005>.

- [126] J. Yu, L. Fan, R. Yan, M. Zhou, Q. Wang, Redox Targeting-Based Aqueous Redox Flow Lithium Battery, *ACS Energy Lett.* 3 (2018) 2314–2320. <https://doi.org/10.1021/ACSENERGYLETT.8B01420>.
- [127] Z. Duan, Z. Qu, Q. Ren, J. Zhang, Review of Bipolar Plate in Redox Flow Batteries: Materials, Structures, and Manufacturing, *Electrochemical Energy Reviews* 2021 4:4. 4 (2021) 718–756. <https://doi.org/10.1007/S41918-021-00108-4>.
- [128] Z. Liang, N.H. Attanayake, K. V. Greco, B.J. Neyhouse, J.L. Barton, A.P. Kaur, W.L. Eubanks, F.R. Brushett, J. Landon, S.A. Odom, Comparison of Separators vs Membranes in Nonaqueous Redox Flow Battery Electrolytes Containing Small Molecule Active Materials, *ACS Appl Energy Mater.* 4 (2021) 5443–5451. [https://doi.org/10.1021/ACSAEM.1C00017/SUPPL\\_FILE/AE1C00017\\_SI\\_001.PDF](https://doi.org/10.1021/ACSAEM.1C00017/SUPPL_FILE/AE1C00017_SI_001.PDF).
- [129] X. Wang, A. Lashgari, J. Chai, J. “Jimmy” Jiang, A membrane-free, aqueous/nonaqueous hybrid redox flow battery, *Energy Storage Mater.* 45 (2022) 1100–1108. <https://doi.org/10.1016/J.ENSM.2021.11.008>.
- [130] G. Li, W. Chen, H. Zhang, Y. Gong, F. Shi, J. Wang, R. Zhang, G. Chen, Y. Jin, T. Wu, Z. Tang, Y. Cui, G. Li, W. Chen, H. Zhang, Y. Gong, F. Shi, J. Wang, R. Zhang, G. Chen, Y. Jin, T. Wu, Y. Cui, Z. Tang, Membrane-Free Zn/MnO<sub>2</sub> Flow Battery for Large-Scale Energy Storage, *Adv Energy Mater.* 10 (2020) 1902085. <https://doi.org/10.1002/AENM.201902085>.
- [131] J. Yuan, Z.Z. Pan, Y. Jin, Q. Qiu, C. Zhang, Y. Zhao, Y. Li, Membranes in non-aqueous redox flow battery: A review, *J Power Sources.* 500 (2021) 229983. <https://doi.org/10.1016/J.JPOWSOUR.2021.229983>.
- [132] X. Shi, O.C. Esan, X. Huo, Y. Ma, Z. Pan, L. An, T.S. Zhao, Polymer Electrolyte Membranes for Vanadium Redox Flow Batteries: Fundamentals and Applications, *Prog Energy Combust Sci.* 85 (2021) 100926. <https://doi.org/10.1016/J.PECS.2021.100926>.

- [133] X.Z. Yuan, H. Li, S. Zhang, J. Martin, H. Wang, A review of polymer electrolyte membrane fuel cell durability test protocols, *J Power Sources*. 196 (2011) 9107–9116. <https://doi.org/10.1016/j.jpowsour.2011.07.082>.
- [134] T. Mohammadi, M. Skyllas-Kazacos, Evaluation of the chemical stability of some membranes in vanadium solution, *J. of Appl. Electrochemistry*. 27 (1996) 153–160. <https://doi.org/10.1023/A:1018495722379>.
- [135] L.F. Arenas, C. Ponce de León, F.C. Walsh, Engineering aspects of the design, construction and performance of modular redox flow batteries for energy storage, *J Energy Storage*. 11 (2017) 119–153. <https://doi.org/10.1016/j.est.2017.02.007>.
- [136] Y. Shi, C. Eze, B. Xiong, W. He, H. Zhang, T.M. Lim, A. Ukil, J. Zhao, Recent development of membrane for vanadium redox flow battery applications: A review, *Appl Energy*. 238 (2019) 202–224. <https://doi.org/10.1016/j.apenergy.2018.12.087>.
- [137] T. Liu, X. Li, H. Zhang, J. Chen, Progress on the electrode materials towards vanadium flow batteries (VFBs) with improved power density, *Journal of Energy Chemistry*. (2018). <https://doi.org/10.1016/j.jechem.2018.07.003>.
- [138] A. Forner-Cuenca, F.R. Brushett, Engineering porous electrodes for next-generation redox flow batteries: recent progress and opportunities, *Curr Opin Electrochem*. 18 (2019) 113–122. <https://doi.org/10.1016/j.coelec.2019.11.002>.
- [139] D. Reynard, H. Vrabel, C.R. Dennison, A. Battistel, H. Girault, On-Site Purification of Copper-Contaminated Vanadium Electrolytes by using a Vanadium Redox Flow Battery, *ChemSusChem*. 12 (2019) 1222–1228. <https://doi.org/10.1002/CSSC.201802895>.
- [140] A. Trovò, W. Zamboni, M. Guarnieri, Multichannel Electrochemical Impedance Spectroscopy and equivalent circuit synthesis of a large-scale vanadium redox flow battery, *J Power Sources*. 493 (2021). <https://doi.org/10.1016/J.JPOWSOUR.2021.229703>.

- [141] C.N. Sun, F.M. Delnick, D.S. Aaron, A.B. Papandrew, M.M. Mench, T.A. Zawodzinski, Probing electrode losses in all-vanadium redox flow batteries with impedance spectroscopy, *ECS Electrochemistry Letters*. 2 (2013). <https://doi.org/10.1149/2.001305EEL>.
- [142] M.A. Goulet, M. Skyllas-Kazacos, E. Kjeang, The importance of wetting in carbon paper electrodes for vanadium redox reactions, *Carbon N Y*. 101 (2016) 390–398. <https://doi.org/10.1016/j.carbon.2016.02.011>.
- [143] P. Mazúr, J. Mrlík, J. Beneš, J. Pocič, J. Vrána, J. Dundálek, J. Kosek, Performance evaluation of thermally treated graphite felt electrodes for vanadium redox flow battery and their four-point single cell characterization, *J Power Sources*. 380 (2018) 105–114. <https://doi.org/10.1016/J.JPOWSOUR.2018.01.079>.
- [144] D. Dixon, D.J. Babu, J. Langner, M. Bruns, L. Pfaffmann, A. Bhaskar, J.J. Schneider, F. Scheiba, H. Ehrenberg, Effect of oxygen plasma treatment on the electrochemical performance of the rayon and polyacrylonitrile based carbon felt for the vanadium redox flow battery application, *J Power Sources*. 332 (2016) 240–248. <https://doi.org/10.1016/J.JPOWSOUR.2016.09.070>.
- [145] T. Liu, X. Li, C. Xu, H. Zhang, Activated Carbon Fiber Paper Based Electrodes with High Electrocatalytic Activity for Vanadium Flow Batteries with Improved Power Density, *ACS Appl Mater Interfaces*. 9 (2017) 4626–4633. <https://doi.org/10.1021/acsami.6b14478>.
- [146] M. Taş, G. Elden, A comprehensive review of carbon-based and metal-based electrocatalysts in the vanadium redox flow battery, *Energy Storage*. (2021) 1–22. <https://doi.org/10.1002/est2.265>.
- [147] J. Charvát, P. Mazúr, J. Dundálek, J. Pocič, J. Vrána, J. Mrlík, J. Kosek, S. Dinter, Performance enhancement of vanadium redox flow battery by optimized electrode compression and operational conditions, *J Energy Storage*. 30 (2020) 101468. <https://doi.org/10.1016/j.est.2020.101468>.

- [148] K. V Greco, A. Forner-cuenca, A. Mularczyk, J. Eller, F.R. Brushett, Elucidating the Nuanced Effects of Thermal Pretreatment on Carbon Paper Electrodes for Vanadium Redox Flow Batteries, (2018). <https://doi.org/10.1021/acsami.8b15793>.
- [149] A. Forner-Cuenca, E.E. Penn, A.M. Oliveira, F.R. Brushett, Exploring the Role of Electrode Microstructure on the Performance of Non-Aqueous Redox Flow Batteries, *J Electrochem Soc.* 166 (2019) A2230–A2241. <https://doi.org/10.1149/2.0611910jes>.
- [150] C.R. Dennison, E. Agar, B. Akuzum, E.C. Kumbur, Enhancing Mass Transport in Redox Flow Batteries by Tailoring Flow Field and Electrode Design, *J Electrochem Soc.* 163 (2015) A5163--A5169. <https://doi.org/10.1149/2.0231601jes>.
- [151] P. Mazur, J. Mrlik, J. Pocedic, J. Vrana, J. Dundalek, J. Kosek, T. Bystron, Effect of graphite felt properties on the long-term durability of negative electrode in vanadium redox flow battery, *J Power Sources.* 414 (2019) 354–365. <https://doi.org/10.1016/j.jpowsour.2019.01.019>.
- [152] T.C. Gokoglan, S.K. Pahari, A. Hamel, R. Howland, P.J. Cappillino, E. Agar, Operando Spectroelectrochemical Characterization of a Highly Stable Bioinspired Redox Flow Battery Active Material, *J Electrochem Soc.* 166 (2019) A1745–A1751. <https://doi.org/10.1149/2.0271910JES/XML>.
- [153] J.D. Saraidaridis, B.M. Bartlett, C.W. Monroe, Spectroelectrochemistry of Vanadium Acetylacetonate and Chromium Acetylacetonate for Symmetric Nonaqueous Flow Batteries, *J Electrochem Soc.* 163 (2016) A1239–A1246. <https://doi.org/10.1149/2.0441607JES/XML>.
- [154] N. Roznyatovskaya, J. Noack, M. Fühl, K. Pinkwart, J. Tübke, Towards an all-vanadium redox-flow battery electrolyte: electrooxidation of V(III) in V(IV)/V(III) redox couple, *Electrochim Acta.* 211 (2016) 926–932. <https://doi.org/10.1016/J.ELECTACTA.2016.06.073>.

- [155] N. Roznyatovskaya, J. Noack, K. Pinkwart, J. Tübke, Aspects of electron transfer processes in vanadium redox-flow batteries, *Curr Opin Electrochem.* 19 (2020) 42–48. <https://doi.org/10.1016/j.coelec.2019.10.003>.
- [156] V. Di Noto, K. Vezzù, G. Crivellaro, G. Pagot, C. Sun, L. Meda, I.A. Rutkowska, P.J. Kulesza, T.A. Zawodzinski, A general electrochemical formalism for vanadium redox flow batteries, *Electrochim Acta.* 408 (2022) 139937. <https://doi.org/10.1016/j.electacta.2022.139937>.
- [157] A.A. Kurilovich, A. Trovò, M. Pugach, K.J. Stevenson, M. Guarnieri, Prospect of Modeling Industrial Scale Flow Batteries – from Experimental Data to Accurate Overpotential Identification, *SSRN Electronic Journal.* (2022). <https://doi.org/10.2139/SSRN.4057894>.
- [158] B. Satola, Review—Bipolar Plates for the Vanadium Redox Flow Battery, *J Electrochem Soc.* 168 (2021) 060503. <https://doi.org/10.1149/1945-7111/AC0177>.
- [159] F. Jiang, W. Liao, T. Ayukawa, S.H. Yoon, K. Nakabayashi, J. Miyawaki, Enhanced performance and durability of composite bipolar plate with surface modification of cactus-like carbon nanofibers, *J Power Sources.* 482 (2021) 228903. <https://doi.org/10.1016/J.JPOWSOUR.2020.228903>.
- [160] P. Qian, H. Zhang, J. Chen, Y. Wen, Q. Luo, Z. Liu, D. You, B. Yi, A novel electrode-bipolar plate assembly for vanadium redox flow battery applications, *J Power Sources.* 175 (2008) 613–620. <https://doi.org/10.1016/J.JPOWSOUR.2007.09.006>.
- [161] B. Satola, C.N. Kirchner, L. Komsysińska, G. Wittstock, Chemical Stability of Graphite-Polypropylene Bipolar Plates for the Vanadium Redox Flow Battery at Resting State, *J Electrochem Soc.* 163 (2016) A2318–A2325. <https://doi.org/10.1149/2.0841610jes>.
- [162] X.Z. Yuan, C. Song, A. Platt, N. Zhao, H. Wang, H. Li, K. Fatih, D. Jang, A review of all-vanadium redox flow battery durability: Degradation mechanisms and

- mitigation strategies, *Int J Energy Res.* 43 (2019) 6599–6638. <https://doi.org/10.1002/ER.4607>.
- [163] F.J. Oldenburg, A. Ouarga, T.J. Schmidt, L. Gubler, Accelerated Stress Test Method for the Assessment of Membrane Lifetime in Vanadium Redox Flow Batteries, *ACS Appl Mater Interfaces.* 11 (2019) 47917–47928. [https://doi.org/10.1021/ACSAMI.9B15736/ASSET/IMAGES/LARGE/AM9B15736\\_0002.JPEG](https://doi.org/10.1021/ACSAMI.9B15736/ASSET/IMAGES/LARGE/AM9B15736_0002.JPEG).
- [164] C. Minke, T. Hickmann, A.R. Dos Santos, U. Kunz, T. Turek, Cost and performance prospects for composite bipolar plates in fuel cells and redox flow batteries, *J Power Sources.* 305 (2016) 182–190. <https://doi.org/10.1016/j.jpowsour.2015.11.052>.
- [165] N.A. Gvozdik, K.J. Stevenson, In situ spectroelectrochemical Raman studies of vanadyl-ion oxidation mechanisms on carbon paper electrodes for vanadium flow batteries, *Electrochim Acta.* 383 (2021) 138300. <https://doi.org/10.1016/j.electacta.2021.138300>.
- [166] D. Aaron, Z. Tang, A.B. Papandrew, T.A. Zawodzinski, Polarization curve analysis of all-vanadium redox flow batteries, *J Appl Electrochem.* 41 (2011) 1175–1182. <https://doi.org/10.1007/s10800-011-0335-7>.
- [167] P. Mazur, J. Mrlik, J. Charvat, J. Pcedic, J. Vrana, J. Dundalek, J. Kosek, A complex four-point method for the evaluation of ohmic and faradaic losses within a redox flow battery single-cell, *MethodsX.* 6 (2019) 534–539. <https://doi.org/10.1016/j.mex.2019.03.007>.
- [168] M. Pavelka, F. Wandschneider, P. Mazur, Thermodynamic derivation of open circuit voltage in vanadium redox flow batteries, *J Power Sources.* 293 (2015) 400–408. <https://doi.org/10.1016/j.jpowsour.2015.05.049>.
- [169] M. Cecchetti, A. Casalegno, M. Zago, Local potential measurement through reference electrodes in vanadium redox flow batteries: Evaluation of overpotentials

- and electrolytes imbalance, *J Power Sources*. 400 (2018) 218–224. <https://doi.org/10.1016/j.jpowsour.2018.08.033>.
- [170] H. Lim, J.S. Yi, D. Lee, Operando studies on through-plane cell voltage losses in vanadium redox flow battery, *J Power Sources*. 422 (2019) 65–72. <https://doi.org/10.1016/j.jpowsour.2019.03.016>.
- [171] E. Ruban, A. Stepashkin, N. Gvozdik, D. Konev, N. Kartashova, A. Antipov, M. Lyange, A. Usenko, Carbonized elastomer composite filled with hybrid carbon fillers for vanadium redox flow battery bipolar plates, *Mater Today Commun*. 26 (2021) 101967. <https://doi.org/10.1016/j.mtcomm.2020.101967>.
- [172] P. Loktionov, N. Kartashova, D. Konev, L. Abunaeva, A. Antipov, E. Ruban, A. Terent'ev, N. Gvozdik, M. Lyange, A. Usenko, K. Stevenson, Fluoropolymer impregnated graphite foil as a bipolar plates of vanadium flow battery, *Int J Energy Res*. (2021) 1–10. <https://doi.org/10.1002/er.7088>.
- [173] E.Y. Kozhunova, N.A. Gvozdik, M. V. Motyakin, O. V. Vyshivannaya, K.J. Stevenson, D.M. Itkis, A. V. Chertovich, Redox-Active Aqueous Microgels for Energy Storage Applications, *Journal of Physical Chemistry Letters*. 11 (2020) 1–5. <https://doi.org/10.1021/acs.jpcllett.0c03164>.
- [174] N.A. Gvozdik, A.A. Kurbatova, N.A. Ovsyannikov, M.A. Pogosova, K.J. Stevenson, Influence of conductive additives in a nano-impact electrochemistry study of single  $\text{LiMn}_2\text{O}_4$  particles, *Electrochem Commun*. (2022) 107304. <https://doi.org/10.1016/j.elecom.2022.107304>.